Evaluating the impact of the spectral configuration of airborne hyperspectral imaging sensors on the accurate estimation of Solar-induced chlorophyll fluorescence (SIF)

Anirudh Belwalkar

ORCID: 0000-0001-6676-5709

Submitted in total fulfilment for the degree of

Doctor of Philosophy

Department of Infrastructure Engineering

Faculty of Engineering and Information Technology

The University of Melbourne

August 2023

Abstract

Climate change has devastated agriculture and food production. In recent decades heatwaves and droughts have made it harder to meet global food demand. Understanding photosynthesis, plant adaptation, and how photosynthetic efficiency affects crop yields is essential for developing stress-resistant plants and increasing crop production. This climate crisis underlines the need for systems that evaluate photosynthetic efficiency to monitor plant health and increase efficiency. Solar-induced chlorophyll fluorescence (SIF) is a faint electromagnetic signal that can indicate plant stress and photosynthetic efficiency. Accurate SIF quantification requires sub-nanometer resolution sensors. However, sub-nanometer resolution imaging sensors onboard airborne platforms are expensive and difficult to operate, hindering their widespread operational use for plant phenotyping, stress detection, and precision agriculture applications. Consideration should therefore turn towards development of adequate airborne imaging sensors and approaches that use physically-based models to accurately interpret SIF from the sensor.

This PhD thesis investigates whether commonly accessible narrow-band imaging sensors could potentially substitute for sub-nanometer imaging sensors in operational SIF retrieval for plant phenotyping, stress detection, and precision agriculture applications. A narrow-band imaging sensor and a sub-nanometer imaging sensor flown in tandem were compared for SIF. Physically-based models and machine learning were used to model the effect of spectral resolution (SR) on narrow-band far-red SIF (SIF_{760}) estimates. Furthermore, an exploratory analysis was conducted to investigate the potential of solar Fraunhofer lines in the SIF emission region for estimating leaf nitrogen concentration across a field and detecting biotic stress in infected trees, using airborne sub-nanometer hyperspectral imagery.

Airborne SIF_{760} retrievals from a narrow-band imaging sensor (5.8-nm FWHM) and a sub-nanometer imaging sensor (0.2-nm FWHM) were compared across two wheat and maize phenotyping

trials grown under varied nitrogen fertiliser rates over the 2019–2021 growing seasons. The correlation between SIF_{760} values obtained from the two sensors was found to be significant (R^2 = 0.77–0.9, $p < 0.01$). Notably, the narrow-band imager yielded higher estimates of SIF_{760} than the sub-nanometer imager did. The findings of this study suggest that narrow-band imaging sensors may accurately detect field-wide variations in relative SIF_{760}, particularly when nitrogen fertilisation levels vary. The next part of this study focused on improving narrow-band-derived absolute SIF_{760} levels to reduce systematic bias. A Soil Canopy Observation, Photochemistry, and Energy fluxes (SCOPE) model with Support Vector Regression (SVR) scaling airborne narrow-band SIF_{760} values to 1-nm FWHM was used. As shown by the normalised root-mean-square error (nRMSE) values of 2.45–5.28% for the SCOPE simulated dataset and 4.5–16% for the airborne hyperspectral dataset, the estimated SIF_{760} at 1-nm FWHM showed good agreement with the reference SIF_{760}. This study suggests that the proposed SIF_{760} modelling approach can improve the understanding of relative SIF_{760} levels quantified by narrow-band hyperspectral imaging sensors in stress detection and plant physiological monitoring applications.

An exploratory investigation of sub-nanometer imagery-derived Fraunhofer lines (FLs) concludes the thesis. The study found that including depths for two FLs near oxygen absorption features improved leaf nitrogen estimation. In addition, it was observed that biotic-induced stress was linked to FL activation in the red and far-red spectral regions. As biotic-induced stress level increased, the sensitivity of FLs in the discernment of and differentiation between symptomatic and asymptomatic trees also increased. These findings indicate the need for additional research on these specialised potential benefits of FLs, which would allow better understanding and more efficient management of the various factors that affect the physiological status of plants.

Declaration

This is to certify that:

1. The thesis comprises only my original work towards the degree of Doctor of Philosophy,
2. Due acknowledgement has been made in the text to all other material used,
3. The thesis has fewer than 80,000 words in length, exclusive of tables, figures, bibliographies, maps, and appendix.

Anirudh Belwalkar

Melbourne, August 2023

Preface

This thesis is comprised of three main research chapters (Chapters 2-4) that are all presented in manuscript format. Chapter two has been published in an international journal as a research article, Chapter three has been submitted for publication, Chapter four is currently being drafted for submission to a journal. These three research Chapters are co-authored with supervisors and research collaborators. The use of 'we' and 'our' in these research chapters reflects the contributions of coauthors. In each publication, I was responsible for over 60% of the authorship, including research conceptualization, modelling, statistical analysis, interpretation of results, and drafting and finalising the manuscripts. Below are the bibliographic details for the three research chapters.

1. Chapter 2 (Paper 1) - **Belwalkar, A.**, Poblete, T., Longmire, A., Hornero, A., Hernandez-Clemente, R., Zarco-Tejada, P.J., 2022. **Evaluation of SIF retrievals from narrow-band and sub-nanometer airborne hyperspectral imagers flown in tandem: modelling and validation in the context of plant phenotyping**. Remote Sens. Environ. 273, 112986. https://doi.org/10.1016/j.rse.2022.112986.

2. Chapter 3 (Paper 2) - **Belwalkar, A.**, Poblete, T., A., Hornero, A., Hernandez-Clemente, R., Zarco-Tejada, P.J. **Accurate SIF quantification from a narrow-band airborne hyperspectral imager using SCOPE: assessment with sub-nanometer imagery** (under review in the journal *Remote Sensing of Environment*).

3. Chapter 4 (Paper 3) - **Belwalkar, A.**, Poblete, T., A., Hornero, A., Hernandez-Clemente, R., Zarco-Tejada, P.J. **Prospects of solar Fraunhofer lines derived from sub-nanometer hyperspectral imagery for assessing a/biotic stress** (currently being drafted for submission to the journal *Remote Sensing of Environment*).

The original version of the published research article is included in Appendix D. In addition to the journal articles, this thesis also produced three conference publications, which are included in

Appendices E through G. The three conference publications correspond to the three research chapters. Below are the bibliographic specifications of the conference publications:

1. **Belwalkar, A.**, Poblete, T., Longmire, A., Hornero, A., Zarco-Tejada, P.J., 2021. **Comparing the retrieval of chlorophyll fluorescence from two airborne hyperspectral imagers with different spectral resolutions for plant phenotyping studies**. In: Proc. IEEE International Geoscience and Remote Sensing Symposium (IGARSS), 12–16 July 2021, Brussels, Belgium, pp. 5845–5848. https://doi.org/10.1109/IGARSS47720.2021.9553265.

2. **Belwalkar, A.**, Poblete, T., Hornero, A., Zarco-Tejada, P.J., 2022. **Accounting for the spectral resolution on SIF retrieval from a narrow-band airborne imager using SCOPE**. In: Proc. IEEE International Geoscience and Remote Sensing Symposium (IGARSS), 17–22 July 2022, Kuala Lumpur, Malaysia, pp. 5440–5443. https://doi.org/10.1109/IGARSS46834.2022.9884564.

3. **Belwalkar, A.,** Poblete, T., Hornero, A., Zarco-Tejada, P.J., 2023. **Evaluating the relative contribution of Photosystems I and II for leaf nitrogen estimation using fractional depth of Fraunhofer lines and SIF derived from sub-nanometer airborne hyperspectral imagery**. In: Proc. IEEE International Geoscience and Remote Sensing Symposium (IGARSS), 16–21 July 2023, Pasadena, CA, USA, pp. 2819–2822.

Further, during the PhD, I was involved in another research project outside this thesis scope, in which I was the joint first author for a published journal article as follows:

Deshpande, P., **Belwalkar, A.**, Dikshit, O., Tripathi, S., 2021. **Historical land cover classification from CORONA imagery using convolutional neural networks and geometric moments**. Int. J. Remote Sens., 42, 5144-5171. https://doi.org/10.1080/01431161.2021.1910365.

Acknowledgements

First and foremost, I would like to thank my principal supervisor, Professor Pablo Zarco-Tejada. Without his continuous intellectual, personal, and financial support, my PhD research would not have been feasible. I will be eternally thankful to him for devoting so much time and energy to my academic and professional progress. I would also like to express my heartfelt gratitude to my co-supervisor, Dr. Tomas Poblete, for his patient advice, unwavering commitment, and wonderful mentoring. Academic exchanges with him supplied me with substantial intellectual input that I cherished the most throughout this journey. He has not only served as a supervisor but also as a trusted confidant, fostering not only my professional development as a researcher but also my personal development as an individual.

Without the companionship of my colleagues and friends, Dr. Manish Patel, Dr. Adrián Gracia Romero, Dr. Na Wang, Andrew Longmire, and Anne Wang, this PhD would not be the same. I especially relished our productive brainstorming, discussion, and collaboration. I am also thankful to the project collaborators, Dr. Albero Hornero and Dr. Rocío Hernández Clemente for their substantial contributions to the several publications that have resulted from this thesis.

Very importantly, I would like to thank my family and my close friends for their accompany for making this journey much more bearable and enjoyable. I am grateful to my parents and my sister for their continuous support and encouragement during this PhD journey. I also feel myself fortunate to have so many friends who are always there for me and have given me so many wonderful memories. My dearest friends Babin, Mahesh, Aditya, Prasad, Kushagra, Achyut and Pramod. Finally, I would like to thank the University of Melbourne for the Graduate Research Scholarship, as well as the university's Research computer Services and the Petascale Campus Initiative for the computing resources.

Table of Contents

List of Figures

List of Tables

47

Chapter 1

Introduction

1.1 Photosynthesis: principles and regulations

The global population is projected to reach 9.7 billion by the year 2050 (United Nations, 2022). A 70% increase in food production will be required to keep up with the demands of the world's expanding population, which equates to an additional 44 million metric tonnes of food per year (Tester and Langridge, 2010). Furthermore, climate change – including varying greenhouse gas concentrations in the atmosphere, rising temperatures, altered precipitation patterns, and increased frequency of extreme weather events – is having a substantial impact on agricultural production and food security (Asseng *et al*., 2015; Cogato *et al*., 2019; Hasegawa *et al*., 2018).

Photosynthesis is the fundamental mechanism governing plant growth and productivity, enabling plants to accumulate biomass (Hofius and Börnke, 2007; Simkin *et al*., 2019; Van Bel *et al*., 2003). It is the process by which plants transform solar energy into the biochemical energy which supports the vast majority of life on earth. As photosynthesis is the primary regulator of plant growth and productivity, it is vital to understand its functioning and plant adaptations to changing environmental conditions, as well as the effects of photosynthetic efficiency on crop yields, in order to increase crop production and develop stress-tolerant plants to meet global food demands (Hussain *et al*., 2021).

Photosynthesis is initiated by the absorption of light by plant photosynthetic pigments, primarily chlorophylls, and involves two distinct sets of reactions: (1) light reactions and (2) carbon fixation reactions (Porcar-Castell *et al*., 2014). The light reactions involve the conversion of absorbed solar radiation into chemical energy in the form of two biochemical products, adenosine triphosphate (ATP) and nicotinamide adenine dinucleotide phosphate (NADPH). The carbon fixation reactions,

on the other hand, involve the synthesis of complex energy-rich biomolecules from the ATP and NADPH using atmospheric CO2. The overall sequence of carbon fixation reactions is called the Calvin-Benson cycle (Stiller, 1962).

The light absorption and energy conversion reactions occur in the photosynthetic apparatus, which consists of four different complexes – two photosystems (PSI and PSII), the cytochrome b_6f, and ATP synthase (F-type ATPase) – encapsulated within the thylakoid membrane of the chloroplasts (Frigerio *et al*., 2008). A photosystem is the collective term for the antenna complex and reaction centre. Antenna complexes are composed of photosynthetic pigments – including chlorophylls, carotenoids, phycoerythrin, and phycocyanin – bound to proteins. The antenna system absorbs light energy and transfers it to the reaction centres. The transferred energy is then used by the reaction centres to drive electron transfer reactions (photochemistry), resulting in charge separation within the thylakoid membrane driven by the transfer of electrons from chlorophyll to pheophytin (Blankenship, 2014). The cytochrome b_6f complex functions as an electron transfer bridge between the two photosystems, enabling the transfer of electrons from PSII to PSI. Additionally, the electron transfer energy is used by the cytochrome b_6f complex for transferring protons from the stroma to the thylakoid lumen. The proton concentration gradient resulting from the accumulation of protons in the thylakoid lumen is then used by the final complex of the photosynthetic apparatus, ATP synthase, to synthesise ATP (Kramer *et al*., 2004).

The rates of production of the two biochemical products, ATP and NADPH, by light reactions and the rate of their consumption by carbon fixation reactions may not always be equivalent, due to the influence of environmental factors like water and sunlight availability, temperature, or pathogen infection (Hatfield and Prueger, 2011; Huner *et al*., 1996; Thiele *et al*., 1998). Consequently, to compensate for these differential rates, plants have evolved a variety of mechanisms to regulate the energy balance between light reactions and carbon fixation reactions (Anderson *et al*., 1995; Walters, 2005). These include changes in chlorophyll concentrations (Giardi *et al*., 1996; Murchie and Horton,

1997), photorespiration (Kozaki and Takeba, 1996), chloroplast and leaf movements (Arena *et al*., 2008; Haupt 1990; Ludlow and Bjorkman 1984; Sarvikas *et al*., 2010), anthocyanin concentrations (Close and Beadle, 2003; Merzlyak *et al*., 2008). Typically, these regulatory mechanisms are able to compensate for detrimental environmental conditions, but prolonged stress can weaken them and cause a substantial decrease in plant productivity. Hence, the quantification of photosynthetic efficiency is critical for monitoring the health of plants and advancing our understanding of how the photosynthetic machinery operates.

1.2 Chlorophyll fluorescence

There are three possible outcomes when chlorophyll pigments within the photosynthetic apparatus absorb solar radiation: (i) the energy can be used to drive photochemistry; (ii) the energy can be dissipated as heat; or (iii) the energy can be re-emitted as an electromagnetic signal known as chlorophyll fluorescence (ChlF) (Krause and Weis, 1984; Maxwell and Johnson, 2000). ChlF originates primarily from the antenna complexes and reaction centres of PSII, with a minor contribution from PSI. The three energy dissipation pathways compete with one another, and therefore any increase in the efficiency of one pathway lowers the yield of the other two (Maxwell and Johnson, 2000).

At the molecular level, light absorption by chlorophyll excites electrons from their ground state (S_0) to a higher energy level known as a 'singlet'. Each electronic energy level has the energy levels of the various rotation and vibration states superimposed on it. There are two major singlet states that exist, depending on the energy of the absorbed photon. The absorption of red light causes excitation of the first singlet (S_1), while blue light causes excitation of the second singlet (S_2). As S_2 is extremely unstable, with a half-life in the order of 10^{-12}–10^{-14} seconds, the excitation energy is exclusively lost as heat through rotations and vibrations until S_1 is attained. The loss of excitation

energy from S_1 to S_0 occurs via a number of pathways: the excitation energy could be used to drive photochemistry; the excitation energy could be transferred to a nearby pigment (Forster energy transfer) (Forster, 1948); the excitation energy could be emitted as ChlF signal (Porcar-Castell *et al.*, 2014); the excitation energy could be dissipated as heat (Heldt and Piechulla, 2011). Furthermore, S_1 can attain a lower excitation state, known as the triplet state, by releasing energy as heat via a process known as intersystem crossing (Clegg, 2004). The relaxation of energy from the triplet state to the ground state, S_0, then occurs via the emission of phosphorescent light. A schematic representation of the entire absorption and energy partitioning process is shown in Fig. 1-1.

1.2.1 Relationship between Chlorophyll Fluorescence and photochemistry

For PSII, the quantum yield (Φ) of an i^{th} process competing against n other de-excitation pathways with k_i as the first-order rate constant can be expressed as (Govindjee, 2004):

$$\Phi_i = \frac{k_i}{\sum_{i=0}^{i=n} k_i} \tag{1.1}$$

When all PSII reaction centres are open, owing to the dark-adapted leaf, the quantum yield of ChlF (Φ_{F_o}) will be at its minimum, resulting in the lowest ChlF emission (F_o), while the quantum yield of photochemistry (Φ_p) will be at its maximum, denoted as Φ_{P_o}. Both quantum yields can be expressed with Eq. (1.1) as (Butler, 1978):

$$\Phi_{P_o} = \frac{k_p}{k_P + k_F + k_O} \tag{1.2}$$

$$\Phi_{F_o} = \frac{k_F}{k_P + k_F + k_O} \tag{1.3}$$

In Eq. (1.2) and Eq. (1.3), k_P, k_F and k_O represent, respectively, the rate constants for photochemistry, ChlF and the other de-excitation pathways, mainly regulated and constitutive heat dissipation, as illustrated in Fig. 1-1. Likewise, when the PSII reaction centres are closed due to the exposure of a dark-adapted leaf to a short actinic pulse of high photosynthetically active photon flux density (PPFD) after reaching F_o, the rate constant for photochemistry is almost zero, resulting in the highest ChlF emission (F_M) and the maximum quantum yield of chlorophyll fluorescence (Φ_{F_M}):

$$\Phi_{F_M} = \frac{k_F}{k_F + k_O} \tag{1.4}$$

Rearranging Equations (1.3) and (1.4) by calculating their difference and dividing by Equation (1.4) yields:

$$\frac{\Phi_{F_M} - \Phi_{F_o}}{\Phi_{F_M}} = \frac{k_P}{k_P + k_F + k_O} = \Phi_{P_o} \tag{1.5}$$

As the ChlF intensity is proportional to the quantum yield with additional terms related to the intensity of the incident light and the absorption cross-section of the leaf, the quantum yield can be substituted for by the corresponding ChlF intensity levels by assuming that the additional terms are constant (Govindjee, 2004) which simplifies Eq. (1.5) as follows:

$$\frac{F_m - F_o}{F_m} = \frac{F_v}{F_m} = \Phi_{P_o} \tag{1.6}$$

In Eq. (1.6), F_v denotes the difference between F_m and F_o in dark-adapted vegetation and is referred to as variable fluorescence. This theoretical derivation (Eq. 1.1 – 1.6) suggests that $\frac{F_v}{F_m}$ could serve as an indicator of the PSII photochemistry efficiency, enabling the assessment of plant health

with measurements of variations in ChlF parameters. However, Φ_{P_o} computed using F_m and F_v cannot be considered a rigorous quantitative measure of the quantum yield of PSII photochemistry because some of the assumptions made to derive Eq. (1.6) may not be applicable under all conditions (Blankenship, 2014). Nevertheless, $\frac{F_v}{F_m}$ provides a reasonable estimation of PSII photochemistry efficiency with a consistent mean value of 0.83 for non-stressed leaves (Björkman and Demmig, 1987).

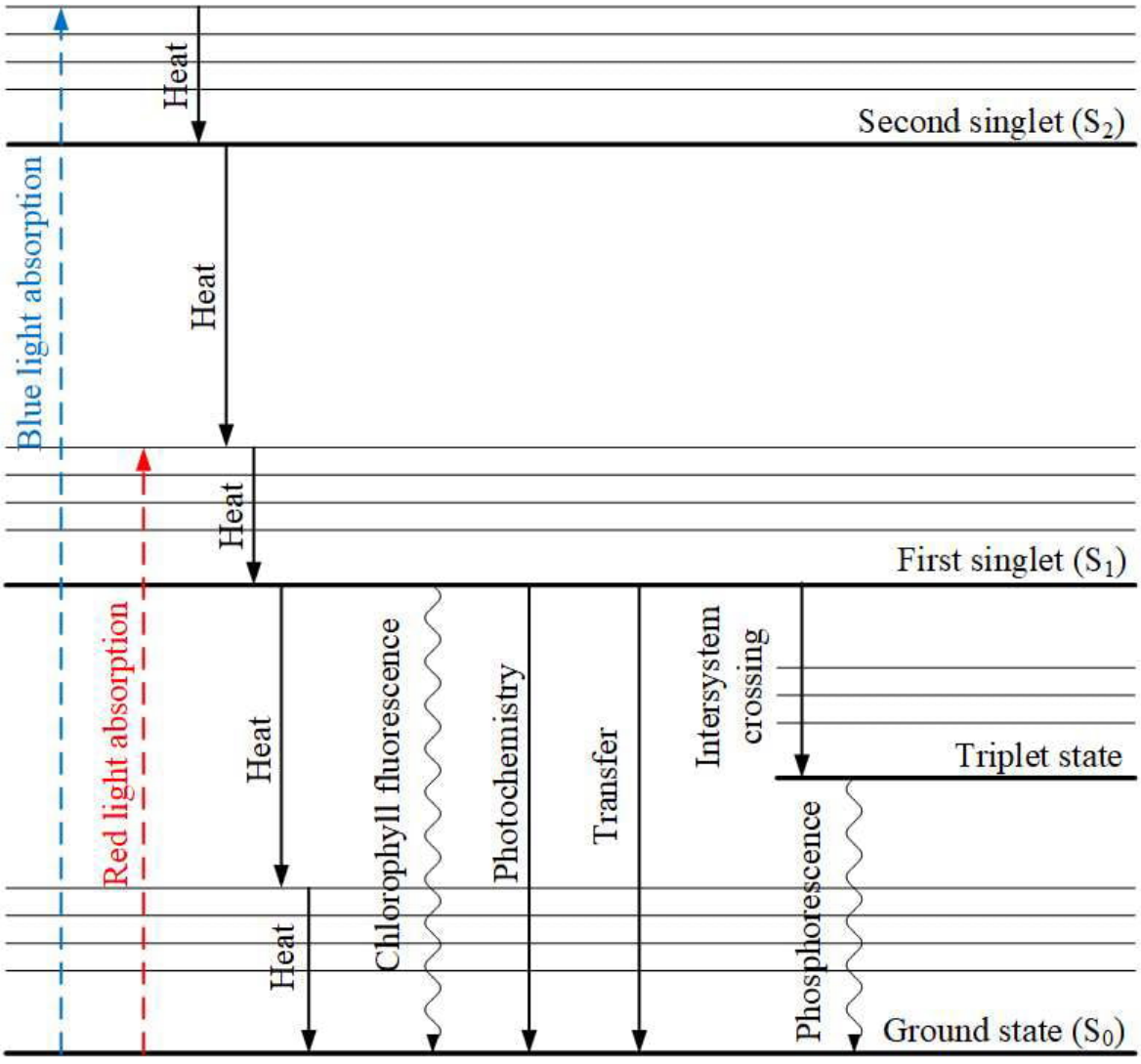

Fig. 1-1. Perrin-Jablonski diagram illustrating the entire absorption and energy partitioning process in a chlorophyll molecule. Fine lines represent various rotational and vibrational energy levels, and solid lines represent electronic energy levels (modified after Heldt and Piechulla, 2011).

On exposing a dark-adapted leaf to strong light, the PSII reaction centres gradually close, resulting in an increase in ChlF yield up to maximum ChlF intensity F_m, but ChlF yield then begins to decrease within a few minutes. This phenomenon of decreased ChlF yield is referred to as fluorescence quenching and can be explained by two concurrent processes: photochemical quenching (PQ), which indicates the availability of open PSII reaction centres for photochemistry; and non-photochemical quenching (NPQ), which indicates the efficiency of energy conversion to heat via regulated non-radiative heat dissipation (Maxwell and Johnson, 2000). Within several minutes of illumination, ChlF attains a steady-state level at intensity F_t. Consequently, in order to estimate PSII photochemistry from ChlF measurements, disentangling these two quenching mechanisms is crucial.

1.2.2 Chlorophyll fluorescence quantification

Based on the light source employed, ChlF estimation methods can be broadly divided into two groups – (1) active methods and (2) passive methods. Active methods rely on an artificial light source, such as pulse-amplitude modulation (PAM) fluorometry or high-power laser diodes, and are typically restricted to leaf-scale. In contrast, passive techniques use solar irradiance and the radiance emitted by vegetation and are generally applicable at canopy-scale.

1.2.2.1 Chlorophyll fluorescence quantification using active methods

PAM fluorometry (Schreiber *et al.*, 1986), which makes use of high-tech electronic instruments called PAM fluorometers, is one of the most popular active methods for estimating ChlF at leaf-scale. PAM fluorometers enable the quantification and isolation of the variations in ChlF yield induced by the pulse-modulating measuring light against a background of ChlF intensity fluctuations originating from actinic and saturating lights that are orders of magnitude larger. This makes fluorometers suitable for experiments under both controlled laboratory conditions and field conditions. There are four types of light sources that are used in PAM fluorometers for their specific functions: a low-intensity pulsed measuring light (ML); a moderate-intensity actinic light (AL); a

high-intensity saturating pulse (SP); and far-red radiation (FR). The measurement is initiated by the application of ML under a dark-adapted state to obtain F_o. Then, F_m is measured in the dark-adapted state with the application of SP for a short duration (usually less than 1 s). The application of SP activates AL, resulting in a rapid increase in ChlF followed by a slow drop to a steady-state intensity, F_t. Both photochemical and non-photochemical mechanisms contribute to these ChlF intensity changes. The application of SP at this precise moment eliminates the contribution of PQ and produces the light-adapted maximal ChlF intensity F_m' which is lower than F_m. Since the difference between F_m and F_m' is accounted for by non-photochemical processes, and the difference between F_m' and F_t is accounted for by photochemical processes, these ChlF parameters can be used to differentiate between the PQ and NPQ contributions (Brooks and Niyogi, 2011). The quantum yield of photochemistry (defined as optimal quantum yield) and of NPQ can be defined as:

$$\Phi_P = \frac{F_m' - F_t}{F_m'} \tag{1.7}$$

$$NPQ = \frac{F_m - F_m'}{F_m'} \tag{1.8}$$

Using Eq. (1.7) eliminates the need to determine F_o, allowing measurements to be conducted under actual field conditions without the need to fully dark-adapt the sample (Genty *et al.*, 1989). The actinic light is subsequently turned off and FR is activated to permit the re-oxidation of PSII in order to obtain the minimal ChlF in the light-adapted state (F_o'). The ChlF induction kinetics recorded using a typical PAM fluorometer, are shown in Fig. 1-2.

In addition to PAM fluorometry, laser-induced fluorescence transient (LIFT) is a newly developed active approach for measuring ChlF. In contrast to PAM fluorometers, which require close proximity to the leaf for ChlF yield estimation, the LIFT method can be used at target distances between 5 and 50 m. LIFT is based on the principle of fast repetition rate fluorometry (FRRF) (Kolber

et al., 1998) and employs a pulsed laser excitation source with a variable duty cycle to modulate the extent of photosynthetic activity and quantify the resulting variations in ChlF yield (Kolber *et al*., 2005).

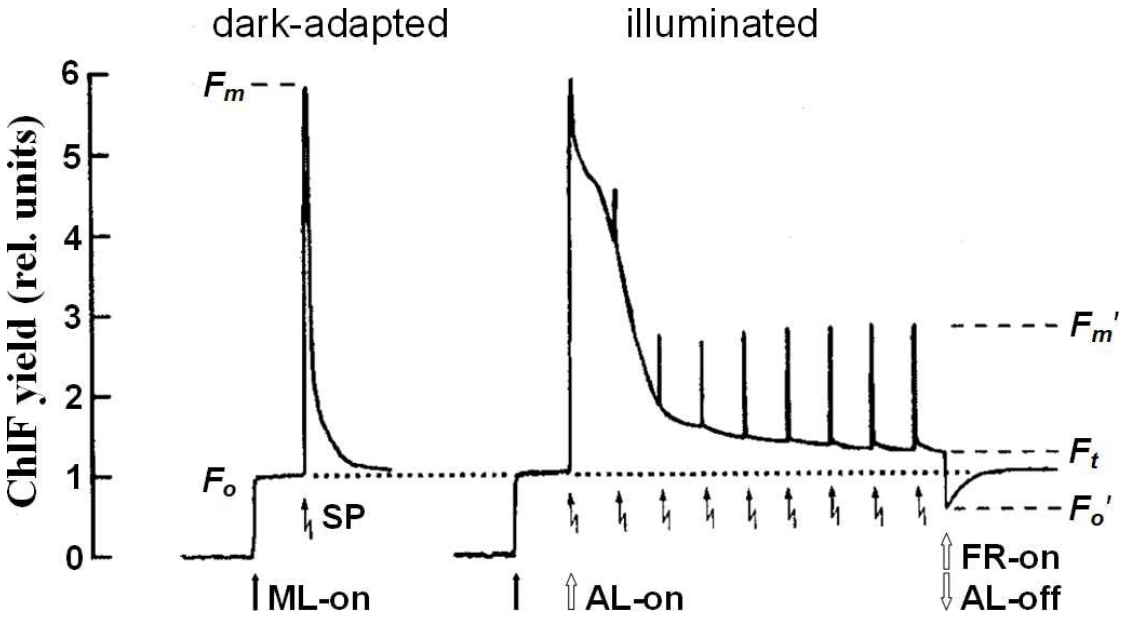

Fig. 1-2. ChlF induction kinetic curve recorded by a typical PAM fluorometer (modified after Schreiber, 2004).

1.2.2.2 Chlorophyll fluorescence quantification using passive methods

Since ChlF is an electromagnetic signal emitted as a by-product of photosynthesis, it can be remotely sensed. Using solar radiation as its energy source, solar-induced chlorophyll fluorescence (SIF) refers to the passive estimation of ChlF primarily at canopy-scale. SIF is a faint electromagnetic signal that superimposes onto reflected solar radiation and accounts for a very small fraction (< 1-2%) of the total upwelling radiance (*L*) from the vegetation target (Frankenberg and Berry, 2018). Consequently, isolating the SIF signal from the *L* signal is challenging because of SIF's negligible contribution.

Spectral emission of SIF ranges from 650–800 nm, with peaks in the red and near-infrared (far-red) spectral regions at approximately 685 nm (SIF_{685}) and 740 nm (SIF_{740}), respectively (Mohammed *et al*., 2019). SIF originates from both PSI and PSII, with PSII being the primary contributor to the complete SIF emission range and PSI contributing mostly in the near-infrared region (Fig. 1-3a). Assuming that both SIF emission and surface reflectance (r) follow Lambert's law, the top-of-canopy (TOC) L detected by a ground-based sensor include contributions from both solar-reflected and SIF emitted radiations and can be represented as follows (Meroni *et al*., 2009):

$$L(\lambda) = \frac{r(\lambda).E(\lambda)}{\pi} + SIF(\lambda) \tag{1.9}$$

where λ and E represent the wavelength and total irradiance (sum of direct and diffused components) incident on the target, respectively. All the terms in Eq. 1.9 are spectrally variable, with ground-based sensors only providing quantifications for E and L, leaving r and SIF to be determined. Since there are these two unknown terms in Eq. 1.9, assumptions regarding the spectral shape of r and SIF are leveraged for SIF estimation.

Reflectance-based approaches and radiance-based approaches can be broadly categorised as the two types of SIF retrieval techniques (Meroni *et al*., 2009). Reflectance-based approaches were the earliest attempt to explore the effects of SIF on the apparent reflectance spectra (r^*) using conventional remote sensing techniques, paving the way for future advances. Since these approaches used r^* to derive spectral indices linked to SIF, they could not retrieve SIF in physical units. The link between SIF and apparent reflectance r^* (Fig. 1-3b) was computed as the ratio between the upwelling and incident fluxes as related to pure reflectance r:

$$r^*(\lambda) = \frac{\pi.L(\lambda)}{E(\lambda)} = r(\lambda) + \frac{\pi.SIF(\lambda)}{E(\lambda)} \tag{1.10}$$

The several spectral indices proposed for SIF retrieval (Dobrowski *et al*., 2006; Pérez-Priego *et al*., 2005; Zarco-Tejada *et al*., 2000a; 2000b) can be grouped into three distinct classes: reflectance ratios (e.g., r_{685}/r_{630} and r_{740}/r_{800}); derivatives (e.g., D_{730}/D_{706}); and subtraction metrics (e.g., $r_{760.59}$-$r_{759.5}$). With the emergence of sensors with sub-nanometer resolution capabilities for estimating SIF in precise physical units, reflectance-based methodologies have been rendered obsolete and replaced with radiance-based approaches.

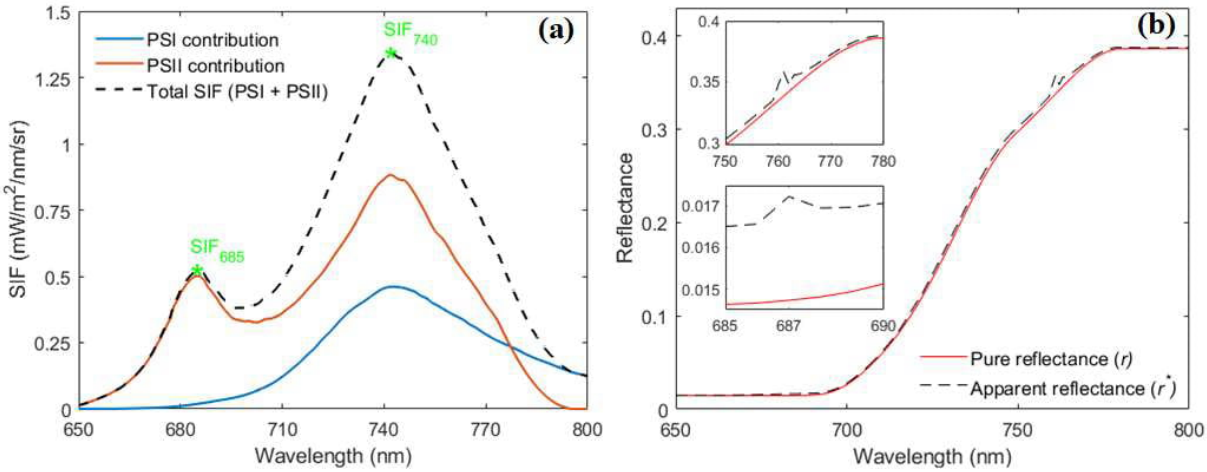

Fig. 1-3. SIF spectra based on the contributions from the two photosystems, PSI and PSII (a) and reflectance spectra (b) in the 650–800 nm SIF emission region, simulated using the Soil-Canopy Observation of Photosynthesis and Energy (SCOPE) radiative transfer model. The insets in (b) show comparisons of r and r^* in the far-red (750–780 nm) and red (685–690 nm) spectral regions, respectively.

Radiance-based approaches retrieve SIF in radiance units from radiometrically calibrated downwelling irradiance and upwelling radiance reflected from vegetation canopies. Several algorithms have been proposed to disentangle the contribution of SIF from that of the reflected solar radiation (see a full review in Mohammed *et al*., 2019). Using these algorithms, SIF can be estimated within specific absorption bands or across the entire emission region. As SIF is a relatively faint signal, its precise estimation requires the use of spectral regions where SIF's proportional contribution to the total reflected radiance is high. Opportunities exist in solar Fraunhofer Lines (FLs) and telluric absorption lines of the solar spectrum, where irradiance is drastically reduced (Mohammed *et al*., 2019). Since these absorption features are quite narrow, their proper characterisation is needed for

271 the accurate estimation of SIF, which necessitates the use of sub-nanometer resolution (full-width-at-
272 half-maximum (FWHM) ≤1-nm) instruments.

273 The majority of SIF quantification methods use oxygen absorption bands (O_2-A and O_2-B)
274 centred around 760 nm (SIF_{760}) and 687 nm (SIF_{687}), respectively, since they are wider and deeper
275 than other absorption features (Meroni *et al*., 2009). The oldest and most extensively used approach
276 for SIF quantification is based on the Fraunhofer Line Depth (FLD) (Plascyk, 1975) principle, which
277 uses the fluorescence *in-filling* effect. Although originally intended for FLs, this approach is currently
278 used for SIF quantification in oxygen absorption bands. Using two flux measurements, one inside
279 and one outside the absorption line, the FLD approach estimates SIF by comparing the depth of
280 absorption lines obtained simultaneously from a fluorescence-free reference and a vegetation target
281 (Fig. 1-4). Assuming both reflectance and SIF remain constant within the narrow absorption region
282 encompassed by the inside (λ_{in}) and outside (λ_{out}) wavelengths, Eq. (1.9) can be written as:

$$L(\lambda_{in}) = \frac{r.E(\lambda_{in})}{\pi} + SIF \tag{1.11}$$

$$L(\lambda_{out}) = \frac{r.E(\lambda_{out})}{\pi} + SIF \tag{1.12}$$

283

284 The above system of equations can be solved using the measurements of *E* and *L* at the two
285 wavelengths from the ground-based sensor to obtain estimates of *r* and SIF:

$$r = \frac{L(\lambda_{out}) - L(\lambda_{in})}{E(\lambda_{out}) - E(\lambda_{in})} \,.\, \pi \tag{1.13}$$

$$SIF = \frac{E(\lambda_{out}).L(\lambda_{in}) - E(\lambda_{in}).L(\lambda_{out})}{E(\lambda_{out}) - E(\lambda_{in})} \tag{1.14}$$

286

Although SIF quantification using the FLD method is simple because it requires only two wavelengths, the assumption of constant *r* and SIF within the narrow absorption line is inadequate. Consequently, numerous variations of the conventional 2-band FLD method have been proposed, including 3-band FLD (3FLD) (Maier *et al*., 2003), corrected FLD (cFLD) (Gómez-Chova *et al*., 2006), extended FLD (eFLD) (Mazzoni *et al*., 2007) and improved FLD (iFLD) (Alonso *et al*., 2008). In particular, 3FLD and iFLD are the most often used FLD-based methods for SIF quantification at oxygen absorption features.

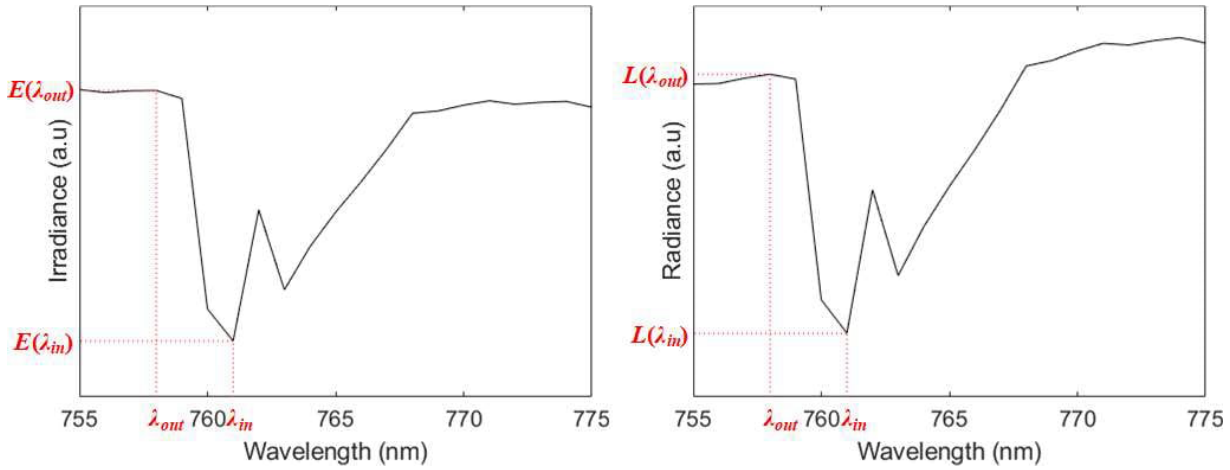

Fig. 1-4. Fraunhofer Line Depth (FLD) principle within the O_2-A absorption region. The spectra were simulated using the SCOPE model.

The 3FLD method assumes that both *r* and SIF vary linearly along the narrow absorption line considered. Rather than employing a single reference band outside the absorption line (λ_{out}), the weighted mean of two reference bands located at the left (λ_{out}^{l}) and right (λ_{out}^{r}) shoulders of the reference band inside the absorption line is used. By substituting for the outside fluxes with the interpolated values in Eq. 1.14, SIF can be quantified as:

$$SIF_{3FLD} = \frac{\left(w_l . E(\lambda_{out}^{l}) + w_r . E(\lambda_{out}^{r})\right) . L(\lambda_{in}) - E(\lambda_{in}) . \left(w_l . L(\lambda_{out}^{l}) + w_r . L(\lambda_{out}^{r})\right)}{w_l . E\left(\lambda_{out}^{l}\right) + w_r . E(\lambda_{out}^{r}) - E(\lambda_{in})} \quad (1.15)$$

$$\text{where } w_l = \frac{\lambda_{out}^{r} - \lambda_{in}}{\lambda_{out}^{r} - \lambda_{out}^{l}} , \; w_r = \frac{\lambda_{in} - \lambda_{out}^{l}}{\lambda_{out}^{r} - \lambda_{out}^{l}} \quad (1.16)$$

The iFLD method makes use of two correction factors (α_r^* and α_F^*) to relate *r* and SIF inside and outside the narrow absorption line. The correction factors are computed as:

$$\alpha_r^* = \frac{r^*(\lambda_{out})}{\tilde{r}(\lambda_{in})} , \qquad \alpha_F^* \approx \frac{E(\lambda_{out})}{\tilde{E}(\lambda_{in})} . \alpha_r^* \tag{1.17}$$

In Eq. (1.17), $\tilde{r}(\lambda_{in})$ denotes the interpolated apparent reflectance inside the absorption line obtained by either using cubic or spline interpolation to eliminate the *in-filling* effect on apparent reflectance (Alonso *et al*., 2008). $\tilde{E}(\lambda_{in})$ represents the absorption free interpolated irradiance inside the absorption line. Interpolations are performed using numerous contiguous, absorption-unaffected bands surrounding the absorption line. Using both the correction factors, SIF can be quantified as:

$$SIF_{iFLD} = \frac{\alpha_r^*. E(\lambda_{out}). L(\lambda_{in}) - E(\lambda_{in}). L(\lambda_{out})}{\alpha_r^*. E(\lambda_{out}) - \alpha_F^*. E(\lambda_{in})} \tag{1.18}$$

Spectral Fitting Methods (SFMs) are a more recent, improved technique for SIF quantification (Cogliati *et al*., 2015; 2019; Meroni *et al*., 2010; Zhao *et al*., 2018). In SFM, the spectral shapes of both *r* and SIF are modelled as smooth mathematical functions employing all available bands within a constrained spectral region known as the fitting window. The most widely used mathematical functions are polynomial functions of orders 1 to 3 and the Gaussian function. The upwelling radiance recorded by the sensor can be expressed as (Meroni *et al*., 2010):

$$L(\lambda) = \frac{r_{mod}(\lambda). E(\lambda)}{\pi} + SIF_{mod}(\lambda) + \varepsilon_{mod}(\lambda) = L_{mod}(\lambda) + \varepsilon_{mod}(\lambda) \tag{1.19}$$

In Eq. (1.19), $r_{mod}(\lambda)$ and $SIF_{mod}(\lambda)$ represents the modelled reflectance and SIF within the fitting window, respectively. $L_{mod}(\lambda)$ and $\varepsilon_{mod}(\lambda)$ represents the modelled upwelling radiance and modelling error at each wavelength. The mathematical system generated using all wavelengths within the fitting window is then solved to obtain the coefficients associated with the parametric functions of modelled reflectance and SIF using least-squares fitting.

Apart from FLD-based approaches and SFM methods, data-driven statistical approaches based on Principal Component Analysis or Singular Value Decomposition (Guanter *et al*., 2013; Joiner *et al*., 2013; Köhler *et al*., 2015) have also been developed for SIF quantification. These approaches have been developed particularly for spaceborne SIF retrievals within the narrow solar Fraunhofer lines around the O_2-A absorption region. Other recent SIF quantification methods include physically-based approaches using numerical inversion of canopy radiative transfer models (RTM) (Celesti *et al*., 2018; Verhoef *et al*., 2018), Partial Least Squares (PLS) regression-based approach exploiting solar Fraunhofer lines (Naethe *et al*., 2022), hybrid machine learning phasor-based approach (Scodellaro *et al*., 2022) and a band shape fitting approach based on the measured shape of the oxygen absorption feature (Van der Tol *et al*., 2023).

1.3 Quantification of SIF at different scales and platforms

The instrumentation used for SIF quantification has undergone significant advances over the past few decades. Sensors capable of quantifying SIF can be deployed on a variety of platforms, including fixed or mobile platforms for ground-based SIF, unmanned aerial vehicles (UAVs) and conventional aircraft for airborne SIF, and spacecraft for spaceborne SIF.

1.3.1 SIF quantification by ground-based spectrometers

SIF has been primarily quantified at ground-level due to the wide availability of ground-based spectrometers that can measure both downwelling irradiance and upwelling radiance and thereby

validate, interpret, and provide data inputs to models for airborne and spaceborne SIF measurements. In conjunction with additional field measurements collected at comparable temporal and spatial scales, ground-based SIF measurements can aid in the interpretation and comprehension of the SIF signal. Several *in situ* automated SIF systems are currently available, in either a bi-hemispherical or hemispherical-conical configuration, with the capacity to acquire continuous high temporal resolution TOC SIF data. Bi-hemispherical configuration systems include Fluorescence Auto-Measurement Equipment (FAME) (Gu *et al*., 2019) and 4S-SIF (Kim *et al*., 2022) whereas hemispherical-conical configuration systems include FLOX (JB Hyperspectral Devices, Düsseldorf, Germany), FluoSpec2 (Yang *et al*., 2018), PhotoSpec (Grossmann *et al*., 2018), AutoSIF (Zhou *et al*., 2016) and SIFSpec (Du *et al*., 2019).

Due to its extremely high signal-to-noise ratio (SNR) of 1000:1 and FWHM of 0.3-nm, QE-Pro (Ocean Insight, Dunedin, FL, USA) has become the most widely used spectrometer for ground-based SIF studies in recent years. Ground-based SIF studies using automated SIF systems have primarily examined the link between far-red SIF and gross primary productivity (GPP), the factors affecting this relationship and the viability of predicting GPP precisely using long-term ground-based SIF measurements based on modelling methods (Chen *et al*., 2022; Damm *et al*., 2010; Dechant *et al*., 2020; Hao *et al*., 2022; Li *et al*., 2020; Liu *et al*., 2017; 2021; Morozumi *et al*., 2023; Yang *et al*., 2015). The detection of vegetation stress caused by factors like, water stress (Butterfield *et al*., 2023; Pérez-Priego *et al*., 2005; De Cannière *et al*., 2021; 2022; Xu *et al*., 2018; 2021), biotic-induced stress (Du *et al*., 2023; Jing *et al*., 2022), heat stress (Kimm *et al*., 2021, and herbicide-induced stress (Carter *et al*., 2004; Meroni and Colombo, 2006), is yet another prominent application for ground-based SIF studies.

1.3.2 SIF quantification from sensors onboard spaceborne platforms

The practical implementation of satellite-based SIF estimation has been facilitated by new insights into the impact of fluorescence on apparent reflectance, along with advances in modelling,

estimation methods, and sensor capabilities, leading to an expansion of SIF's applicability across a wide range of research domains (Mohammed *et al*., 2019; Sun *et al*., 2023b). In 2007, the first retrievals of SIF_{760} were made using the Medium Resolution Imaging Spectrometer (MERIS) (Guanter *et al*., 2007). SIF_{760} quantification from space was confirmed by this regional-scale study, leading to the development of the first global maps of SIF from the Thermal And Near-infrared Sensor for Carbon Observation - Fourier Transform Spectrometer (TANSO-FTS) on the Japanese Greenhouse gases Observing SATellite (GOSAT) (Joiner *et al*., 2011). Since then, a number of satellite sensors that were originally intended for measuring atmospheric trace gases and greenhouse gases (eg., methane, sulphur dioxide, carbon dioxide) have been used to quantify SIF on both a regional and global scale at coarse spatial scales. These satellites include Global Ozone Monitoring Experiment 2 (GOME-2) (Joiner *et al*., 2013), Scanning Imaging Absorption SpectroMeter for Atmospheric CHartographY (SCIAMACHY) (Joiner *et al*., 2012), Orbiting Carbon Observatory 2 (OCO-2) (Frankenberg *et al*., 2014), TROPOspheric Monitoring Instrument (TROPOMI) (Guanter *et al*., 2015), and Chinese Carbon Dioxide Observation Satellite Mission (TanSat) (Du *et al*., 2018).

In addition to the existing satellite missions, in 2024, the European Space Agency (ESA) aims to launch the FLuorescence EXplorer (FLEX) (Drusch *et al*., 2017), designed specifically to measure SIF at a high spectral resolution of 0.3 nm, globally, with a spatial resolution of 300 m. The primary research goal of FLEX is to advance our understanding of physiological signs of plant stress and global seasonal variations in photosynthetic activity and efficiency. Specific outputs expected from the mission include: (1) SIF estimates at the two peaks and at the O_2-A and O_2-B bands (SIF_{685}, SIF_{740}, SIF_{760}, SIF_{687}); (2) estimates of total fluorescence emission; and (3) reflectance-derived indices and biophysical traits (ESA, 2018).

1.3.3 SIF quantification from sensors onboard airborne platforms

Observations of SIF at intermediate scales from airborne platforms are vital for bridging the gap between the field and global scales, allowing for improved interpretation of SIF at high spatial

resolutions. Airborne SIF measurements can be classified based on whether the sensor deployed on the airborne platform is an imaging sensor or a non-imaging spectrometer. Fluorescence mapping using airborne imaging sensors can reveal photosynthetic efficiency and detect early indicators of stress at scales significant for ecology and resource management. Moreover, airborne SIF measurements have gradually become an integral component of the process of calibrating and validating SIF measurements obtained from spaceborne sensors.

The past decade has seen significant technological advances in airborne hyperspectral imagers, particularly the introduction of sub-nanometer imagers that can accurately characterise the narrow absorption features for accurate SIF quantification in physical units. These imagers have now replaced the initially employed coarser resolution narrow-band imagers, which had FWHM greater than 1 nm and could only provide SIF in relative units because of constraints imposed by their spectral configuration. Despite these technological advances, there are still certain challenges to overcome when estimating SIF from airborne platforms. Among these challenges, a precise characterisation of atmospheric effects within the SIF emission region remains the most critical. Atmospheric RTMs are typically used to estimate atmospheric parameters like upwelling transmittance, path scattered radiance, and spherical albedo to account for atmospheric influences, followed by transmittance correction strategy (Damm *et al*., 2015; Siegmann *et al*., 2019) to account for the high uncertainty associated with the estimates. Non-linearity correction, sensor-stray light correction, point-spread-function artefacts, and illumination artefacts arising from geometric optical scattering in high-spatial-resolution data are challenging areas in which improvements need to be made (Mohammed *et al*., 2019).

1.3.3.1 Airborne SIF studies with narrow-band imaging sensors

Before the advent of sub-nanometer imaging sensors capable of accurately quantifying SIF, it could only be quantified in relative units using narrow-band imaging sensors. The Reflective Optics System Imaging Spectrometer (ROSIS, 7-nm FWHM) (Maier *et al*., 2003), Compact Airborne

Spectrographic Imager (CASI, 2.4–14.4 nm FWHM) (Guanter *et al*., 2007; Rossini *et al*., 2015b; Zarco-Tejada *et al*., 2002; 2001), Airborne Imaging Spectrometer (AISA Eagle, 3.3-nm FWHM) (Panigada *et al*., 2014), Airborne Prism Experiment (APEX, 5.7-nm FWHM) (Damm *et al*., 2015), AISA (1.6-nm FWHM) (Corp *et al*., 2006), MCA-6 (Tetracam, Inc., California, USA, 1.57-1.6 nm FWHM with custom-made filters) (Zarco Tejada *et al*., 2009), and AIRFLEX (0.5–5.8 nm FWHM) (Moya *et al*., 2003; 2006) were the earliest narrow-band hyperspectral and multispectral imagers used to quantify SIF_{760}. Currently operational narrow-band hyperspectral imaging sensors for SIF_{760} quantification include micro- and nano-hyperspec VNIR imagers (Headwall Photonics Inc., Boston, MA, USA) with 5.8–6.5 nm FWHM (Pancorbo *et al*., 2023; Poblete *et al*., 2023; Suarez *et al*., 2021; Zarco-Tejada *et al*., 2012).

Several studies have demonstrated the utility of relative SIF levels derived from narrow-band imaging sensors, despite their inability to precisely characterise narrow absorption features within the SIF emission region. Narrow-band SIF estimates have shown the most promising results for the detection of biotic- (Calderón *et al*., 2015; 2013; Camino *et al*., 2021; Hernández-Clemente *et al*., 2017; Hornero *et al*., 2021b; Poblete *et al*., 2020; 2021; 2023; Zarco-Tejada *et al*., 2018; 2021) and abiotic-induced stress (Camino *et al*., 2018a; Panigada *et al*., 2014; Rossini *et al*., 2015b; Zarco-Tejada *et al*., 2009; 2012). By integrating traits related to thermal, fluorescence, and spectral indicators of chlorophyll concentration and structural changes into a machine learning framework, Zarco-Tejada *et al*. (2018) demonstrated that prediction accuracies of over 80% can be achieved for the early detection of infection in olive trees caused by the pathogen *Xylella fastidiosa* (*Xf*). In a subsequent investigation, Zarco-Tejada *et al*. (2021) demonstrated that the degree of infection, which is crucial for distinguishing between biotic- and abiotic-induced stress, affects SIF. Other application areas include assessment of grain protein concentrations (Longmire *et al*., 2022), estimation of leaf nitrogen concentration (Camino *et al*., 2018b; Wang *et al*., 2022), link with GPP (Damm *et* al., 2015; Zarco-Tejada *et al*., 2013) and plant phenotyping (Camino *et al*., 2019; Gonzalez-Dugo *et al*., 2015).

Narrow-band SIF estimates were shown to be useful in the aforementioned studies. However, in absolute terms, narrow-band SIF estimates are overestimated and require careful validation using reliable ground-based and airborne sub-nanometer resolution SIF to investigate their reliability. Furthermore, an efficient modelling strategy needs to be developed to account for the effects of spectral configuration on the absolute SIF levels. Addressing these two factors will pave the way for the widespread adoption of narrow-band quantified SIF in operational settings for plant phenotyping, precision agriculture, and plant physiology monitoring applications.

1.3.3.2 Airborne SIF studies with sub-nanometer imaging sensors

The Hyplant sensor developed by the Finnish company Specim in collaboration with Forschungszentrum Jülich (Germany) was the first sub-nanometer imaging sensor specifically designed for accurate SIF estimation (Rascher *et al*., 2015). It is serving as a demonstrator for the FLEX satellite mission and consists of two modules, DUAL (380–2500 nm) and FLUO (670–780 nm), with spectral resolutions of 0.28 nm for O_2-A and 0.29 nm for O_2-B in the FLUO module allowing for accurate SIF estimation (Siegmann *et al*., 2019). Other sub-nanometer imaging sensors available for accurate SIF estimation include the AISA IBIS Fluorescence Imager (SPECIM, Spectral Imaging Ltd., Oulu, Finland), Hyperspec Solar-Induced Fluorescence Imaging sensor (Headwall Photonics, Fitchburg, MA, USA) (Paynter *et* al., 2020), and chlorophyll fluorescence imaging spectrometer (CFIS) (Frankenberg *et al*., 2018) with SRs of 0.245, ≤0.2, and 0.07 nm respectively.

Rossini *et al*. (2015a) demonstrated for the first time that a sub-nanometer imaging sensor is capable of precisely mapping the two peaks of SIF. Both SIF_{687} and SIF_{760} increased significantly when treated with an herbicide known to selectively elevate fluorescence levels, demonstrating the ability of airborne sub-nanometer SIF observations to accurately monitor photosynthetic efficiency. Rascher *et al*. (2015) presented the first validated maps over diverse land cover types of SIF from Hyplant, showing that SIF varies between crop varieties. Accurate SIF estimation from sub-nanometer imaging sensor has been demonstrated as valuable in a number of subsequent studies for

a wide range of applications, including GPP estimation (Wieneke *et al*., 2016), herbicide stress detection (Pinto *et al*., 2020), downscaling SIF from canopy-level to leaf- and photosystem-level (Liu *et al*., 2019; Siegmann *et al*., 2021), assessing the wide heterogeneity of peatland vegetation traits (Bandopadhyay *et al*., 2019), assessing sensitivity of SIF to heat stress and water stress (Zeng *et al*., 2022), validating the contribution of understory SIF modelled via 3-D RTMs (Hornero *et al*., 2021), assessing SIF responses to soil water-limitation (Damm *et al*., 2022), and validating spaceborne SIF estimates (Sun *et al*., 2017). More recently, R. Wang *et al*. (2022) investigated how sensor type, quantification approach, and atmospheric correction affect SIF values, enabling an improved understanding of spatial and temporal GPP patterns by harmonising SIF products across airborne, stationary, and mobile ground-based platforms. The study presented for the first time the retrieval of the full SIF spectrum with a sub-nanometer imaging sensor (AISA IBIS Fluorescence Imager) and investigated the effect on the accuracy of retrieved spectrum by removing from consideration the 715–740 nm water absorption bands.

Recently, Albert *et al*. (2023) simulated several spectral stray light scenarios and used near-ground-level observations from the Hyperspec Solar-Induced Fluorescence Imaging sensor to examine the sensitivity of SIF retrieval methods to stray light. The O_2-A band and 12 Fraunhofer lines (FLs) without prominent water and oxygen absorption bands were used to quantify SIF with FLD and 3FLD techniques. Although this was the first study to use distinct FLs for SIF quantification with a sub-nanometer imager, as opposed to the more common telluric absorption bands, additional tests are necessary to determine the potential of these narrow FLs when the sensor is onboarding an airborne platform under actual field conditions. The promising opportunity offered by sub-nanometer imaging sensors to detect narrow FLs within the SIF spectrum must be exploited further to investigate their potential for a variety of applications, including biotic and abiotic stress detection, plant physiology monitoring, and nutrient assessment.

1.4 Radiative transfer modelling of SIF

Vegetation RTMs describe the interaction between the incident solar radiation and vegetation (primarily absorption and scattering) using radiative transfer equations to, account for the effect of canopy structure (Jacquemoud *et al*., 2009). The advancements in SIF instrumentation and retrieval methods have been accompanied by progress in modelling methods for SIF estimation. The earliest modelling efforts to incorporate fluorescence into RTMs involved the development of leaf RTMs like the FLSAIL model (Rosema *et al*., 1991) and Fluorescence–Reflectance–Transmittance (FRT) model (Zarco-Tejada *et al*., 2000a, 2000b). The first model simulated the effects of fluorescence caused by laser-induced fluorescence, whereas the second model demonstrated the contribution of fluorescence to apparent reflectance spectra. These earlier attempts laid the foundation for the development of more advanced leaf-level models such as FluorMODleaf (Pedrós *et al*., 2010), Fluspect (Vilfan *et al*., 2016) and Fluorescence Leaf Canopy Vector Radiative Transfer (FluLCVRT) (Kallel, 2020).

To accurately model fluorescence emission at canopy-scale, a canopy-level fluorescence RTM must describe the following three primary processes: (1) incident radiation absorption; (2) subsequent fluorescence emission; and (3) post-emission fluorescence scattering and re-absorption within the canopy typically accomplished by incorporating a leaf-fluorescence model into a canopy reflectance model (Disney, 2016; Mohammed *et al*., 2019). FluorSAIL (Verhoef, 2004) and the Soil-Canopy-Observation of Photosynthesis and Energy fluxes (SCOPE) (Van der Tol *et al*., 2009) were the first canopy-scale models to be developed. Because these models consider the vegetation canopy as a series of uniform layers, they are referred to as one-dimensional (1-D) models and are suitable only for homogenous and uniform canopies. Recent modelling efforts have used more rigorous mathematical frameworks to account for the re-absorption and scattering of chlorophyll fluorescence within the homogenous canopy (Atherton *et al*., 2019; Romero *et al*., 2020; Yang and van der Tol, 2018; Zeng *et al*., 2019).

SCOPE is the most extensively used fluorescence RTM and has undergone numerous enhancements in recent years. Yang *et al*. (2021) provides additional information regarding the enhancements of SCOPE and the new features of the current version (SCOPE 2.0). SCOPE has proven beneficial in numerous studies aimed at elucidating the relationship between photosynthesis and fluorescence-reflectance (Camino *et al*., 2019; Damm *et al*., 2015; Migliavacca *et al*., 2017; Pacheco-Labrador *et al*., 2019; Verrelst *et al*., 2016; Yang *et al*., 2022; Zhang *et al*., 2022; Zhu *et al*., 2023), understanding the impact of spectral resolution and SNR on FLD-based SIF quantification (Liu *et al*., 2015), developing and validating new SIF quantification approaches (Celesti *et al*., 2018; Cogliati *et al*., 2015; 2019; Naethe *et al*., 2022; Scodellaro *et al*., 2022; Van der Tol *et al*., 2023; Verhoef *et al*., 2018; Zhao *et al*., 2019), and disentangling the physiological and non-physiological components of SIF (Wang *et al*. 2023; Xu *et al*., 2021; Yang *et al*., 2020; Zeng *et al*., 2019; 2022).

To address the limitations of 1-D canopy-level fluorescence RTMs in modelling heterogeneous, non-uniform, and complex canopies like forests and row-structured, grid-based crop canopies like vineyards and tree orchards, several ray-tracing-based three-dimensional (3-D) canopy-level fluorescence models have been developed. These include the Fluorescence model with Weight Photon Spread (FluorWPS) for row crops (Zhao *et al*., 2016), the Discrete Anisotropic Radiative Transfer (DART) model for any 3-D vegetation architecture (Gastellu-Etchegorry *et al*., 2017), Forest Light Environmental Simulator for SIF (FLiES-SIF), and FluorFLIGHT for forest canopies (Sakai *et al*., 2020; Hernández-Clemente *et al*., 2017). Although the capacity of these ray-tracing-based 3-D models to provide spatially precise modelling could give valuable insights into the interplay of fluorescence fluxes within complex canopy structures, their high computational costs limit their application at landscape-scale (Mohammed *et al*., 2019; Sun *et al*., 2023a). The newly developed 3-D models FluorRTER (Zeng *et al*., 2020), based on spectral invariant theory, and FluorESRT (Li *et al*., 2022), targeted at pest-damaged forests, are analytically simple, computationally less intensive, and have the potential for large-scale application.

1.5 Research gaps

The following research gaps were identified in the literature reviewed:

1. A number of studies have demonstrated the feasibility of quantifying SIF_{760} using widely available narrow-band hyperspectral sensors, but none have assessed the performance and reliability of narrow-band SIF_{760} measurements by comparing them to estimates of sub-nanometer SIF_{760} acquired simultaneously from ground-based and airborne sensors.
2. Although narrow-band SIF_{760} estimates in absolute physical units are typically overestimated due to the impact of sensor's spectral configurations, no studies have been conducted to investigate how the impact of sensor spectral resolution can be accounted for using RTM-based approaches for retrieving SIF_{760} from narrow-band imaging sensors at appropriate absolute physical levels.
3. While previous studies have demonstrated the significance of SIF_{760} for biotic and abiotic vegetation stress detection and for improving the retrieval of leaf N concentrations, further research on the viability of using the depth of solar Fraunhofer lines within the SIF emission region is required to harness the full potential of the entire SIF emission region.

1.6 Objectives and thesis structure

This thesis focuses primarily on improving the interpretation of SIF_{760} estimates obtained from widely available narrow-band imaging sensors by spectrally scaling narrow-band SIF_{760} estimates with radiative transfer modelling and machine learning approaches. In addition, the potential of solar Fraunhofer lines within the SIF emission region for the estimation of N concentration across the field and for the detection of both biotic and abiotic stress using sub-nanometer hyperspectral imagery is investigated. Based on the research gaps identified, the following specific objectives were defined and addressed in this research:

1. Assessing the impact of using a narrow-band hyperspectral imager (5.8-nm FWHM), as compared to using a sub-nanometer hyperspectral imager (≤0.2 nm FWHM) for SIF_{760} quantification using existing methods.
2. Developing and evaluating a methodology for modelling the effect of sensor spectral resolution on SIF_{760} quantification from narrow-band hyperspectral imagery by integrating RTM-based approaches with machine learning algorithms.
3. Assessing of the capability of the fractional depth of narrow solar Fraunhofer lines within the SIF emission region for estimating leaf nitrogen concentration across the field and for the detection of biotic stress using sub-nanometer resolution (≤0.2 nm FWHM) airborne hyperspectral imagery.

This thesis comprises five chapters. The first chapter provides a general overview, and the last chapter summarises the findings and implications of this study and discusses possible future applications. The middle three chapters 2, 3, and 4 address research objectives 1, 2 and 3, respectively.

Chapter 2 attends to objective 1, focusing on the evaluation of SIF_{760} retrievals from narrow-band and sub-nanometer airborne hyperspectral imagers flown in tandem. The effects of SR and sensor altitude on SIF_{760} accuracy were investigated across three years, comparing SIF_{760} quantified from two hyperspectral imagers with different spectral configurations over three experimental fields with varying nitrogen application rates. Additionally, simulations using the SCOPE model were conducted for theoretical assessment of the effect of SR on absolute SIF levels. Strong significant relationships were obtained among the narrow-band, sub-nanometer, and ground-based SIF_{760} estimates, demonstrating the capability of narrow-band imaging sensors for plant phenotyping, vegetation stress detection and plant physiological condition monitoring applications, all of which require reliable assessment of relative SIF_{760} variability across the experimental field. This chapter has been published in the journal *Remote Sensing of Environment*:

592 **Belwalkar, A.**, Poblete, T., Longmire, A., Hornero, A., Hernandez-Clemente, R., Zarco-Tejada, P.J.,
593 2022. **Evaluation of SIF retrievals from narrow-band and sub-nanometer airborne**
594 **hyperspectral imagers flown in tandem: modelling and validation in the context of plant**
595 **phenotyping**. Remote Sens. Environ. 273, 112986. https://doi.org/10.1016/j.rse.2022.112986.

596

597 **Chapter 3** addresses objective 2 by proposing a methodology for spectrally scaling SIF_{760}
598 estimates from a narrow-band hyperspectral imager with 5.8-nm FWHM to 1-nm FWHM using an
599 empirical approach based on a Support Vector Regression (SVR) algorithm with SIF_{760} at 5.8-nm
600 FWHM and SCOPE-derived leaf biochemical and structural traits as model inputs. The SVR model
601 was evaluated using SCOPE model simulations and airborne data obtained from two airborne
602 hyperspectral imagers flown in tandem on board an aircraft during two distinct wheat and maize
603 phenotyping studies. For both simulated and airborne datasets, the estimated SIF_{760} at 1-nm FWHM
604 matched well with the reference SIF_{760}, implying that this SIF scaling mechanism could be a viable
605 technique for enhancing the interpretation of relative SIF_{760} levels assessed by narrow-band
606 hyperspectral imagers. This chapter is currently under review by the journal *Remote Sensing of*
607 *Environment*:

608 **Belwalkar, A.**, Poblete, T., A., Hornero, A., Hernandez-Clemente, R., Zarco-Tejada, P.J. **Accurate**
609 **SIF quantification from a narrow-band airborne hyperspectral imager using SCOPE:**
610 **assessment with sub-nanometer imagery** (under review by the journal *Remote Sensing of*
611 *Environment*).

612

613 **Chapter 4** targets objective 3. Using sub-nanometer hyperspectral imagery, a set of distinct
614 Fraunhofer lines devoid of water and oxygen absorptions was firstly identified within the SIF
615 emission region. In the subsequent stage, the sensitivity of the depth of these narrow lines for the

identification of biotic-induced stress caused by pathogen infections at varying levels of stress was investigated. Furthermore, the potential of these lines for improved estimation of leaf nitrogen concentration in conjunction with leaf chlorophyll content and SIF_{760} estimations was explored. This chapter is currently being drafted for submission to the journal *Remote Sensing of Environment*.

Belwalkar, A., Poblete, T., A., Hornero, A., Hernandez-Clemente, R., Zarco-Tejada, P.J. **Prospects of solar Fraunhofer lines derived from sub-nanometer hyperspectral imagery for assessing a/biotic stress** (currently being drafted for submission to the journal Remote Sensing of Environment).

References

Albert, L.P., Cushman, K.C., Zong, Y., Allen, D.W., Alonso, L., Kellner, J.R., 2023. Sensitivity of solar-induced fluorescence to spectral stray light in high resolution imaging spectroscopy. Remote Sens. Environ. 285, 113313.

Alonso, L., Gómez-Chova, L., Vila-Francés, J., Amorós-López, J., Guanter, L., Calpe, J., Moreno, J., 2008. Improved Fraunhofer line discrimination method for vegetation fluorescence quantification. IEEE Geosci. Remote Sens. Lett. 5, 620–624.

Anderson, J.M, Chow, W.S, Park, Y.I., 1995. The grand design of photosynthesis: acclimation of the photosynthetic apparatus to environmental cues. Photosynth. Res. 46, 129–139.

Arena, C., Vitale, L., De Santo, A.V., 2008. Paraheliotropism in Robinia pseudoacacia L.: an efficient strategy to optimise photosynthetic performance under natural environmental conditions. Plant Biology 10, 194–201.

Asseng, S., Ewert, F., Martre, P., Rötter, R.P., Lobell, D.B., Cammarano, D., Kimball, B.A., Ottman, M.J., Wall, G.W., White, J.W., Reynolds, M.P., Alderman, P.D., Prasad, P.V.V., Aggarwal, P.K., Anothai, J., Basso, B., Biernath, C., Challinor, A.J., de Sanctis, G., Doltra, J., Fereres, E., Garcia-Vila, M., Gayler, S., Hoogenboom, G., Hunt, L.A., Izaurralde, R.C., Jabloun, M., Jones, C.D., Kersebaum, K.C., Koehler, A.K., Müller, C., Naresh Kumar, S., Nendel, C., O'leary, G., Olesen, J.E., Palosuo, T., Priesack, E., Eyshi Rezaei, E., Ruane, A.C., Semenov, M.A., Shcherbak, I., Stöckle, C., Stratonovitch, P., Streck, T., Supit, I., Tao, F., Thorburn, P.J., Waha, K., Wang, E., Wallach, D., Wolf, J., Zhao, Z., Zhu, Y., 2015. Rising temperatures reduce global wheat production. Nat. Clim. Change 5, 143–147.

Atherton, J., Liu, W., Porcar-Castell, A., 2019. Nocturnal Light Emitting Diode Induced Fluorescence (LEDIF): A new technique to measure the chlorophyll a fluorescence emission spectral distribution of plant canopies in situ. Remote Sens. Environ. 231, 111137.

Bandopadhyay, S., Rastogi, A., Rascher, U., Rademske, P., Schickling, A., Cogliati, S., Julitta, T., Arthur, A. mac, Hueni, A., Tomelleri, E., Celesti, M., Burkart, A., Strózecki, M., Sakowska, K., Gabka, M., Rosadziński, S., Sojka, M., Iordache, M.D., Reusen, I., Van der Tol, C., Damm, A., Schuettemeyer, D., Juszczak, R., 2019. HyPlant-derived sun-induced fluorescence - a new opportunity to disentangle complex vegetation signals from diverse vegetation types. Remote Sens. 11, 1691.

Björkman, O., Demmig, B., 1987. Photon yield of O_2 evolution and chlorophyll fluorescence characteristics at 77 K among vascular plants of diverse origins. Planta 170, 489–504.

Blankenship, R.E., 2014. Molecular Mechanisms of Photosynthesis. John Wiley & Sons, Inc., Hoboken, NJ.

Brooks, M.D., Niyogi, K.K., 2011. Use of a Pulse-Amplitude Modulated Chlorophyll Fluorometer to Study the Efficiency of Photosynthesis in Arabidopsis Plants, in: Jarvis, R. (Eds.) Chloroplast Research in Arabidopsis. Methods in Molecular Biology, vol 775. Humana Press, Totowa, NJ, pp. 299–310.

Butler, W.L., 1978. Energy distribution in the photochemical apparatus of photosynthesis. Annu. Rev. Plant. Physiol. 29, 345–78.

Butterfield, Z., Magney, T., Grossmann, K., Bohrer, G., Vogel, C., Barr, S., Keppel-Aleks, G., 2023. Accounting for changes in radiation improves the ability of SIF to track water stress-induced losses in summer GPP in a temperate deciduous forest. J. Geophys. Res. Biogeosci. 128, e2022JG007352.

Calderón, R., Navas-Cortés, J.A., Lucena, C., Zarco-Tejada, P.J., 2013. High-resolution airborne hyperspectral and thermal imagery for early detection of Verticillium wilt of olive using fluorescence, temperature and narrow-band spectral indices. Remote Sens. Environ. 139, 231–245.

Calderón, R., Navas-Cortés, J.A., Zarco-Tejada, P.J., 2015. Early detection and quantification of Verticillium wilt in olive using hyperspectral and thermal imagery over large areas. Remote Sens. 7, 5584–5610.

Camino, C., Zarco-Tejada, P.J., Gonzalez-Dugo, V., 2018a. Effects of heterogeneity within tree crowns on airborne-quantified SIF and the CWSI as indicators of water stress in the context of precision agriculture. Remote Sens. 10, 604.

Camino, C., González-Dugo, V., Hernandez, P., Sillero, J.C., Zarco-Tejada, P.J., 2018b. Improved nitrogen retrievals with airborne-derived fluorescence and plant traits quantified from VNIR-SWIR hyperspectral imagery in the context of precision agriculture. Int. J. Appl. Earth Obs. Geoinf. 70, 105–117.

Camino, C., Gonzalez-Dugo, V., Hernandez, P., Zarco-Tejada, P.J., 2019. Radiative transfer Vcmax estimation from hyperspectral imagery and SIF retrievals to assess photosynthetic performance in rainfed and irrigated plant phenotyping trials. Remote Sens. Environ. 231, 111186.

Camino, C., Calderón, R., Parnell, S., Dierkes, H., Chemin, Y., Román-Écija, M., Montes-Borrego, M., Landa, B.B., Navas-Cortes, J.A., Zarco-Tejada, P.J., Beck, P.S.A., 2021. Detection of

Xylella fastidiosa in almond orchards by synergic use of an epidemic spread model and remotely sensed plant traits. Remote Sens. Environ. 260, 112420.

Carter, G.A., Freedman, A., Kebabian, P.L., Scott, H.E., 2004. Use of a prototype instrument to detect short-term changes in solar-excited leaf fluorescence. Int. J. Remote Sens. 25, 1779-1784.

Celesti, M., Van der Tol, C., Cogliati, S., Panigada, C., Yang, P., Pinto, F., Rascher, U., Miglietta, F., Colombo, R., Rossini, M., 2018. Exploring the physiological information of sun-induced chlorophyll fluorescence through radiative transfer model inversion. Remote Sens. Environ. 215, 97–108.

Chen, R., Liu, L., Liu, X., 2022. Leaf chlorophyll contents dominates the seasonal dynamics of SIF/GPP ratio: Evidence from continuous measurements in a maize field. Agric. For. Meteorol. 323, 109070.

Clegg, R.M., 2004. Nuts and bolts of excitation energy migration and energy transfer, in: Papageorgiou, G.C., Govindjee (Eds.), Chlorophyll a Fluorescence, a signature of photosynthesis. Advances in Photosynthesis and Respiration, vol 19. Springer, Dordrecht, pp. 83–105.

Close, D.C., Beadle, C.L., 2003. The ecophysiology of foliar anthocyanin. Botanical Review 69, 149–161.

Cogato, A., Meggio, F., De Antoni Migliorati, M., Marinello, F., 2019. Extreme weather events in agriculture: a systematic review. Sustainability 11, 2547.

Cogliati, S., Celesti, M., Cesana, I., Miglietta, F., Genesio, L., Julitta, T., Schuettemeyer, D., Drusch, M., Rascher, U., Jurado, P., Colombo, R., 2019. A spectral fitting algorithm to retrieve the fluorescence spectrum from canopy radiance. Remote Sens. 11.

Cogliati, S., Verhoef, W., Kraft, S., Sabater, N., Alonso, L., Vicent, J., Moreno, J., Drusch, M., Colombo, R., 2015. Retrieval of sun-induced fluorescence using advanced spectral fitting methods. Remote Sens. Environ. 169, 344–357.

Corp L., Middleton E., Daughtry C., Campbell P., 2006. Solar induced fluorescence and reflectance sensing techniques for monitoring nitrogen utilization in corn. In: Proc. IEEE International Geoscience and Remote Sensing Symposium (IGARSS), 31 July–04 August 2006, Denver, CO, USA, pp. 2267-2270.

Damm, A., Elbers, J.A.N., Erler, A., Gioli, B., Hamdi, K., Hutjes, R., Kosvancova, M., Meroni, M., Miglietta, F., Moersch, A., Moreno, J., 2010. Remote sensing of sun-induced fluorescence to improve modeling of diurnal courses of gross primary production (GPP). Glob. Chang. Biol. 16, 171-186.

Damm, A., Guanter, L., Paul-Limoges, E., Van der Tol, C., Hueni, A., Buchmann, N., Eugster, W., Ammann, C., Schaepman, M.E., 2015. Far-red sun-induced chlorophyll fluorescence shows ecosystem-specific relationships to gross primary production: an assessment based on observational and modeling approaches. Remote Sens. Environ. 166, 91–105.

Damm, A., Cogliati, S., Colombo, R., Fritsche, L., Genangeli, A., Genesio, L., Hanus, J., Peressotti, A., Rademske, P., Rascher, U., Schuettemeyer, D., 2022. Response times of remote sensing

measured sun-induced chlorophyll fluorescence, surface temperature and vegetation indices to evolving soil water limitation in a crop canopy. Remote Sens. Environ. 273, 112957.

Daumard, F., Goulas, Y., Ounis, A., Pedros, R., Moya, I., 2007. Atmospheric correction of airborne passive measurements of fluorescence. In: Proc. International Symposium on Physical Measurements and Signatures in Remote Sensing (ISPMSRS), 12–14 March 2007, Davos, Switzerland.

De Cannière, S., Herbst, M., Vereecken, H., Defourny, P., Jonard, F., 2021. Constraining water limitation of photosynthesis in a crop growth model with sun-induced chlorophyll fluorescence. Remote Sens. Environ. 267, 112722.

De Cannière, S., Vereecken, H., Defourny, P., Jonard, F., 2022. Remote sensing of instantaneous drought stress at canopy level using sun-induced chlorophyll fluorescence and canopy reflectance. Remote Sens. 14, 2642.

Dechant, B., Ryu, Y., Badgley, G., Zeng, Y., Berry, J.A., Zhang, Y., Goulas, Y., Li, Z., Zhang, Q., Kang, M., Li, J., Moya, I., 2020. Canopy structure explains the relationship between photosynthesis and sun-induced chlorophyll fluorescence in crops. Remote Sens. Environ. 241, 111733.

Disney, M., 2016. Remote sensing of vegetation: potentials, limitations, developments and applications. In: Hikosaka, K., Niinemets, Ü., Anten, N.P.R. (Eds.), Canopy Photosynthesis: From Basics to Applications. Springer, Dordrecht, pp. 289–331.

Dobrowski, S. Z., Pushnik, J. C., Zarco-Tejada, P. J., and Ustin, S. L., 2005. Simple reflectance indices track heat and water stress-induced changes in steady-state chlorophyll fluorescence at the canopy scale. Remote Sens. Environ. 97, 403–414.

Drusch, M., Moreno, J., Del Bello, U., Franco, R., Goulas, Y., Huth, A., Kraft, S., Middleton, E.M., Miglietta, F., Mohammed, G., Nedbal, L., Rascher, U., Schüttemeyer, D., Verhoef, W., 2017. The FLuorescence EXplorer mission concept - ESA's Earth Explorer 8. IEEE Trans. Geosci. Remote Sens. 55, 1273–1284.

Du, K., Jing, X., Zeng, Y., Ye, Q., Li, B., Huang, J., 2023. An Improved Approach to Monitoring Wheat Stripe Rust with Sun-Induced Chlorophyll Fluorescence. Remote Sens. 15, 693.

Du, S., Liu, L., Liu, X., Guo, J., Hu, J., Wang, S., Zhang, Y., 2019. SIFSpec: Measuring solar-induced chlorophyll fluorescence observations for remote sensing of photosynthesis. Sensors 19, 3009.

Du, S., Liu, L., Liu, X., Zhang, X., Zhang, X., Bi, Y., Zhang, L., 2018. Retrieval of global terrestrial solar-induced chlorophyll fluorescence from TanSat satellite. Sci. Bull. 63, 1502–1512.

ESA (European Space Agency), 2015. Report for Mission Selection: FLEX. ESA SP-1330/2 (2 Volume Series). 197 pp., Noordwijk (The Netherlands). https://esamultimedia.esa.int/docs/EarthObservation/SP1330-2_FLEX.pdf.

Forster, T., 1948. Intermolecular Energy Migration and Fluorescence. Annals of Physics 2, 55-75.

804 Frankenberg, C., O'Dell, C., Berry, J., Guanter, L., Joiner, J., Köhler, P., Pollack, R., Taylor, T.E.,
805 2014. Prospects for chlorophyll fluorescence remote sensing from the Orbiting Carbon
806 Observatory-2. Remote Sens. Environ. 147, 1–12.
807
808 Frankenberg, C., Berry, J., 2018. Solar induced chlorophyll fluorescence: Origins, relation to
809 photosynthesis and retrieval. in: Liang, S. (Eds.), Comprehensive Remote Sensing, vol 3.
810 Elsevier, pp. 143–162.
811
812 Frankenberg, C., Köhler, P., Magney, T.S., Geier, S., Lawson, P., Schwochert, M., McDuffie, J.,
813 Drewry, D.T., Pavlick, R., Kuhnert, A., 2018. The chlorophyll fluorescence imaging
814 spectrometer (CFIS), mapping far red fluorescence from aircraft. Remote Sens. Environ. 217,
815 523–536.
816
817 Frigerio, S., Bassi R., Giacometti G.M., 2008. Light Conversion in Photosynthetic Organisms, in:
818 Pavesi, L., Fauchet, P.M. (Eds.), Biophotonics. Springer, Berlin, Heidelberg, pp. 1–14.
819
820 Gastellu-Etchegorry, J.-P., Lauret, N., Yin, T., Landier, L., Kallel, A., Malenovský, Z., Al Bitar, A.,
821 Aval, J., Benhmida, S., Qi, J., Medjdoub, G., Guilleux, J., Chavanon, E., Cook, B., Morton, D.,
822 Chrysoulakis, N., Mitraka, Z., 2017. DART: recent advances in remote sensing data modeling
823 with atmosphere, polarization, and chlorophyll fluorescence. IEEE J. Sel. Top. Appl. Earth Obs.
824 Remote Sens. 10, 2640–2649.
825
826 Genty, B., Briantais, J.M., Baker, N.R., 1989. The relationship between the quantum yield of
827 photosynthetic electron transport and quenching of chlorophyll fluorescence. Biochim. Biophys.
828 Acta 990, 87–92.
829
830 Giardi, M.T., Cona, A., Geiken, B., Kucera, T., Masajidek, J., Matoo, A.K., 1996. Long-term drought
831 stress induces structural and functional reorganization of photosystem II. Planta, 99, 118–125.
832
833 Gómez-Chova, L., Alonso-Chorda, L., Amoros-Lopez, J., Vila-Frances, J., Del Valle-Tascon, S.,
834 Calpe, J., Moreno, J., 2006. Solar induced fluorescence measurements using a field
835 spectroradiometer. AIP Conf. Proc. 852, 274–281.
836
837 Gonzalez-Dugo, V., Hernandez, P., Solis, I., Zarco-Tejada, P.J., 2015. Using high-resolution
838 hyperspectral and thermal airborne imagery to assess physiological condition in the context of
839 wheat phenotyping. Remote Sens. 7, 13586–13605.
840
841 Govindjee, 2004. Chlorophyll a fluorescence: a bit of basics and history, in: Papageorgiou, G.C.,
842 Govindjee (Eds.), Chlorophyll a Fluorescence, a signature of photosynthesis. Advances in
843 Photosynthesis and Respiration, vol 19. Springer, Dordrecht, pp. 1–42.
844
845 Grossmann, K., Frankenberg, C., Magney, T.S., Hurlock, S.C., Seibt, U., Stutz, J., 2018. PhotoSpec:
846 a new instrument to measure spatially distributed red and far-red solar-induced chlorophyll
847 fluorescence. Remote Sens. Environ. 216, 311–327.
848
849 Gu, L., Wood, J.D., Chang, C.Y., Sun, Y., Riggs, J.S., 2019. Advancing terrestrial ecosystem science
850 with a novel automated measurement system for sun-induced chlorophyll fluorescence for
851 integration with eddy covariance flux networks. J. Geophys. Res. Biogeosci. 124, 127–146.
852
853 Guanter, L., Aben, I., Tol, P., Krijger, J.M., Hollstein, A., Köhler, P., Damm, A., Joiner, J.,
854 Frankenberg, C., Landgraf, J., 2015. Potential of the TROPOspheric Monitoring Instrument

(TROPOMI) onboard the Sentinel-5 precursor for the monitoring of terrestrial chlorophyll fluorescence. Atmos. Meas. Tech. 8, 1337–1352.

Guanter, L., Rossini, M., Colombo, R., Meroni, M., Frankenberg, C., Lee, J.-E., Joiner, J., 2013. Using field spectroscopy to assess the potential of statistical approaches for the retrieval of sun-induced chlorophyll fluorescence from ground and space. Remote Sens. Environ. 133, 52–61.

Guanter, L., Alonso, L., Gómez-Chova, L., Amorós-López, J., Vila, J., Moreno, J., 2007. Estimation of solar-induced vegetation fluorescence from space measurements. Geophys. Res. Lett. 34, L08401.

Hao, D., Zeng, Y., Zhang, Z., Zhang, Y., Qiu, H., Biriukova, K., Celesti, M., Rossini, M., Zhu, P., Asrar, G.R., Chen, M., 2022. Adjusting solar-induced fluorescence to nadir-viewing provides a better proxy for GPP. ISPRS J. Photogramm. Remote Sens. 186, 157-169.

Hasegawa, T., Fujimori, S., Havlík, P., Valin, H., Bodirsky, B.L., Doelman, J.C., Fellmann, T., Kyle, P., Koopman, J.F.L., Lotze-Campen, H., Mason-D'Croz, D., Ochi, Y., Pérez Domínguez, I., Stehfest, E., Sulser, T.B., Tabeau, A., Takahashi, K., Takakura, J., van Meijl, H., van Zeist, W.J., Wiebe, K., Witzke, P., 2018. Risk of increased food insecurity under stringent global climate change mitigation policy. Nat. Clim. Change 8, 699–703.

Hatfield, J.L., Prueger, J.H., 2011. Agroecology: Implications for Plant Response to Climate Change, in: Yadav, S.S., Redden, R.J., Hatfield, J.L., Lotze-Campen, H., Hall, A.E (Eds.), Crop Adaption to Climate Change. Wiley-Blackwell, West Sussex, UK, pp. 27–43.

Haupt, W., 1990. Chloroplast movement. Plant Cell Environ. 13, 595–614.

Heldt, H., Piechulla, B., 2011. Plant Biochemistry, Academic Press, Elsevier, San Diego, CA, USA.

Hernández-Clemente, R., North, P.R.J., Hornero, A., Zarco-Tejada, P.J., 2017. Assessing the effects of forest health on sun-induced chlorophyll fluorescence using the FluorFLIGHT 3-D radiative transfer model to account for forest structure. Remote Sens. Environ. 193, 165–179.

Hofius, D., Börnke; F. A. J., 2007. Photosynthesis, carbohydrate metabolism and source–sink relations. In: Viola, R., Gebhardt, C., MacKerron, D., Vreudenhil, D. (Eds.), Potato biology and biotechnology: advances and perspectives, Elsevier Science B.V., Amsterdam, pp. 257–285.

Hornero, A., North, P.R.J., Zarco-Tejada, P.J., Rascher, U., Martín, M.P., Migliavacca, M., Hernández-Clemente, R., 2021a. Assessing the contribution of understory sun-induced chlorophyll fluorescence through 3-D radiative transfer modelling and field data. Remote Sens. Environ. 253, 112195.

Hornero, A., Zarco-Tejada, P.J., Quero, J.L., North, P.R.J., Ruiz-Gómez, F.J., Sánchez-Cuesta, R., Hernández-Clemente, R., 2021b. Modelling hyperspectral- and thermal-based plant traits for the early detection of Phytophthora-induced symptoms in oak decline. Remote Sens. Environ. 263, 112570.

Huner, N.P.A., Maxwell, D.P., Gray, G.R., Savitch, L.V., Krol, M., Ivanov, A.G., Falk, S., 1996. Sensing environmental temperature change through imbalances between energy supply and energy consumption: redox state of photosystem II. Physiologia Plantarum 98, 358–364.

Hussain, S., Ulhassan, Z., Brestic, M., Zivcak, M., Zhou, W., Allakhverdiev, S.I., Yang, X., Safdar M.E., Yang, W., Liu, W., 2021. Photosynthesis research under climate change. Photosynth. Res. 150, 5–19.

Jacquemoud, S., Verhoef, W., Baret, F., Bacour, C., Zarco-Tejada, P.J., Asner, G.P., François, C., Ustin, S.L., 2009. PROSPECT+SAIL models: a review of use for vegetation characterization. Remote Sens. Environ. 113 (Suppl. 1), S56–S66.

Jing, X., Li, B., Ye, Q., Zou, Q., Yan, J., Du, K., 2022. Integrate the Canopy SIF and Its Derived Structural and Physiological Components for Wheat Stripe Rust Stress Monitoring. Remote Sens. 14, 3427.

Joiner, J., Guanter, L., Lindstrot, R., Voigt, M., Vasilkov, A.P., Middleton, E.M., Huemmrich, K.F., Yoshida, Y., Frankenberg, C., 2013. Global monitoring of terrestrial chlorophyll fluorescence from moderate spectral resolution near-infrared satellite measurements: methodology, simulations, and application to GOME-2. Atmos. Meas. Tech. 6, 2803–2823.

Joiner, J., Yoshida, Y., Vasilkov, A.P., Middleton, E.M., Campbell, P.K.E., Yoshida, Y., Kuze, A., Corp, L.A., 2012. Filling-in of near-infrared solar lines by terrestrial fluorescence and other geophysical effects: simulations and space-based observations from SCIAMACHY and GOSAT. Atmos. Meas. Tech. 5, 809–829.

Joiner, J., Yoshida, Y., Vasilkov, A.P., Yoshida, Y., Corp, L.A., Middleton, E.M., 2011. First observations of global and seasonal terrestrial chlorophyll fluorescence from space. Biogeosci. 8, 637–651.

Kallel, A., 2020. FluLCVRT: Reflectance and fluorescence of leaf and canopy modeling based on Monte Carlo vector radiative transfer simulation. Journal of Quantitative Spectroscopy and Radiative Transfer 253, 107183.

Kim, J., Ryu, Y., Dechant, B., 2022. Development of a filter-based near-surface remote sensing system to retrieve far-red sun-induced chlorophyll fluorescence. Remote Sens. Environ. 283, 113311.

Kimm, H., Guan, K., Jiang, C., Miao, G., Wu, G., Suyker, A.E., Ainsworth, E.A., Bernacchi, C.J., Montes, C.M., Berry, J.A., Yang, X., 2021. A physiological signal derived from sun-induced chlorophyll fluorescence quantifies crop physiological response to environmental stresses in the US Corn Belt. Environ. Res. Lett. 16, 124051.

Köhler, P., Guanter, L., Joiner, J., 2015. A linear method for the retrieval of sun-induced chlorophyll fluorescence from GOME-2 and SCIAMACHY data. Atmos. Meas. Tech. 8, 2589–2608.

Kolber, Z., Klimov, D., Ananyev, G., Rascher, U., Berry, J., Osmond, B., 2005. Measuring photosynthetic parameters at a distance: laser induced fluorescence transient (LIFT) method for remote measurements of photosynthesis in terrestrial vegetation. Photosynth. Res. 84, 121–129.

Kolber, Z., Prasil, O., Falkowski, P.G., 1998. Measurements of variable chlorophyll fluorescence using fast repetition rate techniques: defining methodology and experimental protocols. Biochim Biophys Acta 1367, 88–106.

Kozaki, A., Takeba, G., 1996. Photorespiration protects C3 plants from photooxidation. Nature, 384, 557–560.

Kramer, D.M., Avenson, T.J., Edwards, G.E., 2004. Dynamic flexibility in the light reactions of photosynthesis governed by both electron and proton transfer reactions. Trends Plant Sci. 9, 349–357.

Krause, G.H., Weis, E., 1984. Chlorophyll fluorescence as a tool in plant physiology. II. Interpretation of fluorescence signals. Photosynth. Res. 5, 139–157.

Li, Z., Zhang, Q., Li, J., Yang, X., Wu, Y., Zhang, Z., Wang, S., Wang, H., Zhang, Y., 2020. Solar-induced chlorophyll fluorescence and its link to canopy photosynthesis in maize from continuous ground measurements. Remote Sens. Environ. 236, 111420.

Li, X., Shabanov, N.V., Chen, L., Zhang, Y., Huang, H., 2022. Modeling solar-induced fluorescence of forest with heterogeneous distribution of damaged foliage by extending the stochastic radiative transfer theory. Remote Sens. Environ. 271, 112892.

Liu, L., Liu, X., Hu, J., 2015. Effects of spectral resolution and SNR on the vegetation solar-induced fluorescence retrieval using FLD-based methods at canopy level. Eur. J. Remote Sens. 48, 743–762.

Liu, L., Guan, L., Liu, X., 2017. Directly estimating diurnal changes in GPP for C3 and C4 crops using far-red sun-induced chlorophyll fluorescence. Agric. For. Meteorol. 232, 1-9.

Liu, X., Guanter, L., Liu, L., Damm, A., Malenovský, Z., Rascher, U., Peng, D., Du, S., Gastellu-Etchegorry, J.-P., 2019. Downscaling of solar-induced chlorophyll fluorescence from canopy level to photosystem level using a random forest model. Remote Sens. Environ. 231, 110772.

Liu, X., Liu, Z., Liu, L., Lu, X., Chen, J., Du, S., Zou, C., 2021. Modelling the influence of incident radiation on the SIF-based GPP estimation for maize. Agric. For. Meteorol. 307, 108522.

Longmire, A.R., Poblete, T., Hunt, J.R., Chen, D., Zarco-Tejada, P.J., 2022. Assessment of crop traits retrieved from airborne hyperspectral and thermal remote sensing imagery to predict wheat grain protein content. ISPRS J. Photogramm. Remote Sens. 193, 284–298.

Ludlow, M.M., Bjorkman, O., 1984. Paraheliotropic leaf movement in Siratro as a protective mechanism against drought-induced damage to primary photosynthetic reactions: damage by excessive light and heat. Planta, 161, 505–518.

Maier, S.W., Günther, K.P., Stellmes, M., 2003. Sun-induced fluorescence: a new tool for precision farming. In: Schepers, J., VanToai, T. (Eds.), Digital Imaging and Spectral Techniques: Applications to Precision Agriculture and Crop Physiology. ASA Spec. Publ. 66. ASA, CSSA, and SSSA, Madison (Wisconsin), USA, pp. 209–222.

Maxwell, K., Johnson, G.N., 2000. Chlorophyll fluorescence — a practical guide. J. Exp. Bot. 51, 659–668.

Mazzoni, M., Agati, G., Cecchi, G., Toci, G., Mazzinghi, P., 2007. High resolution measurements of solar induced chlorophyll fluorescence in the Fraunhofer oxigen bands. In Proc. SPIE 10567, International Conference on Space Optics, Noordwijk, Netherlands.

Meroni, M., Busetto, L., Colombo, R., Guanter, L., Moreno, J., Verhoef, W., 2010. Performance of spectral fitting methods for vegetation fluorescence quantification. Remote Sens. Environ. 114, 363–374.

Meroni, M., Rossini, M., Guanter, L., Alonso, L., Rascher, U., Colombo, R., Moreno, J., 2009. Remote sensing of solar-induced chlorophyll fluorescence: review of methods and applications. Remote Sens. Environ. 113, 2037–2051.

Meroni, M., Colombo, R., 2006. Leaf level detection of solar induced chlorophyll fluorescence by means of a subnanometer resolution spectroradiometer. Remote Sens. Environ. 103, 438–448.

Merzlyak, M.N., Chivkunova, O.B., Solovchenko, A.E., Naqvi, K.R., 2008. Light absorption by anthocyanins in juvenile, stressed, and senescing leaves. J. Exp. Bot. 59, 3903–3911.

Migliavacca, M., Perez-Priego, O., Rossini, M., El-Madany, T. S., Moreno, G., Van der Tol, C., Rascher, U., Berninger, A., Bessenbacher, V., Burkart, A., Carrara, A., 2017. Plant functional traits and canopy structure control the relationship between photosynthetic CO2 uptake and far-red sun-induced fluorescence in a Mediterranean grassland under different nutrient availability. New Phytol., 214, 1078–1091.

Mohammed, G.H., Colombo, R., Middleton, E.M., Rascher, U., Van der Tol, C., Nedbal, L., Goulas, Y., Pérez-Priego, O., Damm, A., Meroni, M., Joiner, J., Cogliati, S., Verhoef, W., Malenovský, Z., Gastellu-Etchegorry, J.P., Miller, J.R., Guanter, L., Moreno, J., Moya, I., Berry, J.A., Frankenberg, C., Zarco-Tejada, P.J., 2019. Remote sensing of solar-induced chlorophyll fluorescence (SIF) in vegetation: 50 years of progress. Remote Sens. Environ. 231, 111177.

Morozumi, T., Kato, T., Kobayashi, H., Sakai, Y., Nakashima, N., Buareal, K., Nasahara, K.N., Akitsu, T.K., Murayama, S., Noda, H.M., Muraoka, H., 2023. Contributions of the understory and midstory to total canopy solar-induced chlorophyll fluorescence in a ground-based study in conjunction with seasonal gross primary productivity in a cool-temperate deciduous broadleaf forest. Remote Sens. Environ. 284, 113340.

Moya, I., Daumard, F., Moise, N., Ounis, A., Goulas, Y., 2006. First airborne multiwavelength passive chlorophyll fluorescence measurements over La Mancha (Spain) fields. In: Proc. Recent Advances in Quantitative Remote Sensing, 25–29 September 2006, Torrent, Spain, pp. 820–825.

Murchie, E.H., Horton, P., 1997. Acclimation of photosynthesis to irradiance and spectral quality in British plant species: chlorophyll content, photosynthetic capacity and habitat preference. Plant Cell Environ. 20, 438–448.

Naethe, P., Julitta, T., Chang, C.Y.Y., Burkart, A., Migliavacca, M., Guanter, L., Rascher, U., 2022. A precise method unaffected by atmospheric reabsorption for ground-based retrieval of red and far-red sun-induced chlorophyll fluorescence. Agric. For. Meteorol. 325, 109152.

Pacheco-Labrador, J., Perez-Priego, O., El-Madany, T.S., Julitta, T., Rossini, M., Guan, J., Moreno, G., Carvalhais, N., Martín, M.P., Gonzalez-Cascon, R., Kolle, O., 2019. Multiple-constraint inversion of SCOPE. Evaluating the potential of GPP and SIF for the retrieval of plant functional traits. Remote Sens. Environ. 234, 111362.

Panigada, C., Rossini, M., Meroni, M., Cilia, C., Busetto, L., Amaducci, S., Boschetti, M., Cogliati, S., Picchi, V., Pinto, F., Marchesi, A., Colombo, R., 2014. Fluorescence, PRI and canopy

temperature for water stress detection in cereal crops. Int. J. Appl. Earth Obs. Geoinf. 30, 167–178.

Pancorbo, J.L., Alonso-Ayuso, M., Camino, C., Raya-Sereno, M.D., Zarco-Tejada, P.J., Molina, I., Gabriel, J.L., Quemada, M., 2023. Airborne hyperspectral and Sentinel imagery to quantify winter wheat traits through ensemble modeling approaches. Precision Agric. 24, 1288–1311.

Paynter, I., Cook, B., Corp, L., Nagol, J., McCorkel, J., 2020. Characterization of FIREFLY, an imaging spectrometer designed for remote sensing of solar induced fluorescence. Sensors 20, 4682.

Pedrós, R., Goulas, Y., Jacquemoud, S., Louis, J., Moya, I., 2010. FluorMODleaf: a new leaf fluorescence emission model based on the PROSPECT model. Remote Sens. Environ. 114, 155–167.

Pérez-Priego, O., Zarco-Tejada, P.J., Miller, J.R., Sepulcre-Cantó, G., Fereres, E., 2005. Detection of water stress in orchard trees with a high-resolution spectrometer through chlorophyll fluorescence in-filling of the O2-A band. IEEE Trans. Geosci. Remote Sens. 43, 2860–2869.

Plascyk, J.A., 1975. The MK II Fraunhofer line discriminator (FLD-II) for airborne and orbital remote sensing of solar-stimulated luminescence. Opt. Eng. 14, 144339.

Pinto, F., Celesti, M., Acebron, K., Alberti, G., Cogliati, S., Colombo, R., Juszczak, R., Matsubara, S., Miglietta, F., Palombo, A., Panigada, C., 2020. Dynamics of sun-induced chlorophyll fluorescence and reflectance to detect stress-induced variations in canopy photosynthesis. Plant, cell & environment, 43, 1637-1654.

Poblete, T., Camino, C., Beck, P.S.A., Hornero, A., Kattenborn, T., Saponari, M., Boscia, D., Navas-Cortes, J.A., Zarco-Tejada, P.J., 2020. Detection of Xylella fastidiosa infection symptoms with airborne multispectral and thermal imagery: Assessing bandset reduction performance from hyperspectral analysis. ISPRS J. Photogramm. Remote Sens. 162, 27–40.

Poblete, T., Navas-Cortes, J.A., Camino, C., Calderon, R., Hornero, A., Gonzalez-Dugo, V., Landa, B.B., Zarco-Tejada, P.J., 2021. Discriminating Xylella fastidiosa from Verticillium dahliae infections in olive trees using thermal- and hyperspectral-based plant traits. ISPRS J. Photogramm. Remote Sens. 179, 133–144.

Poblete, T., Navas-Cortes, J.A., Hornero, A., Camino, C., Calderon, R., Hernandez-Clemente, R., Landa, B.B., Zarco-Tejada, P.J., 2023. Detection of symptoms induced by vascular plant pathogens in tree crops using high-resolution satellite data: Modelling and assessment with airborne hyperspectral imagery. Remote Sens. Environ. 295, 113698.

Porcar-Castell, A., Tyystjärvi, E., Atherton, J., Van der Tol, C., Flexas, J., Pfündel, E.E., Moreno, J., Frankenberg, C., Berry, J.A., 2014. Linking chlorophyll a fluorescence to photosynthesis for remote sensing applications: mechanisms and challenges. J. Exp. Bot. 65, 4065–4095.

Rascher, U., Alonso, L., Burkart, A., Cilia, C., Cogliati, S., Colombo, R., Damm, A., Drusch, M., Guanter, L., Hanus, J., Hyvärinen, T., Julitta, T., Jussila, J., Kataja, K., Kokkalis, P., Kraft, S., Kraska, T., Matveeva, M., Moreno, J., Muller, O., Panigada, C., Pikl, M., Pinto, F., Prey, L., Pude, R., Rossini, M., Schickling, A., Schurr, U., Schüttemeyer, D., Verrelst, J., Zemek, F., 2015.

Sun-induced fluorescence - a new probe of photosynthesis: first maps from the imaging spectrometer HyPlant. Glob. Chang. Biol. 21, 4673–4684.

Romero, J.M., Cordon, G.B., Lagorio, M.G., 2020. Re-absorption and scattering of chlorophyll fluorescence in canopies: A revised approach. Remote Sens. Environ. 246, 111860.

Rosema, A., Verhoef, W., Schroote, J., Snel, J.F.H., 1991. Simulating fluorescence light canopy interaction in support of laser-induced fluorescence measurements. Remote Sens. Environ. 37, 117–130.

Rossini, M., Nedbal, L., Guanter, L., Ač, A., Alonso, L., Burkart, A., Cogliati, S., Colombo, R., Damm, A., Drusch, M., Hanus, J., Janoutova, R., Julitta, T., Kokkalis, P., Moreno, J., Novotny, J., Panigada, C., Pinto, F., Schickling, A., Schüttemeyer, D., Zemek, F., Rascher, U., 2015a. Red and far-red sun-induced chlorophyll fluorescence as a measure of plant photosynthesis. Geophys. Res. Lett. 42, 1632–1639.

Rossini, M., Panigada, C., Cilia, C., Meroni, M., Busetto, L., Cogliati, S., Amaducci, S., Colombo, R., 2015b. Discriminating irrigated and rainfed maize with diurnal fluorescence and canopy temperature airborne maps. ISPRS Int. J. Geoinf. 4, 626-646.

Sakai, Y., Kobayashi, H., Kato, T., 2020. FLiES-SIF version 1.0: three-dimensional radiative transfer model for estimating solar induced fluorescence. Geosci. Model Dev. 13, 4041-4066.

Sarvikas, P., Hakala-Yatkin, M., Dönmez, S., Tyystjärvi, E., 2010. Short flashes and continuous light have similar photoinhibitory efficiency in intact leaves. J. Exp. Bot. 61, 4239–4247.

Schreiber, U., 2004. Pulse-Amplitude-Modulation (PAM) Fluorometry and Saturation Pulse Method: An Overview. in: Papageorgiou, G.C., Govindjee (Eds.), Chlorophyll a Fluorescence. Advances in Photosynthesis and Respiration, vol 19. Springer, Dordrecht, pp. 279–319.

Schreiber, U., Schliwa, U., Bilger, W., 1986. Continuous recording of photochemical and nonphotochemical fluorescence quenching with a new type of modulation fluorometer. Photosynth. Res. 10, 51–62.

Scodellaro, R., Cesana, I., D'Alfonso, L., Bouzin, M., Collini, M., Chirico, G., Colombo, R., Miglietta, F., Celesti, M., Schuettemeyer, D., Cogliati, S., Sironi, L., 2022. A novel hybrid machine learning phasor-based approach to retrieve a full set of solar-induced fluorescence metrics and biophysical parameters. Remote Sens. Environ. 280, 113196.

Siegmann, B., Alonso, L., Celesti, M., Cogliati, S., Colombo, R., Damm, A., Douglas, S., Guanter, L., Hanuš, J., Kataja, K., Kraska, T., Matveeva, M., Moreno, J., Muller, O., Pikl, M., Pinto, F., Vargas, J.Q., Rademske, P., Rodriguez-Morene, F., Sabater, N., Schickling, A., Schüttemeyer, D., Zemek, F., Rascher, U., 2019. The high-performance airborne imaging spectrometer HyPlant-from raw images to top-of-canopy reflectance and fluorescence products: Introduction of an automatized processing chain. Remote Sens. 11, 2760.

Siegmann, B., Cendrero-Mateo, M.P., Cogliati, S., Damm, A., Gamon, J., Herrera, D., Jedmowski, C., Junker-Frohn, L.V., Kraska, T., Muller, O., Rademske, P., 2021. Downscaling of far-red solar-induced chlorophyll fluorescence of different crops from canopy to leaf level using a diurnal data set acquired by the airborne imaging spectrometer HyPlant. Remote Sens. Environ. 264, 112609.

Simkin, A.J., López-Calcagno, P.E., Raines, C.A., 2019. Feeding the world: improving photosynthetic efficiency for sustainable crop production. J. Exp. Bot. 70, 1119–1140.

Stiller, M., 1962. The path of carbon in photosynthesis. Ann. Rev. Plant Physiol. 13, 151-170.

Suarez, L., Zhang, P., Sun, J., Wang, Y., Poblete, T., Hornero, A., Zarco-Tejada, P.J., 2021. Assessing wine grape quality parameters using plant traits derived from physical model inversion of hyperspectral imagery. Agric. For. Meteorol. 306, 108445.

Sun, Y., Frankenberg, C., Wood, J.D., Schimel, D.S., Jung, M., Guanter, L., Drewry, D.T., Verma, M., Porcar-Castell, A., Griffis, T.J., Gu, L., Magney, T.S., Köhler, P., Evans, B., Yuen, K., 2017. OCO-2 advances photosynthesis observation from space via solar induced chlorophyll fluorescence. Science 358, eaam5747.

Sun, Y., Wen, J., Gu, L., Joiner, J., Chang, C. Y.-Y., van der Tol, C., Porcar-Castell, A., Magney, T. S., Wang, L., Hu, L., Rascher, U., Zarco-Tejada, P. J., Barrett, C. B., Lai, J., Han, J., Luo, Z., 2023a. From remotely sensed solar-induced chlorophyll fluorescence to ecosystem structure, function, and service: Part I—Harnessing theory. Glob. Chang. Biol. 29, 2926–2952.

Sun, Y., Gu, L., Wen, J., van der Tol, Y., Porcar-Castell, A., Joiner, J., Chang, C.Y., Magney, T., Wang, L., Hu, L., Rascher, U., Zarco-Tejada, P.J., Barrett, C.B., Lai, J., Han, J., Luo, Z., 2023b. From remotely sensed solar-induced chlorophyll fluorescence to ecosystem structure, function, and service: Part II—Harnessing data, Glob. Chang. Biol. 29, 2893–2925.

Tester, M., Langridge, P., 2010. Breeding technologies to increase crop production in a changing world. Science 327, 818–822.

Thiele, A., Krause, G.H., Winter, K., 1998. In situ study of photoinhibition of photosynthesis and xanthophyll cycle activity in plants growing in natural gaps of the tropical forest. Aust. J. Plant. Physiol. 25, 189–195.

United Nations, 2022. World Population Prospects 2022: Summary of Results. UN DESA/POP/2022/TR/NO. 3.

Van Bel, A.J.E., Offler, C.E., Patrick, J.W., 2003. Photosynthesis and Partitioning | Sources and Sinks, in: Thomas, B. (Eds.), Encyclopedia of Applied Plant Sciences, Elsevier, pp. 724-734.

Van der Tol, C., Verhoef, W., Timmermans, J., Verhoef, A., Su, Z., 2009. An integrated model of soil-canopy spectral radiances, photosynthesis, fluorescence, temperature and energy balance. Biogeosci. 6, 3109–3129.

Van der Tol, C., Julitta, T., Yang, P., Sabater, N., Reiter, I., Tudoroiu, M., Schuettemeyer, D., Drusch, M., 2023. Retrieval of chlorophyll fluorescence from a large distance using oxygen absorption bands. Remote Sens. Environ. 284, 113304.

Verhoef, W., 2004. Extension of SAIL to model solar - induced canopy fluorescence spectra. In: Proc. 2nd International Workshop on Remote Sensing of Vegetation Fluorescence, 17–19 November 2004, Montreal, Canada.

Verhoef, W., Van der Tol, C., Middleton, E.M., 2018. Hyperspectral radiative transfer modeling to explore the combined retrieval of biophysical parameters and canopy fluorescence from FLEX – Sentinel-3 tandem mission multi-sensor data. Remote Sens. Environ. 204, 942–963.

Verrelst, J., Van der Tol, C., Magnani, F., Sabater, N., Rivera, J. P., Mohammed, G., and Moreno, J., 2016. Evaluating the predictive power of sun-induced chlorophyll fluorescence to estimate net photosynthesis of vegetation canopies: A SCOPE modeling study. Remote Sens. Environ. 176, 139–151.

Vilfan, N., Van der Tol, C., Muller, O., Rascher, U., Verhoef, W., 2016. Fluspect-B: a model for leaf fluorescence, reflectance and transmittance spectra. Remote Sens. Environ. 186, 596–615.

Walters, R.G., 2005. Towards an understanding of photosynthetic acclimation. J. Exp. Bot. 56, 435–447.

Wang, Y., Suarez, L., Poblete, T., Gonzalez-Dugo, V., Ryu, D., Zarco-Tejada, P.J., 2022. Evaluating the role of solar-induced fluorescence (SIF) and plant physiological traits for leaf nitrogen assessment in almond using airborne hyperspectral imagery. Remote Sens. Environ. 279, 113141.

Wang, R., Gamon, J.A., Hmimina, G., Cogliati, S., Zygielbaum, A.I., Arkebauer, T.J., Suyker, A., 2022. Harmonizing solar induced fluorescence across spatial scales, instruments, and extraction methods using proximal and airborne remote sensing: A multi-scale study in a soybean field. Remote Sens. Environ. 281, 113268.

Wang, N., Yang, P., Clevers, J.G., Wieneke, S., Kooistra, L., 2023. Decoupling physiological and non-physiological responses of sugar beet to water stress from sun-induced chlorophyll fluorescence. Remote Sens. Environ. 286, 113445.

Wieneke, S., Ahrends, H., Damm, A., Pinto, F., Stadler, A., Rossini, M., Rascher, U., 2016. Airborne based spectroscopy of red and far-red sun-induced chlorophyll fluorescence: Implications for improved estimates of gross primary productivity. Remote Sens. Environ. 184, 654–667.

Xu, S., Atherton, J., Riikonen, A., Zhang, C., Oivukkamäki, J., MacArthur, A., Honkavaara, E., Hakala, T., Koivumäki, N., Liu, Z., Porcar-Castell, A., 2021. Structural and photosynthetic dynamics mediate the response of SIF to water stress in a potato crop. Remote Sens. Environ. 263, 112555.

Xu, S., Liu, Z., Zhao, L., Zhao, H., Ren, S., 2018. Diurnal response of sun-induced fluorescence and PRI to water stress in maize using a near-surface remote sensing platform. Remote Sens. 10, 1510.

Yang, P., van der Tol, C., 2018. Linking canopy scattering of far-red sun induced chlorophyll fluorescence with reflectance. Remote Sens. Environ. 209, 456–467.

Yang, P., van der Tol, C., Campbell, P.K., Middleton, E.M., 2020. Fluorescence Correction Vegetation Index (FCVI): A physically based reflectance index to separate physiological and non-physiological information in far-red sun-induced chlorophyll fluorescence. Remote Sens. Environ. 240, 111676.

Yang, S., Yang, J., Shi, S., Song, S., Zhang, Y., Luo, Y., Du, L., 2022. An exploration of solar-induced chlorophyll fluorescence (SIF) factors simulated by SCOPE for capturing GPP across vegetation types. Ecol. Model. 472, 110079.

Yang, X., Shi, H., Stovall, A., Guan, K., Miao, G., Zhang, Y., Zhang, Y., Xiao, X., Ryu, Y., Lee, J.-E., 2018. FluoSpec 2—an automated field spectroscopy system to monitor canopy solar-induced fluorescence. Sensors 18, 2063.

Yang, X., Tang, J., Mustard, J.F., Lee, J.E., Rossini, M., Joiner, J., Munger, J.W., Kornfeld, A., Richardson, A.D., 2015. Solar-induced chlorophyll fluorescence that correlates with canopy photosynthesis on diurnal and seasonal scales in a temperate deciduous forest. Geophys. Res. Lett. 42, 2977-2987.

Yang, P., Prikaziuk, E., Verhoef, W., Van der Tol, C., 2021. SCOPE 2.0: A model to simulate vegetated land surface fluxes and satellite signals. Geosci. Model Dev. 14, 4697–4712.

Zarco-Tejada, P.J., Miller, J.R., Mohammed, G.H., Noland, T.L., 2000a. Chlorophyll fluorescence effects on vegetation apparent reflectance: I. Leaf-level measurements and model simulation. Remote Sens. Environ. 74, 582–595.

Zarco-Tejada, P.J., Miller, J.R., Mohammed, G.H., Noland, T.L., Sampson, P.H., 2000b. Chlorophyll fluorescence effects on vegetation apparent reflectance: II. Laboratory and airborne canopy-level measurements with hyperspectral data. Remote Sens. Environ. 74, 596–608.

Zarco-Tejada, P.J., Miller, J.R., Mohammed, G.H., Noland, T.L., Sampson, P.H., 2001. Estimation of chlorophyll fluorescence under natural illumination from hyperspectral data. Int. J. Appl. Earth Obs. Geoinf. (Special Issue on Applications of Imaging Spectroscopy) 3, 321–327.

Zarco-Tejada, P.J., Miller, J.R., Mohammed, G.H., Noland, T.L., Sampson, P.H., 2002. Vegetation stress detection through chlorophyll a+b estimation and fluorescence effects on hyperspectral imagery. J. Environ. Qual. 31, 1433–1441.

Zarco-Tejada, P.J., Berni, J.A., Suárez, L., Sepulcre-Cantó, G., Morales, F. and Miller, J.R., 2009. Imaging chlorophyll fluorescence with an airborne narrow-band multispectral camera for vegetation stress detection. Remote Sens. Environ. 113, 1262-1275.

Zarco-Tejada, P.J., González-Dugo, V., Berni, J.A.J., 2012. Fluorescence, temperature and narrow-band indices acquired from a UAV platform for water stress detection using a micro-hyperspectral imager and a thermal camera. Remote Sens. Environ. 117, 322–337.

Zarco-Tejada, P.J., Camino, C., Beck, P.S.A., Calderon, R., Hornero, A., Hernández-Clemente, R., Kattenborn, T., Montes-Borrego, M., Susca, L., Morelli, M., Gonzalez-Dugo, V., North, P.R.J., Landa, B.B., Boscia, D., Saponari, M., Navas-Cortes, J.A., 2018. Previsual symptoms of Xylella fastidiosa infection revealed in spectral plant-trait alterations. Nat. Plants 4, 432–439.

Zarco-Tejada, P.J., Poblete, T., Camino, C., Gonzalez-Dugo, V., Calderon, R., Hornero, A., Hernandez-Clemente, R., Román-Écija, M., Velasco-Amo, MP., Landa, BB., Beck, PSA., Saponari, M., Boscia, D., Navas-Cortes, JA., 2021. Divergent abiotic spectral pathways unravel pathogen stress signals across species. Nat. Commun. 12, 6088.

Zeng, Y., Badgley, G., Dechant, B., Ryu, Y., Chen, M., Berry, J. A., 2019. A practical approach for estimating the escape ratio of near-infrared solar-induced chlorophyll fluorescence. Remote Sens. Environ. 232, 111209.

Zeng, Y., Badgley, G., Chen, M., Li, J., Anderegg, L. D. L., Kornfeld, A., Liu, Q., Xu, B., Yang, B., Yan, K., Berry, J. A., 2020. A radiative transfer model for solar induced fluorescence using spectral invariants theory. Remote Sens. Environ. 240, 111678.

Zeng, Y., Chen, M., Hao, D., Damm, A., Badgley, G., Rascher, U., Johnson, J.E., Dechant, B., Siegmann, B., Ryu, Y., Qiu, H., 2022. Combining near-infrared radiance of vegetation and fluorescence spectroscopy to detect effects of abiotic changes and stresses. Remote Sens. Environ. 270, 112856.

Zhang, Z., Zhang, X., Porcar-Castell, A., Chen, J.M., Ju, W., Wu, L., Wu, Y. and Zhang, Y., 2022. Sun-induced chlorophyll fluorescence is more strongly related to photosynthesis with hemispherical than nadir measurements: Evidence from field observations and model simulations. Remote Sens. Environ. 279, 113118.

Zhao, F., Dai, X., Verhoef, W., Guo, Y., Van der Tol, C., Li, Y., Huang, Y., 2016. FluorWPS: a Monte Carlo ray-tracing model to compute sun-induced chlorophyll fluorescence of three-dimensional canopy. Remote Sens. Environ. 187, 385–399.

Zhao, F., Li, R., Verhoef, W., Cogliati, S., Liu, X., Huang, Y., Guo, Y., Huang, J., 2018. Reconstruction of the full spectrum of solar-induced chlorophyll fluorescence: intercomparison study for a novel method. Remote Sens. Environ. 219, 233–246.

Zhou, X., Liu, Z., Xu, S., Zhang, W., Wu, J., 2016. An automated comparative observation system for sun-induced chlorophyll fluorescence of vegetation canopies. Sensors 16, 775.

Zhu, K., Chen, J., Wang, S., Fang, H., Chen, B., Zhang, L., Li, Y., Zheng, C., Amir, M., 2023. Characterization of the layered SIF distribution through hyperspectral observation and SCOPE modeling for a subtropical evergreen forest. ISPRS J. Photogramm. Remote Sens. 201, 78-91.

Chapter 2

SIF quantification from narrow-band and sub-nanometer airborne hyperspectral imagers for vegetation monitoring

This chapter resulted in two research articles.

1. **Belwalkar, A.**, Poblete, T., Longmire, A., Hornero, A., Hernandez-Clemente, R., Zarco-Tejada, P.J., 2022. **Evaluation of SIF retrievals from narrow-band and sub-nanometer airborne hyperspectral imagers flown in tandem: modelling and validation in the context of plant phenotyping**. Remote Sens. Environ. 273, 112986. https://doi.org/10.1016/j.rse.2022.112986
2. **Belwalkar, A.,** Poblete, T., Longmire, A., Hornero, A., Zarco-Tejada, P.J., 2021. **Comparing the retrieval of chlorophyll fluorescence from two airborne hyperspectral imagers with different spectral resolutions for plant phenotyping studies.** In: Proc. IEEE International Geoscience and Remote Sensing Symposium (IGARSS), 12–16 July 2021, Brussels, Belgium, pp. 5845–5848. https://doi.org/10.1109/IGARSS47720.2021.9553265.

Abstract

Solar-induced chlorophyll fluorescence (SIF) can be used as an indicator of crop photosynthetic activity and a proxy for vegetation stress in plant phenotyping and precision agriculture applications. SIF quantification is sensitive to the spectral resolution (SR), and its accurate retrieval requires sensors with sub-nanometer resolutions. However, for accurate SIF quantification from imaging sensors onboard airborne platforms, sub-nanometer imagers are costly and more difficult to operate than the commonly available narrow-band imagers (i.e., 4- to 6-nm bandwidths), which can also be installed on drones and lightweight aircraft. Although a few theoretical and experimental studies have evaluated narrow-band spectra for SIF quantification, there is a lack of research focused on comparing the effects of the SR on SIF from airborne hyperspectral imagers in practical applications. This study investigates the effects of SR and sensor altitude on SIF accuracy, comparing SIF quantified at the 760-nm O_2-A band (SIF_{760}) from two hyperspectral imagers with different spectral configurations (full width at half-maximum resolutions of ≤0.2 nm and 5.8 nm) flown in tandem on board an aircraft. SIF_{760} retrievals were compared from two different wheat and maize phenotyping trials grown under different nitrogen fertiliser application rates over the 2019–2021 growing seasons. SIF_{760} from the two sensors were correlated (R^2 = 0.77–0.9, $p < 0.01$), with the narrow-band imager producing larger SIF_{760} estimates than the sub-nanometer imager (root mean square error (RMSE) 3.28–4.69 mW/m^2/nm/sr). Ground-level SIF_{760} showed strong relationships with both sub-nanometer (R^2 = 0.90, $p < 0.001$, RMSE = 0.07 mW/m^2/nm/sr) and narrow-band (R^2 = 0.88, $p < 0.001$, RMSE = 3.26 mW/m^2/nm/sr) airborne retrievals. Simulation-based assessments of SIF_{760} for SRs ranging from 1 to 5.8 nm using the SCOPE model were consistent with experimental results showing significant relationships among SIF_{760} quantified at different SRs. Predictive algorithms of leaf nitrogen concentration using SIF_{760} from either the narrow-band or sub-nanometer sensor yielded similar performance, supporting the use of narrow-band resolution imagery for

assessing the spatial variability of SIF in plant phenotyping, vegetation stress detection and precision agriculture contexts.

Keywords: Solar-induced chlorophyll fluorescence, SIF, plant phenotyping, stress detection, airborne, hyperspectral, hyperspectral imager

2.1 Introduction

Solar radiation reaching a plant canopy cannot be fully used for photosynthesis, and the resulting excess radiation is partly re-emitted as a weak electromagnetic signal termed solar-induced chlorophyll fluorescence (SIF) (see a full review on SIF in Mohammed *et al.,* 2019). SIF flux originates from photosystem II (PSII) and has a spectral range of 650–800 nm with one peak at 685 nm (SIF_{685}) and a second peak at 740 nm (SIF_{740}). The SIF energy dissipation pathway directly competes with the PSII photochemistry and heat dissipation (Krause and Weis, 1984; Lichtenthaler and Rinderle, 1988). Thus, SIF is a proxy for plant photosynthetic rate, which may be related to plant stress levels (Genty *et al*., 1989; Weis and Berry, 1987; Zarco-Tejada *et al*., 2016). However, SIF emitted from the canopy constitutes a small fraction (1–5%) of the total reflected solar radiation, making it difficult to quantify (Meroni *et al*., 2009).

Specialised algorithms are necessary for decoupling SIF from total reflected solar radiation. These algorithms are classified based on whether SIF is retrieved within specific absorption bands or over the whole SIF emission region (Mohammed *et al*., 2019). Most methods use discrete solar or telluric absorption lines of the solar spectrum, where the contribution of SIF to the total radiance signal is relatively higher. The terrestrial oxygen absorption bands (O_2-A and O_2-B) centred around 760 nm and 687 nm, respectively, are broader and deeper than the other absorption features and, therefore, commonly used for quantifying SIF (Meroni *et al*., 2009). The fluorescence *in-filling* method, based on the Fraunhofer Line Depth (FLD) principle (Plascyk, 1975), depends on a few

discrete spectral bands inside and outside the oxygen absorption features and is the most widely used method for SIF retrieval due to its ease of implementation. By contrast, spectral fitting methods (SFMs) model the fluorescence and reflectance spectrum by spectral curve fitting, using all the contiguous wavelengths within a fixed spectral window mostly centered around oxygen absorption bands (Meroni et al., 2010; Meroni and Colombo, 2006).

The earliest attempt to incorporate leaf fluorescence into a radiative transfer model (RTM) was the Fluorescence–Reflectance–Transmittance (FRT) model (Zarco-Tejada *et al*., 2000a; 2000b). This attempt led to the development of the leaf model FluorMODleaf (Pedrós *et al*., 2008) and a canopy-level RTM named FluorSAIL (Verhoef, 2004). These models prompted the development of an integrated, vertical, one-dimensional, leaf-canopy fluorescence–temperature–photosynthesis model named Soil-Canopy-Observation of Photosynthesis and Energy fluxes (SCOPE) (Van der Tol *et al*., 2009), which is widely used to assess the linkage between fluorescence–reflectance and photosynthesis (Camino *et al*., 2019; Celesti *et al*., 2018; Verhoef *et al*., 2018). SCOPE simulates top-of-canopy radiance, chlorophyll fluorescence and reflectance for homogenous canopies. It has been used to quantify the effects of the leaf biochemistry, maximum carboxylation rate (Vcmax), and canopy structure on apparent reflectance, including fluorescence effects. Recently, three-dimensional canopy RTMs integrating fluorescence have been developed, such as FluorFLIGHT (Hernández-Clemente *et al*., 2017), the Fluorescence model with Weight Photon Spread (FluorWPS) (Zhao *et al*., 2016), and the Discrete Anisotropic Radiative Transfer (DART) model (Gastellu-Etchegorry *et al*., 2017). These models simulate scattering within the canopy components and thus account for canopy structural heterogeneity.

The earliest experiments involving ground-based sub-nanometer-resolution spectrometers quantified SIF at both leaf (Meroni and Colombo, 2006) and canopy levels (Pérez-Priego *et al*., 2005), detecting herbicide- and water-induced stress, respectively. The development of sub-nanometer-resolution hyperspectral sensors in the past decade has enabled SIF retrievals from airborne platforms.

Sensors include the Chlorophyll Fluorescence Imaging Spectrometer (CFIS) (Frankenberg *et al*., 2018), the high-resolution airborne imaging spectrometer HyPlant (Rascher *et al*., 2015), and the Hyperspec High-Resolution Chlorophyll Fluorescence Sensor (Headwall Photonics, Fitchburg, MA, USA) (Belwalkar *et al*., 2021) with spectral resolutions (SRs) of 0.1, 0.28 and ≤0.2 nm, respectively. Sub-nanometer-resolution SIF observations at the global scale are available from satellite sensors such as OCO-2 (Orbiting Carbon Observatory-2) (Frankenberg *et al*., 2014), GOSAT (Greenhouse gases Observing SATellite) (Guanter *et al*., 2012), and TROPOMI (TROPOspheric Monitoring Instrument) (Guanter *et al*., 2015) with spatial resolutions of 1.29 km × 2.25 km, 50 km × 50 km and 5.5 km × 3.5 km, respectively. The European Space Agency is also set to launch the FLuorescence EXplorer (FLEX) (Drusch *et al*., 2017) in 2024, a mission solely dedicated to measuring SIF at a high SR of 0.3 nm across the globe at 300-m spatial resolution.

As a result of these technical and methodological advances, SIF is frequently used for monitoring crop photosynthesis. SIF is measured from a variety of platforms, including ground-based spectrometers (Cogliati *et al*., 2015; Daumard *et al*., 2012; Grossmann *et al*., 2018; Kim *et al*., 2021; Li *et al*., 2020; Pérez-Priego *et al*., 2005; Rossini *et al*., 2016), drones and manned aircraft (Bandopadhyay *et al*., 2019; Damm *et al*., 2014; 2015; Siegmann *et al*., 2019; Tagliabue *et al*., 2020; Zarco-Tejada *et al*., 2012; 2013a) and satellite platforms (Frankenberg *et al*., 2014; Guanter *et al*., 2012; 2015). SIF observations at intermediate scales obtained from airborne platforms are important for i) improving the interpretation of SIF at coarser spatial resolutions and thus bridging the gap between field and global scales, ii) disentangling the contribution of different scene components in aggregated pixels (Hornero *et al*., 2021a; Zarco-Tejada *et al*., 2013b), and iii) evaluating the sensitivity of SIF for describing plant physiological processes at high spatial resolutions (e.g., as an early indicator of biotic and abiotic stress in precision agriculture and forestry).

Modelling studies (Damm *et al*., 2011; Liu *et al*., 2015) of FLD-based SIF retrieval have shown that sensor SR and the signal-to-noise ratio (SNR) (collectively accounting for more than 80%

of the retrieval error) strongly affect SIF measurement accuracy. Several studies have demonstrated the potential of sub-nanometer airborne hyperspectral imagers for precise SIF quantification in a variety of contexts, including estimating gross primary productivity (GPP) (Wieneke *et al*., 2016), validating satellite-based SIF retrievals (Sun *et al*., 2017), assessing the physiological effects of age on loblolly pine forest (Colombo *et al*., 2018) and quantifying functional diversity of terrestrial ecosystems (Tagliabue *et al*., 2020). Although sub-nanometer-resolution imaging sensors are recommended for obtaining absolute measurements of SIF, relative SIF measurements from narrow-band sensors are useful in a variety of settings, including water stress detection (Camino *et al*., 2018a; Panigada *et al.,* 2014; Zarco-Tejada *et al*., 2012), plant phenotyping (Camino *et al*., 2019; 2018b; Gonzalez-Dugo *et al*., 2015), biotic-induced stress detection (Calderón *et al*., 2015; 2013; Hernández-Clemente *et al*., 2017; Hornero *et al*., 2021b; Poblete *et al*., 2020; 2021; Zarco-Tejada *et al*., 2018) and linking canopy-level SIF_{760} and GPP using sensors such as the Airborne Prism Experiment (APEX) with a full width at half-maximum resolution (FWHM) of 5.7 nm over perennial grassland, cropland and mixed temperate forest (Damm *et al*., 2015). In these studies, the reported higher levels of the quantified SIF_{760} were consistent with other modelling and experimental studies (Julitta *et al*., 2016; Nakashima *et al*., 2021; Nichol *et al*., 2019; Süß *et al*., 2016).

The impacts of SR on FLD-based SIF retrievals have been previously assessed with models (Damm *et al*., 2011; Dechant *et al*., 2017; Hernández-Clemente *et al*., 2017; Liu *et al*., 2015) and experiments (Julitta *et al*., 2016). Julitta *et al.* (2016) compared SIF retrievals at both the O_2-A and O_2-B bands using four portable field spectrometers with different spectral sampling intervals (SSIs), SRs, and SNRs simultaneously measuring the same vegetation target. SIF estimates at the O_2-A band from three of the four spectrometers with sub-nanometer resolution (FWHM $\leq$ 1 nm) were consistent with the expected ranges from ground-based SIF observations over lawn grassland reported by Rossini *et al.* (2016). In contrast, the average SIF from the coarsest-resolution spectrometer (FWHM = 5.5 nm) was six times higher than the values obtained from the other three spectrometers, reaching

values above 4 mW/m^2/nm/sr. Our study expands on this previous work by assessing the effects of SR and flight altitude on airborne-based SIF retrievals, which are commonly used in precision agriculture applications. This is, to the best of our knowledge, the first study to do so. Aspects regarding the effects of the atmosphere, flight altitude, and performance of imaging sensors on SIF retrievals need to be studied in addition to the theoretical work and the assessments carried out using close-range spectrometer data.

The need for sub-nanometer imagers for the accurate quantification of SIF brings important challenges in precision agriculture, plant phenotyping and biosecurity applications due to their complexity, higher cost and increased operational difficulties. Standard narrow-band hyperspectral imagers (i.e., with SR in the range of 4–6 nm FWHM) are an appealing alternative that are increasingly being used with drones and lightweight aircraft to collect high-spatial-resolution imagery (Aasen *et al*., 2018). However, it is unclear how useful SIF_{760} estimates from these imagers are for plant physiological assessments when compared to ground-based or sub-nanometer airborne SIF_{760} estimates. Such assessment is critical, particularly when the relative quantification of fluorescence across the landscape could be readily used to detect biotic- and abiotic-induced vegetation stress. Empirical work is needed to evaluate whether SIF_{760} retrievals from these narrow-band hyperspectral imagers are sufficient for detecting physiological stress in crops, relative to measurements from sub-nanometer instruments.

Monitoring crop nutrient status is one potentially important application of airborne SIF_{760} quantification (Camino *et al*., 2018b; Wang *et al*., 2021). Accurate assessments of plant nutrition across a field can help to ensure crop yields by allowing for more efficient use of N-fertilisers. Excessive N fertiliser application can result in the loss of reactive forms of N (ammonia, nitrate, and nitrogen oxides) to the environment, causing water pollution, climate forcing, and biodiversity loss. As a result, assessing crop response to N-fertilisers is critical for ensuring resource efficiency while optimising yields.

In this study, we compared SIF_{760} measured from a 5.8-nm FWHM narrow-band hyperspectral imager to a sub-nanometer hyperspectral imager of ≤0.2 nm FWHM flown in tandem at multiple sensor altitudes and across two wheat and maize trials grown under different nitrogen application rates and for three growing seasons. We validated airborne measures with sub-nanometer ground retrievals and evaluated results against SCOPE simulations. We then assessed the performance of sub-nanometer and narrow-band SIF_{760} estimates for predicting nitrogen concentration using machine learning models. Our findings provide important insights that support the operational use of standard, commercially available narrow-band hyperspectral imagers for quantifying relative SIF levels. This is especially important for precision agriculture and plant physiology monitoring purposes that require accurate assessment of the SIF variability within and across experimental fields.

2.2 Materials and methods

2.2.1 Study sites and field data collection

Experiments took place at two field trial sites in Victoria, Australia, in 2019, 2020 and 2021 (Fig. 2-1a and 2-1b). Experiment 1 was conducted over 15 plots of dryland wheat (cv. Scepter) (Yang *et al*., 2018) located at site 1 in Yarrawonga (36°02′55"S, 145°59′02"E). Plots were 26 m^2 (2 m × 13 m) and planted in May 2019. Plots were grown with five different rates of nitrogen fertiliser in the form of urea (46% N) (T1: 0 kg N/ha, T2: 46 kg N/ha, T3: 92 kg N/ha, T4: 138 kg N/ha, T5: 184 kg N/ha). The surrounding areas were planted with several varieties of wheat grown under various physiological conditions and nitrogen fertiliser application rates (Fig. 2-1a).

Experiments 2 and 3 were conducted in 2020 and 2021 at site 2 in Peechelba East (36°10′04"S, 146°16′23"E) over irrigated maize plots. Experiment 2 consisted of 8 plots and experiment 3 consisted of 20 plots. Plots were sown in October 2019 and October 2020 with two urea application rates for experiment 2 (T1: 207 kg N/ha, T2: 387 kg N/ha) and three for experiment 3 (T1: 0 kg N/ha,

T2: 180 kg N/ha, T3: 315 kg N/ha). The plot sizes were 15 m^2 (3 m × 5 m) for experiment 2 and 36 m^2 (3 m × 12 m) for experiment 3. The climate at both field trial sites is humid subtropical (Cfa) according to the Köppen classification. At site 1, the mean annual temperature is 16.3 °C and average rainfall is 559 mm. At site 2, the mean annual temperature is 15.2 °C and average rainfall is 642 mm.

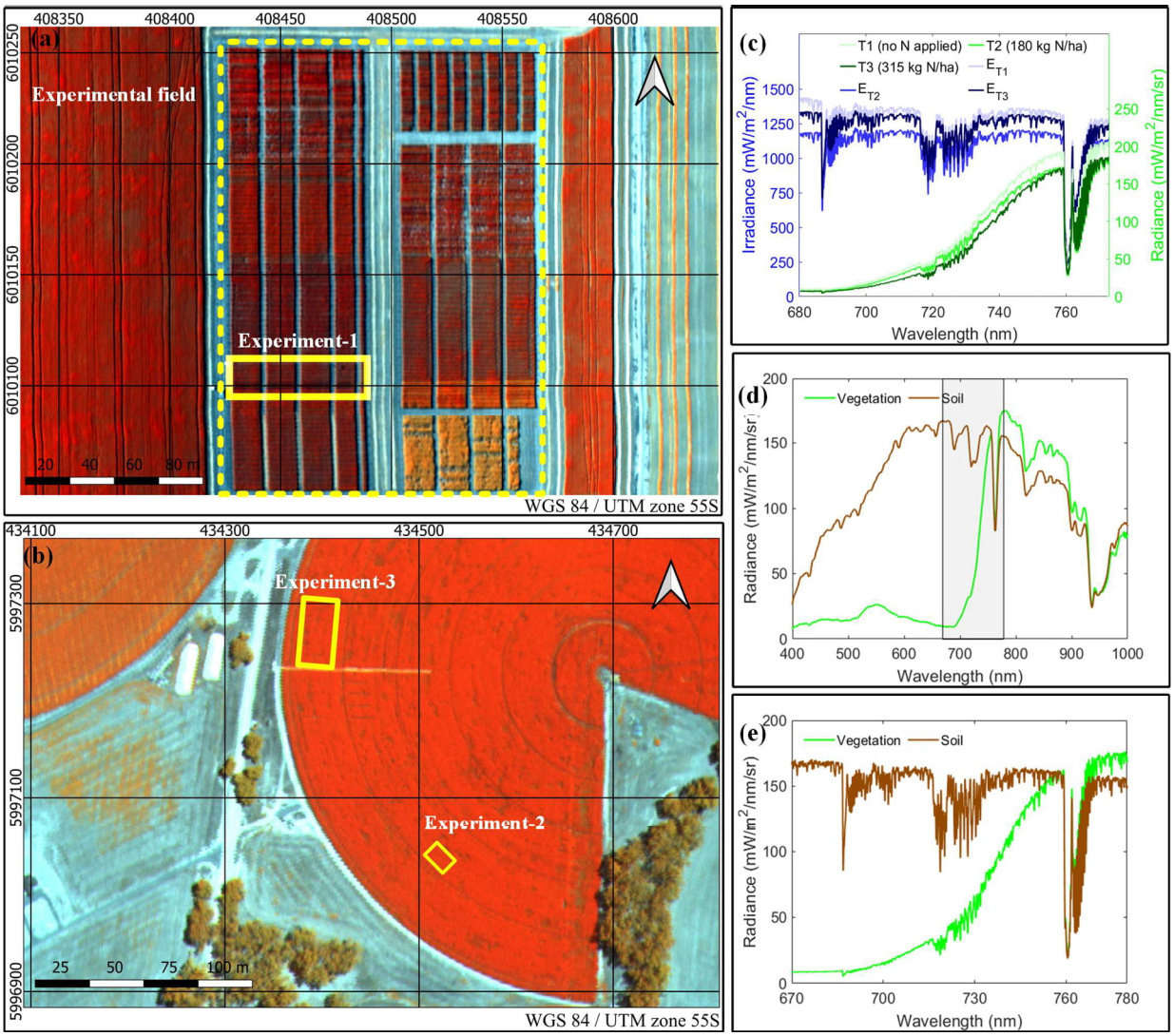

Fig. 2-1. Overview of experiments at field trial sites 1 (a) and 2 (b). Sample average radiance and the corresponding irradiance (E) spectra for experimental plots subjected to different nitrogen treatments at experiment 3 obtained from HR-2000 (c). Sample radiance spectra acquired from the narrow-band hyperspectral imager (d) and sub-nanometer hyperspectral imager (e) corresponding to the same vegetation and soil targets. (a) was acquired with the narrow-band hyperspectral imager (composite: 760 (R), 710 (G) and 680 (B) nm). (b) was obtained with the sub-nanometer hyperspectral imager (composite: 760 (R), 710 (G) and 680 (B) nm). The solid yellow boxes in (a) and (b) show the location of the plots across the three experiments and the dashed yellow box in (a) shows the location of plots across the entire field. The transparent grey box in (d) shows the spectral region covered by the sub-nanometer hyperspectral imager.

For experiment-3, field measurements of top-of-canopy (TOC) spectral radiances for the computation of ground-based SIF_{760} were collected from all 20 plots on 20 January 2021 at midday from 11:45 to 16:30 solar time under clear sky conditions. TOC spectral radiance was measured using a 0.065-nm FWHM HR-2000 spectrometer (Ocean Insight, Dunedin, FL, USA). The total incoming irradiance was calculated using the radiance reflected from a white reference panel (Labsphere Inc., North Sutton, NH, USA) measured by the spectrometer. The spectral measurements were acquired from the nadir using bare optical fiber, with an angular field of view of 25°, mounted on a tripod of 2.5 m height. The vegetation targets were measured at a distance of 1 m above the canopy. Radiance measurements were recorded at five different locations within each plot and then averaged to reduce noise. Incident solar radiation was measured prior to radiance measurements, and radiance/irradiance measurements were completed within 3 minutes for each plot. Examples of radiance and irradiance measurements are shown in Fig. 2-1c, with visible differences in spectra associated with applied nitrogen rate.

A summary of the physiological measurements performed at each experiment is shown in Table 2-1. The growth stages during the airborne campaigns corresponded to i) grain filling (milking stage) for wheat in 2019, ii) dough stage for maize in 2020, and iii) silking stage for maize in 2021. A portable weather station (model WXT510, Vaisala, Helsinki, Finland) was installed in the field for concurrent readings of meteorological conditions at the time of hyperspectral image acquisitions. For experiments 1 and 3, leaf measurements were carried out under field conditions, coincident with the airborne campaigns. For experiment 2, leaf measurements were performed 4 days prior to the airborne campaign under similar meteorological conditions (Table 2-1). Measurements were made on 10–15 leaves per plot for experiment 1 and 5–10 leaves per plot for experiments 2 and 3. Measurements were made on leaves at the top of the canopy at noon, under clear skies. Chlorophyll content, nitrogen balance index (NBI), flavonols and anthocyanin content were measured using a handheld Dualex leaf-clip sensor (FORCE-A, Orsay, France). Steady-state leaf fluorescence yield (Ft) was measured

using the FluorPen FP110-LM (Photon Systems Instruments, Drásov, Czech Republic) handheld fluorometer. Random samples of 10–15 leaves per plot for experiment 1 and 4–5 leaves per plot for experiments 2 and 3 from the top of the canopy were selected for determining the total N concentration (%) destructively in the laboratory, following the Kjeldahl method (Kjeldahl, 1883). To verify the impacts of fertilisation rate on leaf physiological traits, measurements were evaluated using analysis of variance (ANOVA) followed by a Dunnett's test at $\alpha < 0.05$. In addition to the 15 plots at site 1, leaf-level measurements from more than 100 adjacent plots within the entire experimental field (dashed yellow box in Fig. 2-1a) were also conducted to investigate the intra-field variability.

Table 2-1. Field measurements and meteorological conditions coincident with flights.

Field trial site	Experiment #	Treatment (kg N/ha)	Growth stage	Field measurements	Meteorological conditions		
					T_a	RH	P_a
Yarrawonga (Site 1)	1	T1:0, T2:46, T3:92, T4:138, T5:184	Grain filling	Ft, Chl, NBI, Flav, Anth, TN	19.2	30.1	1002.8
Peechelba (Site 2)	2	T1:207, T2:387	Dough	Ft, Chl, NBI, Flav, Anth, TN	23.3	36.2	1008.5
	3	T1:0, T2:180, T3:315	Silking	Ft, Chl, NBI, Flav, Anth, TN, TOC L	25.3	33.5	1003.6

Ft = Steady-state chlorophyll fluorescence, Chl = Chlorophyll content (μg/cm^2), NBI = Nitrogen balanced index (Dualex unit (d.u)), Flav = Flavonols (Dualex unit), Anth = Anthocyanins (Dualex unit), TN = Total Nitrogen concentration (%), TOC L = Top-of-canopy radiance (mW/m^2/nm/sr) from HR-2000, T_a = Average air temperature (°C), RH = Relative humidity (%) and P_a = Average air pressure (mBar).

2.2.2 Airborne hyperspectral campaigns

Airborne campaigns were conducted in 2019, 2020 and 2021 (Table 2-2), flying with the aircraft's heading on the solar plane. Two hyperspectral imagers were installed in tandem on a Cessna-172 aircraft operated by the HyperSens Laboratory, University of Melbourne's Airborne Remote Sensing Facility. The first hyperspectral imager was a Hyperspec VNIR E-Series model

(Headwall Photonics, Fitchburg, MA, USA) and the second hyperspectral imager was a high-resolution Hyperspec Fluorescence sensor (Headwall Photonics, Fitchburg, MA, USA). The spectral characteristics of both hyperspectral imagers are shown in Table 2-3. Both hyperspectral imagers were radiometrically calibrated in the laboratory using an integrating sphere (Labsphere XTH2000C, Labsphere Inc., North Sutton, NH, USA); as a result, coefficients derived from the constant light source at four different illumination levels were calculated for the flight configuration of each imager. The atmospheric correction for the VNIR imager was performed using the SMARTS model (Gueymard, 2001), with the aerosol optical depth measured at 550 nm with a Microtops II sunphotometer (Solar LIGHT Co., Philadelphia, PA, USA), allowing the conversion of the radiance values to reflectance. Image orthorectification was conducted with PARGE (ReSe Applications Schläpfer, Wil, Switzerland) using inputs from the solidly installed and synchronized inertial measurement units (VN-300-VectorNav Technologies LLC, Dallas, TX, USA for VNIR imager and Trimble APX-15 UAV, Applanix Corporation, Ontario, Canada for Fluorescence imager); more information on data preprocessing and image correction can be found in Zarco-Tejada *et al*. (2016).

Table 2-2. Flight dates, flight altitudes and spatial resolution of the acquired hyperspectral images during the three airborne campaigns.

Flight date	Flight time (local)	Experiment	AGL (m)		Spatial resolution (m)	
			NB	SN	NB	SN
09/10/19	15:40 - 16:30	1	400	900	0.25	0.20
16/03/20	12:50 - 13:50	2	700	850	0.50	0.20
			900	900	0.65	0.20
20/01/21	11:40 - 12:20	3	1200	1200	0.9	0.30
			2200	2200	1.7	0.55

NB = Narrow-band hyperspectral imager
SN = Sub-nanometer hyperspectral imager
AGL= above ground level

Differences in radiance spectra corresponding to vegetation and soil targets acquired from the two hyperspectral imagers were visually identified as a function of spectral configurations (Fig. 2-1d and 1e). Above-ground-level (AGL) altitudes and spatial resolutions of the imagery are detailed in

Table 2-2. The spatial resolution of imagery from both airborne hyperspectral imagers was sufficient for identification of individual plots over the experimental sites (Fig. 2-2). Differences in fertilisation rate could be visually discriminated based on radiance spectra acquired from both the hyperspectral imagers over the entire spectral range (Fig. 2-3a and 2-3c) and in the O_2-A absorption feature (Fig. 2-3b and 2-3d) for experiment 1.

Table 2-3. Spectral characteristics of the airborne hyperspectral imagers.

Configuration	**Fluorescence sensor (Sub-nanometer imager)**	**VNIR E-Series sensor (Narrow-band imager)**
Spectral range	670-780 nm	400-1000 nm
Number of spectral bands	2160	371
Spectral sampling interval	0.051 nm	1.626 nm
FWHM	≤0.2 nm	5.8 nm
Number of un-binned spatial pixels	1600	1600
SNR	>300:1*	>300:1*
Field of view	23.5°	66°
Aperture	f/2.5	f/2.5
Bit depth	16	16

*with spatial binning

To investigate the impact of sensor altitude on the inter-comparison of airborne-quantified SIF_{760} from both hyperspectral imagers and with ground-based SIF_{760}, images from both hyperspectral imagers were acquired at three different altitudes (900 m, 1200 m and 2200 m) for experiment 3 (Table 2-2). All images were acquired within a 20-minute time interval to minimize the impact of sun-sensor geometry and changes in atmospheric conditions on the SIF_{760} retrievals. The effect of sensor height on O_2-A absorption feature depth and SIF_{760} quantifications was assessed using ANOVA followed by Tukey's honest significant difference (HSD) post-hoc test at $\alpha < 0.05$. Fig. 2-4 shows the impact of the sensor altitude on the radiance spectra for the sub-nanometer imager. The radiance imagery acquired from the sub-nanometer imager at three different altitudes over the entire field (Fig. 2-4a, 2-4b and 2-4c) and over the experimental plots (Fig. 2-4d, 2-4e and 2-4f) differed in the 670- to 780-nm spectral region (Fig. 2-4g) and in the oxygen absorption features (Fig. 2-4h and 2-4i).

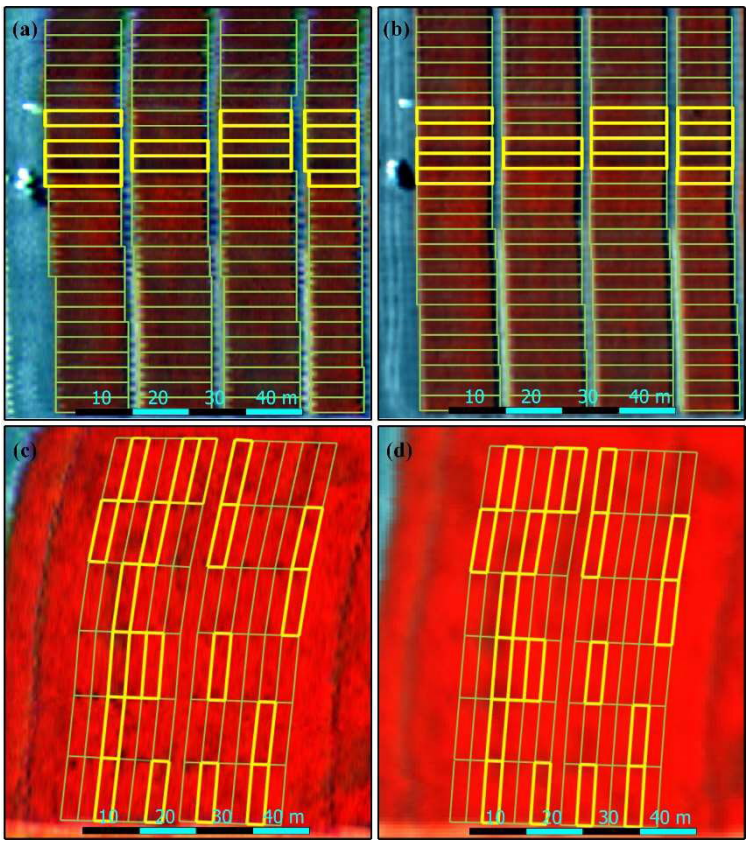

Fig. 2-2. Hyperspectral imagery showing zoomed-in plots from identical locations in experiments 1 (a, b) and 3 (c, d). Images (a) and (c) were acquired with the sub-nanometer hyperspectral imager (composite: 760 (R), 710 (G) and 680 (B) nm). Images (b) and (d) were acquired with the narrow-band hyperspectral imager (composite: 760 (R), 710 (G) and 680 (B) nm). Green polygons indicate plots under different nitrogen treatments, and yellow polygons indicate the selected plots corresponding to five and three nitrogen treatments, respectively, for experiments 1 and 3.

2.2.3 SIF quantification from field data and airborne hyperspectral imagery

A thresholding approach based on the normalised difference vegetation index (NDVI) was used to select the pixels corresponding to vegetation in each individual plot. To ensure that only pure vegetation pixels were considered for the analysis, all pixels with an NDVI greater than 0.6 were selected. For each plot, mean radiance spectra were calculated by averaging spectra from all pure vegetation pixels within the plot, excluding boundary pixels, from hyperspectral images acquired from both imagers. This object-based analysis strategy was used to reduce the uncertainty when using pixel-based SIF retrievals due to the SNR of the instrument. For experiment 1, the total incoming irradiance at the flight time was measured using the HR-2000 spectrometer with a CC-3 VIS-NIR cosine corrector diffuser. Due to the unavailability of cosine corrector diffuser for experiments 2 and

3, the total incoming irradiance at the flight time was calculated by measuring the radiance reflected from the white reference panel by the spectrometer. Ground-based SIF_{760} from eight plots measured concurrently with airborne image acquisition were used to validate the airborne SIF_{760} calculated from both imagers. The relative root mean square error (rRMSE) was calculated between the airborne and ground-based SIF_{760} following Eq. (2.1):

$$rRMSE = \sqrt{\frac{\sum_{i=1}^{n}\left(\frac{F_{airborne,i} - F_{ground,i}}{F_{ground,i}}\right)^2}{n}} \times 100\% \quad (2.1)$$

where $F_{airborne,i}$ and $F_{ground,i}$ are the SIF_{760} values retrieved from airborne and ground-based spectrometers, respectively, for plot *i,* with *n* representing the number of plots.

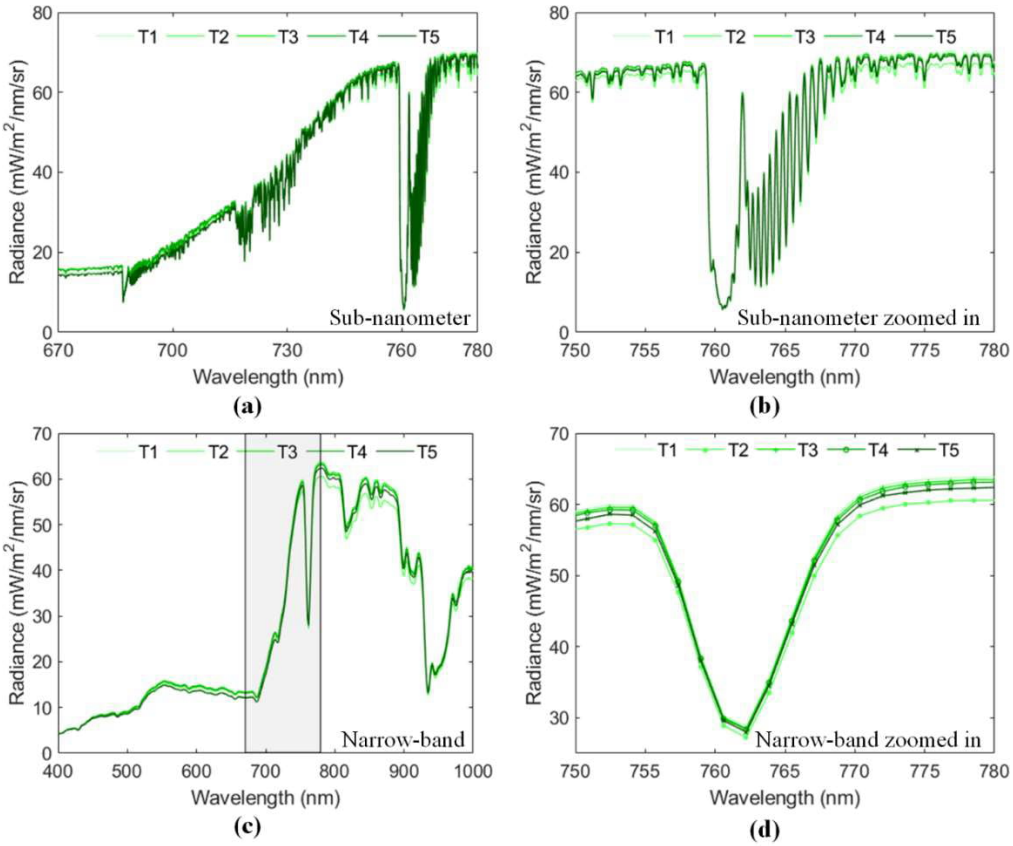

Fig. 2-3. Average radiance spectra for treated plots in experiment 1. Spectra obtained from (a) the sub-nanometer imager in the 670- to 780-nm region, (b) the sub-nanometer imager in the O_2-A absorption region, (c) the narrow-band imager in the 400- to 1000-nm region and (d) the narrow-band imager in the O_2-A absorption region. The transparent grey box in (c) shows the spectral region covered by the sub-nanometer hyperspectral imager. Codes T1-T5 correspond to the applied nitrogen fertilisation rates shown in Table 2-1.

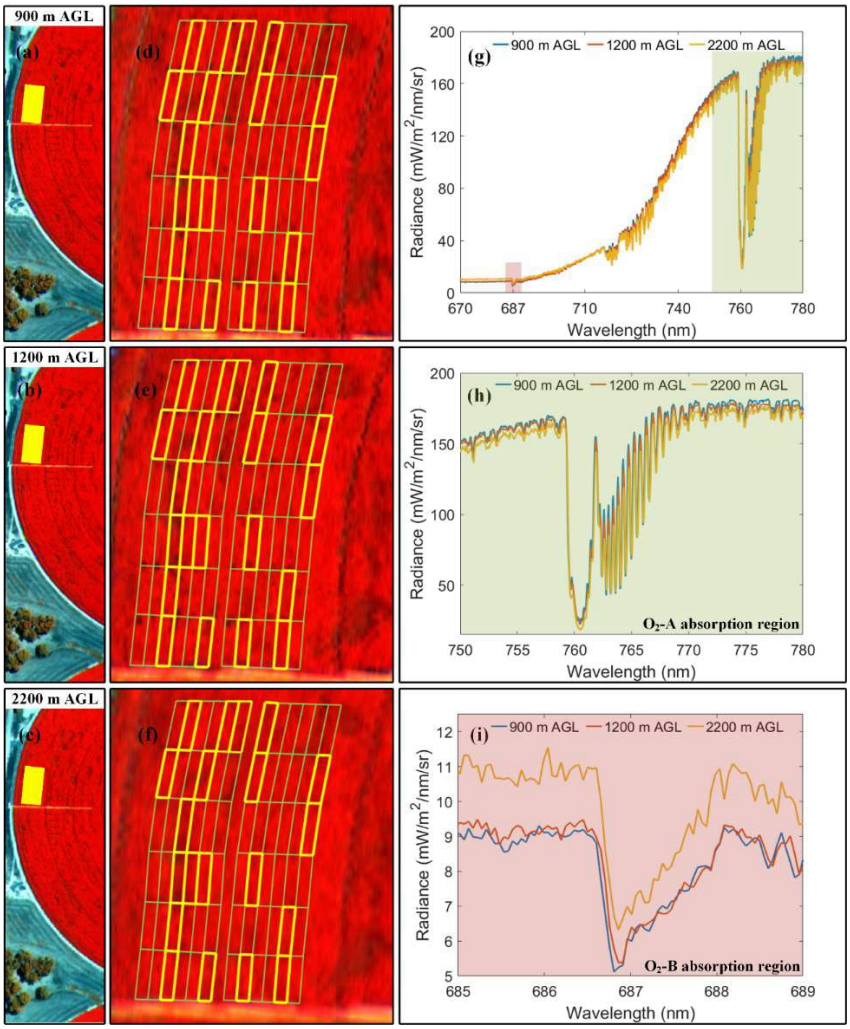

Fig. 2-4. Hyperspectral imagery from experiment 3. (a–f) Sub-nanometer composite imagery (760 (R), 710 (G) and 680 (B) nm) at various altitudes. (g–i) Average radiance spectra acquired for one of the experimental plots in the 670- to 780-nm region (g), O_2-A absorption region (h) and O_2-B absorption region (i). Area of yellow filled polygons (a, b, c) shown in detail in (d), (e) and (f), respectively. Green polygons indicate plots under different nitrogen treatments, and yellow polygons indicate the selected plots corresponding to three nitrogen treatments.

Field spectrometer radiances/irradiances were calibrated using coefficients derived from a uniform calibrated light source and an integrating sphere (Labsphere XTH2000C). To match the SR of the radiance images acquired from both sensors, the high-resolution irradiance spectra acquired with the HR-2000 spectrometer was resampled through Gaussian convolution (Hornero *et al*., 2021b; Suarez *et al*., 2021) corresponding to the SR of the airborne hyperspectral imagers. As the spectral characteristics of the narrow-band hyperspectral imager do not meet the requirements (Drusch *et al*., 2017; ESA, 2015) for quantifying SIF at the O_2-B (SIF_{687}) absorption feature, SIF_{687} values for

hyperspectral imagers were not compared. This limitation also affects the applicability of SFMs with the narrow-band hyperspectral imager, as it requires sub-nanometer resolution for accurate SIF quantification. Thus, the retrieval of SIF_{760} using irradiance derived from HR-2000 measurements and average radiance derived from airborne hyperspectral images and ground-based HR-2000 measurements was performed using the O_2-A-band *in-filling* method through the FLD principle, based on a total of three spectral bands (3FLD) (Maier *et al*., 2003). The spectral window for '*in*' and '*out*' irradiance (E) and radiance (L) used in 3FLD computation was selected based on the spectral characteristics of the measuring instruments. For the narrow-band imager, E_{in}/L_{in} corresponds to the E/L minima in the 755–765 nm region. The minima for both E and L was observed at 762 nm, and this was consistent for all datasets. E_{out}/L_{out} corresponds to the weighted mean of E/L maxima in the spectral regions of 750–755 nm and 771–776 nm, respectively following the methodology proposed in Damm *et al*. (2011). The spectral window for both ground-based and airborne sub-nanometer sensors was selected using the methodology proposed in Julitta *et al*. (2017)[1], which considers the FWHM of the sub-nanometer resolution instrument and uses the mean of E/L in the left and right shoulder regions to reduce noise. An additional data quality check was performed for the matching of the *'in'* band for E/L, and in the event of a mismatch, E_{in}/L_{in} was defined as the mean of E_{in}/L_{in} of adjacent wavelengths. The absolute depth (in radiance units) and relative depth (in percent) of the O_2-A band feature were calculated in addition to the airborne SIF_{760} quantification. The absolute depth was calculated as the difference between the solar radiance at the left shoulder wavelength and the wavelength at the bottom of the O_2-A absorption feature, and the relative depth was calculated as the ratio of absolute depth and the solar radiance at the left shoulder wavelength. The wavelength providing the highest radiance in the 750–759 nm range was selected as the left shoulder wavelength.

In the absence of atmospheric correction, SIF_{760} values could be negative even for fluorescent targets (see Fig. 6 in Marrs *et al*., 2021). The atmospheric correction process involves estimating

[1] R code available on GitHub platform at https://github.com/tommasojulitta

several atmospheric parameters such as upwelling transmittance, path scattered radiance, and spherical albedo using atmospheric RTMs. Additionally, to account for uncertainties in the estimation of atmospheric parameters, the transmittance correction technique (Damm *et al*., 2014; Guanter *et al*., 2010; Siegmann *et al*. 2019) is a commonly used approach that forces the non-fluorescent targets to give zero SIF_{760}. Due to the complexities involved in accurately estimating the atmospheric parameters, RTM-based atmospheric correction was not performed in the current study. Instead, on account of the successful implementation of a rescaling scheme to correct negative airborne SIF_{760} and SIF_{687} values in Bandopadhyay *et al*. (2019), we used a simplified correction technique based on the same principle of using non-fluorescent targets (i.e., bare soil) as in the widely used transmittance correction technique, to compensate for negative SIF_{760} values related to calibration and atmospheric factors such as aerosol scattering and surface pressure. Any deviation from the non-fluorescent behaviour of bare soil targets identified in each image was attributed to spectral miscalibration or atmospheric effects. The method relies on forcing the non-fluorescent target to give zero SIF_{760}, and the non-zero SIF_{760} served as an offset to correct the SIF_{760} from vegetation targets following Eq. (2.2):

$$SIF_{corrected} = SIF_{vegetation\ target} - SIF_{non-fluorescent\ target} \quad (2.2)$$

To minimize the directional effects on the airborne-quantified SIF_{760}, the corrected SIF_{760} was normalised to a reference-viewing angle using a reflectance-based angular correction approach (Hao *et al*., 2021). The normalisation method employs a reference SIF_{760} corresponding to a reference viewing angle, as well as near-infrared reflectance of vegetation (NIRv) (Badgley *et al*., 2017), to normalise SIF_{760} quantified at any viewing direction to a reference viewing angle. Two different approaches were used to compute the reference SIF_{760} for normalisation. In the first approach, a single plot located at the centre of each hyperspectral image was selected as the reference SIF_{760} on account of being a nadir-view. In the second approach, locations of the ground-based spectral measurements were identified in the hyperspectral images and used for calculating the reference SIF_{760}. Since the

ground-based spectral measurements were primarily conducted along the plot's centre, only pure vegetation pixels located along the plot's centre were used to compute mean radiance for the reference SIF_{760} calculation. This differs from the airborne SIF_{760} corresponding to individual plots, which was calculated using mean radiance from all pure vegetation pixels excluding the boundaries. The second approach was only applied for experiment 3 to validate the airborne-quantified SIF_{760} with the ground-based HR-2000 SIF_{760} measurements so that the reference viewing direction remained identical for ground-based and airborne SIF_{760}. Normalisation was conducted according to the nadir-viewing angle for all inter-comparisons of airborne SIF_{760} from both imagers.

The study focused on assessing the spectral configuration of the two instruments, with attempts made to reduce distortions caused by other factors. We used pixels close to the nadir-viewing angle and avoided evaluating areas close to the image borders to reduce the potential effects of instrument 'smile' on assessment of the two instruments. Moreover, the angular correction used to normalise SIF_{760} minimizes the potential instrument smile effects (detailed above). Further work and a corresponding paper will evaluate sensor smile effects and corrections needed when using narrow-band instruments for SIF_{760} retrievals. This additional work is important because entire images, rather than just nadir pixels, are needed for practical applications in precision agriculture.

2.2.4 Modelling the spectral resolution effects on SIF quantification using SCOPE

The SCOPE model integrates three radiative transfer modules and an energy balance module to estimate outgoing radiation spectra, turbulent heat fluxes, photosynthesis rates and chlorophyll fluorescence (Van der Tol *et al*., 2009). Surface reflectance and fluorescence spectra are simulated by linking several energy balance, photosynthesis and canopy biophysical parameters with TOC radiance, with SSI and SR of 1.0 nm each. The model assumes a homogenous canopy structure, and the canopy radiative transfer equations are based on the widely used SAIL model (Verhoef, 1984). Net radiation over the canopy is calculated by integrating the contribution from the individual layers with shaded and sunlit leaves at different leaf angles over the canopy depth. The canopy reflectance

modelling is conducted based on four different Bidirectional Reflectance Distribution Function (BRDF) terms representing direct and diffused hemispherical contribution from the surrounding and the direct and diffused reflectance in the viewing direction. The leaf-level fluorescence spectra are modelled within the 640- to 850-nm spectral region based on the FLUSPECT model (Vilfan *et al*., 2016) by using the leaf reflectance and fluorescence outputs derived from the PROSPECT model (Jacquemoud and Baret, 1990).

A simulated dataset using the SCOPE model (version 2.0) was generated to evaluate the influence of the SR of the airborne hyperspectral sensors on the 3FLD-based SIF_{760} quantification. The dataset consisted of 400,000 simulations generated by randomly varying specific input parameters, drawing from a uniform distribution within ranges shown in Table 2-4. All other SCOPE input parameters were kept at their default values. The air temperature and air pressure inputs for the SCOPE model were measured with a portable weather station during the airborne campaign at field trial site 1. Details regarding the definition and ranges of all input parameters can be found in Table A-1 (Appendix A). For each case, the TOC spectra of total upwelling radiance, SIF radiance and the corresponding irradiance were simulated using the default 1.0-nm SR and 1.0-nm SSI obtained from SCOPE. To compare the SIF_{760} retrieval performance for SR corresponding to the narrow-band hyperspectral imager, SCOPE-simulated spectra were resampled to 5.8-nm FWHM through Gaussian convolution matching the SSI with the narrow-band imager. The resampled radiance spectra in the 400- to 1000-nm spectral region were compared with the average radiance spectra obtained from the narrow-band imager at experimental field trial site 1 using RMSE as the cost function. For each narrow-band airborne radiance spectrum, we selected the 10 closest resampled radiance spectra from the 400,000 simulations along with their corresponding resampled-irradiance for the analysis. Fig. 2-5a shows the measured radiance spectra from the narrow-band imager. Fig. 2-5b and 2-5c show the SCOPE-simulated SIF and radiance spectra at 1-nm FWHM corresponding to the selected simulations. A comparison of the simulated SCOPE radiance spectra against the narrow-band imager

is shown in Fig. 2-5d. Additionally, radiance and irradiance spectra corresponding to SRs of 2.0 nm, 3.0 nm, 4.0 nm and 5.0 nm were generated by resampling SCOPE-simulated 1.0-nm SR spectra with Gaussian convolution but keeping the SSI at 1.0-nm. Fig. 2-5e and 2-5f show the comparison between the radiance spectra simulated by SCOPE at different SRs in the O_2-B and O_2-A absorption regions, respectively. The O_2-B absorption feature could only be identified at the default 1.0-nm SR. The decrease of SR from the default 1 nm to 5.8 nm resulted in O_2-A-band depth reduction and an increment in the radiance signal corresponding to the absorption minima.

Table 2-4. Range of the SCOPE input parameters used in this study.

Parameter	Range/Value	Unit	Description
C_{a+b}	10–50	$\mu g \cdot cm^{-2}$	Chlorophyll *a*+*b* content
C_{dm}	0.001–0.05	$g \cdot m^{-2}$	Dry matter content
C_w	0.001–0.05	cm	Leaf water equivalent layer
N	1.2–1.8	–	Leaf thickness parameters
Vcmax	20–120	$\mu mol \cdot m^{-1} \cdot s^{-1}$	Maximum carboxylation capacity at 25 °C
fqe	0.001–0.015	–	Fluorescence quantum yield efficiency at photosystem level
LAI	2–6	$m^2 \cdot m^{-2}$	Leaf area index
$LIDF_a$	−1–0	–	Leaf inclination
$LIDF_b$	0	–	Variation in leaf inclination
R_{in}	600–1000	$W \cdot m^{-2}$	Broadband incoming shortwave radiation
Ta	19.2	°C	Air temperature
p	1002.8	hPa	Air pressure
tts	35.42	deg.	Solar zenith angle

2.2.5 Nitrogen assessments using narrow-band and sub-nanometer SIF retrievals

The effects of sensor SR on nitrogen estimation were assessed using models with chlorophyll content and SIF traits as inputs (Camino *et al.,* 2018b). Nitrogen content was predicted using Random Forest (RF) (Breiman, 2001) models fit to data from field trial site 1, using i) C_{a+b} derived from the narrow-band hyperspectral imagery through the inversion of PRO4SAIL RTM and ii) SIF_{760} quantified from each of the hyperspectral imagers as inputs. The PRO4SAIL model used coupled PROSPECT-D (Féret *et al*., 2021) and 4SAIL (Verhoef *et al*., 2007) to retrieve the biochemical constituents and canopy structural parameters, respectively. A look-up table with 200,000 simulations

was built by randomly varying the biochemical and biophysical parameters with a uniform distribution within the ranges shown in Table 2-5.

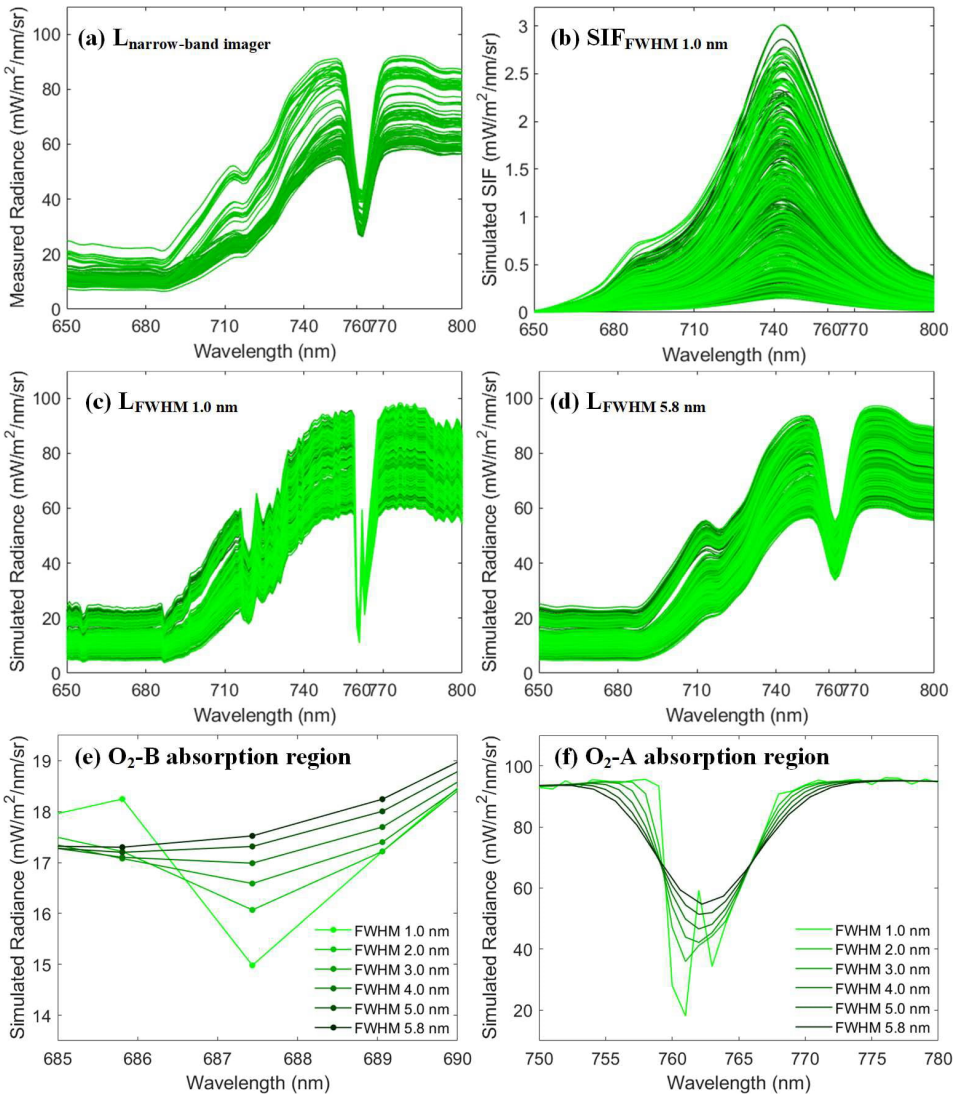

Fig. 2-5. (a) Measured radiance from the narrow-band imager. (b) SCOPE-simulated SIF at 1.0-nm FWHM. (c) SCOPE-simulated radiance at 1.0-nm FWHM. (d) SCOPE-simulated radiance corresponding to the narrow-band imager's spectral characteristics (FWHM = 5.8 nm, SSI = 1.626 nm). SCOPE-simulated radiance at different SRs in the O_2-B (e) and O_2-A absorption regions (f).

Support vector machines (SVMs) were trained using simulated reflectance as inputs. Reflectance spectra were matched with the spectral resolution of the narrow-band hyperspectral imager (5.8-nm FWHM). SVMs were first trained in parallel (MATLAB parallel computing toolbox) using a radial basis function and optimising the hyperparameters during training to predict C_{a+b}. Then, using the average reflectance spectra extracted from pure-vegetation pixels, C_{a+b} was estimated for

each experimental plot. Subsequently, RF regression models were fit for each hyperspectral sensor, using crop N concentration as a response variable and the estimated C_{a+b} from the narrow-band VNIR reflectance spectra ($C_{a+b\text{-}narrow}$) and SIF_{760} derived from each hyperspectral imager (i.e., $C_{a+b\text{-}narrow}$ + $SIF_{760\text{-}narrow}$ vs. $C_{a+b\text{-}narrow}$ + $SIF_{760\text{-}sub\text{-}nanometer}$) as predictors.

Table 2-5. Parameters and ranges used for the look-up table generation for the PRO4SAIL RTM.

Parameter	Abbreviation	Value/range
Chlorophyll *a*+*b* content [µg/cm²]	C_{a+b}	4–70
Carotenoid content [µg/cm²]	C_{x+c}	1–20
Anthocyanin content [µg/cm²]	Anth	0–15
Dry matter content [g/cm²]	C_m	0.007
Water content [g/cm²]	C_w	0.001
Mesophyll structure Coeff.	N	0.5–3
Leaf area index [m²/m²]	LAI	0.3–5
Average leaf angle [deg.]	$LIDF_a$	0–90
Hot spot parameter	h	0.01
Soil reflectance	R_{soil}	PRO4SAIL dry soil spectra
Observer angle [deg.]	tt_o	0
Sun zenith angle [deg.]	tt_s	35.42
Relative azimuth angle [deg.]	Ψ	0

2.3 Results

In experiment 1, leaf physiological traits were significantly different in plots fertilised at different rates ($p < 0.05$; Fig. 2-6). For experiments 2 and 3, differences were non-significant, but there was visible variation in leaf physiological variables among plots receiving different nitrogen treatments (Fig. 2-6). Differences in leaf total N concentration measured by destructive sampling were generally consistent with the trends observed in leaf steady-state fluorescence (Ft) with minor exceptions (e.g., values observed for T3 in experiment 1). Ft was lower in plots with the least N applied compared to other plots in all the experiments (Fig. 2-6, Ft and Total N panels). Fertilisation

rate was positively associated with chlorophyll *a*+*b* content and the leaf nitrogen balance index (NBI), while leaf flavonols and anthocyanins were inversely associated with fertilisation rate. Leaf physiological values were more variable in experiment 1 (T1–T5: 0–184 kg N/ha) than in experiments 2 (T1–T2: 207–387 kg N/ha) or 3 (T1–T3: 0–315 kg N/ha).

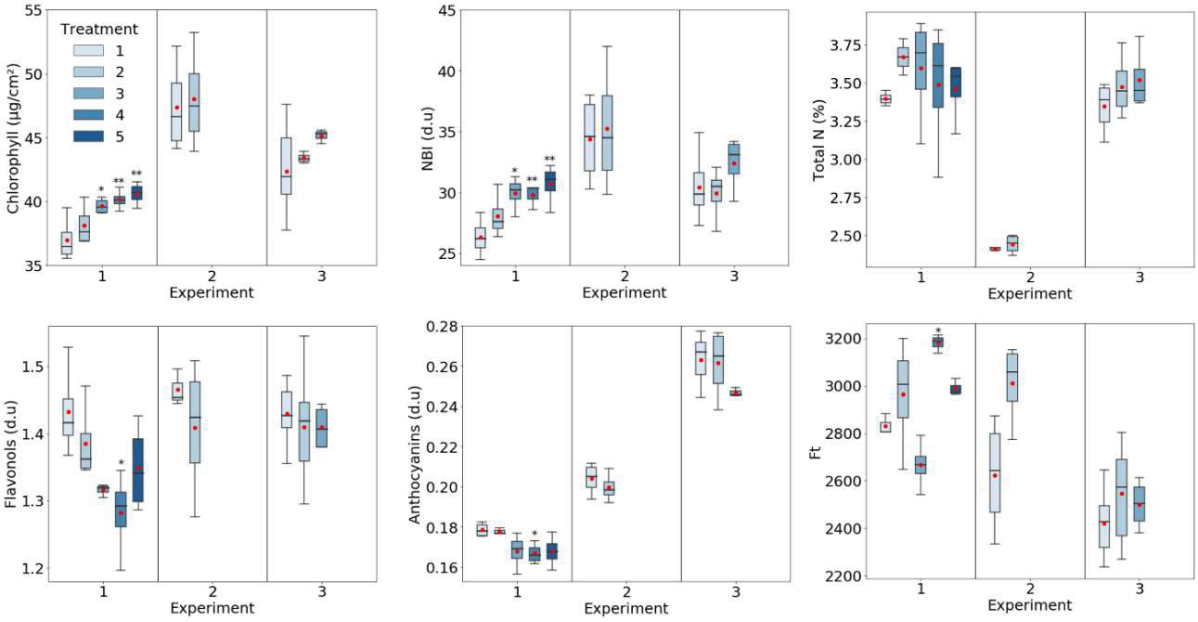

Fig. 2-6. Leaf physiological traits by fertilisation rate across experiments. Average values indicated by red points. The black lines within boxes represent medians, and the top and bottom of each box represent the 75th and 25th quartile, respectively. Whiskers represent ± 1.5 × Inter Quartile Range. Asterisks indicate significant differences from the treatment 1 plots according to Dunnett's test at $\alpha <$ 0.05. *$p \leq 0.05$; **$p \leq 0.01$.

The absorption features at O_2-A and O_2-B absorption regions were evident in the radiance spectra from both airborne hyperspectral imagers (Fig. 2-7). However, their shape and depth were strongly influenced by the SR. As a result of the coarser SR of the narrow-band imager, the absorption feature at the O_2-B band in the 685- to 690-nm spectral region could not be identified in the narrow-band radiance spectra (Fig. 2-7, inset). This result restricts the comparison between the narrow-band and sub-nanometer hyperspectral imagers for the calculation of SIF at the O_2-B band. Moreover, a reduction in the depth of the O_2-A absorption feature in the 750- to 780-nm spectral region and the corresponding increment in the radiance signal at the absorption minima were observed for the

narrow-band radiance spectra, as expected (Fig. 2-7, inset). The wavelength corresponding to the radiance minimum was shifted towards higher wavelengths when compared to sub-nanometer radiance spectra, as shown in several studies (Cendrero-Mateo *et al*., 2019; Damm *et al*., 2011; Julitta *et al*., 2016; Liu *et al*., 2015).

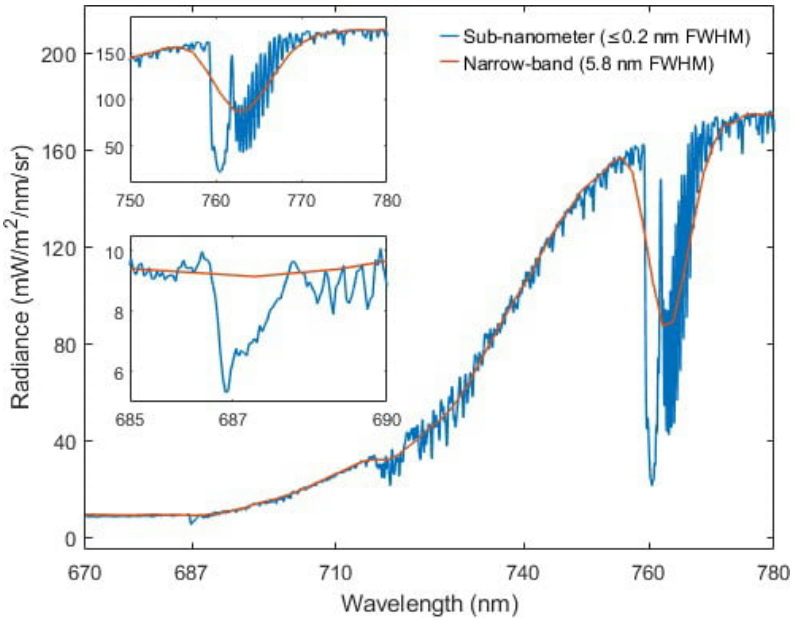

Fig. 2-7. Comparison of average radiance spectra from one of the plots within experiment-3 in the 670- to 780-nm region obtained from both hyperspectral imagers. The insets show the comparison within O_2-A and O_2-B absorption features in the 750- to 780-nm region and 685- to 690-nm region, respectively.

At site 1, the depths of the O_2-A absorption feature from each of the two imagers were strongly correlated (R^2 = 0.90, p < 0.001; Fig. 2-8a), when using data from the full set of >100 plots. Nevertheless, the range of SIF_{760} values quantified with the 3FLD method ($SIF_{760\text{-}3FLD}$) differed between sub-nanometer imager (0.05–1.95 mW/m^2/nm/sr) and the narrow-band imager (0.37–8.12 mW/m^2/nm/sr; Fig. 2-8b). Although there was some lack of correspondence in $SIF_{760\text{-}3FLD}$ between the two imagers (RMSE = 3.86 mW/m^2/nm/sr), the two were significantly correlated (R^2 = 0.85, p < 0.001; Fig. 2-8b).

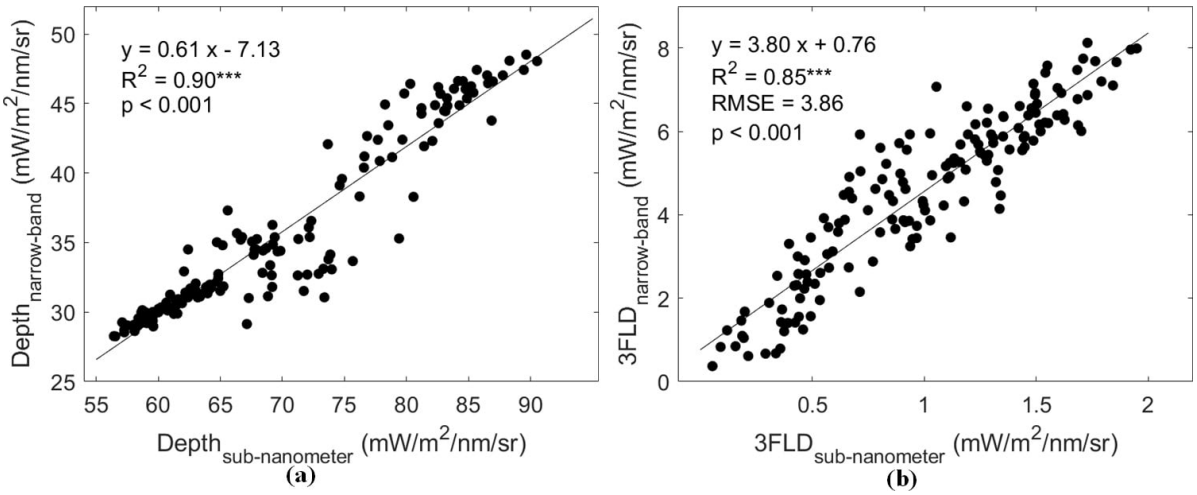

Fig. 2-8. Relationship between depth at the O_2-A absorption feature (a) and $SIF_{760\text{-}3FLD}$ (b) over the experimental field at site 1 from both hyperspectral imagers. The range of absolute $SIF_{760\text{-}3FLD}$ levels derived from the narrow-band imager was higher than the typical range of 0–3 mW/m^2/nm/sr quantified from healthy vegetation due to the impact of the spectral resolution of the instrument.

Airborne $SIF_{760\text{-}3FLD}$ estimates from both hyperspectral imagers are compared in Fig. 2-9. The best agreement between measures was observed in experiment 3 (R^2 = 0.9, RMSE = 3.28 mW/m^2/nm/sr, $p < 0.001$). Measures from each sensor were also well correlated in experiments 1 (R^2 = 0.87, RMSE = 4.69 mW/m^2/nm/sr, $p < 0.001$; Fig. 2-9a) and 2 (R^2 = 0.77, RMSE = 3.95 mW/m^2/nm/sr, $p < 0.01$; Fig. 2-9b). The error between estimates was consistent across experiments, yielding RMSEs within 3.28–4.69 mW/m^2/nm/sr.

Low-resolution SCOPE-simulated $SIF_{760\text{-}3FLD}$ values (2- to 5.8-nm FWHM) were significantly correlated with $SIF_{760\text{-}3FLD}$ simulated at 1-nm FWHM ($p < 0.001$, R^2 0.70–0.99; Fig. 2-10). RMSE values tended to increase with decreasing SR (Fig. 2-10). The pattern of differing absolute $SIF_{760\text{-}3FLD}$ values but stable relative differences across SRs observed with the SCOPE-simulated data was consistent with the experimental results from the airborne hyperspectral imagers.

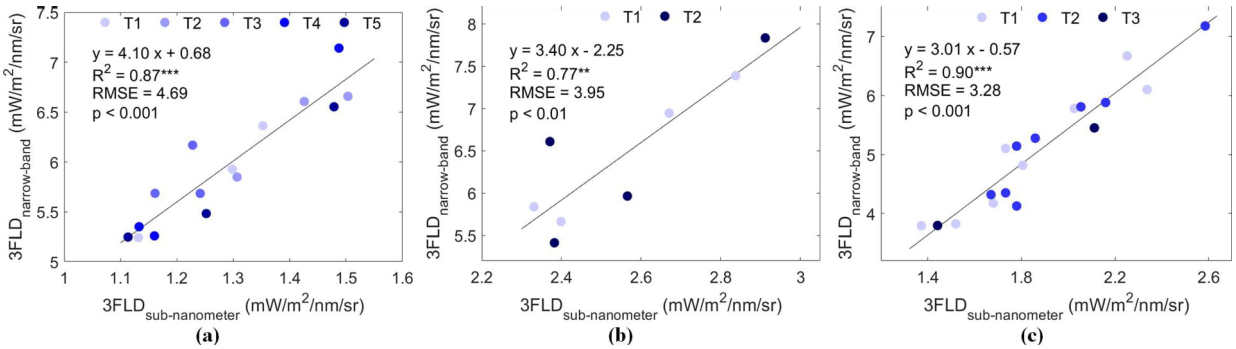

Fig. 2-9. Relationship between airborne $SIF_{760\text{-}3FLD}$ measures from different hyperspectral imagers across experiments 1 (a), 2 (b) and 3 (c). The range of absolute $SIF_{760\text{-}3FLD}$ levels derived from the narrow-band imager was higher than the typical range of 0–3 $mW/m^2/nm/sr$ quantified from healthy vegetation due to the impact of the spectral resolution of the instrument.

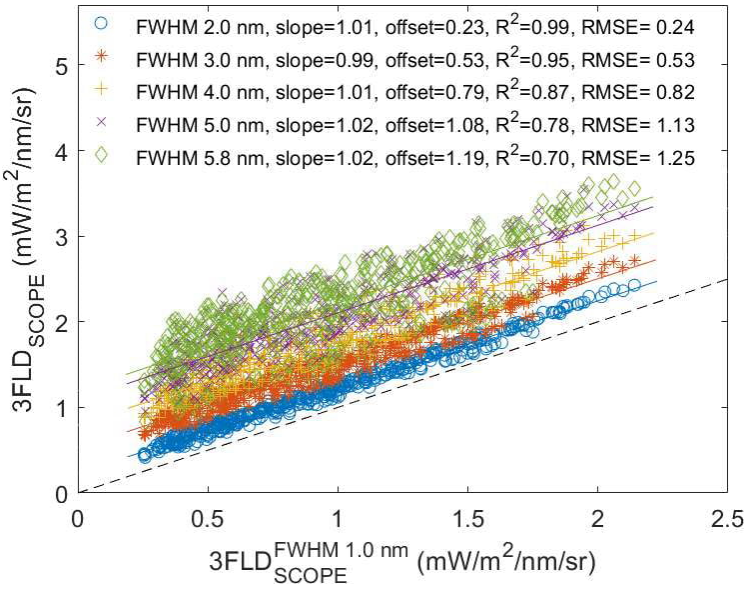

Fig. 2-10. Relationships between $SIF_{760\text{-}3FLD}$ for SCOPE simulations with different SRs against $SIF_{760\text{-}3FLD}$ quantified at 1-nm FWHM. The dotted line represents the 1:1 line.

A comparison of airborne SIF_{760} retrievals to ground-based $SIF_{760\text{-}3FLD}$ retrievals in experiment 3 is shown in Fig. 2-11. Ground-based measures were significantly correlated with both the sub-nanometer (R^2 = 0.90, p < 0.001; Fig. 2-11a) and the narrow-band (R^2 = 0.88, p < 0.001) hyperspectral imagers (Fig. 2-11b). $SIF_{760\text{-}3FLD}$ from the sub-nanometer imager showed strong agreement with the ground-based $SIF_{760\text{-}3FLD}$ values (RMSE = 0.07 $mW/m^2/nm/sr$, rRMSE = 3.7%), whereas the narrow-band imager exhibited greater overall differences from ground-based measures (RMSE = 3.26 $mW/m^2/nm/sr$, rRMSE = 170.5%). SIF-yield, which was estimated by normalising

the corrected $SIF_{760\text{-}3FLD}$ by the average NIR radiance in the 776–780-nm spectral region, was also significantly correlated with the leaf-level steady-state chlorophyll fluorescence in experiment 1 ($R^2 = 0.53$, $p < 0.01$ for sub-nanometer imager; $R^2 = 0.34$, $p < 0.05$ for narrow-band imager).

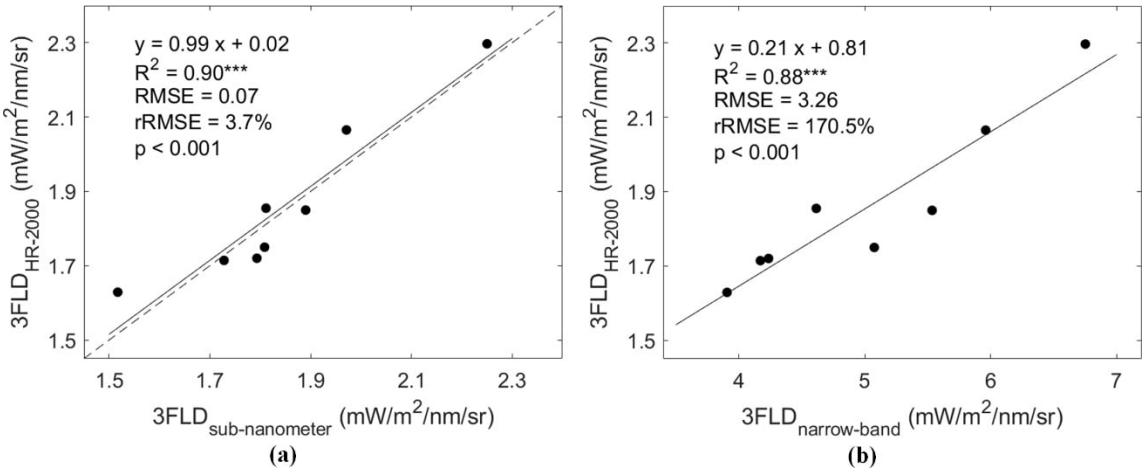

Fig. 2-11. Relationship between ground-based $SIF_{760\text{-}3FLD}$ quantified from the HR-2000 field spectrometer and airborne $SIF_{760\text{-}3FLD}$ quantified from the sub-nanometer (a) and the narrow-band (b) hyperspectral imagers for experiment 3. The dotted line represents the 1:1 line. The range of absolute $SIF_{760\text{-}3FLD}$ levels derived from the narrow-band imager was higher than the typical range of 0–3 $mW/m^2/nm/sr$ quantified from healthy vegetation due to the impact of the spectral resolution of the instrument.

Measures of O_2-A band depth and airborne $SIF_{760\text{-}3FLD}$ at different altitudes are presented in Fig. 2-12. $SIF_{760\text{-}3FLD}$ measures with the narrow-band imager at 2200 m AGL were excluded because pixels were too coarse (1.7 m) relative to plot size (3 m × 12 m). O_2-A absorption feature depth and $SIF_{760\text{-}3FLD}$ differed significantly with altitude (Fig. 2-12). The depth of the O_2-A absorption feature increased with sensor altitude, and $SIF_{760\text{-}3FLD}$ decreased with sensor altitude for both airborne imagers (Fig. 2-12).

Sub-nanometer $SIF_{760\text{-}3FLD}$ retrievals were significantly correlated with narrow-band imager retrievals in experiment 3 at both 900 m AGL ($R^2 = 0.85$, $p < 0.001$; Fig. 2-13a) and 1200 AGL ($R^2 = 0.9$, $p < 0.001$; Fig. 2-13a). The slope of the relationship between sub-nanometer and narrow-band retrievals was steeper for 900 m AGL than for 1200 m AGL. RMSE at 900 m AGL (4.29 $mW/m^2/nm/sr$) was higher than that of 1200 m AGL (3.28 $mW/m^2/nm/sr$), possibly explained by larger $SIF_{760\text{-}3FLD}$ values at lower altitudes. $SIF_{760\text{-}3FLD}$ at 900 m AGL was significantly correlated with

$SIF_{760\text{-}3FLD}$ at 1200 m AGL ($R^2 = 0.92$, $p < 0.001$; Fig. 2-13b) and 2200 m AGL ($R^2 = 0.8$, $p < 0.001$; Fig. 2-13b) using the sub-nanometer imager. $SIF_{760\text{-}3FLD}$ values decreased with imager altitude, and the relationship between low-altitude and high-altitude measurements also changed, with shallower slopes at higher altitudes (Fig. 2-13b). RMSE was higher at 2200 m AGL than at 1200 m AGL altitude, when compared to 900 m AGL. A similar pattern was observed for narrow-band $SIF_{760\text{-}3FLD}$ retrievals, with an overall significant correlation ($R^2 = 0.82$, RMSE = 1.36 mW/m^2/nm/sr, $p < 0.001$; Fig. 2-13c) and lower $SIF_{760\text{-}3FLD}$ values at higher altitudes.

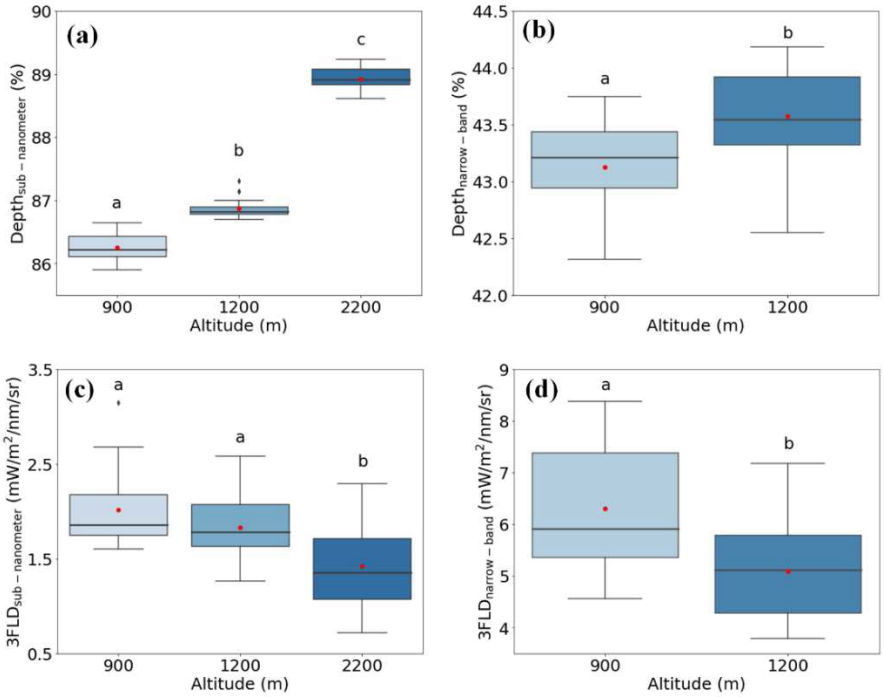

Fig. 2-12. Effect of sensor altitude on O_2-A band depth and $SIF_{760\text{-}3FLD}$ in experiment 3. Letters (a, b and c) within each plot represent the results of Tukey's honest significant difference (HSD) post-hoc comparisons of group means with $\alpha < 0.05$. Groups sharing the same letter are not significantly different. In the boxplots, the average values are shown with a red circle. The black line within the box is the median, and the top and bottom of the box is the 75th and 25th quartile, respectively. The whiskers represent ± 1.5 × Interquartile range. The outliers are represented as diamonds. The range of absolute $SIF_{760\text{-}3FLD}$ levels derived from the narrow-band imager was higher than the typical range of 0–3 mW/m^2/nm/sr quantified from healthy vegetation due to the impact of the spectral resolution of the instrument. $SIF_{760\text{-}3FLD}$ measures with the narrow-band imager at 2200 m AGL were excluded because pixels were too coarse (1.7 m) relative to plot size (3 m × 12 m).

Sub-nanometer $SIF_{760\text{-}3FLD}$ was significantly correlated with ground-based $SIF_{760\text{-}3FLD}$ at all sensor altitudes ($p < 0.001$, all $R^2 > 0.9$; Fig. 2-14a). RMSEs between airborne and ground-based SIF retrievals at 900 and 1200 m AGL were lower than 0.1 mW/m^2/nm/sr and rRMSEs were lower than

4%. $SIF_{760\text{-}3FLD}$ at 2200 m AGL consistently underestimated ground-based SIF (RMSE = 0.5 $mW/m^2/nm/sr$ and rRMSE = 28.2%; Fig. 2-14a). Ground-based $SIF_{760\text{-}3FLD}$ was also significantly correlated with airborne $SIF_{760\text{-}3FLD}$ from the narrow-band imager ($p < 0.001$, $R^2 > 0.85$) at both altitudes (Fig. 2-14b). Narrow-band imager $SIF_{760\text{-}3FLD}$ estimates at 1200 m AGL tended to be smaller than ground-based measures (Fig. 2-14b), and error was high for both 900 m AGL (RMSE = 3.77 $mW/m^2/nm/sr$, rRMSE = 200.8%) and 1200 m AGL (RMSE = 3.26 $mW/m^2/nm/sr$, rRMSE = 170.5%).

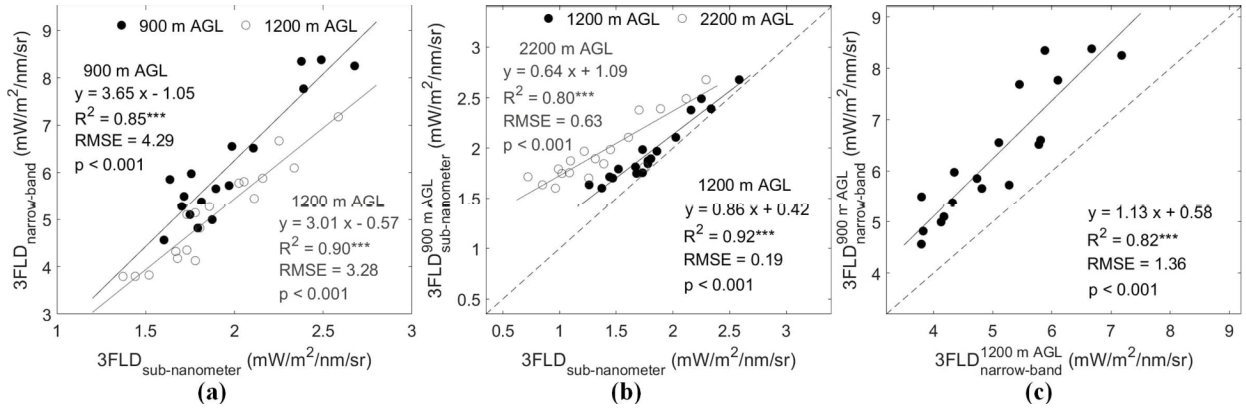

Fig. 2-13. (a) Relationships between $SIF_{760\text{-}3FLD}$ estimates from narrow-band and sub-nanometer hyperspectral imagers by sensor altitude. (b) Relationships between airborne $SIF_{760\text{-}3FLD}$ from sub-nanometer imager at 1200 and 2200 m AGL compared to the $SIF_{760\text{-}3FLD}$ quantified at 900 m AGL. (c) Relationship between airborne $SIF_{760\text{-}3FLD}$ from the narrow-band hyperspectral imager at 900 and 1200 m AGL. The range of absolute $SIF_{760\text{-}3FLD}$ levels derived from the narrow-band imager was higher than the typical range of 0–3 $mW/m^2/nm/sr$ quantified from healthy vegetation due to the impact of the spectral resolution of the instrument. $SIF_{760\text{-}3FLD}$ measures with the narrow-band imager at 2200 m AGL were excluded because pixels were too coarse (1.7 m) relative to plot size (3 m × 12 m).

Nitrogen predictions from both RF models were significantly correlated ($p < 0.01$) with the field-level nitrogen content measurements obtained by destructive sampling (Fig. 2-15). $SIF_{760\text{-}FLD}$ from the sub-nanometer hyperspectral imager by itself was significantly correlated with field-level nitrogen content ($R^2 = 0.71$, $p < 0.001$; Fig. 2-15a), as was SIF_{760} quantified from the narrow-band imager ($R^2 = 0.67$, $p < 0.001$; Fig. 2-15b). The RF algorithm using $SIF_{760\text{-sub-nanometer}}$ performed slightly better ($R^2 = 0.93$, RMSE = 0.09%; Fig. 2-15c) than the RF using $SIF_{760\text{-narrow-band}}$ ($R^2 = 0.87$, RMSE = 0.12 %; Fig. 2-15d).

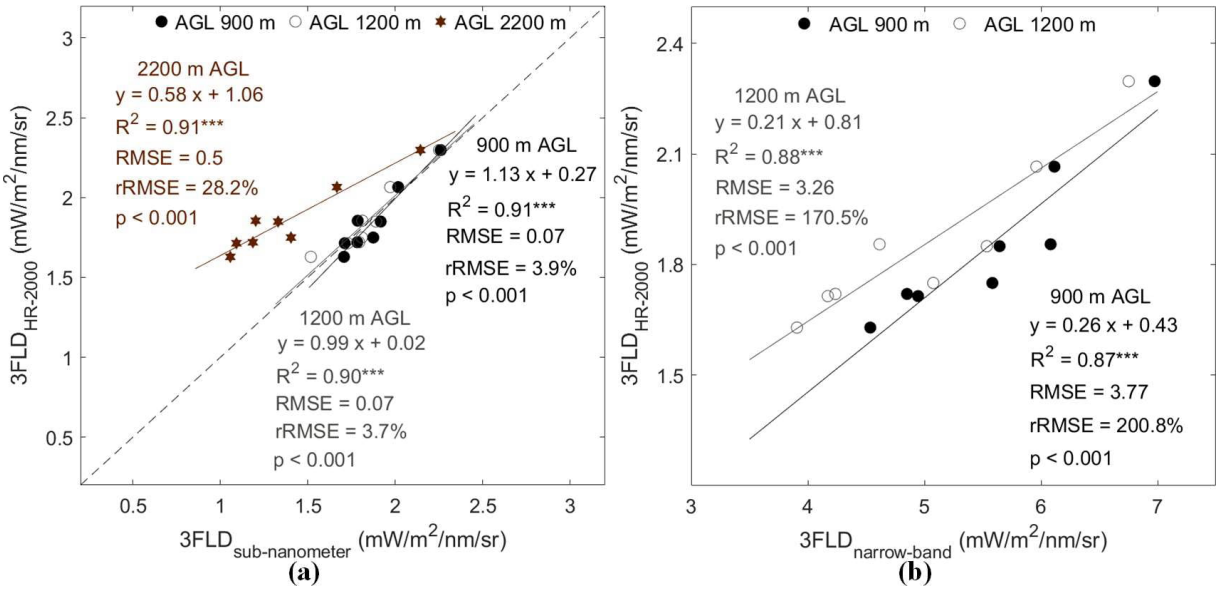

Fig. 2-14. Relationship between ground-based $SIF_{760\text{-}3FLD}$ quantified with a HR-2000 field spectrometer and airborne $SIF_{760\text{-}3FLD}$ at 900 m, 1200 m and 2200 m AGL retrieved from the sub-nanometer imager (a) and the narrow-band imager (b). The range of absolute $SIF_{760\text{-}3FLD}$ levels derived from the narrow-band imager was higher than the typical range of 0–3 $mW/m^2/nm/sr$ quantified from healthy vegetation due to the impact of the spectral resolution of the instrument. $SIF_{760\text{-}3FLD}$ measures with the narrow-band imager at 2200 m AGL were excluded because pixels were too coarse (1.7 m) relative to plot size (3 m × 12 m).

2.4 Discussion

In this study we examined the relationship between airborne $SIF_{760\text{-}3FLD}$ quantified using sub-nanometer resolution (i.e., ≤0.2 nm FWHM) and narrow-band resolution (i.e., 5.8-nm FWHM) hyperspectral imagers in the context of plant phenotyping for homogenous crop canopies. Our results support the assertion that airborne SIF retrievals from narrow-band hyperspectral imagers can successfully track small physiological changes induced by plant pathogens and environmental stresses, as reported elsewhere (Calderon *et al*., 2015; 2013; Camino *et al*., 2021; 2018a; Hernandez-Clemente *et al*., 2017; Panigada *et al*., 2014; Poblete *et al*., 2021; 2020; Zarco-Tejada *et al*., 2018; 2012). Precise SIF_{760} quantification at absolute scales was not essential for detecting plant stress in these studies. In our study, narrow-band airborne $SIF_{760\text{-}3FLD}$ was significantly associated with both sub-nanometer airborne and ground-based SIF observations. Our results particularly illustrate the

capability of these narrow-band hyperspectral imagers for characterising the intra-field SIF_{760} variability induced by different nitrogen fertilisation rates.

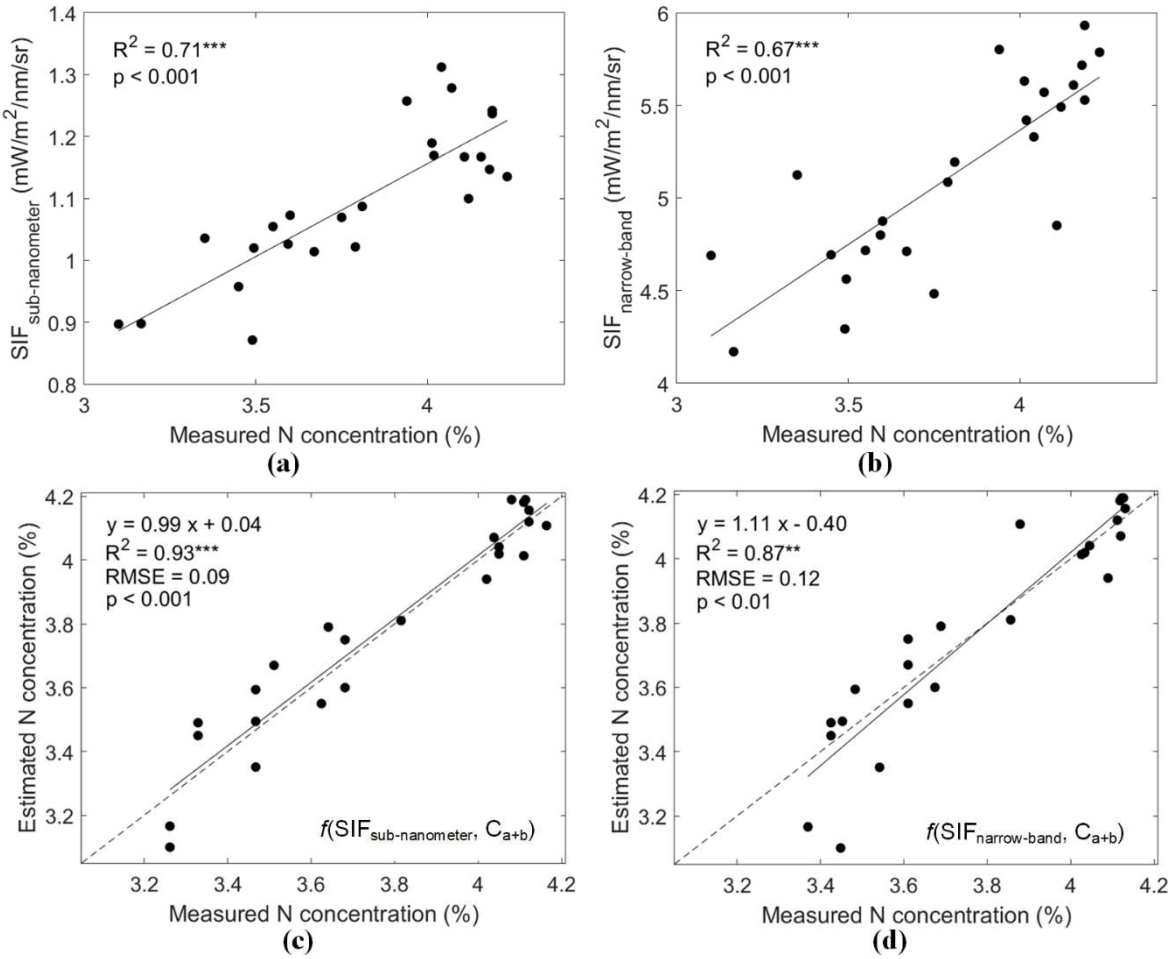

Fig. 2-15. Relationships between N concentration and airborne $SIF_{760\text{-}3FLD}$ quantified from a sub-nanometer (a) and narrow-band imager (b). Measured vs. estimated N concentration using Random Forest regression models, which included RTM-based C_{a+b} and $SIF_{760\text{-}3FLD}$ generated from either a sub-nanometer (c) or narrow-band imager (d). The dotted line represents the 1:1 line. The range of absolute $SIF_{760\text{-}3FLD}$ levels derived from the narrow-band imager was higher than the typical range of 0–3 $mW/m^2/nm/sr$ quantified from healthy vegetation due to the impact of the spectral resolution of the instrument.

Previous studies have highlighted the importance of sensor configuration for detecting spectral absorption features occurring over very narrow spectral ranges, particularly the need for high SR and SNR when quantifying SIF (Mohammed *et al.*, 2019). The literature has emphasised the need for instruments with sub-nanometer resolutions to accurately characterise narrow absorption features for reliable SIF estimates in physical units (Cogliati *et al.*, 2015; Julitta *et al.*, 2016; Meroni and Colombo, 2006; Meroni *et al.*, 2011; Rossini *et al.*, 2010). The experimental results from these studies

1985 are consistent with modelling studies based on FluorSAIL3 (Damm *et al*., 2011; Cendrero-Mateo *et*
1986 *al*., 2019) and SCOPE (Liu *et al*., 2015), which showed an increase in the SIF_{760} retrieval accuracy
1987 with increasing sensor SR. These modelling studies also found strong correlations between modelled
1988 and estimated SIF_{760} for low SR (5 nm) instruments using 3FLD (r = 0.78, RMSE = 0.31
1989 $mW/m^2/nm/sr$) and iFLD (r = 0.81, RMSE = 0.081 $mW/m^2/nm/sr$) (Damm *et al*., 2011). The SCOPE
1990 modelling results presented in this study support the findings of previous modelling efforts,
1991 illustrating statistically significant relationships ($p < 0.001$, R^2 = 0.70–0.99, RMSE = 0.24–1.25
1992 $mW/m^2/nm/sr$; Fig. 2-10) between $SIF_{760\text{-}3FLD}$ at 1 nm and $SIF_{760\text{-}3FLD}$ at coarser SRs ranging from 2-
1993 nm to 5.8-nm FWHM. The offset of the linear relationship with $SIF_{760\text{-}3FLD}$ at 1 nm increased steadily
1994 as the SR decreased from 2 to 5.8 nm, while the slope remained close to 1. This offset increase can
1995 be attributed to differences in radiance corresponding to the O_2-A band minima, which showed a
1996 200% increase (Fig. 2-5f) when resampling radiance spectra from_1 to 5.8 nm SR. Our modelling
1997 results and those of previous studies suggest that narrow-band resolution sensors (4- to 6-nm FWHM)
1998 with sufficient SNR can sufficiently characterise relative SIF_{760} levels despite their inability to
1999 provide reliable absolute SIF_{760} estimates.

2000 Differential nitrogen application rates in the three experiments were associated with
2001 variability of leaf physiological measurements (Fig. 2-6) and airborne $SIF_{760\text{-}3FLD}$. Narrow-band and
2002 sub-nanometer $SIF_{760\text{-}3FLD}$ estimates were strongly correlated across experiments, and both differed
2003 by nitrogen fertilisation level. The best correlation, observed in experiment 3, may be attributed to
2004 the identical flight altitude at which the narrow-band and the sub-nanometer hyperspectral images
2005 were collected for this experiment (site 2; Table 2-2) in addition to the higher relative $SIF_{760\text{-}3FLD}$
2006 variability observed within the experimental plots compared to experiments 1 and 2 (Fig. 2-9). The
2007 results demonstrated consistency across experimental sites and airborne campaigns carried out at
2008 different times, flight altitudes and years, showing robust relationships in terms of the relative $SIF_{760\text{-}3FLD}$
2009 variability quantified by the two hyperspectral imagers. The differences obtained in absolute

2010 levels of $SIF_{760\text{-}3FLD}$ quantified in the three experiments can be associated with the differences in crop
2011 varieties, crop growth stages and the slightly different acquisition times of the airborne hyperspectral
2012 images. These results are consistent with previous studies showing differences in both ground-based
2013 and airborne SIF_{760} measurements according to nitrogen treatment (Cendrero-Mateo *et al*., 2016; Jia
2014 *et al*., 2018; 2021; Quemada *et al*., 2014; Watt *et al*., 2020a; 2020b).

2015 Sensor altitude was identified as a critical factor in determining SIF accuracy (Daumard *et al*.,
2016 2015; Ni *et al*., 2016). MODTRAN (Berk et al., 2014) was used in these studies to show that the
2017 depth of the O_2-A absorption feature increases with sensor altitude. This is consistent with our
2018 findings, which show that the O_2-A band depth increased with altitude for both airborne hyperspectral
2019 imagers (Fig. 2-12) due to an increase in the radiance of the O_2-A band minima (Fig. 2-4h). Despite
2020 correcting for the atmospheric effects, $SIF_{760\text{-}3FLD}$ decreased with altitude for both airborne
2021 hyperspectral imagers. Such a decrease is linked to the correction method used, which relies on non-
2022 fluorescent targets. The relative increase in O_2-A band depth with increasing altitude is greater for
2023 vegetation targets than for bare soil targets (Daumard *et al*. 2015). This difference results in a bias in
2024 the corrected $SIF_{760\text{-}3FLD}$. Although $SIF_{760\text{-}3FLD}$ was overestimated at higher altitudes with both
2025 hyperspectral imagers, airborne estimates remained well correlated with ground-based measurements
2026 across altitudes (Fig. 2-12 and 2-14). This result has important implications for drone and airborne-
2027 based SIF quantifications in plant phenotyping studies and precision agriculture applications, in
2028 which sensor altitude is generally adapted depending on the flight efficiency and areal coverage.
2029 Although the relative variability needs to be assessed for detecting physiological changes induced by
2030 biotic or abiotic factors, understanding the effects of sensor altitude on SIF retrievals is critical for
2031 accurately interpreting SIF when used as input in stress-detection models.

2032 Few studies have validated airborne-quantified SIF_{760} from narrow-band hyperspectral
2033 imagers against ground-based observations from high-resolution field spectrometers, due to the
2034 challenges associated with complex and heterogenous canopies including forest areas and cash crops

such as vineyards and tree orchards. Damm *et al*. (2015) demonstrated the relationship between the medium-resolution Airborne Prism Experiment (APEX) sensor and a ground-based ASD (PANalytical, Boulder, US) field spectrometer for three different types of ecosystems. Measures were correlated (R^2 = 0.71), but airborne SIF_{760} systematically overestimated ground-based SIF_{760} by a proportionality factor (slope of airborne vs. ground SIF_{760} relationship) of 1.93 and an rRMSE of 28.9%. Guanter *et al*. (2007) found good agreement (R^2 = 0.85) between airborne SIF_{760} derived from the Compact Airborne Spectrographic Imager (CASI, Itres Research Ltd., Canada) and ground-based SIF_{760} derived from the ASD FieldSpec FR spectroradiometer. The airborne vs. ground-based relationship found in the current study (R^2 = 0.88, proportionality factor = 4.76) is consistent with the results from both studies above. Due to the impact of SR on the absolute $SIF_{760\text{-}3FLD}$ quantification, larger deviations in terms of rRMSE and proportionality factor were observed compared with the results from Damm *et al*. (2015), which can be attributed to the sub-nanometer resolution (0.065-nm FWHM) of the reference ground-based HR-2000 spectrometer used in our study as compared to the moderate spectral resolution of ASD spectrometers (>1.0-nm FWHM) used elsewhere.

The potential effects of the canopy structure are important to consider when comparing the narrow-band vs. sub-nanometer SIF retrievals. The TOC SIF observations from ground-based, airborne and spaceborne platforms are strongly affected by plant canopy structure due to the re-absorption and scattering of light within the canopy (Fournier *et al*., 2012; Porcar-Castell *et al*., 2014; Dechant *et al*., 2020; Yang and Van der Tol, 2018; Zeng *et al*., 2019). This structure is usually characterised by parameters such as leaf area index and the leaf inclination distribution function and may be approximated with vegetation indices such as Modified Triangular Vegetation Index (MTVI2) (Haboudane *et al*., 2004) and Enhanced Vegetation Index (EVI) (Huete *et al*., 2002) when assessing the effects of structure on SIF. In our study, the structural differences across experimental plots were generally small as structural changes were generally not associated with experimental treatments. Nevertheless, we tested whether treatment-associated variability in canopy structure could

be related to $SIF_{760\text{-}3FLD}$ from the narrow-band hyperspectral imager. We found that the relationships of both MTVI2 and EVI with narrow-band airborne $SIF_{760\text{-}3FLD}$ were weak and non-significantly correlated at both field trial sites ($p > 0.1$, $R^2 = 0 – 0.11$; Fig. 2-16). These results suggest that the $SIF_{760\text{-}3FLD}$ variability captured by the narrow-band imager in the experiments was not driven by changes arising from structural effects. Moreover, it shows that the fluorescence *in-filling* at the O_2-A band was unaffected by structure, with the variability across experimental plots due to subtle physiological differences.

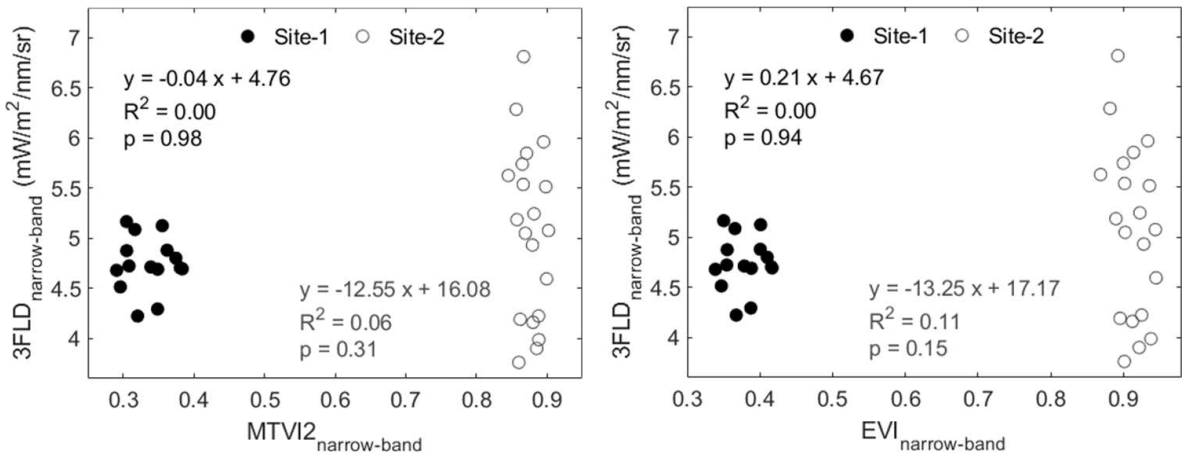

Fig. 2-16. Relationships between airborne $SIF_{760\text{-}3FLD}$ from the narrow-band hyperspectral imager and MTVI2 (a) and EVI (b). The range of absolute $SIF_{760\text{-}3FLD}$ levels derived from the narrow-band imager was higher than the typical range of 0–3 $mW/m^2/nm/sr$ quantified from healthy vegetation due to the impact of the spectral resolution of the instrument.

Predictive models of leaf N concentration improved only slightly when using SIF_{760} from the sub-nanometer imager compared to the narrow-band imager, with a marginal increase in the model performance (R^2 = 0.87 vs. 0.93) and a decrease in the error (RMSE = 0.12% vs. 0.09%). The direction of this improvement is consistent with the greater accuracy of the sub-nanometer SR imager. Nevertheless, these results suggest that data from the narrow-band hyperspectral imager may be sufficient for predicting N concentration in plant phenotyping and precision agriculture applications. Narrow-band imagery may be particularly suitable since relative changes in SIF linked to physiological conditions, nutritional deficiencies and stress levels are often the focus of such studies.

For assessing crop physiological status, standard commercially available hyperspectral imagers with 4- to 6-nm FWHM and SNRs greater than 300:1 can provide reliable relative SIF_{760} estimates (Zarco-Tejada *et al*., 2012; 2013a). These sensors are lightweight and can be carried on drone platforms that provide very high spatial resolution images due to low flying altitude. This capacity to generate very high spatial resolution imagery with narrow spectral bands is particularly important for plant phenotyping and precision agriculture applications for mapping physiological condition (Mohammed *et al*., 2019). Additional work using RTMs such as SCOPE and others is needed for improving the interpretation of SIF quantified using broader resolutions in precision agriculture.

2.5 Conclusions

1. Strong significant relationships were observed between SIF_{760} quantified with narrow-band and sub-nanometer hyperspectral imagers flown in tandem across experimental sites and airborne campaigns conducted at different times, flight altitudes and years. These results demonstrate robust quantification of relative SIF_{760} variability at lower spectral resolution, demonstrating its validity for detecting stress levels.
2. The experimental results obtained for SIF_{760} from the two hyperspectral imagers were successfully validated via SCOPE modelling, confirming the reliability of narrow-band SIF_{760} estimates for stress-detection applications requiring the assessment of the relative variability across the experimental field.
3. The estimation of leaf nitrogen concentration using SIF_{760} obtained similar results at both spectral resolutions (i.e. sub-nanometer vs. narrow-band SIF_{760}), suggesting that the relative SIF_{760} levels obtained from narrow-band hyperspectral imagers enable the prediction of nitrogen concentration for plant phenotyping and precision agriculture applications.

4. The SIF_{760} variability detected by the narrow-band hyperspectral imager was not related to canopy structural alterations, but rather to distinct physiological responses to various nitrogen fertilisation levels across the experimental plots. These results demonstrate the potential of narrow-band SIF_{760} to track small physiological changes caused due to nutrient variability.

Acknowledgements

The authors gratefully acknowledge the Foundation for Arable Research Australia, in particular Michael Straight and Ben Morris; the Grains Research and Development Corporation Australia; and Riverine Plains Incorporated for their provision and management of the field trials. A. Gracia Romero and Y. Wang are acknowledged for their technical support during the field and airborne campaigns.

References

Aasen, H., Honkavaara, E., Lucieer, A., Zarco-Tejada, P.J., 2018. Quantitative Remote Sensing at Ultra-High Resolution with UAV Spectroscopy: A Review of Sensor Technology, Measurement Procedures, and Data Correction Workflows. Remote Sens. 10, 1091.

Badgley, G., Field, C.B., Berry, J.A., 2017. Canopy near-infrared reflectance and terrestrial photosynthesis. Sci. Adv. 3, e1602244.

Bandopadhyay, S., Rastogi, A., Rascher, U., Rademske, P., Schickling, A., Cogliati, S., Julitta, T., Arthur, A. mac, Hueni, A., Tomelleri, E., Celesti, M., Burkart, A., Strózecki, M., Sakowska, K., Gabka, M., Rosadziński, S., Sojka, M., Iordache, M.D., Reusen, I., Van der Tol, C., Damm, A., Schuettemeyer, D., Juszczak, R., 2019. HyPlant-derived sun-induced fluorescence - a new opportunity to disentangle complex vegetation signals from diverse vegetation types. Remote Sens. 11, 1691.

Belwalkar, A., Poblete, T., Longmire, A., Hornero, A., Zarco-Tejada, P.J., 2021. Comparing the retrieval of chlorophyll fluorescence from two airborne hyperspectral imagers with different spectral resolutions for plant phenotyping studies. In: Proc. IEEE International Geoscience and Remote Sensing Symposium (IGARSS), 12–16 July 2021, Brussels, Belgium, pp. 5845–5848.

Berk, A., Conforti, P., Kennett, R., Perkins, T., Hawes, F., Van den Bosch, J., 2014. MODTRAN6: A major upgrade of the MODTRAN radiative transfer code. In: Proc. SPIE 9088, Algorithms and Technologies for Multispectral, Hyperspectral, and Ultraspectral Imagery XX, 90880H, 13 June 2014.

Breiman, L., 2001. Random Forests. Mach. Learn. 45, 5–32.

Calderón, R., Navas-Cortés, J.A., Lucena, C., Zarco-Tejada, P.J., 2013. High-resolution airborne hyperspectral and thermal imagery for early detection of Verticillium wilt of olive using fluorescence, temperature and narrow-band spectral indices. Remote Sens. Environ. 139, 231–245.

Calderón, R., Navas-Cortés, J.A., Zarco-Tejada, P.J., 2015. Early detection and quantification of Verticillium wilt in olive using hyperspectral and thermal imagery over large areas. Remote Sens. 7, 5584–5610.

Camino, C., Zarco-Tejada, P.J., Gonzalez-Dugo, V., 2018a. Effects of heterogeneity within tree crowns on airborne-quantified SIF and the CWSI as indicators of water stress in the context of precision agriculture. Remote Sens. 10, 604.

Camino, C., González-Dugo, V., Hernandez, P., Sillero, J.C., Zarco-Tejada, P.J., 2018b. Improved nitrogen retrievals with airborne-derived fluorescence and plant traits quantified from VNIR-SWIR hyperspectral imagery in the context of precision agriculture. Int. J. Appl. Earth Obs. Geoinf. 70, 105–117.

Camino, C., Gonzalez-Dugo, V., Hernandez, P., Zarco-Tejada, P.J., 2019. Radiative transfer Vcmax estimation from hyperspectral imagery and SIF retrievals to assess photosynthetic performance in rainfed and irrigated plant phenotyping trials. Remote Sens. Environ. 231, 111186.

Camino, C., Calderón, R., Parnell, S., Dierkes, H., Chemin, Y., Román-Écija, M., Montes-Borrego, M., Landa, B.B., Navas-Cortes, J.A., Zarco-Tejada, P.J., Beck, P.S.A., 2021. Detection of Xylella fastidiosa in almond orchards by synergic use of an epidemic spread model and remotely sensed plant traits. Remote Sens. Environ. 260, 112420.

Celesti, M., Van der Tol, C., Cogliati, S., Panigada, C., Yang, P., Pinto, F., Rascher, U., Miglietta, F., Colombo, R., Rossini, M., 2018. Exploring the physiological information of Sun-induced chlorophyll fluorescence through radiative transfer model inversion. Remote Sens. Environ. 215, 97–108.

Cendrero-Mateo, M.P., Moran, M.S., Papuga, S.A., Thorp, K.R., Alonso, L., Moreno, J., Ponce-Campos, G., Rascher, U., Wang, G., 2016. Plant chlorophyll fluorescence: active and passive measurements at canopy and leaf scales with different nitrogen treatments. J. Exp. Bot. 67, 275–286.

Cendrero-Mateo, M.P., Wieneke, S., Damm, A., Alonso, L., Pinto, F., Moreno, J., Guanter, L., Celesti, M., Rossini, M., Sabater, N., Cogliati, S., Julitta, T., Rascher, U., Goulas, Y., Aasen, H., Pacheco-Labrador, J., Mac Arthur, A., 2019. Sun-induced chlorophyll fluorescence III: benchmarking retrieval methods and sensor characteristics for proximal sensing. Remote Sens. 11, 962.

Cogliati, S., Rossini, M., Julitta, T., Meroni, M., Schickling, A., Burkart, A., Pinto, F., Rascher, U., Colombo, R., 2015. Continuous and long-term measurements of reflectance and sun-induced chlorophyll fluorescence by using novel automated field spectroscopy systems. Remote Sens. Environ. 164, 270–281.

Colombo, R., Celesti, M., Bianchi, R., Campbell, P.K.E., Cogliati, S., Cook, B.D., Corp, L.A., Damm, A., Domec, J.C., Guanter, L., Julitta, T., Middleton, E.M., Noormets, A., Panigada, C., Pinto, F., Rascher, U., Rossini, M., Schickling, A., 2018. Variability of sun-induced chlorophyll fluorescence according to stand age-related processes in a managed loblolly pine forest. Glob. Chang. Biol. 24, 2980–2996.

Damm, A., Erler, A., Hillen, W., Meroni, M., Schaepman, M.E., Verhoef, W., Rascher, U., 2011. Modeling the impact of spectral sensor configurations on the FLD retrieval accuracy of sun-induced chlorophyll fluorescence. Remote Sens. Environ. 115, 1882–1892.

Damm, A., Guanter, L., Laurent, V.C.E., Schaepman, M.E., Schickling, A., Rascher, U., 2014. FLD-based retrieval of sun-induced chlorophyll fluorescence from medium spectral resolution airborne spectroscopy data. Remote Sens. Environ. 147, 256–266.

Damm, A., Guanter, L., Paul-Limoges, E., Van der Tol, C., Hueni, A., Buchmann, N., Eugster, W., Ammann, C., Schaepman, M.E., 2015. Far-red sun-induced chlorophyll fluorescence shows ecosystem-specific relationships to gross primary production: An assessment based on observational and modeling approaches. Remote Sens. Environ. 166, 91–105.

Daumard, F., Goulas, Y., Champagne, S., Fournier, A., Ounis, A., Olioso, A., Moya, I., 2012. Continuous monitoring of canopy level sun-induced chlorophyll fluorescence during the growth of a sorghum field. IEEE Trans. Geosci. Remote Sens. 50, 4292–4300.

Daumard, F., Goulas, Y., Ounis, A., Pedrós, R., Moya, I., 2015. Measurement and correction of atmospheric effects at different altitudes for remote sensing of sun-induced fluorescence in oxygen absorption bands. IEEE Trans. Geosci. Remote Sens. 53, 5180–5196.

Dechant, B., Ryu, Y., Badgley, G., Zeng, Y., Berry, J.A., Zhang, Y., Goulas, Y., Li, Z., Zhang, Q., Kang, M., Li, J., Moya, I., 2020. Canopy structure explains the relationship between photosynthesis and sun-induced chlorophyll fluorescence in crops. Remote Sens. Environ. 241, 111733.

Dechant, B., Ryu, Y., Yang K., Kim J., 2017. A comprehensive analysis of spectral resolution effects on SIF retrieval and potential correction methods. In: Proc. American Geophysical Union, Fall Meeting, 11–15 December 2017, New Orleans, USA.

Drusch, M., Moreno, J., Del Bello, U., Franco, R., Goulas, Y., Huth, A., Kraft, S., Middleton, E.M., Miglietta, F., Mohammed, G., Nedbal, L., Rascher, U., Schüttemeyer, D., Verhoef, W., 2017. The FLuorescence EXplorer mission concept - ESA's Earth Explorer 8. IEEE Trans. Geosci. Remote Sens. 55, 1273–1284.

ESA (European Space Agency), 2015. Report for Mission Selection: FLEX. ESA SP-1330/2 (2 Volume Series). 197 pp., Noordwijk (The Netherlands). https://esamultimedia. esa.int/docs/EarthObservation/SP1330-2_FLEX.pdf.

Féret, J.B., Berger, K., de Boissieu, F., Malenovský, Z., 2021. PROSPECT-PRO for estimating content of nitrogen-containing leaf proteins and other carbon-based constituents. Remote Sens. Environ. 252, 112173.

Fournier, A., Daumard, F., Champagne, S., Ounis, A., Goulas, Y., Moya, I., 2012. Effect of canopy structure on sun-induced chlorophyll fluorescence. ISPRS J. Photogramm. Remote Sens. 68, 112–120.

Frankenberg, C., O'Dell, C., Berry, J., Guanter, L., Joiner, J., Köhler, P., Pollack, R., Taylor, T.E., 2014. Prospects for chlorophyll fluorescence remote sensing from the Orbiting Carbon Observatory-2. Remote Sens. Environ. 147, 1–12.

Frankenberg, C., Köhler, P., Magney, T.S., Geier, S., Lawson, P., Schwochert, M., McDuffie, J., Drewry, D.T., Pavlick, R., Kuhnert, A., 2018. The chlorophyll fluorescence imaging spectrometer (CFIS), mapping far red fluorescence from aircraft. Remote Sens. Environ. 217, 523–536.

Gastellu-Etchegorry, J.-P., Lauret, N., Yin, T., Landier, L., Kallel, A., Malenovský, Z., Al Bitar, A., Aval, J., Benhmida, S., Qi, J., Medjdoub, G., Guilleux, J., Chavanon, E., Cook, B., Morton, D., Chrysoulakis, N., Mitraka, Z., 2017. DART: recent advances in remote sensing data modeling with atmosphere, polarization, and chlorophyll fluorescence. IEEE J. Sel. Top. Appl. Earth Obs. Remote Sens. 10, 2640–2649.

Genty, B., Briantais, J.M., Baker, N.R., 1989. The relationship between the quantum yield of photosynthetic electron transport and quenching of chlorophyll fluorescence. Biochim. Biophys. Acta 990, 87–92.

Gonzalez-Dugo, V., Hernandez, P., Solis, I., Zarco-Tejada, P.J., 2015. Using high-resolution hyperspectral and thermal airborne imagery to assess physiological condition in the context of wheat phenotyping. Remote Sens. 7, 13586–13605.

Grossmann, K., Frankenberg, C., Magney, T.S., Hurlock, S.C., Seibt, U., Stutz, J., 2018. PhotoSpec: a new instrument to measure spatially distributed red and far-red solar-induced chlorophyll fluorescence. Remote Sens. Environ. 216, 311–327.

Guanter, L., Alonso, L., Gómez-Chova, L., Amorós-López, J., Vila, J., Moreno, J., 2007. Estimation of solar-induced vegetation fluorescence from space measurements. Geophys. Res. Lett. 34, L08401.

Guanter, L., Alonso, L., Gómez-Chova, L., Meroni, M., Preusker, R., Fischer, J., & Moreno, J., 2010. Developments for vegetation fluorescence retrieval from spaceborne high-resolution spectrometry in the O_2-A and O_2-B absorption bands. J. Geophys. Res. 115, 19303.

Guanter, L., Frankenberg, C., Dudhia, A., Lewis, P.E., Gómez-Dans, J., Kuze, A., Suto, H., Grainger, R.G., 2012. Retrieval and global assessment of terrestrial chlorophyll fluorescence from GOSAT space measurements. Remote Sens. Environ. 121, 236–251.

Guanter, L., Aben, I., Tol, P., Krijger, J.M., Hollstein, A., Köhler, P., Damm, A., Joiner, J., Frankenberg, C., Landgraf, J., 2015. Potential of the TROPOspheric Monitoring Instrument (TROPOMI) onboard the Sentinel-5 Precursor for the monitoring of terrestrial chlorophyll fluorescence. Atmos. Meas. Tech. 8, 1337–1352.

Gueymard, C.A., 2001. Parameterized transmittance model for direct beam and circumsolar spectral irradiance. Sol. Energy 71, 325–346.

Haboudane, D., Miller, J.R., Pattey, E., Zarco-Tejada, P.J., Strachan, I.B., 2004. Hyperspectral vegetation indices and novel algorithms for predicting green LAI of crop canopies: modeling and validation in the context of precision agriculture. Remote Sens. Environ. 90, 337–352.

Hao, D., Zeng, Y., Qiu, H., Biriukova, K., Celesti, M., Migliavacca, M., Rossini, M., Asrar, G.R., Chen, M., 2021. Practical approaches for normalizing directional solar-induced fluorescence to a standard viewing geometry. Remote Sens. Environ. 255, 112171.

Hernández-Clemente, R., North, P.R.J., Hornero, A., Zarco-Tejada, P.J., 2017. Assessing the effects of forest health on sun-induced chlorophyll fluorescence using the FluorFLIGHT 3-D radiative transfer model to account for forest structure. Remote Sens. Environ. 193, 165–179.

Hornero, A., North, P.R.J., Zarco-Tejada, P.J., Rascher, U., Martín, M.P., Migliavacca, M., Hernández-Clemente, R., 2021a. Assessing the contribution of understory sun-induced chlorophyll fluorescence through 3-D radiative transfer modelling and field data. Remote Sens. Environ. 253, 112195.

Hornero, A., Zarco-Tejada, P.J., Quero, J.L., North, P.R.J., Ruiz-Gómez, F.J., Sánchez-Cuesta, R., Hernández-Clemente, R., 2021b. Modelling hyperspectral- and thermal-based plant traits for the early detection of Phytophthora-induced symptoms in oak decline. Remote Sens. Environ. 263, 112570.

Huete, A., Didan, K., Miura, T., Rodriguez, E.P., Gao, X., Ferreira, L.G., 2002. Overview of the radiometric and biophysical performance of the MODIS vegetation indices. Remote Sens. Environ. 83, pp. 195–213.

Jacquemoud, S., Baret, F., 1990. PROSPECT: a model of leaf optical properties spectra. Remote Sens. Environ. 34, 75–91.

Jia, M., Zhu, J., Ma, C., Alonso, L., Li, D., Cheng, T., Tian, Y., Zhu, Y., Yao, X., Cao, W., 2018. Difference and potential of the upward and downward sun-induced chlorophyll fluorescence on detecting leaf nitrogen concentration in wheat. Remote Sens. 10, 1315.

Jia, M., Colombo, R., Rossini, M., Celesti, M., Zhu, J., Cogliati, S., Cheng, T., Tian, Y., Zhu, Y., Cao, W., Yao, X., 2021. Estimation of leaf nitrogen content and photosynthetic nitrogen use efficiency in wheat using sun-induced chlorophyll fluorescence at the leaf and canopy scales. Eur. J. Agron. 122, 126192.

Julitta, T., Corp, L.A., Rossini, M., Burkart, A., Cogliati, S., Davies, N., Hom, M., Arthur, A. Mac, Middleton, E.M., Rascher, U., Schickling, A., Colombo, R., 2016. Comparison of sun-induced chlorophyll fluorescence estimates obtained from four portable field spectroradiometers. Remote Sens. 8, 122.

Julitta, T., Wutzler, T., Rossini, M., Colombo, R., Cogliati, S., Meroni, M., Burkart, A., Migliavacca, M., 2017. An R package for field spectroscopy: From system characterization to sun-induced chlorophyll fluorescence Retrieval. In: Proc. 6th International Workshop on Remote Sensing of Vegetation Fluorescence, 17–19 January 2017, Frascatti, Italy.

Kim, J., Ryu, Y., Dechant, B., Lee, H., Kim, H.S., Kornfeld, A., Berry, J.A., 2021. Solar- induced chlorophyll fluorescence is non-linearly related to canopy photosynthesis in a temperate evergreen needleleaf forest during the fall transition. Remote Sens. Environ. 258, 112362.

Kjeldahl, J., 1883. Neue Methode zur Bestimmung des Stickstoffs in organischen. J. Anal. Chem. 22, 366–382.

Krause, G. H., Weis, E., 1984. Chlorophyll fluorescence as a tool in plant physiology. II. Interpretation of fluorescence signals. Photosynth. Res. 5, 139–157.

Li, Z., Zhang, Q., Li, J., Yang, X., Wu, Y., Zhang, Z., Wang, S., Wang, H., Zhang, Y., 2020. Solar-induced chlorophyll fluorescence and its link to canopy photosynthesis in maize from continuous ground measurements. Remote Sens. Environ. 236, 111420.

Lichtenthaler, H. K., Rinderle, U., 1988. The role of chlorophyll fluorescence in the detection of stress conditions in plants. Crit. Rev. Anal. Chem. 19 (Suppl. 1), S29–S85.

Liu, L., Liu, X., Hu, J., 2015. Effects of spectral resolution and SNR on the vegetation solar-induced fluorescence retrieval using FLD-based methods at canopy level. Eur. J. Remote Sens. 48, 743–762.

Maier, S.W., Günther, K.P., Stellmes, M., 2003. Sun-induced fluorescence: a new tool for precision farming. In: Schepers, J., VanToai, T. (Eds.), Digital Imaging and Spectral Techniques: Applications to Precision Agriculture and Crop Physiology. ASA Spec. Publ. 66. ASA, CSSA, and SSSA, Madison (Wisconsin), USA, pp. 209–222.

Marrs, J.K., Jones, T.S., Allen, D.W., Hutyra, L.R., 2021. Instrumentation sensitivities for tower-based solar-induced fluorescence measurements. Remote Sens. Environ. 259, 112413.

Meroni, M., Colombo, R., 2006. Leaf level detection of solar induced chlorophyll fluorescence by means of a subnanometer resolution spectroradiometer. Remote Sens. Environ. 103, 438–448.

Meroni, M., Rossini, M., Guanter, L., Alonso, L., Rascher, U., Colombo, R., Moreno, J., 2009. Remote sensing of solar-induced chlorophyll fluorescence: review of methods and applications. Remote Sens. Environ. 113, 2037–2051.

Meroni, M., Busetto, L., Colombo, R., Guanter, L., Moreno, J., Verhoef, W., 2010. Performance of Spectral Fitting Methods for vegetation fluorescence quantification. Remote Sens. Environ. 114, 363–374.

Meroni, M., Barducci, A., Cogliati, S., Castagnoli, F., Rossini, M., Busetto, L., & Di Cella, U.M., 2011. The hyperspectral irradiometer, a new instrument for long-term and unattended field spectroscopy measurements. Rev. Sci. Instrum. 82, 043106.

Mohammed, G.H., Colombo, R., Middleton, E.M., Rascher, U., Van der Tol, C., Nedbal, L., Goulas, Y., Pérez-Priego, O., Damm, A., Meroni, M., Joiner, J., Cogliati, S., Verhoef, W., Malenovský, Z., Gastellu-Etchegorry, J.P., Miller, J.R., Guanter, L., Moreno, J., Moya, I., Berry, J.A., Frankenberg, C., Zarco-Tejada, P.J., 2019. Remote sensing of solar-induced chlorophyll fluorescence (SIF) in vegetation: 50 years of progress. Remote Sens. Environ. 231, 111177.

Nakashima, N., Kato, T., Morozumi, T., Tsujimoto, K., Akitsu, T.K., Nasahara, K.N., Murayama, S., Muraoka, H., Noda, H.M., 2021. Area-ratio Fraunhofer line depth (aFLD) method approach to estimate solar-induced chlorophyll fluorescence in low spectral resolution spectra in a cool-temperate deciduous broadleaf forest. J. Plant Res. 134, 713–728.

Ni, Z., Liu, Z., Li, Z.L., Nerry, F., Huo, H., Sun, R., Yang, P., Zhang, W., 2016. Investigation of atmospheric effects on retrieval of sun-induced fluorescence using hyperspectral imagery. Sensors 16, 480.

Nichol, C.J., Drolet, G., Porcar-Castell, A., Wade, T., Sabater, N., Middleton, E.M., Maclellan, C., Levula, J., Mammarella, I., Vesala, T., Atherton, J., 2019. Diurnal and Seasonal Solar Induced Chlorophyll Fluorescence and Photosynthesis in a Boreal Scots Pine Canopy. Remote Sens. 11, 273.

Panigada, C., Rossini, M., Meroni, M., Cilia, C., Busetto, L., Amaducci, S., Boschetti, M., Cogliati, S., Picchi, V., Pinto, F., Marchesi, A., Colombo, R., 2014. Fluorescence, PRI and canopy temperature for water stress detection in cereal crops. Int. J. Appl. Earth Obs. Geoinf. 30, 167–178.

Pedrós, R., Moya, I., Goulas, Y., Jacquemoud, S., 2008. Chlorophyll fluorescence emission spectrum inside a leaf. Photochem. Photobiol. Sci. 7, 498–502.

Pérez-Priego, O., Zarco-Tejada, P.J., Miller, J.R., Sepulcre-Cantó, G., Fereres, E., 2005. Detection of water stress in orchard trees with a high-resolution spectrometer through chlorophyll fluorescence *in-filling* of the O_2-A band. IEEE Trans. Geosci. Remote Sens. 43, 2860–2869.

Poblete, T., Camino, C., Beck, P.S.A., Hornero, A., Kattenborn, T., Saponari, M., Boscia, D., Navas-Cortes, J.A., Zarco-Tejada, P.J., 2020. Detection of Xylella fastidiosa infection symptoms with airborne multispectral and thermal imagery: Assessing bandset reduction performance from hyperspectral analysis. ISPRS J. Photogramm. Remote Sens. 162, 27–40.

Poblete, T., Navas-Cortes, J.A., Camino, C., Calderon, R., Hornero, A., Gonzalez-Dugo, V., Landa, B.B., Zarco-Tejada, P.J. (2021), Discriminating *Xylella fastidiosa* from *Verticillium dahliae* infections in olive trees using thermal- and hyperspectral-based plant traits. ISPRS J. Photogramm. Remote Sens. 179, 133–144.

Porcar-Castell, A., Tyystj¨arvi, E., Atherton, J., Van der Tol, C., Flexas, J., Pfündel, E.E., Moreno, J., Frankenberg, C., Berry, J.A., 2014. Linking chlorophyll a fluorescence to photosynthesis for remote sensing applications: mechanisms and challenges. J. Exp. Bot. 65, 4065–4095.

Plascyk, J.A., 1975. The MK II Fraunhofer line discriminator (FLD-II) for airborne and orbital remote sensing of solar-stimulated luminescence. Opt. Eng. 14, 144339.

Quemada, M., Gabriel, J.L., Zarco-Tejada, P., 2014. Airborne hyperspectral images and ground-level optical sensors as assessment tools for maize nitrogen fertilization. Remote Sens. 6, 2940–2962.

Rascher, U., Alonso, L., Burkart, A., Cilia, C., Cogliati, S., Colombo, R., Damm, A., Drusch, M., Guanter, L., Hanus, J., Hyvärinen, T., Julitta, T., Jussila, J., Kataja, K., Kokkalis, P., Kraft, S., Kraska, T., Matveeva, M., Moreno, J., Muller, O., Panigada, C., Pikl, M., Pinto, F., Prey, L., Pude, R., Rossini, M., Schickling, A., Schurr, U., Schüttemeyer, D., Verrelst, J., Zemek, F., 2015. Sun-induced fluorescence - a new probe of photosynthesis: first maps from the imaging spectrometer HyPlant. Glob. Chang. Biol. 21, 4673–4684.

Rossini, M., Meroni, M., Migliavacca, M., Manca, G., Cogliati, S., Busetto, L., Picchi, V., Cescatti, A., Seufert, G., Colombo, R., 2010. High resolution field spectroscopy measurements for estimating gross ecosystem production in a rice field. Agric. For. Meteorol. 150, 1283–1296.

Rossini, M., Meroni, M., Celesti, M., Cogliati, S., Julitta, T., Panigada, C., Rascher, U., Van der Tol, C., Colombo, R., 2016. Analysis of red and far-red sun-induced chlorophyll fluorescence and their ratio in different canopies based on observed and modeled data. Remote Sens. 8, 412.

Siegmann, B., Alonso, L., Celesti, M., Cogliati, S., Colombo, R., Damm, A., Douglas, S., Guanter, L., Hanuš, J., Kataja, K., Kraska, T., Matveeva, M., Moreno, J., Muller, O., Pikl, M., Pinto, F., Vargas, J.Q., Rademske, P., Rodriguez-Morene, F., Sabater, N., Schickling, A., Schüttemeyer, D., Zemek, F., Rascher, U., 2019. The high-performance airborne imaging spectrometer HyPlant-from raw images to top-of-canopy reflectance and fluorescence products: Introduction of an automatized processing chain. Remote Sens. 11, 2760.

Suarez, L., Gonzalez-Dugo, V., Camino, C., Hornero, A., Zarco-Tejada, P.J., 2021. Physical model inversion of the green spectral region to track assimilation rate in almond trees with an airborne nano-hyperspectral imager. Remote Sens. Environ. 252, 112147.

Sun, Y., Frankenberg, C., Wood, J.D., Schimel, D.S., Jung, M., Guanter, L., Drewry, D.T., Verma, M., Porcar-Castell, A., Griffis, T.J., Gu, L., Magney, T.S., Köhler, P., Evans, B., Yuen, K., 2017. OCO-2 advances photosynthesis observation from space via solar induced chlorophyll fluorescence. Science 358, eaam5747.

Süß, A., Hank, T., Mauser, W., 2016. Deriving diurnal variations in sun-induced chlorophyll-a fluorescence in winter wheat canopies and maize leaves from ground-based hyperspectral measurements. Int. J. Remote Sens. 37, 60–77.

Tagliabue, G., Panigada, C., Celesti, M., Cogliati, S., Colombo, R., Migliavacca, M., Rascher, U., Rocchini, D., Schüttemeyer, D., Rossini, M., 2020. Sun–induced fluorescence heterogeneity as a measure of functional diversity. Remote Sens. Environ. 247, 111934.

Van der Tol, C., Verhoef, W., Timmermans, J., Verhoef, A., Su, Z., 2009. An integrated model of soil-canopy spectral radiances, photosynthesis, fluorescence, temperature and energy balance. Biogeosci. 6, 3109–3129.

Verhoef, W., 1984. Light scattering by leaf layers with application to canopy reflectance modeling: the SAIL model. Remote Sens. Environ. 16, 125–141.

Verhoef, W., 2004. Extension of SAIL to model solar - induced canopy fluorescence spectra. In: Proc. 2nd International Workshop on Remote Sensing of Vegetation Fluorescence, 17–19 November 2004, Montreal, Canada.

Verhoef, W., Jia, L., Xiao, Q., Su, Z., 2007. Unified optical-thermal four-stream radiative transfer theory for homogeneous vegetation canopies. IEEE Trans. Geosci. Remote Sens. 45, 1808–1822.

Verhoef, W., Van der Tol, C., Middleton, E.M., 2018. Hyperspectral radiative transfer modeling to explore the combined retrieval of biophysical parameters and canopy fluorescence from FLEX – Sentinel-3 tandem mission multi-sensor data. Remote Sens. Environ. 204, 942–963.

Vilfan, N., Van der Tol, C., Muller, O., Rascher, U., Verhoef, W., 2016. Fluspect-B: a model for leaf fluorescence, reflectance and transmittance spectra. Remote Sens. Environ. 186, 596–615.

Wang, Y., Suarez, L., Qian, X., Poblete, T., Gonzalez-Dugo, V., Ryu, D., Zarco-Tejada, P.J., 2021. Assessing the contribution of airborne-retrieved chlorophyll fluorescence for nitrogen

assessment in almond orchards. In: Proc. IEEE International Geoscience and Remote Sensing Symposium (IGARSS), 12–16 July 2021, Brussels, Belgium, pp. 5853–5856.

Watt, M.S., Buddenbaum, H., Leonardo, E.M.C., Estarija, H.J., Bown, H.E., Gomez-Gallego, M., Hartley, R.J.L., Pearse, G.D., Massam, P., Wright, L., Zarco-Tejada, P.J., 2020a. Monitoring biochemical limitations to photosynthesis in N and P-limited radiata pine using plant functional traits quantified from hyperspectral imagery. Remote Sens. Environ. 248, 112003.

Watt, M.S., Buddenbaum, H., Leonardo, E.M.C., Estarija, H.J.C., Bown, H.E., Gomez-Gallego, M., Hartley, R., Massam, P., Wright, L., Zarco-Tejada, P.J., 2020b. Using hyperspectral plant traits linked to photosynthetic efficiency to assess N and P partition. ISPRS J. Photogramm. Remote Sens. 169, 406–420.

Weis, E., Berry, J.A., 1987. Quantum efficiency of photosystem II in relation to 'energy'- dependent quenching of chlorophyll fluorescence. Biochim. Biophys. Acta 894, 198–208.

Wieneke, S., Ahrends, H., Damm, A., Pinto, F., Stadler, A., Rossini, M., Rascher, U., 2016. Airborne based spectroscopy of red and far-red sun-induced chlorophyll fluorescence: Implications for improved estimates of gross primary productivity. Remote Sens. Environ. 184, 654–667.

Yang, R., Juhasz, A., Zhang, Yujuan, Chen, X., Zhang, Yinjun, She, M., Zhang, J., Maddern, R., Edwards, I., Diepeveen, D., Islam, S., Ma, W., 2018. Molecular characterisation of the NAM-1 genes in bread wheat in Australia. Crop Pasture Sci. 69, 1173–1181.

Yang, P., Van der Tol, C., 2018. Linking canopy scattering of far-red sun-induced chlorophyll fluorescence with reflectance. Remote Sens. Environ. 209, 456–467.

Zarco-Tejada, P.J., Miller, J.R., Mohammed, G.H., Noland, T.L., 2000a. Chlorophyll fluorescence effects on vegetation apparent reflectance: I. Leaf-level measurements and model simulation. Remote Sens. Environ. 74, 582–595.

Zarco-Tejada, P.J., Miller, J.R., Mohammed, G.H., Noland, T.L., Sampson, P.H., 2000b. Chlorophyll fluorescence effects on vegetation apparent reflectance: II. Laboratory and airborne canopy-level measurements with hyperspectral data. Remote Sens. Environ. 74, 596–608.

Zarco-Tejada, P.J., González-Dugo, V., Berni, J.A.J., 2012. Fluorescence, temperature and narrow-band indices acquired from a UAV platform for water stress detection using a micro-hyperspectral imager and a thermal camera. Remote Sens. Environ. 117, 322–337.

Zarco-Tejada, P.J., Catalina, A., González, M.R., Martín, P., 2013a. Relationships between net photosynthesis and steady-state chlorophyll fluorescence retrieved from airborne hyperspectral imagery. Remote Sens. Environ. 136, 247–258.

Zarco-Tejada, P.J., Suarez, L., Gonzalez-Dugo, V., 2013b. Spatial resolution effects on chlorophyll fluorescence retrieval in a heterogeneous canopy using hyperspectral imagery and radiative transfer simulation. IEEE Geosci. Remote Sens. Lett. 10, 937–941.

Zarco-Tejada, P.J., González-Dugo, M.V., Fereres, E., 2016. Seasonal stability of chlorophyll fluorescence quantified from airborne hyperspectral imagery as an indicator of net photosynthesis in the context of precision agriculture. Remote Sens. Environ. 179, 89–103.

Zarco-Tejada, P.J., Camino, C., Beck, P.S.A., Calderon, R., Hornero, A., Hernández- Clemente, R., Kattenborn, T., Montes-Borrego, M., Susca, L., Morelli, M., Gonzalez- Dugo, V., North, P.R.J., Landa, B.B., Boscia, D., Saponari, M., Navas-Cortes, J.A., 2018. Previsual symptoms of Xylella fastidiosa infection revealed in spectral plant-trait alterations. Nat. Plants 4, 432–439.

Zeng, Y., Badgley, G., Dechant, B., Ryu, Y., Chen, M., Berry, J.A., 2019. A practical approach for estimating the escape ratio of solar-induced chlorophyll fluorescence. Remote Sens. Environ. 232, 111209.

Zhao, F., Dai, X., Verhoef, W., Guo, Y., Van der Tol, C., Li, Y., Huang, Y., 2016. FluorWPS: a Monte Carlo ray-tracing model to compute sun-induced chlorophyll fluorescence of three-dimensional canopy. Remote Sens. Environ. 187, 385–399.

Chapter 3

Spectral effects of medium resolution airborne hyperspectral imagers on SIF quantification

This chapter resulted in two research articles.

1. **Belwalkar, A.,** Poblete, T., A., Hornero, A., Hernandez-Clemente, R., Zarco-Tejada, P.J. **Accurate SIF quantification from a narrow-band airborne hyperspectral imager using SCOPE: assessment with sub-nanometer imagery** (currently under review by the journal *Remote Sensing of Environment*)

2. **Belwalkar, A.**, Poblete, T., Hornero, A., Zarco-Tejada, P.J., 2022. **Accounting for the spectral resolution on SIF retrieval from a narrow-band airborne imager using SCOPE**. In: Proc. IEEE International Geoscience and Remote Sensing Symposium (IGARSS), 17–22 July 2022, Kuala Lumpur, Malaysia, pp. 5440–5443. https://doi.org/10.1109/IGARSS46834.2022.9884564.

Abstract

Hyperspectral imaging of solar-induced chlorophyll fluorescence (SIF) is useful for large-scale plant phenotyping and stress detection. However, the most accurate instruments for SIF quantification, such as sub-nanometer (≤1-nm full-width at half-maximum, FWHM) airborne hyperspectral imagers, are expensive and complex to use. Previous studies have demonstrated that standard narrow-band hyperspectral imagers (i.e., 4–6-nm FWHM) are more cost-effective and are able to provide far-red SIF (SIF_{760}) estimations that correlate strongly with precise sub-nanometer resolution measurements. Nevertheless, narrow-band SIF_{760} estimates are subject to systematic overestimation due to the influence of spectral resolution (SR) on SIF_{760} levels. In this study, we investigated ways to address this bias using simulations from the Soil Canopy Observation, Photochemistry and Energy fluxes (SCOPE) model with Support Vector Regression (SVR) to estimate SIF_{760} at 1-nm SR from narrow-band resolution spectra. The performance of the proposed approach was evaluated using SCOPE model simulations and airborne imagery acquired from the two airborne hyperspectral imagers (FWHM ≤0.2 nm and 5.8 nm) flown in tandem on board an aircraft that collected data from two different wheat and maize phenotyping trials. The estimated SIF_{760} at 1-nm SR matched well with the reference SIF_{760} for both simulated (normalised root mean square error (nRMSE) 2.45–5.28%) and airborne hyperspectral (nRMSE = 4.5–16%) datasets. These results suggest that the proposed SIF_{760} modelling approach could be a useful strategy for improving the interpretation of relative SIF_{760} levels quantified from narrow-band hyperspectral imagers in studies focused on stress detection assessing plant physiological conditions.

Keywords: Solar-induced chlorophyll fluorescence, SIF, narrow-band, SCOPE, SVR, airborne, hyperspectral, hyperspectral imager

3.1 Introduction

Solar-induced chlorophyll fluorescence (SIF) is a weak electromagnetic signal emitted by chlorophyll *a* that provides useful information about plant photosynthetic activity and stress (Lichtenthaler and Rinderle, 1988; Campbell *et al*., 2008; Malenovský *et al*., 2009; Zarco-Tejada *et al*., 2016; 2021). Direct measurement of the SIF signal is complex due to its superimposition on the reflected solar radiation and small magnitude (1–5% of total upwelling radiance in the near infrared) (Meroni *et al*., 2009). Since sensor capabilities impact the shape of absorption features commonly used for SIF estimation, instruments with sufficient spectral resolution (SR) and signal-to-noise ratio (SNR) are required for detecting subtle variations across narrow absorption features for accurate SIF quantification (Mohammed *et al*., 2019). Sensors with a sub-nanometer resolution are thus recommended for obtaining SIF estimates in precise physical units and absolute terms.

SIF signal can be retrieved using a range of platforms, including ground-based spectrometers (Acebron *et al*., 2021; Cogliati *et al*., 2015; Damm *et al*., 2021; Grossmann *et al*., 2018; Hao *et al*., 2022; Kim *et al*., 2021; Li *et al*., 2020; Pacheco-Labrador *et al*., 2019), drones (Bendig *et al*., 2019; Chang *et al*., 2020; Suarez *et al*., 2021; N. Wang *et al*., 2021; Xu *et al*., 2021; Zarco-Tejada *et al*., 2012), piloted aircrafts (Damm *et al*., 2015; 2022; Poblete *et al*., 2020; Rascher *et al*., 2015; Siegmann *et al*., 2021), and satellites (Braghiere *et al*., 2021; Köhler *et al*., 2018; Sun *et al*., 2018). For airborne SIF estimation, there are several imaging sensors with sub-nanometer resolution capabilities, such as the chlorophyll fluorescence imaging spectrometer (CFIS) (Frankenberg *et al*., 2018), the high-resolution airborne imaging spectrometer HyPlant (Rascher *et al*., 2015), the AISA IBIS Fluorescence Imager (SPECIM, Spectral Imaging Ltd., Oulu, Finland) (R. Wang *et al*., 2022), and the Hyperspec Solar-Induced Fluorescence Imaging sensor (Headwall Photonics, Fitchburg, MA, USA) (Paynter *et al*., 2020) with SRs of 0.07, 0.28, 0.245, and ≤0.2 nm, respectively. These sub-nanometer imaging sensors can precisely characterise narrow absorption features needed for the accurate quantification of SIF in physical units.

Despite their potential, sub-nanometer imaging sensors pose significant challenges that restrict their widespread use for plant physiology monitoring, precision agriculture, and plant phenotyping applications. Their radiometric calibration is among the most challenging aspects. Since these sensors have narrow contiguous bands with a spectral sampling interval (SSI) on the order of 10^{-1} nm, a sophisticated calibration facility is required for accurate characterisation of the detector's spectral response (Brown *et al*., 2006). A further obstacle is the difficulty in processing different flight lines, which is primarily due to the large amount of data generated, which makes mosaicking multiple flight lines a challenging task. Furthermore, these sensors have a spectral range limited to the SIF emission region (650–800 nm). Consequently, they cannot be used to simultaneously estimate SIF, plant traits, and vegetation indices, necessitating the integration of an additional sensor into the airborne platform. In addition, their weights make these sensors incompatible with drones, requiring lightweight aircraft to be used as the aerial platform (Frankenberg *et al*., 2018; Headwall Photonics, 2021; Specim, 2022).

In recent years, there has been rapid progress in the use of hyperspectral imaging sensors with narrow-band SRs in the 4–6-nm FWHM range, in conjunction with drones and lightweight aircraft (Aasen *et al*., 2018). A variety of compact, lightweight, and low-cost narrow-band hyperspectral imaging sensors in the visible and near-infrared spectral range (400–1000 nm) are now widely available, such as Specim FX10 (5.5-nm FWHM, SPECIM, Spectral Imaging Ltd., Oulu, Finland), Micro- and Nano-Hyperspec (5.8- and 6-nm FWHM, respectively, Headwall Photonics Inc., Boston, MA, USA), Pika L and Pika XC2 (3.3- and 1.9-nm FWHM, respectively, Resonon Inc., Bozeman, MT, USA), and FireflEYE 185 (8-nm FWHM, Cubert GmbH, Ulm, Baden-Württemberg, Germany), among others. These sensors have the capability of retrieving narrow-band hyperspectral vegetation indices and estimating numerous plant functional traits, which could provide substantial insight into the health of the plant. Furthermore, these sensors can be mounted on either piloted or non-piloted airborne platforms. These standard narrow-band hyperspectral imagers could provide a cost-effective

and more operationally viable alternative to sub-nanometer imagers for quantifying far-red SIF, hereafter SIF_{760}. Several past studies have demonstrated the utility of relative SIF_{760} levels derived from narrow-band imaging sensors for a variety of applications, such as biotic-induced stress detection (Calderón *et al*., 2015; 2013; Hernández-Clemente *et al*., 2017; Hornero *et al*., 2021; Poblete *et al*., 2021; 2020; Zarco-Tejada *et al*., 2021; 2018), water stress detection (Camino *et al*., 2018a; Panigada *et al*., 2014; Zarco-Tejada *et al*., 2012), plant phenotyping (Camino *et al*., 2019; 2018b; Gonzalez-Dugo *et al*., 2015), nutrient assessment (Longmire *et al*., 2022; Y. Wang *et al*., 2022; Watt *et al*., 2020) and its link with gross primary production (GPP) (Damm *et* al., 2015; Zarco-Tejada *et al*., 2013). More recently, Belwalkar *et al*. (2022) found strong correlations between airborne SIF_{760} estimates from a narrow-band hyperspectral imager with 5.8-nm FWHM and sub-nanometer SIF_{760} estimates acquired concurrently using an airborne sub-nanometer hyperspectral imager with ≤0.2-nm FWHM and a ground-based spectrometer with 0.065-nm FWHM. Although narrow-band SIF_{760} estimates were larger than sub-nanometer SIF_{760} estimates (root mean square error, RMSE = 3.28–4.69 $mW/m^2/nm/sr$), SIF_{760} levels estimated from both airborne sensors were strongly correlated (R^2 = 0.77–0.9) across multiple experimental sites. Thus, we hypothesise that spectrally scaling narrow-band SIF_{760} imaging to finer resolutions using physically-based models could facilitate the quantification of absolute SIF_{760} levels at finer spatial resolutions.

Due to the re-absorption and scattering of light within the leaves and canopy, plant pigments and canopy structure have strong effects on top-of-canopy (TOC) SIF (Dechant *et al*., 2020; Migliavacca *et al*., 2017; Porcar-Castell *et al*., 2014; Van der Tol *et al*., 2016; Yang and Van der Tol, 2018; Zeng *et al*., 2019). Previous studies using physically-based models successfully accounted for these light re-absorption and scattering effects when downscaling SIF from the canopy level to the leaf level (Liu *et al*., 2019; Romero *et al*., 2020; 2018; Yang and Van der Tol, 2018). In addition, prior studies have demonstrated that SIF spectra and vegetation biophysical traits can be retrieved simultaneously, either with radiative transfer model (RTM) inversion alone (Celesti *et al*., 2018;

Verhoef *et al*., 2018) or through RTM combined with machine learning modelling (Scodellaro *et al*., 2022). The widely used RTM Soil-Canopy-Observation of Photosynthesis and Energy fluxes (SCOPE) (Van der Tol *et al.*, 2009) can model light re-absorption and scattering mechanisms while taking canopy structure into consideration. A sensitivity analysis of the SCOPE model revealed that canopy structure and leaf optical properties primarily determine TOC SIF variability when considering only vegetation parameters (Verrelst *et al*., 2015). Consequently, the interpretation of narrow-band SIF_{760} estimates could be improved by including plant trait information derived from RTMs, such as SCOPE. We hypothesise that incorporating canopy structure and pigment content parameters through the SCOPE-based modelling approach could potentially aid in the estimation of SIF_{760} at finer spectral resolution from narrow-band resolution sensors, enabling retrieval of appropriate absolute SIF_{760} levels in physical units.

Although Belwalkar *et al*. (2022) demonstrated significant correlations between SIF_{760} estimates derived from narrow-band and sub-nanometer airborne hyperspectral imagers flown in tandem, these narrow-band SIF_{760} estimates were accurate only in relative terms, and their conversion to absolute SIF_{760} levels in physical units required further investigation. Furthermore, several prior studies have demonstrated that sensors with broader spectral specifications overestimate SIF_{760} (Damm *et al*., 2015; Julitta *et al*., 2016; Maimaitiyiming *et al*., 2020; Nichol *et al*., 2019; Süß *et al*., 2016). The magnitude of this bias depends on both the spectral resolution and the spectral sampling interval of the instrument, and additional modelling is needed for accurate SIF quantification in practical applications. Although previous studies have demonstrated the impact of the spectral resolution on SIF (Belwalkar *et al*., 2022; Cendrero-Mateo *et al*., 2019; Damm *et al*., 2011; Julitta *et al*., 2016; Liu *et al*., 2015), they have mostly focused on modelling efforts and on hand-held spectrometer data collected at the near-field scale. There is a lack of research focusing on assessing the impact of SR and SSI on SIF from airborne narrow-band imaging sensors under ambient field conditions. Studies carried out under such conditions with operational sensors will make progress on

the operational use of cost-efficient and simpler sensors for fluorescence quantification and photosynthesis assessment.

Our study extends the prior work of Belwalkar *et al*. (2022) by modelling the effect of SR on narrow-band SIF_{760} estimations to optimise their interpretation, with the intention of addressing the limitations associated with the absolute SIF_{760} levels quantified from narrow-band airborne hyperspectral imagers. We used an empirical approach based on SCOPE modelling and Support Vector Regression (SVR) to estimate SIF_{760} at a finer target resolution. Due to SCOPE's default spectral characteristics and the experimental results of Julitta *et al*. (2016) indicating that spectrometers with FWHM $\leq$ 1 nm can estimate the absolute value of SIF_{760}, we selected 1-nm FWHM as the target resolution for validation purposes. Input data consisted of 5.8-nm FWHM resolution narrow-band airborne hyperspectral imager data deriving SIF_{760} and SCOPE model inverted leaf biochemical and structural traits as predictor variables.

3.2 Materials and methods

3.2.1 Study sites

The study was conducted at two sites in Victoria, Australia (Fig. 3-1). Site 1 was located in Yarrawonga (36°02′55″S, 145°59′02″) and was planted with several varieties of rainfed wheat grown under various physiological conditions and fertilisation treatments. The airborne campaign was conducted during grain filling in 2019 (Fig. 3-1a). Plots were 26 m^2 (2 m × 13 m) in size and were planted in May 2019. The second trial site (Site 2) was managed under irrigated conditions using an overhead pivot in Peechelba East (36°10′04"S, 146°16′23"E) in 2021. A single variety of maize (Pioneer Hybrid 1756) was grown across the entire experimental field under different nitrogen fertiliser application rates. The growth stage during the airborne campaign corresponded to silking (Fig. 3-1b). Plots measured 36 m^2 (3 m × 12 m) and were planted in October 2020.

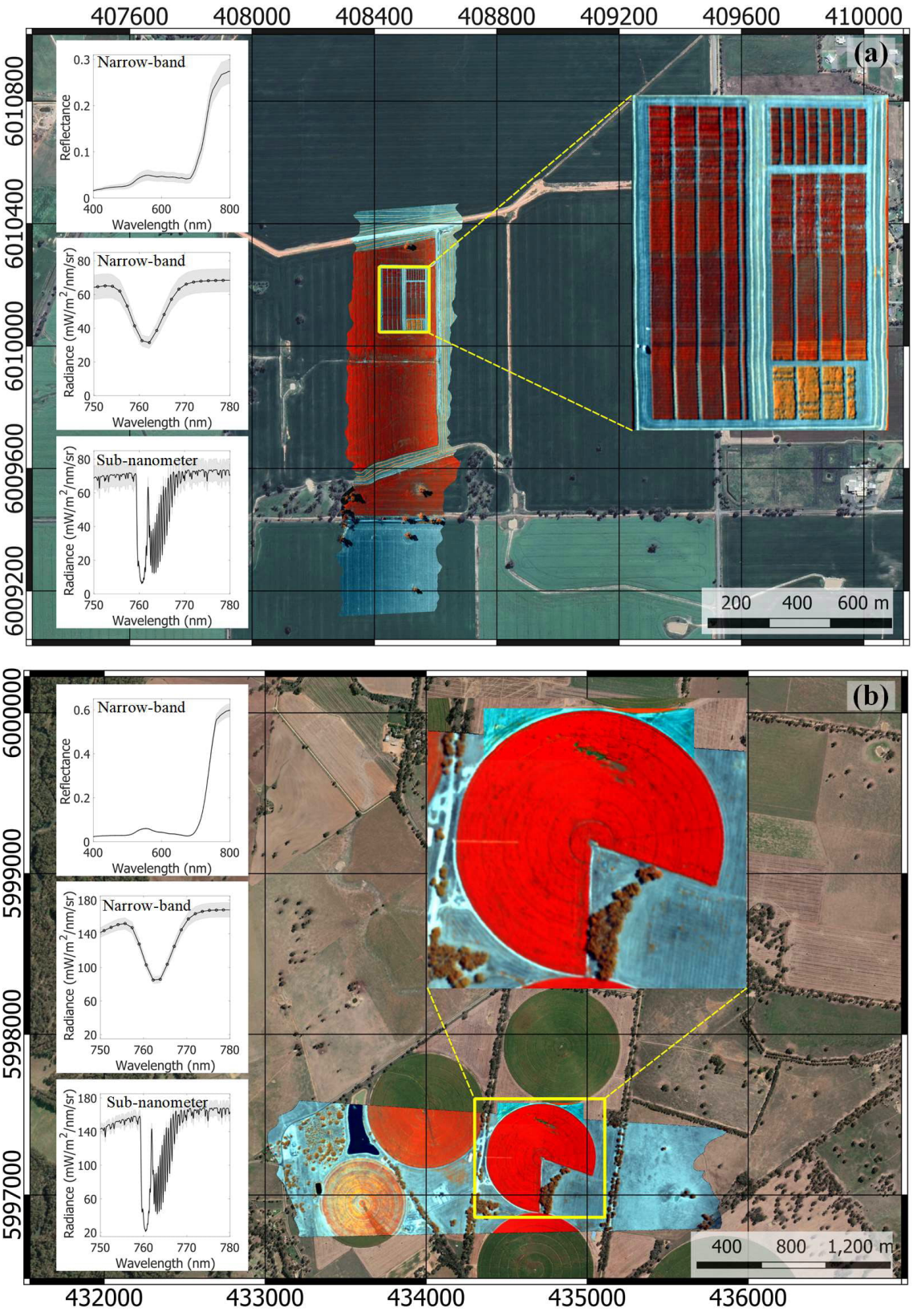

Fig. 3-1. Overview of experimental fields at Sites 1 (a) and 2 (b) acquired with the narrow-band hyperspectral imager (composite: 760 (R), 710 (G), and 680 (B) nm). The black lines correspond to the average radiance spectra in the O_2-A absorption region used for SIF quantification and the average reflectance spectra in the 400–800-nm spectral region used for plant trait estimation for all plots. Shaded areas in the reflectance and radiance plots represent the ±1 standard deviation of the average reflectance and radiance.

At both trial sites, leaf measurements were carried out in the field simultaneously with airborne campaigns. Handheld leaf-clip sensors (Dualex, FORCE-A, Orsay, France and FluorPen FP110-LM, Photon Systems Instruments, Drásov, Czech Republic) were used to measure leaf chlorophyll content, nitrogen balance index (NBI), flavonol content, anthocyanin content, and steady-state leaf fluorescence yield (F_t). Details of leaf-level measurements can be found in Belwalkar *et al.* (2022). A portable weather station (model WXT510, Vaisala, Helsinki, Finland) was set up for concurrent readings of meteorological conditions (air temperature and air pressure) during the hyperspectral image acquisition over both of the trial sites. The total incoming irradiance (E) was measured continuously during flights with a 0.065-nm FWHM HR-2000 spectrometer (Ocean Insight, Dunedin, FL, USA) set up at each field site. The spectrometer at Site 1 was equipped with a CC-3 VIS-NIR cosine corrector-diffuser probe, whereas at Site 2, irradiance was measured using the radiance (L) reflected from a white reference panel (Labsphere Inc., North Sutton, NH, USA). The irradiance measured from the HR-2000 spectrometer was calibrated using coefficients derived from a uniform calibrated light source and an integrating sphere (Labsphere XTH2000C, Labsphere Inc., North Sutton, NH, USA).

3.2.2 Hyperspectral airborne campaigns

For both airborne campaigns, two hyperspectral imagers were flown in tandem on a Cessna 172R operated by the HyperSens Laboratory, the University of Melbourne's Airborne Remote Sensing Facility, to acquire high-resolution hyperspectral imagery over the two study sites. The first hyperspectral imager (Hyperspec VNIR E-Series model, Headwall Photonics, Fitchburg, MA, USA) captured images in the 400–1000-nm spectral range with 5.8-nm FWHM resolution, and the second hyperspectral imager (Hyperspec Solar-Induced Fluorescence Imaging sensor, Headwall Photonics, Fitchburg, MA, USA) operated in the 670–780-nm spectral range with ≤0.2-nm FWHM resolution. Further technical details of the imaging and flight data can be found in Table 3-1.

Table 3-1. Spectral characteristics of hyperspectral imagers and acquisition details

Characteristics of hyperspectral imagers		
	VNIR E-Series (Narrow-band)	**Solar-Induced Fluorescence Imaging (Sub-nanometer)**
Spectral range	400–1000 nm	670–780 nm
Number of spectral bands	371	2160
Spectral sampling interval (SSI)	1.626 nm	0.051 nm
FWHM	5.8 nm	≤0.2 nm
Number of un-binned spatial pixels	1600	1600
Signal-to-noise ratio (SNR)	>300:1*	>300:1*
Field of view	66°	23.5°
Radiometric resolution	16	16
Image acquisition details		
	Site 1	**Site 2**
Acquisition dates	9th October 2019, 15:40 – 16:30 (local time)	20th January 2021, 11:40 – 12:20 (local time)
Flight altitude (above ground level)	400 m (VNIR imager) 900 m (Fluorescence imager)	1200 m (both imagers)
Mean spatial resolution	0.2 m (both imagers)	0.7 m (VNIR imager) 0.3 m (Fluorescence imager)

*Applicable only for plot-level mean radiance/reflectance computation

The radiometric calibration of the two hyperspectral imagers was performed by means of an integrating sphere (Labsphere XTH2000C) using coefficients derived from the calibrated light source at four different illumination levels. The SMARTS model (Gueymard, 2001) was used to perform atmospheric correction for the VNIR E-Series (narrow-band) imager to convert radiance images to reflectance images. Aerosol optical depth measurements in the 440-, 500-, 675-, 870-, and 936-nm spectral bands obtained from a Microtops II sun photometer (Solar Light Co., Philadelphia, PA, USA) and meteorological measurements from the portable weather station were used for input parameters. Hyperspectral images were ortho-rectified using inertial measurement units and GPS data (VN-300-VectorNav Technologies LLC, Dallas, TX, USA for the narrow-band imager and Trimble APX-15 UAV, Applanix Corporation, Ontario, Canada for the sub-nanometer imager) recorded during the flights using the Parametric Geocoding & Ortho-rectification for Airborne Optical Scanner Data

software (PARGE, ReSe Applications Schläpfer, Wil, Switzerland). Additional information on data pre-processing and image correction can be found in Zarco-Tejada *et al*. (2016).

We used the Normalised Difference Vegetation Index (NDVI) as a thresholding strategy to identify vegetational pixels within each plot, as described in Belwalkar *et al*. (2022). Mean radiance from both narrow-band and sub-nanometer imagers and reflectance spectra from the narrow-band imager were calculated for each plot by averaging all selected vegetation pixels, excluding the boundary pixels (Belwalkar *et al*., 2022). The average radiance spectra from the narrow-band hyperspectral imager (Fig. 3-1) were used to quantify SIF_{760} using the O_2-A band *in-filling* approach, employing the Fraunhofer Line Depth (FLD) principle (Plascyk, 1975) and a total of three spectral bands (3FLD) (Maier *et al*., 2003), named here as $SIF_{760\text{-}3FLD}$. The irradiance measured from HR-2000 spectrometer was convolved assuming a Gaussian band spectral response function of 5.8-nm FWHM resolution to match the spectral characteristics of the narrow-band hyperspectral imager. The '*in*' E and L were selected as the E/L minima in the 755–765-nm spectral region, while the '*out*' E and L were selected as the weighted mean of E/L local maxima in the 750–759-nm and 771–780-nm spectral regions, respectively. In case of multiple local maxima within the spectral regions, the local maximum closest to the '*in*' band was selected (Cendrero-Mateo *et al*., 2019). The airborne $SIF_{760\text{-}3FLD}$ was further corrected using non-fluorescent soil targets identified in the imagery and then normalised using a reflectance-based angular normalisation approach (Hao *et al*., 2021) to account for atmospheric and directional effects as described in Belwalkar *et al.* (2022).

3.2.3 Modelling methods

3.2.3.1 SCOPE model simulations

The SCOPE model (version 2.0) (Yang *et al*., 2021) was used to account for the effect of the sensor's spectral resolution on SIF_{760} quantification. SCOPE simulations were used in two stages: 1) a theoretical sensitivity analysis of the effect of plant traits on the inter-relationship between $SIF_{760\text{-}}$

$_{3FLD}$ and SR, and 2) the development of a machine learning–based estimation model to scale narrow-band $SIF_{760\text{-}3FLD}$ estimates to 1-nm FWHM resolution.

In the first stage, a local sensitivity analysis was used to determine how individual plant traits independently affect $SIF_{760\text{-}3FLD}$ estimates from narrow-band hyperspectral imagery. This differs from previous modelling-based studies (Damm *et al*., 2011; Liu *et al*., 2015) that varied multiple plant traits simultaneously. In simulations for Stage 1, the plant traits leaf chlorophyll content (C_{a+b}), leaf area index (LAI), leaf inclination distribution function ($LIDF_a$), and maximum rate of carboxylation (Vcmax) were selected for analysis based on their association with SIF variability in a global SCOPE-sensitivity study (Verrelst *et al*., 2015). SCOPE simulations at the default 1-nm FWHM and 1-nm SSI were generated by randomly varying input parameters drawn from a uniform distribution within the following ranges: C_{a+b} (10–50), LAI (1–5), $LIDF_a$ (–0.8–0.8), and Vcmax (40–200). A total of 1000 simulations (Simulated Dataset-1) were obtained for each trait while holding other parameters constant. All other SCOPE inputs were set at their default values. SCOPE simulations were then convolved to match the SR, SSI, and band centres of the narrow-band hyperspectral image, assuming a Gaussian band spectral response function. $SIF_{760\text{-}3FLD}$ was estimated from simulated irradiance and TOC total upwelling radiance at both 1- and 5.8-nm FWHM resolutions following the same methodology outlined in Section 2.2 and compared across simulations of the four leaf biochemical and structural traits.

Stage 2 consisted of using SCOPE model simulations to develop prediction models for estimating SIF_{760} at 1-nm FWHM resolution from narrow-band resolution spectra (Fig. 3-2). Due to differences in crop type, crop growth stage, image acquisition time, and meteorological conditions between the two study sites, SCOPE simulations were conducted separately for each study site. An alternative strategy would have been to generate a global SCOPE-simulated data set that could be applied to any study site. However, due to the complexity of SCOPE input parameters that would be needed for such a model (leaf, canopy, soil, and micrometeorology), we used site-specific simulations

based on spatially stable micrometeorological conditions likely to occur during airborne imaging sensor acquisition in practice (Verrelst *et al*., 2015).

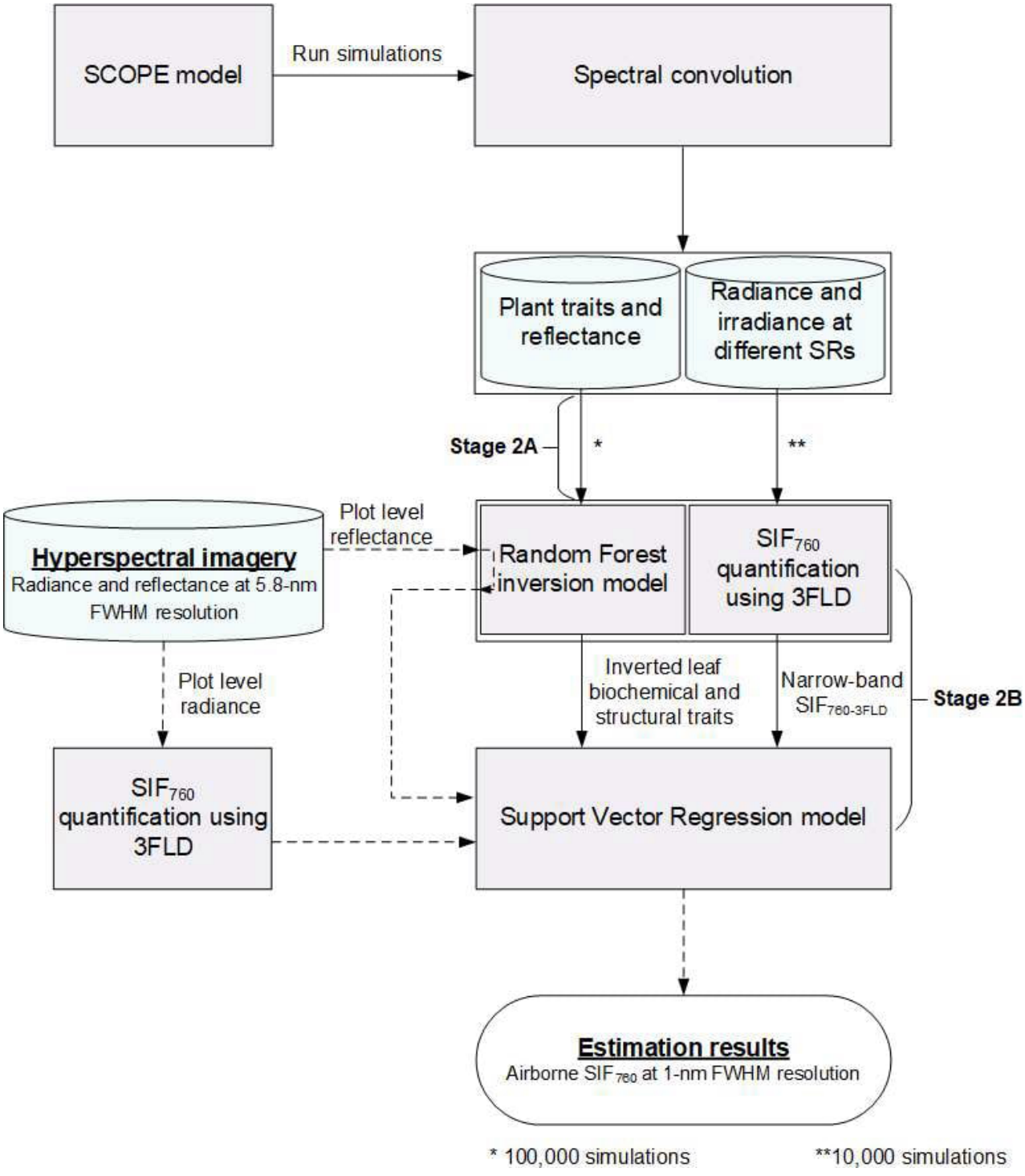

Fig. 3-2. Overview of the methodology used for estimating SIF_{760} at 1-nm FWHM from the narrow-band airborne hyperspectral imager.

Two distinct sets of simulations were generated for each study site, using parameter values drawn from random uniform distributions detailed in Table 3-2. The ranges of input parameters for the simulated datasets were determined using field measurements from each study site as well as estimates from the existing literature (detailed in Table B-1, Appendix B). The meteorological variables (air temperature and air pressure) were determined from the portable weather station. SCOPE defaults were used for other parameters and spectral characteristics. One dataset of 100,000 simulations (Simulated Dataset-$2_{site\ 1}$ and Simulated Dataset-$2_{site\ 2}$) was used for the estimation of plant traits (Stage 2A, Section 2.3.2). A second dataset of 10,000 simulations (Simulated Dataset-$3_{site\ 1}$ and Simulated Dataset-$3_{site\ 2}$) was used for SIF_{760} estimation at 1-nm FWHM resolution (Stage 2B, Section 2.3.3). As with other simulations, 1-nm SR outputs were convolved to match the spectral resolution of the narrow-band hyperspectral imager using a Gaussian spectral response function. Additionally, radiance and irradiance spectra were convolved to 2-, 3-, 4-, 5-, and 6-nm SR for Simulated Dataset-$2_{site\ 1}$ and Simulated Dataset-$3_{site\ 1}$ while maintaining the Nyquist criterion (SSI = SR/2) (Damm *et al*., 2011). A list of the SCOPE simulations used at each stage is provided in Table 3-3.

3.2.3.2 Plant trait estimation using RTM-based hybrid approach

In Stage 2A (Fig. 3-2), an RTM-based hybrid inversion method was used to estimate leaf biochemical and structural traits using the TOC reflectance spectra from the narrow-band imagery at both study sites. Only traits with the highest variable importance scores as determined by the predictor screening approach (detailed in Section 3.2.3.3) were estimated. A similar method combining RTMs and machine learning regression models, such as Gaussian process regression (GPR), support vector machines (SVMs), and random forest (RF), have successfully been used in previous studies to obtain plant traits from airborne and spaceborne hyperspectral imagery (Camino *et al*., 2021; Danner *et al*., 2021; De Grave *et al*. 2020; Poblete *et al*., 2021). A set of RF regression models (Camino *et al*., 2021; S. Wang *et al*., 2021) was trained using a look-up table containing 100,000 simulations corresponding

to Simulated Dataset-2 (Table-3-3) for each site. The simulated 5.8-nm FWHM reflectance spectra were used as inputs to the RF-inversion models, with each plant trait as output. RF-inversion models were also trained using 2-, 3-, 4-, 5-, and 6-nm SR data from Simulated Dataset-$2_{site\ 1}$. RF-inversion models were trained in parallel (MATLAB parallel computing toolbox) with 10-fold cross-validation. Hyperparameters were optimised using Bayesian optimisation (Mockus, 2012) in MATLAB during training (MATLAB; Statistics and Machine Learning toolbox; MathWorks Inc., Natick, MA, USA). Finally, the trained RF-inversion models were used to predict plant traits using narrow-band airborne reflectance imagery (Fig. 3-1) at the plot level.

Table 3-2. Range of SCOPE input parameters used in this study

Parameter	Range/Value		Unit	Description
	Site 1	Site 2		
C_{a+b}	10–70	40–80	$\mu g \cdot cm^{-2}$	Leaf chlorophyll concentration
C_{ca}	1–20	1–20	$\mu g \cdot cm^{-2}$	Leaf carotenoid concentration
C_{ant}	0–8	0–8	$\mu g \cdot cm^{-2}$	Anthocyanin content
C_{dm}	0.001–0.05	0–0.001	$g \cdot m^{-2}$	Dry matter content
C_w	0.001–0.05	0.001–0.05	Cm	Leaf water equivalent layer
N	1–1.5	1–2.5	–	Leaf thickness parameters
Vcmax	30–110	40–250	$\mu mol \cdot m^{-1} \cdot s^{-1}$	Maximum carboxylation capacity at 25°C
LAI	0.5–5	2–6	$m^2 \cdot m^{-2}$	Leaf area index
$LIDF_a$	−1–1	−1–1	–	Leaf inclination parameter for the mean leaf zenith angle
$LIDF_b$	0	0	–	Bimodality of the leaf angle distribution
R_{in}	700	900	$W \cdot m^{-2}$	Broadband incoming shortwave radiation
Ta*	19.2	25.3	°C	Air temperature
p*	1002.8	1003.6	hPa	Air pressure
tts	35.42	34.93	deg.	Solar zenith angle

* Meteorological variables retrieved from portable weather station during the airborne campaign

3.2.3.3. SIF estimation at 1-nm FWHM using the support vector regression model

In Stage 2B (Fig. 3-2), a simulated SIF training dataset comprising $SIF_{760\text{-}3FLD}$ values corresponding to 1-, 2-, 3-, 4-, 5-, 6-, and 5.8-nm FWHM for Site 1 and $SIF_{760\text{-}3FLD}$ values corresponding to 1- and 5.8-nm FWHM for Site 2 was generated using TOC radiance and irradiance

corresponding to Simulated Dataset-$3_{site\ 1}$ and Simulated Dataset-$3_{site\ 2}$, respectively (Table 3-3). $SIF_{760\text{-}3FLD}$ for all SCOPE simulated data was computed following the same methodology as outlined in section 2.2. We evaluated two sets of models for estimating 1-nm SR SIF_{760} from the narrow-band resolution spectra. The first model, referred to as the linear model, used the slope and intercept of the linear relationship between convolved coarse-SR $SIF_{760\text{-}3FLD}$ and 1-nm SR $SIF_{760\text{-}3FLD}$ from the simulated SIF training dataset. The second model used an SVR algorithm as detailed below.

Table 3-3. Description of the SCOPE simulations used in this study

Stage	Dataset (Simulation count)	Data type	Objective
1	Simulated Dataset-1 (1,000)	Radiance and irradiance	Assessment of the impact of leaf biochemical and structural traits on $SIF_{760\text{-}3FLD}$ relationships across two different SRs
2A	Simulated Dataset-2 (100,000)	Reflectance	Development of hybrid inversion models for plant traits estimation
2B	Simulated Dataset-3 (10,000)	Radiance, irradiance and reflectance	Development of SVR models to estimate SIF_{760} at 1-nm FWHM
Validation	Simulated Dataset-4 (50,000)	Radiance, irradiance and reflectance	Quantitative evaluation of different SIF_{760} estimation models

First, for each of the six SRs corresponding to the Simulated Dataset-$3_{site\ 1}$, we selected inputs for SVR models from a pool of eight potential predictor variables: seven SCOPE plant traits and the corresponding narrow-band $SIF_{760\text{-}3FLD}$. Candidate plant traits included leaf water content (C_w), leaf dry matter content (C_{dm}), the mesophyll structural parameter (N), C_{a+b}, LAI, $LIDF_a$, and Vcmax. Potential predictors were screened using variable importance scores from an RF model fit to 1-nm SR SIF_{760} data using the 'oobPermutedPredictorImportance' function in MATLAB (Schneider *et al*., 2020; Thomas *et al*., 2021), which generates permutations of out-of-bag (OOB) observations from regression trees and evaluates their impact on prediction. The four predictors with the highest scores were selected as SVR model inputs. Several SVR models were then built with all possible permutations of this subset of predictors, with the inclusion of narrow-band $SIF_{760\text{-}3FLD}$ as a required predictor variable for each model. Plant trait inputs required for SVR models were derived from the

simulated reflectance corresponding to Simulated dataset-3 using the RF-inversion models built in Stage 2A. SVR models were trained in parallel using the MATLAB parallel computing toolbox with 10-fold cross-validation, and the hyperparameters were optimised during training using Bayesian optimisation.

For each site, an independent test dataset using 50,000 SCOPE simulations (Simulated Dataset-4) was used to evaluate the SIF_{760} estimation models (Table 3-3). This dataset was generated using the same input parameter ranges (Table 3-2) and methodology described in sections 2.3.1 and 2.3.2. Plot-level 1-nm SR SIF_{760} estimated from regression models was compared to the SCOPE-simulated reference $SIF_{760\text{-}3FLD}$ using coefficient of determination (R^2), root mean square error (RMSE), and normalised root mean square error (nRMSE) as evaluation metrics. The nRMSE was computed as the ratio of RMSE and mean of reference $SIF_{760\text{-}3FLD}$. Regression model predictions were also generated for the airborne datasets at both study sites, using the estimated plant traits and $SIF_{760\text{-}3FLD}$ quantified from 5.8-nm FWHM narrow-band imagery as inputs. The performance evaluation of the regression models for the airborne datasets was conducted using sub-nanometer-resolution airborne hyperspectral imagery acquired concurrently with narrow-band resolution imagery. The sub-nanometer resolution radiance spectra corresponding to the selected validation plots (as in Belwalkar *et al.*, 2022) were convolved to the default SCOPE spectral characteristics to compute 1-nm SR $SIF_{760\text{-}3FLD}$, which served as a reference to validate the estimated 1-nm SR SIF_{760} from the 5.8-nm FWHM resolution narrow-band hyperspectral imager. The computation of 1-nm SR $SIF_{760\text{-}3FLD}$ from the convolved sub-nanometer-resolution airborne spectra was carried out following the same procedure as outlined in Section 2.2 for quantifying $SIF_{760\text{-}3FLD}$ from the narrow-band hyperspectral imager.

Airborne datasets corresponding to the other five narrow-band SRs were not available for the evaluation of best-performing regression models for SIF_{760} estimation at 1-nm FWHM resolution. Therefore, sub-nanometer resolution airborne radiance spectra and ground-based irradiance spectra

for Site 1 were convolved to generate $SIF_{760\text{-}3FLD}$ at these SRs, with SSI following the Nyquist criterion. Because the sub-nanometer and narrow-band hyperspectral imagers were flown in tandem, the estimates of plant traits that were obtained from the narrow-band hyperspectral imager at Site 1 were used as the other three inputs in the SVR model.

3.3 Results

The sensitivity of the relationship between SCOPE-derived $SIF_{760\text{-}3FLD}$ at different SRs to leaf biochemical and structural traits is presented in Fig. 3-3. Overall, $SIF_{760\text{-}3FLD}$ increased with increasing values of C_{a+b}, LAI, $LIDF_a$, and Vcmax for all scenarios; however, the relationship between SIF at 1- and 5.8-nm SRs varied widely across simulations. Narrow-band $SIF_{760\text{-}3FLD}$ tended to be overestimated as plant trait parameters increased, with a non-linear response to changing C_{a+b} (Fig. 3-3a-c) and LAI (Fig. 3-3d-f), but a linear response to varying $LIDF_a$ (Fig. 3-3g-i) and Vcmax (Fig. 3-3j-l).

Narrow-band $SIF_{760\text{-}3FLD}$, $LIDF_a$, C_{a+b}, and LAI were identified as the most important parameters for 1-nm SR SIF_{760} estimation, with a combined importance of close to 95% (Fig. 3-4). The ranges of values for the three most important plant traits (C_{a+b}, LAI, and $LIDF_a$) estimated via the SCOPE-based hybrid inversion approach are shown in Fig. 3-5. The substantial differences in estimated plant traits between the two study sites can be attributed to differences in crop type, irrigation regime, and weather. All three estimated plant traits were more variable at Site 1 than at Site 2, as expected, given the use of multiple cultivars and a wider range of nitrogen treatments. The resulting plot-scale spatial variability associated with the estimated C_{a+b} and LAI within the entire experimental field at Site 1 is depicted in Fig. 3-6.

Validation statistics for models estimating 1-nm SR SIF_{760} based on SCOPE-simulated data are shown in Table 3-4A. The SVR model using 5.8-nm SR $SIF_{760\text{-}3FLD}$ and all three plant traits as

inputs performed the best at both Site 1 (nRMSE = 5.28%) and Site 2 (nRMSE = 2.45%). The subset of SVR models that included $LIDF_a$ as a predictor (Models 4, 6, 7, and 8 in Table 3-4A) performed best at Site 1 (nRMSE < 7%), while the subset of SVR models that included LAI as a predictor (Models 3, 5, 7, and 8 in Table 3-4A) performed best at Site 2 (nRMSE < 6%).

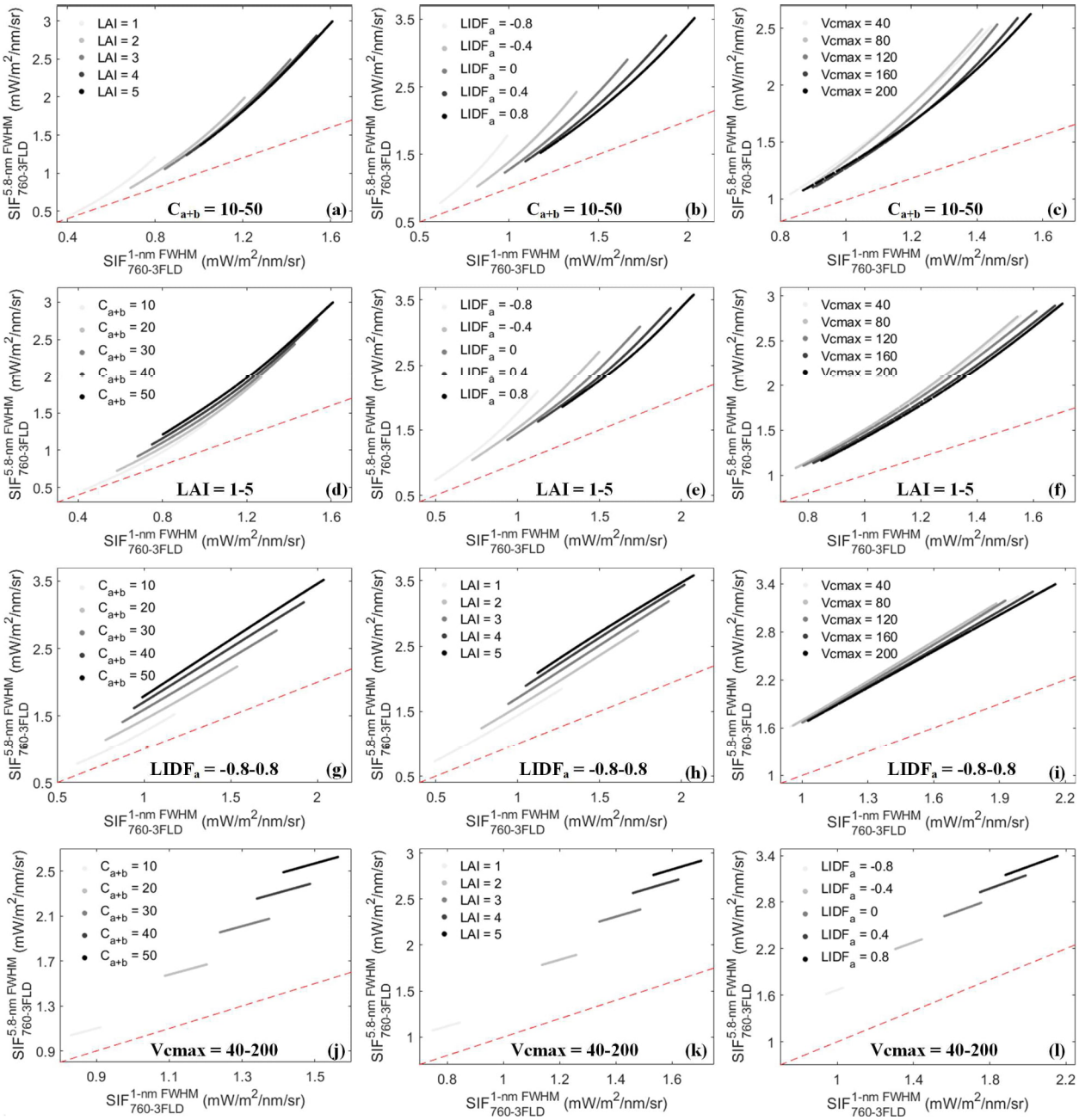

Fig. 3-3. Effects of leaf biochemical and structural traits on the relationship between SCOPE-simulated $SIF_{760\text{-}3FLD}$ at two different spectral resolutions. Traits include C_{a+b} (a-c), LAI (d-f), $LIDF_a$ (g-i), and Vcmax (j-l). All other SCOPE input parameters were left at their default settings. The dashed red line depicts the 1:1 line.

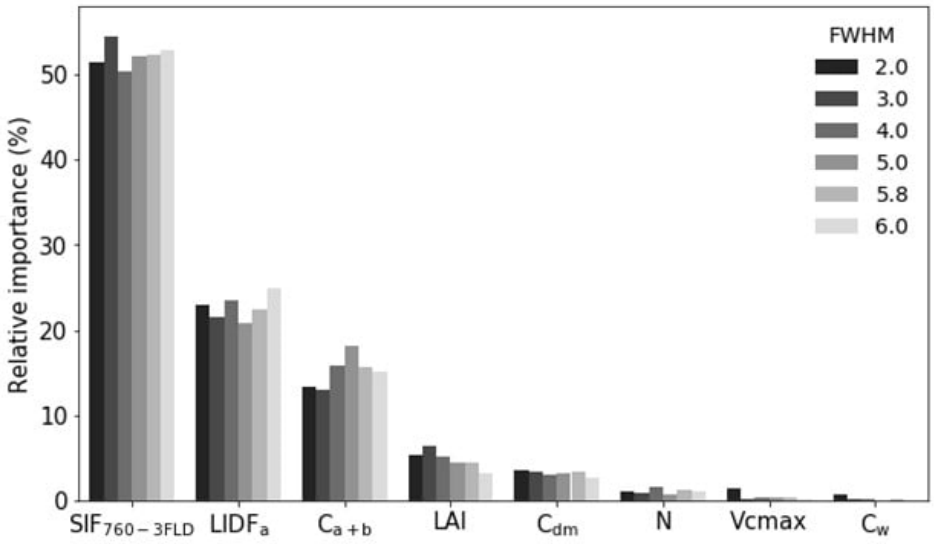

Fig. 3-4. Relative importance of the eight potential predictor variables at different SRs for estimating SIF_{760} at 1-nm FWHM using Simulated Dataset-$3_{site\ 1}$. The relative importance score was obtained using out-of-bag (OOB) error.

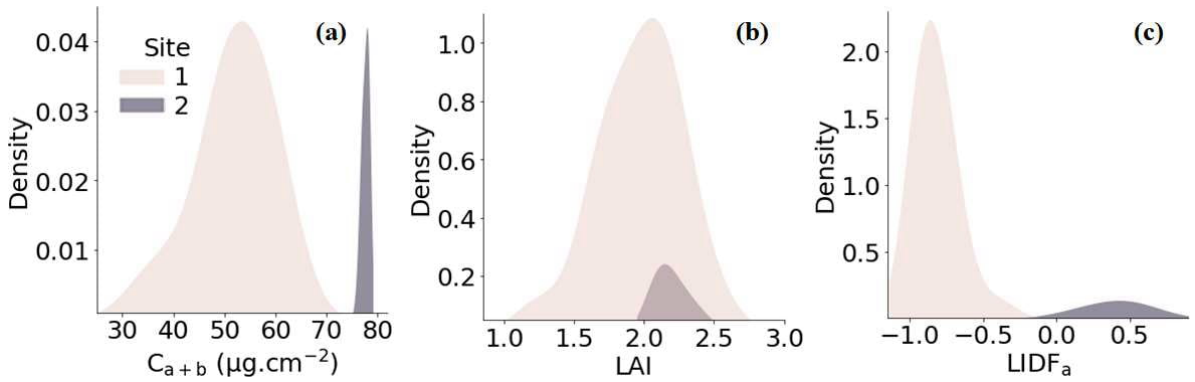

Fig. 3-5. Ranges of variation for the leaf biochemical and structural traits estimated from the narrow-band hyperspectral imagery at the two study sites: C_{a+b} (a), LAI (b), and $LIDF_a$ (c).

The performance of the linear and SVR models using airborne data corresponding to the validation plots is presented in Table 3-4B. As observed with the simulated datasets, the set of SVR models that included $LIDF_a$ at Site 1 and LAI at Site 2 performed better than models without these predictors. At Site 1, the SVR model including all four predictors (Model 8 in Table 3-4B) did not have the lowest nRMSE, unlike the results for the simulated datasets. However, the best-performing SVR model at Site 1 (Model 6 in Table 3-4B) had an nRMSE within 0.5% of the full model. Nevertheless, results for the full SVR model (Model 8 in Table 3-4) were relatively consistent for

simulated and airborne data across study sites. Thus, Model 8 was deemed the best-performing SVR model and was used exclusively for the remainder of the analysis.

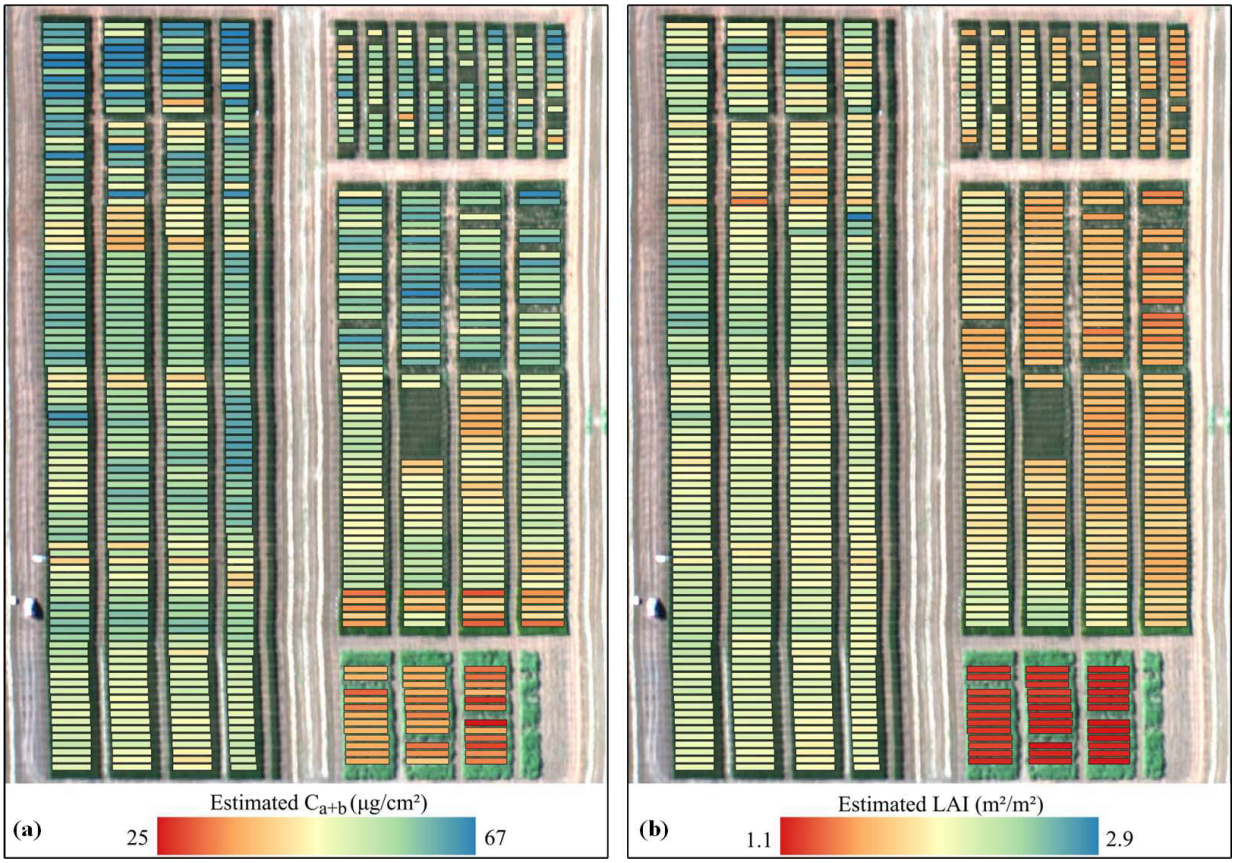

Fig. 3-6. Maps of estimated C_{a+b} (µg/cm^2) (a) and LAI (m^2/m^2) (b) at plot scale depicting the within-field variability at Site 1.

Comparisons between estimated and reference 1-nm SR SIF_{760} for the linear and the SVR models using SCOPE-simulated data are shown in Fig. 3-7. Both model estimates were significantly correlated with the reference values ($R^2 \geq 0.91$; $p < 0.001$; Fig. 3-7a and b), with most points located close to the 1:1 line. The SVR model performed better than the linear model, with an RMSE of less than 0.1 mW/m^2/nm/sr (Fig. 3-7c and d). We further evaluated the performance of the SIF_{760} scaling methodology using five other narrow-band SRs for Simulated Dataset-4 at Site 1. The estimates from both models were significantly correlated with reference values across narrow-band SRs ($R^2 \geq 0.94$; $p < 0.001$) (Fig. 3-8). RMSE values tended to increase as SR decreased for both linear (Fig. 3-8a-e) and SVR (Fig. 3-8f-j) models. The SVR model outperformed the linear model for all five narrow-

band SRs, with RMSEs ranging from 0.037–0.136 mW/m^2/nm/sr for the linear model and 0.027–0.076 mW/m^2/nm/sr for the SVR model.

Table 3-4. Performance of linear and SVR models built to estimate SIF_{760} at 1-nm FWHM resolution from the 5.8-nm FWHM resolution SCOPE-simulated and airborne datasets

Estimation model	Site 1		Site 2	
A: Simulated data	**RMSE**	**nRMSE**	**RMSE**	**nRMSE**
Linear Model: $SIF_{1\ nm} = f(SIF_{5.8\ nm})$	0.114	9.52%	0.243	7.13%
SVR Model 1: $SIF_{1\ nm} = f(SIF_{5.8\ nm})$	0.104	8.69%	0.229	6.72%
SVR Model 2: $SIF_{1\ nm} = f(SIF_{5.8\ nm}, C_{a+b})$	0.091	7.65%	0.216	6.33%
SVR Model 3: $SIF_{1\ nm} = f(SIF_{5.8\ nm}, LAI)$	0.100	8.40%	0.199	5.85%
SVR Model 4: $SIF_{1\ nm} = f(SIF_{5.8\ nm}, LIDF_a)$	0.076	6.39%	0.235	6.88%
SVR Model 5: $SIF_{1\ nm} = f(SIF_{5.8\ nm}, C_{a+b}, LAI)$	0.085	7.09%	0.124	3.63%
SVR Model 6: $SIF_{1\ nm} = f(SIF_{5.8\ nm}, C_{a+b}, LIDF_a)$	0.068	5.72%	0.212	6.22%
SVR Model 7: $SIF_{1\ nm} = f(SIF_{5.8\ nm}, LAI, LIDF_a)$	0.076	6.39%	0.178	5.22%
SVR Model 8: $SIF_{1\ nm} = f(SIF_{5.8\ nm}, C_{a+b}, LAI, LIDF_a)$	0.063	5.28%	0.084	2.45%
B: Airborne data				
Linear Model: $SIF_{1\ nm} = f(SIF_{5.8\ nm})$	0.517	30.35%	0.308	11.76%
SVR Model 1: $SIF_{1\ nm} = f(SIF_{5.8\ nm})$	0.413	24.25%	0.168	6.42%
SVR Model 2: $SIF_{1\ nm} = f(SIF_{5.8\ nm}, C_{a+b})$	0.387	22.70%	0.149	5.69%
SVR Model 3: $SIF_{1\ nm} = f(SIF_{5.8\ nm}, LAI)$	0.435	25.53%	0.151	5.79%
SVR Model 4: $SIF_{1\ nm} = f(SIF_{5.8\ nm}, LIDF_a)$	0.270	15.86%	0.141	5.39%
SVR Model 5: $SIF_{1\ nm} = f(SIF_{5.8\ nm}, C_{a+b}, LAI)$	0.426	24.96%	0.154	5.88%
SVR Model 6: $SIF_{1\ nm} = f(SIF_{5.8\ nm}, C_{a+b}, LIDF_a)$	0.265	15.53%	0.145	5.56%
SVR Model 7: $SIF_{1\ nm} = f(SIF_{5.8\ nm}, LAI, LIDF_a)$	0.266	15.60%	0.123	4.70%
SVR Model 8: $SIF_{1\ nm} = f(SIF_{5.8\ nm}, C_{a+b}, LAI, LIDF_a)$	0.273	16.00%	0.118	4.50%

The relationships between reference airborne 1-nm SR $SIF_{760\text{-}3FLD}$ and SIF_{760} estimated by the linear and SVR models are shown in Fig. 3-9. $SIF_{760\text{-}3FLD}$ estimates derived from the narrow-band imager were overestimated compared to the 1-nm SR reference (RMSE = 2.23 mW/m^2/nm/sr for Site 1 and RMSE = 2.117 mW/m^2/nm/sr for site 2) due to the spectral characteristics of the narrow-band imager. Nevertheless, narrow-band $SIF_{760\text{-}3FLD}$ was significantly correlated with the high-SR reference at both Site 1 ($R^2 = 0.93$, $p < 0.001$; Fig. 3-9a) and Site 2 ($R^2 = 0.95$, $p < 0.001$; Fig. 3-9b). The RMSEs for narrow-band SIF_{760} estimates scaled with both the linear and SVR models were less than 0.6 mW/m^2/nm/sr. The linear model overestimated 1-nm SR SIF_{760} at Site 1 (nRMSE = 30.35%;

Fig. 3-9c) and underestimated it at Site 2 (nRMSE = 11.76%; Fig. 3-9d). SIF_{760} estimated using the SVR model was more accurate at both sites (nRMSE = 16% for Site 1 and nRMSE = 4.5% for Site 2; Fig. 3-9e and f), with the majority of points near the 1:1 line. A plot-scale visualization of scaled SVR estimates from the narrow-band hyperspectral imager for the entire field at Site 1 is shown in Fig. 3-10.

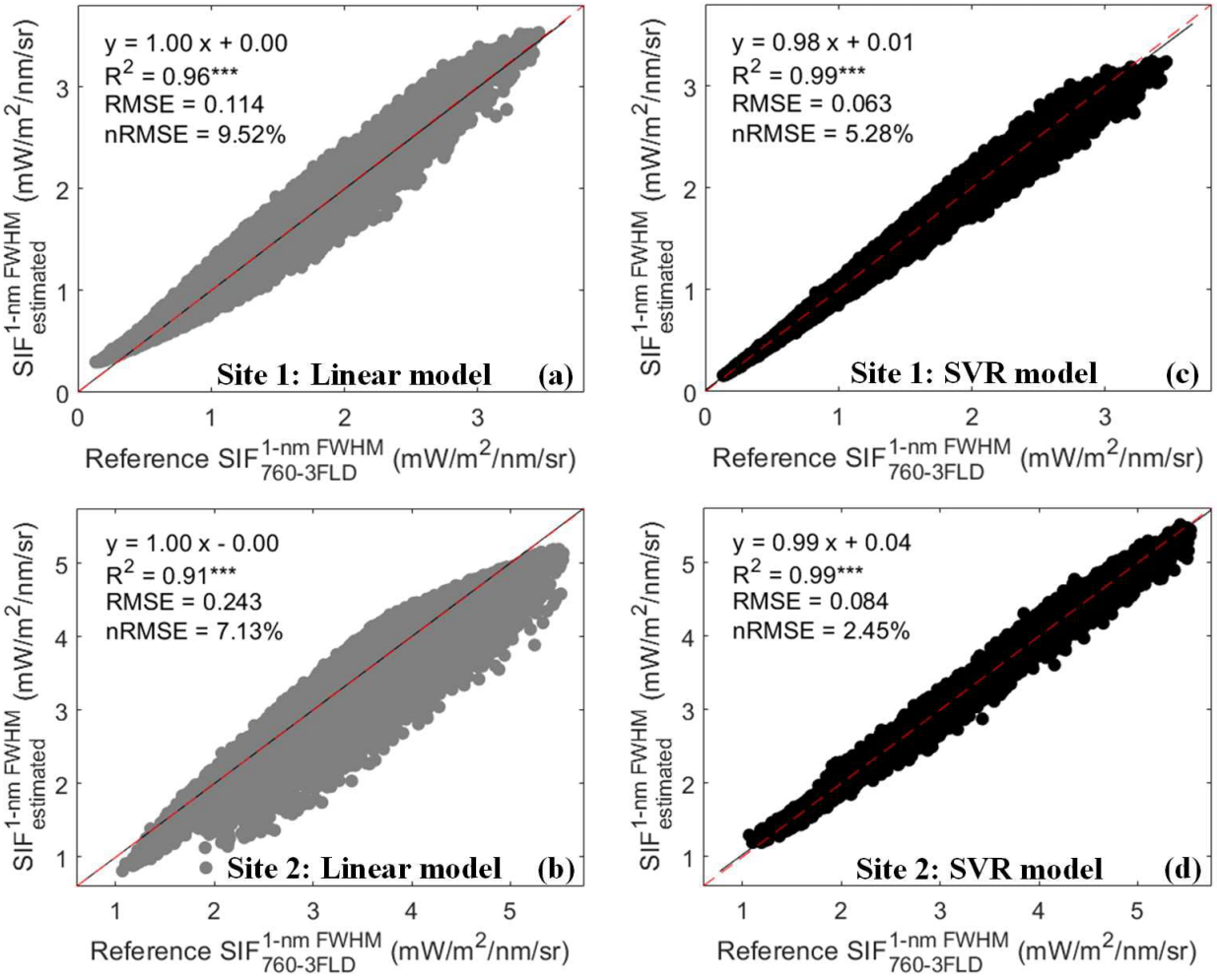

Fig. 3-7. Relationships between the $SIF_{760\text{-}3FLD}$ at the default 1-nm FWHM simulated by SCOPE (used here as the reference SIF) and the SIF_{760} estimated at 1-nm FWHM by the linear model (a, b) and by the SVR model (c, d) from 5.8-nm FWHM spectra for SCOPE-simulated test datasets corresponding to Site 1 and Site 2. The red dashed and black solid lines depict the 1:1 line and regression line, respectively. ****p*-value < 0.001.

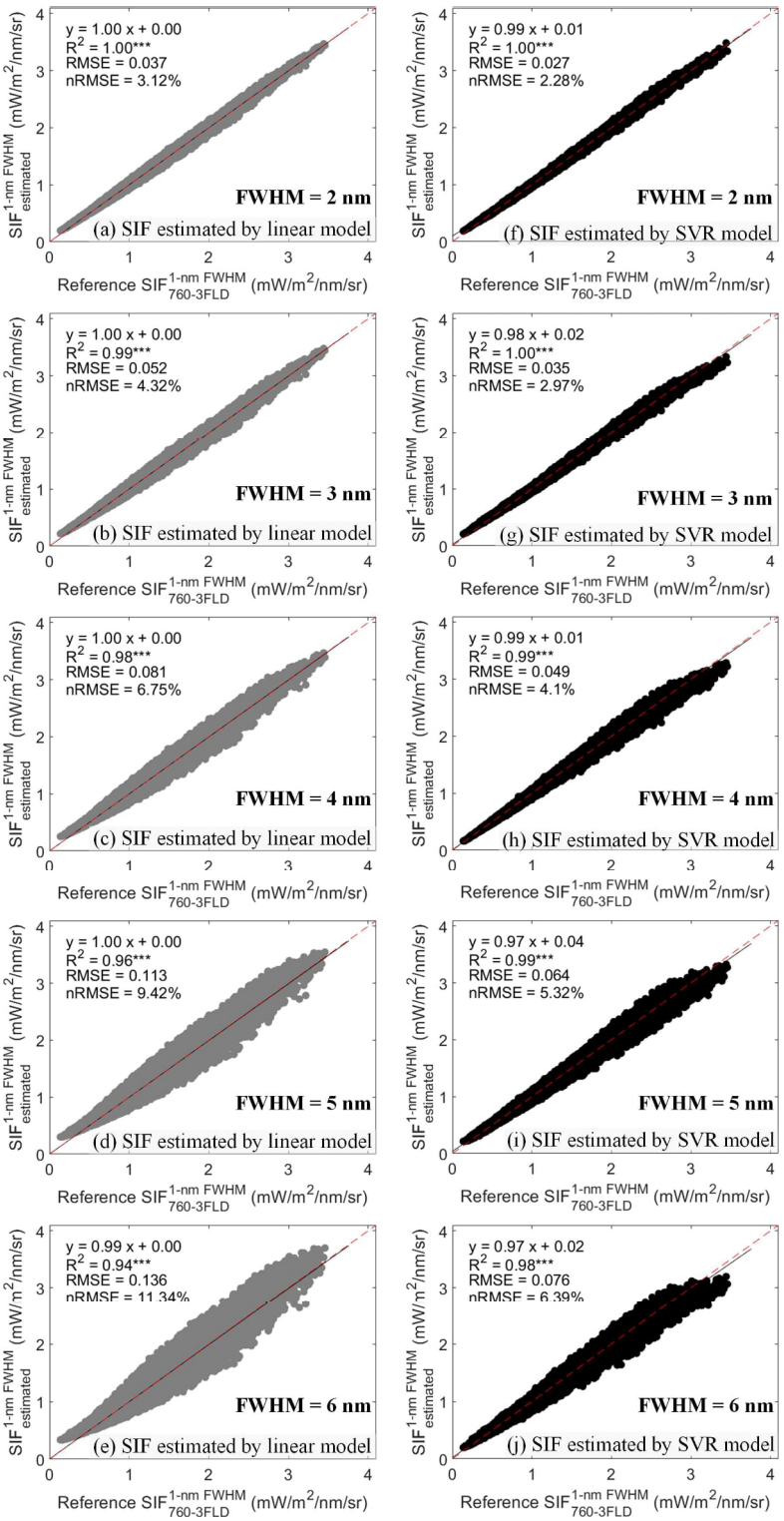

Fig. 3-8. Relationships between $SIF_{760\text{-}3FLD}$ at 1-nm FWHM simulated by SCOPE (used here as the reference SIF) and SIF_{760} estimated by the linear model (a-e) and by the SVR model (f-j) from different SRs for SCOPE-simulated test datasets corresponding to Site 1. SSI was related to SR according to the Nyquist criterion (SR = SSI×2). The red dashed and black solid lines depict the 1:1 line and regression line, respectively. ****p*-value < 0.001.

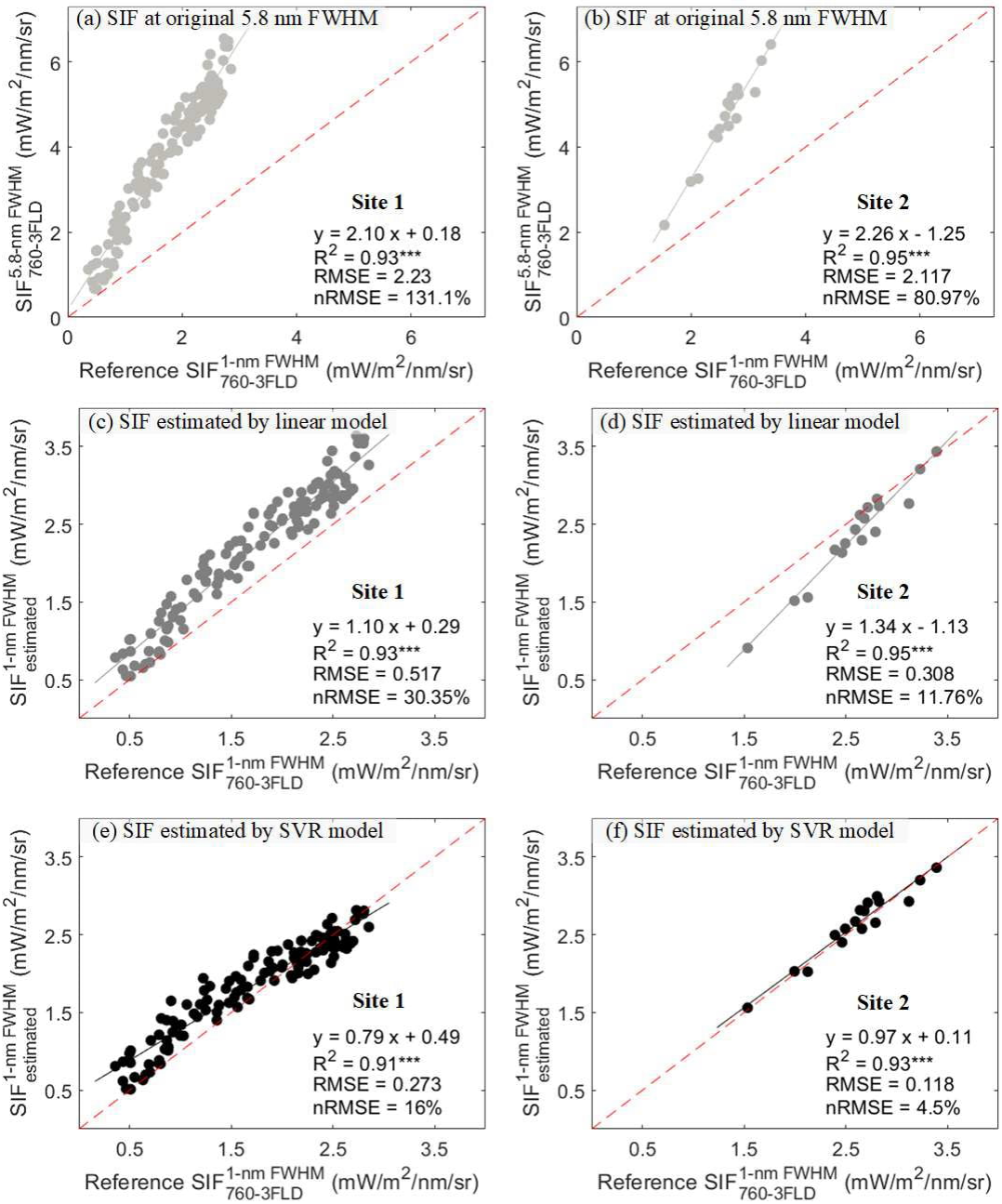

Fig. 3-9. Relationships between the airborne $SIF_{760\text{-}3FLD}$ quantified from the sub-nanometer imager (used here as the reference SIF) and narrow-band imager (5.8-nm FWHM) for validation plots corresponding to both sites (a,b). Relationships between the airborne $SIF_{760\text{-}3FLD}$ quantified from the sub-nanometer imager and the airborne 1-nm SR SIF_{760} estimated by the linear model (c,d) and SVR model (e,f) from the 5.8-nm SR narrow-band airborne spectra for both sites. The reference 1-nm SR $SIF_{760\text{-}3FLD}$ was obtained by convolving the sub-nanometer resolution spectra to 1-nm FWHM. The red dashed and black solid lines depict the 1:1 line and regression line, respectively. ***p-value < 0.001.

The relationships between the reference airborne 1-nm SR $SIF_{760\text{-}3FLD}$ and SIF_{760} estimated from multiple SRs are shown in Fig. 3-11. Significant correlations were found at all SRs (R^2 = 0.88–0.97, $p < 0.001$). At coarser resolutions, $SIF_{760\text{-}3FLD}$ estimates tended to be larger than reference values

(RMSE = 0.36–3.88 mW/m^2/nm/sr; Fig. 3-11a-e) and relationships to reference $SIF_{760\text{-}3FLD}$ were less linear. This non-linearity and higher absolute $SIF_{760\text{-}3FLD}$ values at coarser SRs can be attributed to sensor noise from the convolution of the 0.065-nm FWHM irradiance spectra from the ground-based HR-2000 spectrometer and the ≤0.2-nm FWHM radiance spectra from the sub-nanometer airborne imager. The process of Gaussian convolution influences the absolute $SIF_{760\text{-}3FLD}$ levels at narrow-band resolution and produces higher $SIF_{760\text{-}3FLD}$ levels in absolute units. Both linear (Fig. 3-11a-e) and SVR models reduced this bias (reduction in slope). The SVR model (nRMSE = 8.19–43.30%; Fig. 3-11k–o) outperformed the linear model (nRMSE = 8.30–68.64%; Fig. 3-11f–j) for all SRs. However, the estimated SIF_{760} from both models was higher than the reference $SIF_{760\text{-}3FLD}$, except for 2-nm SR, for which the points were close to the 1:1 line.

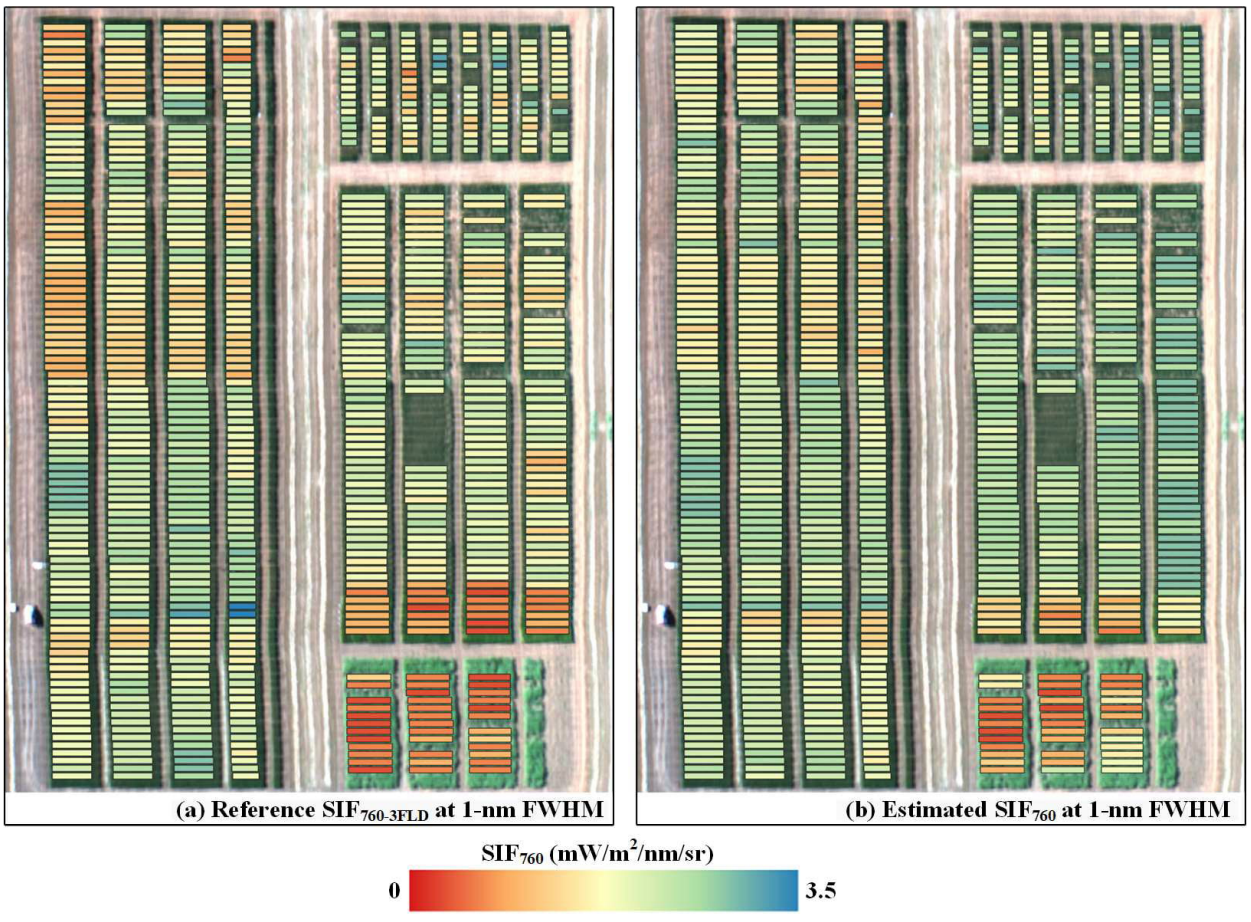

Fig. 3-10. Plot-scale maps of reference $SIF_{760\text{-}3FLD}$ from sub-nanometer imager (a) and estimated SIF_{760} from narrow-band imager (b) using the SVR model at 1-nm FWHM for Site 1. The reference 1-nm SR $SIF_{760\text{-}3FLD}$ was obtained by convolving the sub-nanometer resolution spectra to 1-nm FWHM.

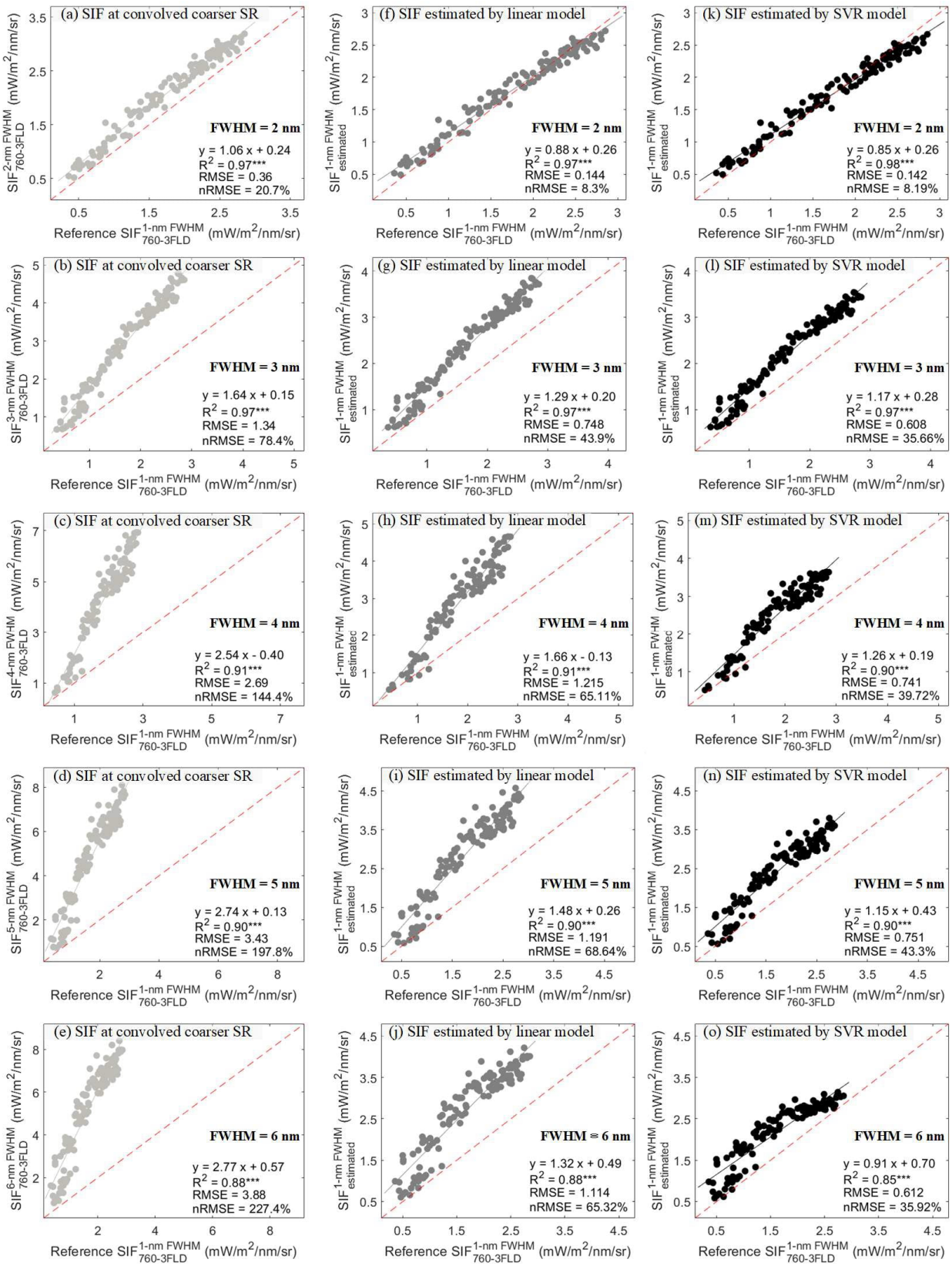

Fig. 3-11. Relationships between the airborne $SIF_{760\text{-}3FLD}$ quantified from the sub-nanometer imager by convolving to different SRs against $SIF_{760\text{-}3FLD}$ convolved to 1-nm FWHM (used here as the reference SIF) for validation plots corresponding to Site 1 (a-e). Relationships between the reference $SIF_{760\text{-}3FLD}$ and the airborne SIF_{760} at 1-nm FWHM estimated by the linear model (f-j) and SVR model (k-o) from the sub-nanometer airborne spectra convolved to different SRs. The red dashed and black solid lines depict the 1:1 line and regression line, respectively. ***p-value < 0.001.

3.4 Discussion

In precision agriculture, plant phenotyping studies, and other high-throughput applications, the complexity and operational costs of sub-nanometer airborne imaging sensors make alternative sensors appealing, if SIF can be measured accurately. Previous theoretical work using the SCOPE model has evaluated the most critical parameters affecting SIF via global sensitivity analysis (Verrelst *et al*., 2015). Our study builds on this theoretical work by considering how narrow-band sensors affect SIF retrieval and by validating theoretical estimates against high-resolution experimental field data. Extending recent work by Belwalkar *et al*. (2022), we evaluated a novel modelling methodology to accurately quantify SIF_{760} at 1-nm FWHM from narrow-band-resolution imaging sensors using SCOPE RTM and support vector regression.

Our results revealed that the SIF_{760} quantified from broader SR hyperspectral imager (5.8-nm FWHM) aligned well (R^2 = 0.91–0.93; RMSE = 0.118–0.273 $mW/m^2/nm/sr$) with $SIF_{760\text{-}3FLD}$ quantified at 1-nm FWHM from the sub-nanometer airborne imager flown in tandem and used for validation across two plant phenotyping experimental sites showing nutrient stress variability. Our findings support the operational viability of using standard, commercially accessible, low-cost narrow-band hyperspectral imaging sensors to obtain accurate absolute SIF_{760} levels in phenotyping trials of homogeneous and uniform canopies.

In our approach, we found that site-specific parameters were required to generate SCOPE-simulated datasets that could characterise the correct structural and ambient conditions of the fields under study for the accurate estimation of SIF_{760} (Table 3-4). This highlights the need for precise parametrization of SCOPE, or any other physically-based model, to generate site-specific training datasets reflecting the actual field conditions observed at a given study site. The global SCOPE-sensitivity study (Verrelst *et al*., 2015) has identified a set of SCOPE model inputs related to leaf, canopy, soil, and micrometeorology as having outsized impact on SIF quantification. Future research could consider ways to account for all these inputs at scale to enable generalized applications for any

location and set of ambient conditions. However, the development of such a training dataset is still in progress owing to the extensive effort and computational cost required in the parametrization of the SCOPE model to meet a wide range of field and ambient conditions.

Interpreting SIF_{760} from narrow-band sensors requires careful consideration of the scaling approach employed to account for sensor spectral specification. The combination of incoming photosynthetically active radiation (PAR) and SIF_{760}-based indices such as near-infrared reflectance of vegetation (NIRv) (Badgley *et al*., 2017) and the Fluorescence Correction Vegetation Index (FCVI) (Yang *et al*., 2020), denoted NIRvP and FCVIP, respectively, has recently been demonstrated to provide reliable structural proxies for photosynthesis and SIF (Dechant *et al*., 2022). These indices could be used to scale SIF_{760} through a less complex approach than that proposed in this paper. Using SCOPE-simulated datasets, we examined whether these indices could provide more accurate SIF_{760} estimates than the proposed approach. SIF_{760} estimates obtained from the two indices were found to be inferior to those obtained using the proposed linear and SVR models, suggesting that $SIF_{760\text{-}3FLD}$ calculated with 5.8-nm FWHM radiance is preferable to FCVIP and NIRvP as a predictor variable (detailed in Appendix B).

The effect of sensor noise on the SIF_{760} scaling methodology proposed in this study is important to consider in an operational context, as SIF is strongly influenced by sensor SNR. Because the SVR model was trained on noise-free simulated SCOPE spectra in this study, this method is not recommended for pixel-based analysis using sensors with low SNR levels. Instead, analyses should be limited to an object-based scale in which pixels are averaged across individual areas. Future research could characterise the effect of sensor noise on the simulated training dataset, thereby enabling the estimation of SIF_{760} at the pixel scale and the generation of SIF_{760} pixel-level maps from narrow-band imaging sensors with low SNR. In the current study, the SIF_{760} scaling approach was designed and validated for phenotyping experiments involving nutrient variability as part of nitrogen application treatments, causing nutrient deficiency and stress. Future research will focus on

evaluating the proposed scaling approach for canopies subjected to other abiotic stresses, such as under water limiting conditions, and under biotic-induced stress (see Zarco-Tejada *et al*. (2021) for the significance of SIF for separating biotic from abiotic stress). Such research will be critical for understanding the potential of narrow-band imaging sensors for estimating accurate SIF_{760} across a wide range of ecosystems.

Although a recent version of the SCOPE model (version 2.0) accounts for the vertical heterogeneity of the canopy biophysical and biochemical properties, it retains the assumption of homogeneity in the horizontal direction (Yang *et al*., 2021). Thus, our methods based on SCOPE parametrization are most applicable in experimental fields with homogeneous crop canopies. It will also be important to further investigate the scaling approach described in this study over complex and heterogeneous canopies, such as forests, and row-structured and grid-based crop canopies such as vineyards and tree orchards. Such efforts will require the extraction of crown spectra from pure vegetation pixels from very-high-spatial-resolution hyperspectral imagery to minimize the impact of the structural heterogeneity. Alternatively, three-dimensional canopy RTMs capable of directly simulating canopies with tree crowns, such as FluorFLIGHT (Hernández-Clemente *et al*., 2017), the Fluorescence model with Weight Photon Spread (FluorWPS) (Zhao *et al*., 2016), and the Discrete Anisotropic Radiative Transfer (DART) model (Gastellu-Etchegorry *et al*., 2017), could be employed. Such studies would be relevant for future missions such as the FLuorescence EXplorer (FLEX) (Drusch *et al*., 2017) when attempting to monitor the fluorescence emission in forests and heterogeneous crops.

In summary, the need for an accurate estimation of SIF is critical from an operational perspective, and dedicated sub-nanometer hyperspectral imagers may not be readily available in many agronomic settings. Consequently, it is essential to consider the adoption of suitable airborne imaging sensors, as well as the development of methods based on physically-based models for correctly interpreting SIF from the selected sensor, particularly in cases where sensors have coarser spectral

resolutions (greater than 1-nm FWHM). The selection of appropriate physically-based models based on the type of ecosystem under consideration, especially for complex heterogeneous canopies, and the proper modelling approach are additional factors to consider. Accounting for the aforementioned considerations will facilitate the use of accurately quantified SIF from imaging sensors onboard piloted and unmanned airborne platforms for the advancement of research on photosynthesis, physiological assessment and pre-visual stress detection.

3.5 Conclusions

1. The overestimated SIF_{760} levels obtained from narrow-band resolution imaging sensors can be scaled to the appropriate absolute SIF_{760} levels quantified from sub-nanometer (FWHM≤1nm) resolution imagers. A modelling framework integrating SCOPE RTM and a machine learning method was proposed and validated.
2. Following extensive testing with SCOPE simulations covering a wide range of spectral characteristics, it was determined that the best results could be achieved with an SVR model employing $SIF_{760\text{-}3FLD}$ at narrow-band resolution and the SCOPE-derived leaf biochemical and structural traits (C_{a+b}, LAI, and $LIDF_a$) as predictor variables.
3. The robustness of the proposed approach was demonstrated by the high degree of agreement between the estimated SIF_{760} at 1-nm FWHM and the reference $SIF_{760\text{-}3FLD}$ quantified from the airborne sub-nanometer resolution imager at two experimental sites with different crop types, irrigation regimes, and weather conditions.
4. The findings of this study pave the way for the widespread adoption of hyperspectral imagers with FWHM > 1 nm for operational applications of SIF requiring retrievals of chlorophyll fluorescence emission in absolute physical units.

Acknowledgements

This research was supported by The University of Melbourne's Research Computing Services and the Petascale Campus Initiative. The authors gratefully acknowledge the Foundation for Arable Research Australia, in particular Michael Straight and Ben Morris; the Grains Research and Development Corporation Australia; and Riverine Plains Incorporated for their provision and management of the field trials. A. Longmire, A. Gracia-Romero and Y. Wang are acknowledged for their technical support during the field and airborne campaigns.

References

Aasen, H., Honkavaara, E., Lucieer, A., Zarco-Tejada, P.J., 2018. Quantitative Remote Sensing at Ultra-High Resolution with UAV Spectroscopy: A Review of Sensor Technology, Measurement Procedures, and Data Correction Workflows. Remote Sens. 10, 1091.

Acebron, K., Matsubara, S., Jedmowski, C., Emin, D., Muller, O., Rascher, U., 2021. Diurnal dynamics of nonphotochemical quenching in Arabidopsis npq mutants assessed by solar-induced fluorescence and reflectance measurements in the field. New Phytol. 229, 2104–2119.

Badgley, G., Field, C.B., Berry, J.A., 2017. Canopy near-infrared reflectance and terrestrial photosynthesis. Sci. Adv. 3, e1602244.

Belwalkar, A., Poblete, T., Longmire, A., Hornero, A., Hernandez-Clemente, R., Zarco-Tejada, P.J., 2022. Evaluation of SIF retrievals from narrow-band and sub-nanometer airborne hyperspectral imagers flown in tandem: modelling and validation in the context of plant phenotyping. Remote Sens. Environ. 273, 112986.

Bendig, J., Malenovský, Z., Gautam, D., Lucieer, A., 2020. Solar-induced chlorophyll fluorescence measured from an unmanned aircraft system: sensor Etaloning and platform motion correction. IEEE Trans. Geosci. Remote Sens. 58, 3437–3444.

Braghiere, R.K., Wang, Y., Doughty, R., Sousa, D., Magney, T., Widlowski, J.L., Longo, M., Bloom, A.A., Worden, J., Gentine, P., Frankenberg, C., 2021. Accounting for canopy structure improves hyperspectral radiative transfer and sun-induced chlorophyll fluorescence representations in a new generation earth system model. Remote Sens. Environ. 261, 11249.

Brown, S.W., Eppeldauer, G.P., Lykke, K.R., 2006. Facility for spectral irradiance and radiance responsivity calibrations using uniform sources. Appl. Opt. 45, 8218–8237.

Campbell, P.K.E., Middleton, E.M., Corp, L.A., Kim, M.S., 2008. Contribution of chlorophyll fluorescence to the apparent vegetation reflectance. Sci. Total Environ. 404, 433–439.

Calderón, R., Navas-Cortés, J.A., Lucena, C., Zarco-Tejada, P.J., 2013. High-resolution airborne hyperspectral and thermal imagery for early detection of Verticillium wilt of olive using fluorescence, temperature and narrow-band spectral indices. Remote Sens. Environ. 139, 231–245.

Calderón, R., Navas-Cortés, J.A., Zarco-Tejada, P.J., 2015. Early detection and quantification of Verticillium wilt in olive using hyperspectral and thermal imagery over large areas. Remote Sens. 7, 5584–5610.

Camino, C., Zarco-Tejada, P.J., Gonzalez-Dugo, V., 2018a. Effects of heterogeneity within tree crowns on airborne-quantified SIF and the CWSI as indicators of water stress in the context of precision agriculture. Remote Sens. 10, 604.

Camino, C., González-Dugo, V., Hernandez, P., Sillero, J.C., Zarco-Tejada, P.J., 2018b. Improved nitrogen retrievals with airborne-derived fluorescence and plant traits quantified from VNIR-SWIR hyperspectral imagery in the context of precision agriculture. Int. J. Appl. Earth Obs. Geoinf. 70, 105–117.

Camino, C., Gonzalez-Dugo, V., Hernandez, P., Zarco-Tejada, P.J., 2019. Radiative transfer Vcmax estimation from hyperspectral imagery and SIF retrievals to assess photosynthetic performance in rainfed and irrigated plant phenotyping trials. Remote Sens. Environ. 231, 111186.

Camino, C., Calderón, R., Parnell, S., Dierkes, H., Chemin, Y., Román-Écija, M., Montes-Borrego, M., Landa, B.B., Navas-Cortes, J.A., Zarco-Tejada, P.J., Beck, P.S.A., 2021. Detection of Xylella fastidiosa in almond orchards by synergic use of an epidemic spread model and remotely sensed plant traits. Remote Sens. Environ. 260, 112420.

Cendrero-Mateo, M.P., Wieneke, S., Damm, A., Alonso, L., Pinto, F., Moreno, J., Guanter, L., Celesti, M., Rossini, M., Sabater, N., Cogliati, S., Julitta, T., Rascher, U., Goulas, Y., Aasen, H., Pacheco-Labrador, J., Mac Arthur, A., 2019. Sun-induced chlorophyll fluorescence III: benchmarking retrieval methods and sensor characteristics for proximal sensing. Remote Sens. 11, 962.

Celesti, M., van der Tol, C., Cogliati, S., Panigada, C., Yang, P., Pinto, F., Rascher, U., Miglietta, F., Colombo, R., Rossini, M., 2018. Exploring the physiological information of Sun-induced chlorophyll fluorescence through radiative transfer model inversion. Remote Sens. Environ. 215, 97–108.

Chang, C.Y, Zhou, R., Kira, O., Marri, S., Skovira, J., Gu, L., Sun, Y., 2020. An Unmanned Aerial System (UAS) for concurrent measurements of solar-induced chlorophyll fluorescence and hyperspectral reflectance toward improving crop monitoring. Agric. For. Meteorol. 294, 108145.

Cogliati, S., Rossini, M., Julitta, T., Meroni, M., Schickling, A., Burkart, A., Pinto, F., Rascher, U., Colombo, R., 2015. Continuous and long-term measurements of reflectance and sun-induced chlorophyll fluorescence by using novel automated field spectroscopy systems. Remote Sens. Environ. 164, 270–281.

Danner, M., Berger, K., Wocher, M., Mauser, W., Hank, T., 2021. Efficient RTM-based training of machine learning regression algorithms to quantify biophysical & biochemical traits of agricultural crops. ISPRS J. Photogramm. Remote Sens. 173, 278–296.

Damm, A., Erler, A., Hillen, W., Meroni, M., Schaepman, M.E., Verhoef, W., Rascher, U., 2011. Modeling the impact of spectral sensor configurations on the FLD retrieval accuracy of sun-induced chlorophyll fluorescence. Remote Sens. Environ. 115, 1882–1892.

Damm, A., Guanter, L., Paul-Limoges, E., Van der Tol, C., Hueni, A., Buchmann, N., Eugster, W., Ammann, C., Schaepman, M.E., 2015. Far-red sun-induced chlorophyll fluorescence shows ecosystem-specific relationships to gross primary production: An assessment based on observational and modeling approaches. Remote Sens. Environ. 166, 91–105.

Damm, A., Haghighi, E., Paul-Limoges, E., van der Tol, C., 2021. On the seasonal relation of sun-induced chlorophyll fluorescence and transpiration in a temperate mixed forest. Agric. For. Meteorol. 304–305, 108386.

Damm, A., Cogliati, S., Colombo, R., Fritsche, L., Genangeli, A., Genesio, L., Hanus, J., Peressotti, A., Rademske, P., Rascher, U., Schuettemeyer, D., Siegmann, B., Sturm, J., Miglietta, F., 2022. Response times of remote sensing measured sun-induced chlorophyll fluorescence, surface temperature and vegetation indices to evolving soil water limitation in a crop canopy. Remote Sens. Environ. 273, 112957.

Dechant, B., Ryu, Y., Badgley, G., Zeng, Y., Berry, J.A., Zhang, Y., Goulas, Y., Li, Z., Zhang, Q., Kang, M., Li, J., Moya, I., 2020. Canopy structure explains the relationship between photosynthesis and sun-induced chlorophyll fluorescence in crops. Remote Sens. Environ. 241, 111733.

Dechant, B., Ryu, Y., Badgley, G., Köhler, P., Rascher, U., Migliavacca, M., Zhang, Y., Tagliabue, G., Guan, K., Rossini, M., Goulas, Y., Zeng, Y., Frankenberg, C., Berry, J.A., 2022. NIRvP: A robust structural proxy for sun-induced chlorophyll fluorescence and photosynthesis across scales. Remote Sens. Environ. 268, 112763.

De Grave, C., Verrelst, J., Morcillo-Pallarés, P., Pipia, L., Rivera-Caicedo, J.P., Amin, E., Belda, S., Moreno, J., 2020. Quantifying vegetation biophysical variables from the Sentinel-3/FLEX tandem mission: evaluation of the synergy of OLCI and FLORIS data sources. Remote Sens. Environ. 251, 112101.

Fournier, A., Daumard, F., Champagne, S., Ounis, A., Goulas, Y., Moya, I., 2012. Effect of canopy structure on sun-induced chlorophyll fluorescence. ISPRS J. Photogramm. Remote Sens. 68, 112–120.

Frankenberg, C., Köhler, P., Magney, T.S., Geier, S., Lawson, P., Schwochert, M., McDuffie, J., Drewry, D.T., Pavlick, R., Kuhnert, A., 2018. The chlorophyll fluorescence imaging spectrometer (CFIS), mapping far red fluorescence from aircraft. Remote Sens. Environ. 217, 523–536.

Fu, P., Meacham-Hensold, K., Siebers, M. H., & Bernacchi, C. J., 2021. The inverse relationship between solar-induced fluorescence yield and photosynthetic capacity: benefits for field phenotyping. J. Experim. Bot., 72, 1295–1306.

Gastellu-Etchegorry, J.-P., Lauret, N., Yin, T., Landier, L., Kallel, A., Malenovský, Z., Al Bitar, A., Aval, J., Benhmida, S., Qi, J., Medjdoub, G., Guilleux, J., Chavanon, E., Cook, B., Morton, D., Chrysoulakis, N., Mitraka, Z., 2017. DART: recent advances in remote sensing data modeling

with atmosphere, polarization, and chlorophyll fluorescence. IEEE J. Sel. Top. Appl. Earth Obs. Remote Sens. 10, 2640–2649.

Gonzalez-Dugo, V., Hernandez, P., Solis, I., Zarco-Tejada, P.J., 2015. Using high-resolution hyperspectral and thermal airborne imagery to assess physiological condition in the context of wheat phenotyping. Remote Sens. 7, 13586–13605.

Grossmann, K., Frankenberg, C., Magney, T.S., Hurlock, S.C., Seibt, U., Stutz, J., 2018. PhotoSpec: a new instrument to measure spatially distributed red and far-red solar-induced chlorophyll fluorescence. Remote Sens. Environ. 216, 311–327.

Gueymard, C.A., 2001. Parameterized transmittance model for direct beam and circumsolar spectral irradiance. Sol. Energy 71, 325–346.

Hao, D., Zeng, Y., Qiu, H., Biriukova, K., Celesti, M., Migliavacca, M., Rossini, M., Asrar, G.R., Chen, M., 2021. Practical approaches for normalizing directional solar-induced fluorescence to a standard viewing geometry. Remote Sens. Environ. 255, 112171.

Hao, D., Zeng, Y., Zhang, Z., Zhang, Y., Qiu, H., Biriukova, K., Celesti, M., Rossini, M., Zhu, P., Asrar, G.R., Chen, M., 2022. Adjusting solar-induced fluorescence to nadir-viewing provides a better proxy for GPP. ISPRS J. Photogramm. Remote Sens. 186, 157–169.

Headwall Photonics, 2021. Headwall Solar-Induced-Fluorescence-Imaging-Sensor. URL: https://headwallphotonics.sharefile.com/share/view/sf435916f5c104db8b062a06e58786bef [Online; accessed 25. Oct. 2022].

Hernández-Clemente, R., North, P.R.J., Hornero, A., Zarco-Tejada, P.J., 2017. Assessing the effects of forest health on sun-induced chlorophyll fluorescence using the FluorFLIGHT 3-D radiative transfer model to account for forest structure. Remote Sens. Environ. 193, 165–179.

Hornero, A., Zarco-Tejada, P.J., Quero, J.L., North, P.R.J., Ruiz-Gómez, F.J., Sánchez-Cuesta, R., Hernández-Clemente, R., 2021. Modelling hyperspectral- and thermal-based plant traits for the early detection of Phytophthora-induced symptoms in oak decline. Remote Sens. Environ. 263, 112570.

Jia, J., Wang, Y., Chen, J., Guo, R., Shu, R., Wang, J., 2020. Status and application of advanced airborne hyperspectral imaging technology: A review. Infrared Phys. Technol. 104, 103115.

Julitta, T., Corp, L.A., Rossini, M., Burkart, A., Cogliati, S., Davies, N., Hom, M., Arthur, A. Mac, Middleton, E.M., Rascher, U., Schickling, A., Colombo, R., 2016. Comparison of sun-induced chlorophyll fluorescence estimates obtained from four portable field spectroradiometers. Remote Sens. 8, 122.

Kattenborn, T., Fassnacht, F.E., Pierce, S., Lopatin, J., Grim, J.P., Schmidtlein, S., 2017. Linking plant strategies and plant traits derived by radiative transfer modelling. J. Veg. Sci. 28, 717–727.

Kim, J., Ryu, Y., Dechant, B., Lee, H., Kim, H.S., Kornfeld, A., Berry, J.A., 2021. Solar- induced chlorophyll fluorescence is non-linearly related to canopy photosynthesis in a temperate evergreen needleleaf forest during the fall transition. Remote Sens. Environ. 258, 112362.

Köhler, P., Frankenberg, C., Magney, T.S., Guanter, L., Joiner, J., Landgraf, J., 2018. Global retrievals of solar-induced chlorophyll fluorescence with TROPOMI: first results and intersensor comparison to OCO-2. Geophys. Res. Lett. 45, 10, 456–10, 463.

Li, Z., Zhang, Q., Li, J., Yang, X., Wu, Y., Zhang, Z., Wang, S., Wang, H., Zhang, Y., 2020. Solar-induced chlorophyll fluorescence and its link to canopy photosynthesis in maize from continuous ground measurements. Remote Sens. Environ. 236, 111420.

Lichtenthaler, H. K., Rinderle, U., 1988. The role of chlorophyll fluorescence in the detection of stress conditions in plants. Crit. Rev. Anal. Chem. 19 (Suppl. 1), S29–S85.

Liu, L., Liu, X., Hu, J., 2015. Effects of spectral resolution and SNR on the vegetation solar-induced fluorescence retrieval using FLD-based methods at canopy level. Eur. J. Remote Sens. 48, 743–762.

Liu, X., Guanter, L., Liu, L., Damm, A., Malenovský, Z., Rascher, U., Peng, D., Du, S., Gastellu-Etchegorry, J.-P., 2019. Downscaling of solar-induced chlorophyll fluorescence from canopy level to photosystem level using a random forest model. Remote Sens. Environ. 231, 110772.

Longmire, A.R., Poblete, T., Hunt, J.R., Chen, D., Zarco-Tejada, P.J., 2022. Assessment of crop traits retrieved from airborne hyperspectral and thermal remote sensing imagery to predict wheat grain protein content. ISPRS J. Photogramm. Remote Sens. 193, 284–298.

Lu, B., Dao, P.D., Liu, J., He, Y., Shang, J., 2020. Recent advances of hyperspectral imaging technology and applications in agriculture. Remote Sens. 12, 2659.

Maimaitiyiming, M., Sagan, V., Sidike, P., Maimaitijiang, M., Miller, A.J., Kwasniewski, M., 2020. Leveraging very-high spatial resolution hyperspectral and thermal UAV imageries for characterizing diurnal indicators of grapevine physiology. Remote Sens. 12, 3216.

Malenovský, Z., Mishra, K.B., Zemek, F., Rascher, U., Nedbal, L., 2009. Scientific and technical challenges in remote sensing of plant canopy reflectance and fluorescence. J. Exp. Bot. 60, 2987–3004.

Malenovský, Z., Regaieg, O., Yin, T., Lauret, N., Guilleux, J., Chavanon, E., Duran, N., Janoutová, R., Delavois, A., Meynier, J., Medjdoub, G., Yang, P., van der Tol, C., Morton, D., Cook, B.D., Gastellu-Etchegorry, J.P., 2021. Discrete anisotropic radiative transfer modelling of solar-induced chlorophyll fluorescence: Structural impacts in geometrically explicit vegetation canopies. Remote Sens. Environ. 263, 112564.

Meroni, M., Rossini, M., Guanter, L., Alonso, L., Rascher, U., Colombo, R., Moreno, J., 2009. Remote sensing of solar-induced chlorophyll fluorescence: review of methods and applications. Remote Sens. Environ. 113, 2037–2051.

Migliavacca, M., Perez-Priego, O., Rossini, M., El-Madany, T.S., Moreno, G., Van der Tol, C., Rascher, U., Berninger, A., Bessenbacher, V., Burkart, A., Carrara, A., Fava, F., Guan, J.-H., Hammer, T.W., Henkel, K., Juarez-Alcalde, E., Julitta, T., Kolle, O., Martín, M.P., Musavi, T., Pacheco-Labrador, J., Pérez-Burgueño, A., Wutzler, T., Zaehle, S., Reichstein, M., 2017. Plant functional traits and canopy structure control the relationship between photosynthetic CO2 uptake and far-red sun-induced fluorescence in a Mediterranean grassland under different nutrient availability. New Phytol. 214, 1078–1091.

Mockus, J., 2012. Bayesian Approach to Global Optimization: Theory and Applications, vol. 37. Springer Science & Business.

Mohammed, G.H., Colombo, R., Middleton, E.M., Rascher, U., Van der Tol, C., Nedbal, L., Goulas, Y., P´erez-Priego, O., Damm, A., Meroni, M., Joiner, J., Cogliati, S., Verhoef, W., Malenovský, Z., Gastellu-Etchegorry, J.P., Miller, J.R., Guanter, L., Moreno, J., Moya, I., Berry, J.A., Frankenberg, C., Zarco-Tejada, P.J., 2019. Remote sensing of solar-induced chlorophyll fluorescence (SIF) in vegetation: 50 years of progress. Remote Sens. Environ. 231, 111177.

Ni, Z., Liu, Z., Li, Z.L., Nerry, F., Huo, H., Sun, R., Yang, P., Zhang, W., 2016. Investigation of atmospheric effects on retrieval of sun-induced fluorescence using hyperspectral imagery. Sensors 16, 480.

Nichol, C.J., Drolet, G., Porcar-Castell, A., Wade, T., Sabater, N., Middleton, E.M., Maclellan, C., Levula, J., Mammarella, I., Vesala, T., Atherton, J., 2019. Diurnal and Seasonal Solar Induced Chlorophyll Fluorescence and Photosynthesis in a Boreal Scots Pine Canopy. Remote Sens. 11, 273.

Pacheco-Labrador, J., Perez-Priego, O., El-Madany, T.S., Julitta, T., Rossini, M., Guan, J., Moreno, G., Carvalhais, N., Martín, M.P., Gonzalez-Cascon, R., Kolle, O., Reischtein, M., van der Tol, C., Carrara, A., Martini, D., Hammer, T.W., Moossen, H., Migliavacca, M., 2019. Multiple-constraint inversion of SCOPE. Evaluating the potential of GPP and SIF for the retrieval of plant functional traits. Remote Sens. Environ. 234, 111362.

Panigada, C., Rossini, M., Meroni, M., Cilia, C., Busetto, L., Amaducci, S., Boschetti, M., Cogliati, S., Picchi, V., Pinto, F., Marchesi, A., Colombo, R., 2014. Fluorescence, PRI and canopy temperature for water stress detection in cereal crops. Int. J. Appl. Earth Obs. Geoinf. 30, 167–178.

Paynter, I., Cook, B., Corp, L., Nagol, J., McCorkel, J., 2020. Characterization of FIREFLY, an imaging spectrometer designed for remote sensing of solar induced fluorescence. Sensors 20, 4682.

Plascyk, J.A., 1975. The MK II Fraunhofer line discriminator (FLD-II) for airborne and orbital remote sensing of solar-stimulated luminescence. Opt. Eng. 14, 144339.

Poblete, T., Camino, C., Beck, P.S.A., Hornero, A., Kattenborn, T., Saponari, M., Boscia, D., Navas-Cortes, J.A., Zarco-Tejada, P.J., 2020. Detection of Xylella fastidiosa infection symptoms with airborne multispectral and thermal imagery: Assessing bandset reduction performance from hyperspectral analysis. ISPRS J. Photogramm. Remote Sens. 162, 27–40.

Poblete, T., Navas-Cortes, J.A., Camino, C., Calderon, R., Hornero, A., Gonzalez-Dugo, V., Landa, B.B., Zarco-Tejada, P.J., 2021. Discriminating Xylella fastidiosa from Verticillium dahliae infections in olive trees using thermal- and hyperspectral-based plant traits. ISPRS J. Photogramm. Remote Sens. 179, 133–144.

Porcar-Castell, A., Tyystj¨arvi, E., Atherton, J., Van der Tol, C., Flexas, J., Pfündel, E.E., Moreno, J., Frankenberg, C., Berry, J.A., 2014. Linking chlorophyll a fluorescence to photosynthesis for remote sensing applications: mechanisms and challenges. J. Exp. Bot. 65, 4065–4095.

Rascher, U., Alonso, L., Burkart, A., Cilia, C., Cogliati, S., Colombo, R., Damm, A., Drusch, M., Guanter, L., Hanus, J., Hyvärinen, T., Julitta, T., Jussila, J., Kataja, K., Kokkalis, P., Kraft, S., Kraska, T., Matveeva, M., Moreno, J., Muller, O., Panigada, C., Pikl, M., Pinto, F., Prey, L., Pude, R., Rossini, M., Schickling, A., Schurr, U., Schüttemeyer, D., Verrelst, J., Zemek, F., 2015. Sun-induced fluorescence - a new probe of photosynthesis: first maps from the imaging spectrometer HyPlant. Glob. Chang. Biol. 21, 4673–4684.

Romero, J.M., Cordon, G.B., Lagorio, M.G., 2018. Modeling re-absorption of fluorescence from the leaf to the canopy level. Remote Sens. Environ. 204, 138–146.

Romero, J.M., Cordon, G.B., Lagorio, M.G., 2020. Re-absorption and scattering of chlorophyll fluorescence in canopies: A revised approach. Remote Sens. Environ. 246, 111860.

Schneider, F.D., Ferraz, A.A., Hancock, S., Duncanson, L.I., Dubayah, R.O., Pavlick, R.P., Schimel, D.S., 2020. Towards mapping the diversity of canopy structure from space with GEDI. Environ. Res. Lett. 15, 115006.

Siegmann, B., Cendrero-Mateo, M.P., Cogliati, S., Damm, A., Gamon, J., Herrera, D., Jedmowski, C., Junker-Frohn, L.V., Kraska, T., Muller, O., Rademske, P., van der Tol, C., Quiros-Vargas, J., Yang, P., Rascher, U., 2021. Downscaling of far-red solar-induced chlorophyll fluorescence of different crops from canopy to leaf level using a diurnal data set acquired by the airborne imaging spectrometer HyPlant. Remote Sens. Environ. 264, 112609.

Scodellaro, R., Cesana, I., D'Alfonso, L., Bouzin, M., Collini, M., Chirico, G., Colombo, R., Miglietta, F., Celesti, M., Schuettemeyer, D., Cogliati, S., Sironi, L., 2022. A novel hybrid machine learning phasor-based approach to retrieve a full set of solar-induced fluorescence metrics and biophysical parameters. Remote Sens. Environ. 280, 113196.

Specim, 2022. AISA IBIS Fluorescence Imager. URL: https://www.specim.fi/downloads/AisaIBIS_Datasheet-ver1-15.pdf [Online; accessed 25. Oct. 2022].

Stuart, M.B., McGonigle, A.J.S., Willmott, J.R., 2019. Hyperspectral Imaging in Environmental Monitoring: A Review of Recent Developments and Technological Advances in Compact Field Deployable Systems. Sensors 19, 3071.

Suarez, L., Gonzalez-Dugo, V., Camino, C., Hornero, A., Zarco-Tejada, P.J., 2021. Physical model inversion of the green spectral region to track assimilation rate in almond trees with an airborne nano-hyperspectral imager. Remote Sens. Environ. 252, 112147.

Sun, Y., Frankenberg, A., Jung, M., Joiner, J., Guanter, L., Köhler, P., Magney, T.S., 2018. Overview of solar-induced chlorophyll fluorescence (SIF) from the orbiting carbon observatory-2: retrieval, cross-mission comparison, and global monitoring for GPP. Remote Sens. Environ. 209, 808–823.

Süß, A., Hank, T., Mauser, W., 2016. Deriving diurnal variations in sun-induced chlorophyll-a fluorescence in winter wheat canopies and maize leaves from ground-based hyperspectral measurements. Int. J. Remote Sens. 37, 60–77.

Thomas, V.A., Wynne, R.H., Kauffman, J., McCurdy, W., Brooks, E. B., Thomas, R. Q., Rakestraw, J., 2021. Mapping thins to identify active forest management in southern pine plantations using Landsat time series stacks. Remote Sens. Environ. 252, 112127.

Van der Tol, C., Verhoef, W., Timmermans, J., Verhoef, A., Su, Z., 2009. An integrated model of soil-canopy spectral radiances, photosynthesis, fluorescence, temperature and energy balance. Biogeosci. 6, 3109–3129.

Van der Tol, C., Rossini, M., Cogliati, S., Verhoef, W., Colombo, R., Rascher, U., Mohammed, G., 2016. A model and measurement comparison of diurnal cycles of sun-induced chlorophyll fluorescence of crops. Remote Sens. Environ. 186, 663–677.

Van Wittenberghe, S., Alonso, L., Verrelst, J., Moreno, J., Samson, R., 2015. Bidirectional sun-induced chlorophyll fluorescence emission is influenced by leaf structure and light scattering properties – a bottom-up approach. Remote Sens. Environ. 158, 169–179.

Verhoef, W., van der Tol, C., Middleton, E.M., 2018. Hyperspectral radiative transfer modeling to explore the combined retrieval of biophysical parameters and canopy fluorescence from FLEX – Sentinel-3 tandem mission multi-sensor data. Remote Sens. Environ. 204, 942–963.

Verrelst, J., Rivera, J.P., Van der Tol, C., Magnani, F., Mohammed, G., Moreno, J., 2015. Global sensitivity analysis of the SCOPE model: what drives simulated canopy-leaving sun-induced fluorescence? Remote Sens. Environ. 166, 8–21.

Verrelst, J., Van der Tol, C., Magnani, F., Sabater, N., Rivera, J.P., Mohammed, G., Moreno, J., 2016. Evaluating the predictive power of sun-induced chlorophyll fluorescence to estimate net photosynthesis of vegetation canopies: a SCOPE modelling study. Remote Sens. Environ. 176, 139–151.

Wang, N., Suomalainen, J., Bartholomeus, H., Kooistra, L., Masiliūnas, D., Clevers, J.G.P.W., 2021. Diurnal variation of sun-induced chlorophyll fluorescence of agricultural crops observed from a point-based spectrometer on a UAV. Int. J. Appl. Earth Obs. Geoinf. 96, 102276.

Wang, R., Gamon, J.A., Hmimina, G., Cogliati, S., Zygielbaum, A.I., Arkebauer, T.J., Suyker, A., 2022. Harmonizing solar induced fluorescence across spatial scales, instruments, and extraction methods using proximal and airborne remote sensing: A multi-scale study in a soybean field. Remote Sens. Environ. 281, 113268.

Wang, S., Guan, K., Wang, Z., Ainsworth, E.A., Zheng, T., Townsend, P.A., Liu, N., Nafziger, E., Masters, M.D., Li, K., Wu, G., 2021. Airborne hyperspectral imaging of nitrogen deficiency on crop traits and yield of maize by machine learning and radiative transfer modeling. Int. J. Appl. Earth Obs. Geoinf. 105, 102617.

Wang, Y., Suarez, L., Poblete, T., Gonzalez-Dugo, V., Ryu, D., Zarco-Tejada, P.J., 2022. Evaluating the role of solar-induced fluorescence (SIF) and plant physiological traits for leaf nitrogen assessment in almond using airborne hyperspectral imagery. Remote Sens. Environ. 279, 113141.

Watt, M.S., Buddenbaum, H., Leonardo, E.M.C., Estarija, H.J.C., Bown, H.E., Gomez-Gallego, M., Hartley, R., Massam, P., Wright, L., Zarco-Tejada, P.J., 2020. Using hyperspectral plant traits

linked to photosynthetic efficiency to assess N and P partition. ISPRS J. Photogramm. Remote Sens. 169, 406–420.

Xu, S., Atherton, J., Riikonen, A., Zhang, C., Oivukkamäki, J., MacArthur, A., Honkavaara, E., Hakala, T., Koivumäki, N., Liu, Z., 2021. Structural and photosynthetic dynamics mediate the response of SIF to water stress in a potato crop. Remote Sens. Environ. 263, 11255.

Yang, P., Van der Tol, C., 2018. Linking canopy scattering of far-red sun-induced chlorophyll fluorescence with reflectance. Remote Sens. Environ. 209, 456–467.

Yang, P., Van der Tol, C., Campbell, P.K., Middleton, E.M., 2020. Fluorescence Correction Vegetation Index (FCVI): A physically based reflectance index to separate physiological and non-physiological information in far-red sun-induced chlorophyll fluorescence. Remote Sens. Environ. 240, 111676.

Yang, P., Prikaziuk, E., Verhoef, W., Van der Tol, C., 2021. SCOPE 2.0: A model to simulate vegetated land surface fluxes and satellite signals. Geosci. Model Dev. 14, 4697–4712.

Zarco-Tejada, P.J., González-Dugo, V., Berni, J.A.J., 2012. Fluorescence, temperature and narrow-band indices acquired from a UAV platform for water stress detection using a micro-hyperspectral imager and a thermal camera. Remote Sens. Environ. 117, 322–337.

Zarco-Tejada, P.J., Morales, A., Testi, L., Villalobos, F.J., 2013. Spatio-temporal patterns of chlorophyll fluorescence and physiological and structural indices acquired from hyperspectral imagery as compared with carbon fluxes measured with eddy covariance. Remote Sens. Environ. 133, 102–115.

Zarco-Tejada, P.J., González-Dugo, M.V., Fereres, E., 2016. Seasonal stability of chlorophyll fluorescence quantified from airborne hyperspectral imagery as an indicator of net photosynthesis in the context of precision agriculture. Remote Sens. Environ. 179, 89–103.

Zarco-Tejada, P.J., Camino, C., Beck, P.S.A., Calderon, R., Hornero, A., Hernández-Clemente, R., Kattenborn, T., Montes-Borrego, M., Susca, L., Morelli, M., Gonzalez-Dugo, V., North, P.R.J., Landa, B.B., Boscia, D., Saponari, M., Navas-Cortes, J.A., 2018. Previsual symptoms of Xylella fastidiosa infection revealed in spectral plant-trait alterations. Nat. Plants 4, 432–439.

Zarco-Tejada, P.J., Poblete, T., Camino, C., Gonzalez-Dugo, V., Calderon, R., Hornero, A., Hernandez-Clemente, R., Román-Écija, M., Velasco-Amo, MP., Landa, BB., Beck, PSA., Saponari, M., Boscia, D., Navas-Cortes, JA., 2021. Divergent abiotic spectral pathways unravel pathogen stress signals across species. Nat. Commun. 12, 6088.

Zeng, Y., Badgley, G., Dechant, B., Ryu, Y., Chen, M., Berry, J.A., 2019. A practical approach for estimating the escape ratio of solar-induced chlorophyll fluorescence. Remote Sens. Environ. 232, 111209.

Zhao, F., Dai, X., Verhoef, W., Guo, Y., Van der Tol, C., Li, Y., Huang, Y., 2016. FluorWPS: a Monte Carlo ray-tracing model to compute sun-induced chlorophyll fluorescence of three-dimensional canopy. Remote Sens. Environ. 187, 385–399.

Chapter 4

Prospects of solar Fraunhofer lines derived from sub-nanometer hyperspectral imagery for assessing a/biotic stress

This chapter resulted in two research articles.

1. **Belwalkar, A.,** Poblete, T., A., Hornero, A., Hernandez-Clemente, R., Zarco-Tejada, P.J. **Prospects of solar Fraunhofer lines derived from sub-nanometer hyperspectral imagery for assessing a/biotic stress** (currently being drafted for submission to the journal Remote Sensing of Environment).

2. **Belwalkar, A.**, Poblete, T., Hornero, A., Zarco-Tejada, P.J., 2023. **Evaluating the relative contribution of Photosystems I and II for leaf nitrogen estimation using fractional depth of Fraunhofer lines and SIF derived from sub-nanometer airborne hyperspectral imagery.** In: Proc. IEEE International Geoscience and Remote Sensing Symposium (IGARSS), 16–21 July 2023, Pasadena, California, USA, pp. 2819–2822.

Abstract

With the advent of sub-nanometer resolution imaging sensors capable of characterising narrow absorption features, Fraunhofer lines (FLs) can now potentially be identified. This opens up a promising avenue for the exploration of these FLs for vegetation monitoring and precision agriculture applications. This study is an exploratory analysis which seeks to examine the prospects of using individual FL depths derived from sub-nanometer airborne hyperspectral imagery for a potential improvement of leaf nitrogen (N) estimates and to detect biotic-induced stress in infected vegetation. A sub-nanometer hyperspectral imager with ≤0.2 nm full-width at half-maximum (FWHM) resolution and a narrow-band hyperspectral imager with 5.8-nm FWHM were flown in tandem over a rainfed winter wheat field for leaf N estimation (Experiment-1) and over a commercial olive orchard infected with the fungus *Verticillium dahliae* (*Vd*) for biotic stress detection (Experiment-2). For Experiment-1, wheat plots were fertilised with variable concentrations of N to produce nutrient variability. To estimate leaf N concentration, regression models using Gaussian process regression (GPR) were built with different permutations of solar-induced chlorophyll fluorescence (SIF), leaf chlorophyll content (C_{a+b}), and depths of individual FLs. For Experiment-2, the sensitivity of different FLs and the two oxygen absorption features (O_2-A and O_2-B) for detecting disease progression at different stages was examined by comparing the absorption depths of asymptomatic trees with those of symptomatic trees with increasing levels of disease severity. The results for Experiment-1 showed that GPR models incorporating the depth of distinct Fraunhofer lines as predictor variables performed better than the benchmark model constructed using C_{a+b} and far-red SIF (SIF_{760}) alone. The best leaf N-estimation model built with FLs from the red and far-red regions (C_{a+b}, $FL_{682.97\ nm}$, $FL_{757.002\ nm}$) yielded an R^2 of 0.71, outperforming the standard approach used in previous works (C_{a+b}, SIF_{760}) (R^2 = 0.56). The results of the biotic-induced stress detection experiment demonstrated that the depth of individual FLs could distinguish between different stages of disease progression. $FL_{671.73\ nm}$ and $FL_{756.90\ nm}$, as well as oxygen-based O_2-B (686.86 nm), were found to be responsive throughout all stages of disease progression. Further FLs were found to be

sensitive as disease severity progressed. These results from both experiments suggest that narrow FLs derived from sub-nanometer resolution imagery are useful for vegetation stress detection, providing the foundation for future research into the utility of FLs for plant physiology monitoring applications.

Keywords: Solar-induced chlorophyll fluorescence, SIF, airborne, hyperspectral, leaf nitrogen, sub-nanometer, Fraunhofer lines, stress detection, *Verticillium dahlia*

4.1 Introduction

The frequency of extreme weather events and large fluctuations in precipitation and temperature patterns are predicted to rise globally because of climate change (Cogato *et al*., 2019; Schmidhuber *et al*., 2007; Zampieri *et al*., 2017). Consequently, biotic and/or abiotic vegetation stresses will become more common and, without prompt and efficient management responses, may result in declines in global food production (Atzberger, 2013). It is thus increasingly crucial to detect signs of vegetation stress as early as possible, before any permanent damage is done, so that corrective agrotechnical actions can be taken to prevent production loss (Berger *et al*., 2022).

Olive trees are infected by more than a hundred different pests and pathogens which cause decreased yields and higher overall production costs (Fernández-Escobar *et al*., 2013). The soil-borne fungus *Verticillium dahliae* (*Vd*) Kleb, responsible for Verticillium wilt (VW), is one of the major threats to olive production around the world (Jiménez-Díaz *et al*., 2012). In more than 400 plant species, this pathogen colonises the vascular system, restricting water flow and leading to water stress (Pegg and Brady, 2002).

Traditional methods for detecting *Vd* infections have relied on *in situ* observations followed by laboratory studies. While these methods are effective, they are also too laborious, costly, and time-consuming to be practical for widespread monitoring (Gramaje *et al*., 2013). Hence, developing

robust methods for large-scale plant scanning is crucial for detecting detrimental crop pathogens and ensuring they are eradicated quickly or contained in an effective manner (Stokstad, 2015). In this context, multi-sensor strategies involving airborne narrow-band hyperspectral and thermal imaging sensors have demonstrated encouraging findings for the early detection of infectious plant diseases at large scales (Calderón *et al*., 2015; 2013; Camino *et al*., 2021; Poblete *et al*., 2023; 2021; Zarco-Tejada *et al*., 2021; 2018).

Thermal imagery-derived normalised canopy temperature, Crop Water Stress Index (CWSI), and narrow-band hyperspectral imagery-derived SIF_{760} and vegetation indices related to structure, xanthophyll, chlorophyll, carotenoid, and disease indices have been demonstrated to be the best indicators for detecting symptoms in *Vd*-infected olive trees (Calderón *et al*., 2015; 2013). Zarco-Tejada *et al*. (2018) used a machine learning framework that considered pigment, structural, fluorescence, and thermal-based plant traits (PSFTs) to detect infection caused by the bacterium *Xylella fastidiosa* (*Xf*) in olive trees with an overall accuracy of over 80%. In a subsequent study, Poblete *et al*. (2021) demonstrated that hyperspectral and thermal traits can be used to detect and differentiate symptoms in olive trees caused by *Vd* and *Xf* infection from a mixed (*Xf* + *Vd*) dataset, which can exhibit visually similar symptoms, using a three-stage machine learning-based approach. In a subsequent study, Zarco-Tejada *et al*. (2021) demonstrated the capability of hyperspectral and thermal traits to distinguish between symptoms caused by *Vd* and *Xf* infections and those caused by water stress, thereby reducing the uncertainty of *Xf* detections across different hosts to less than 6%. In all the aforementioned studies, narrow-band SIF_{760} was found to be one of the most important indicators for detecting biotic stress. Due to the limitations regarding the spectral characteristics of narrow-band hyperspectral imagers used in these studies, only the capability of SIF_{760} for biotic stress detection was investigated. It would be beneficial to explore other spectral regions within the SIF emission regions, as those regions may provide valuable insights for pre-visual stress detection.

Nitrogen (N) is a macronutrient which plays a crucial role in plant development, yield and grain quality, and which is often the dominant limiting factor in photosynthesis (Evans, 1989; Lemaire *et al*., 2008). Accurate field-wide assessments of leaf N concentration (N%) enable more targeted use of N-fertilisers, thereby mitigating the environmental effects of N-overfertilisation while improving crop yields. Standard destructive sampling for leaf N determination relies on the laboratory analysis of leaf tissue using methods such as Kjeldahl digestion and Dumas combustion. Although accurate, these techniques are time-consuming and expensive for monitoring the leaf N status of large areas. In recent decades, the use of remote sensing technologies has increased, particularly through hyperspectral imagery, for mapping the spatial and temporal variations of crop leaf N concentration at paddock-scale (Berger *et al*., 2020).

Recent studies using narrow-band airborne and spaceborne hyperspectral imagers have demonstrated that accurate determination of leaf N concentration can be achieved by combining the radiative transfer model (RTM)-derived leaf biochemical constituents with SIF_{760} acquired from high-resolution airborne hyperspectral imagery (Camino *et al*., 2018; Y. Wang *et al*., 2022a; 2022b). Even though these studies have demonstrated improved leaf N retrievals when including SIF_{760}, the potential of other spectral features within the 650-800 nm SIF emission region to characterise both PSI and PSII photosystems has not yet been explored. Moreover, the potential information extracted from the red spectral region, i.e. SIF quantified at the O_2-B absorption band centred around 687 nm (SIF_{687}), and from the depth of solar Fraunhofer lines (FLs), which are absorption lines in the solar spectrum, could provide valuable insights for improved characterisation of photosynthesis and leaf N variability.

The depth of FLs within particular spectral windows devoid of significant terrestrial absorptions ('pure FLs' hereafter) is practically unaffected by atmospheric scattering, making SIF retrieval at individual pure FLs in these spectral windows nearly insensitive to atmospheric effects (Frankenberg *et al*., 2011; 2018; Guanter *et al*., 2013). With the recently developed sub-nanometer

resolution airborne hyperspectral imagers, it is now possible to investigate the potential of these narrow pure FLs within the SIF emission region. However, the quantification of *in-filling* at individual FLs and its conversion to SIF would require accurate characterisation of the shape of individual FLs in the reference solar irradiance spectrum. This irradiance spectrum either needs to be acquired from the sub-nanometer imager using ground-based reference targets (Wang *et al*., 2022) or from the explicit modelling of the instrument spectral response function (Guanter *et al*., 2012; Sun *et al*., 2018). However, reference irradiance spectrum may not be always available, preventing the quantification of SIF at individual FLs. Since the depths of solar FLs decrease in the presence of SIF (Plascyk and Gabriel, 1975), we hypothesise that, under identical solar conditions, the depth of the distinct pure FLs detected from different vegetation targets within the sub-nanometer airborne hyperspectral imagery can be used as a proxy for SIF, i.e. by assessing the FL depth in relative terms within a single image.

The first part of this study aims to assess the relative contribution of the SIF emitted by each of the two photosystems (PSI and PSII) in explaining leaf N variability across the field. SIF_{760}, SIF_{687} and the depth of distinct pure solar FLs inside PSI and PSII emission regions derived from sub-nanometer airborne hyperspectral imagery were all evaluated. The second part of this study investigates the sensitivity of distinct pure FLs derived from sub-nanometer imagery to differentiate between asymptomatic and symptomatic trees with different stages of disease progression caused by *Vd* infections, comparing their performance against standard methods of SIF quantification using oxygen absorption features.

4.2 Materials and methods

4.2.1 Study sites and field data collection

The first experiment regarding the estimation of leaf nitrogen concentration was conducted at a phenotyping trial site located in Yarrawonga, northeast Victoria, Australia (36°02′55″S, 145°59′02″E) in 2019. According to the Köppen climate classification system, the climate at the field trial location is humid subtropical (Cfa), with average temperature of 16.3 °C and average annual rainfall of 559 mm. The plot sizes were 26 m^2 (2 m × 13 m) and were planted in May 2019. Several cultivated varieties of rainfed wheat were grown under varying physiological conditions and N fertilisation treatments. More details about the study site can be found in Belwalkar *et al*. (2022a).

The second experiment, regarding biotic stress detection, was carried out at a *Vd* infected commercial olive orchard located in Boundary Bend, northwest Victoria, Australia (34°44′23″S, 143°10′27″E) in 2023 (Fig. 4-1a). The region has a Mediterranean climate, with warm dry summers and cool wet winters, and average annual rainfall of 335.8 mm. In December 2022, visual disease severity (SEV) assessments were performed using a scale of 0–3 depending on the proportion of the tree canopy displaying symptoms of the disease. Of the 111 olive trees examined, 32 were deemed to be asymptomatic (SEV = 0), whereas 79 showed signs of disease and were reported as symptomatic (21 trees, SEV = 1; 26 trees, SEV = 2; and 32 trees, SEV = 3; Fig. 4-1c).

4.2.2 Airborne campaigns using hyperspectral imagers

Airborne campaigns operated by the HyperSens Laboratory at the University of Melbourne's Airborne Remote Sensing Facility corresponding to Experiment-1 and Experiment-2 under clear sky conditions were conducted on 9 October 2019 and 31 January 2023, respectively. For both experiments, a sub-nanometer hyperspectral imager (FWHM ≤0.2 nm; 670–780 nm) and a narrow-band hyperspectral imager (FWHM = 5.8 nm; 400–1000 nm) (Headwall Photonics Inc., Fitchburg, MA, USA) were used to acquire airborne hyperspectral imagery with spatial resolutions of 20 cm and

30 cm for Experiment-1 and Experiment-2, respectively (Fig. 4-2). Further details regarding the spectral configuration of the two hyperspectral imagers can be found in Belwalkar *et al*. (2022a).

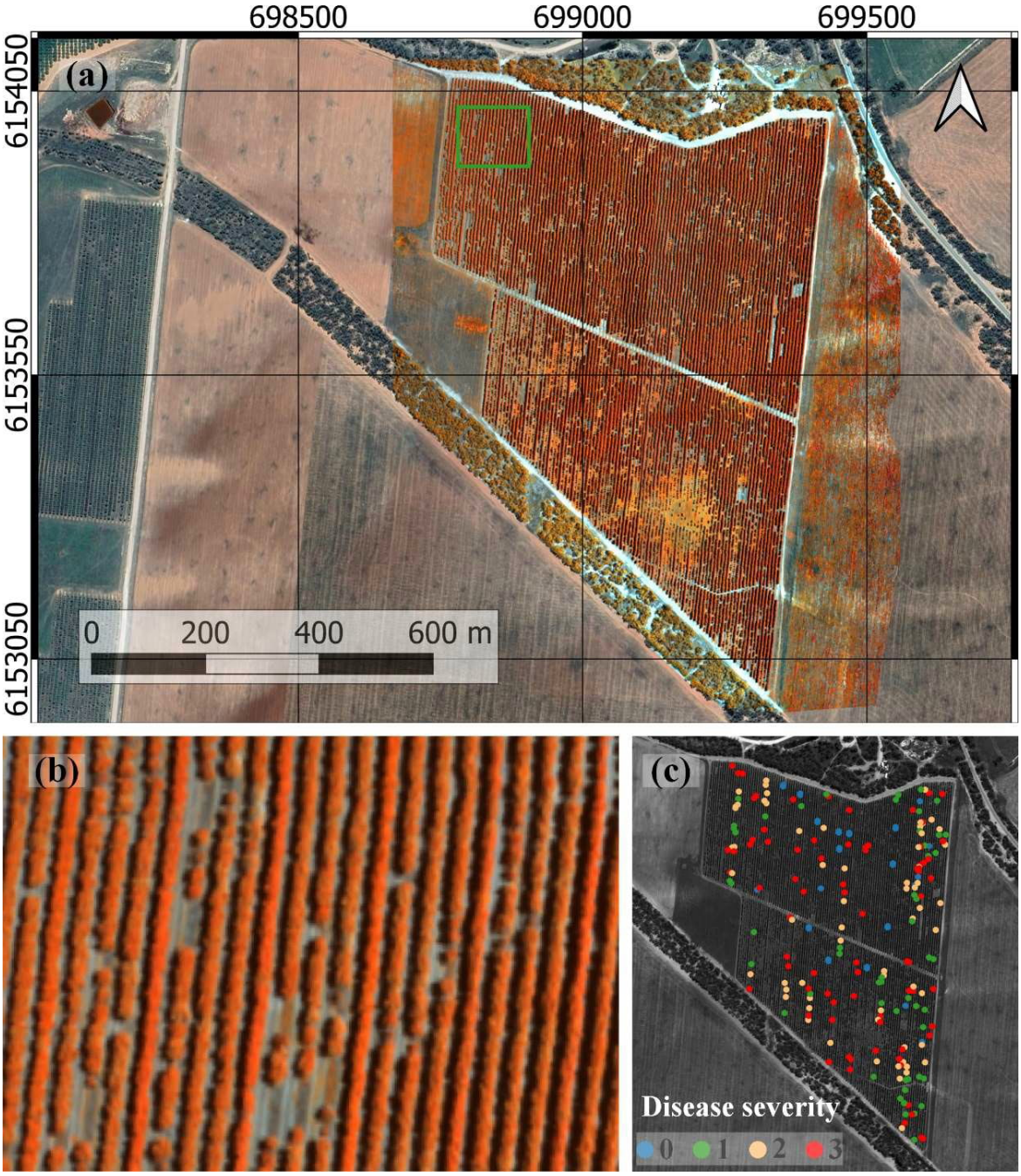

Fig. 4-1. (a) Overview of Experiment-2 at the Boundary Bend study site. (b) Zoomed-in view of tree crowns identified in the scene within the green rectangle in (a). (c) Spatial distribution of visual assessments of *Verticillium dahliae* (*Vd*) infection.

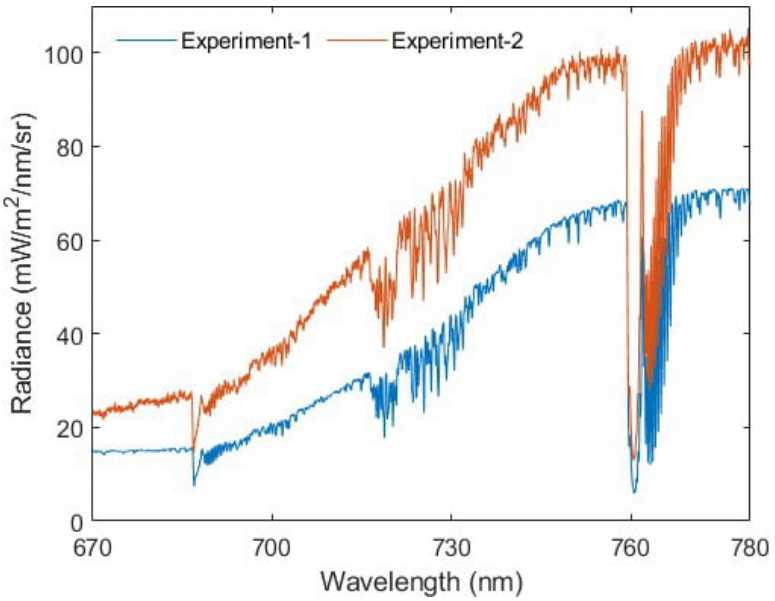

Fig. 4-2. Sample radiance spectra acquired from the sub-nanometer imaging sensor at the two experimental sites.

For Experiment-1, ground spectral measurements were taken concurrently with the flight, using a CC-3 VIS-NIR cosine corrector diffuser attached to an HR-2000 spectrometer (Ocean Insight, Dunedin, FL, USA) with a 0.065-nm FWHM, for continuous measurement of the total incident radiation (Fig. 4-3a). Pure vegetation pixels were extracted within individual wheat plots using a thresholding approach based on the normalised difference vegetation index (NDVI), and mean radiance spectra corresponding to the sub-nanometer imager and mean reflectance spectra from the narrow-band hyperspectral imager were retrieved. Belwalkar *et al.* (2022a) provide a full description of the airborne campaign, data preprocessing, and image correction. In addition, the total leaf N concentration (%) was determined in the laboratory using the Kjeldahl method of destructive testing, with samples consisting of 10–15 leaves randomly selected per plot.

For Experiment-2, four different sets of sub-nanometer resolution radiance imagery covering the entire orchard were acquired within a 40-minute time interval. The total incoming irradiance concurrent with the airborne campaign was calculated using the radiance reflected from a white reference panel (Labsphere Inc., North Sutton, NH, USA) measured by the HR-2000 spectrometer (Fig. 4-3b). Sunlit tree-crown pixels corresponding to individual trees were extracted from each sub-

nanometer radiance imagery using a two-stage approach. In the first stage, automatic object-based segmentation of the sub-nanometer radiance imagery was carried out using Fiji (Abràmoff *et al*., 2004) combining Sauvola's binarisation (Sauvola and Pietikäinen, 2000) methods on the near-infrared band (mean of 774-776 nm), and Phansalkar's thresholding method (Phansalkar *et* al., 2011) on the Normalised Difference Red Edge (NDRE) index. This stage allowed for the separation of pure sunlit tree-crowns from the soil background, as well as within-crown shadows. In the second stage, following Zarco-Tejada *et al*. (2018), a binary watershed-based segmentation using the Euclidean distance map was applied to individual objects obtained in the first stage to extract sunlit tree-crown pixels corresponding to individual trees. Using NDVI and the near-infrared band (800 nm), we followed a similar procedure to extract sunlit tree-crown pixels for individual trees from narrow-band radiance imagery. The sunlit tree-crown pixels were then used to obtain mean radiance spectra for each individual tree from both sub-nanometer and narrow-band imagery.

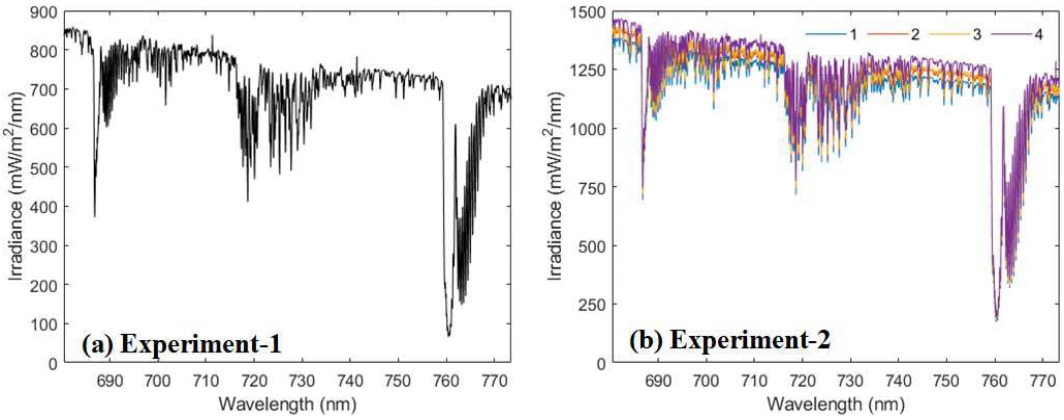

Fig. 4-3. Irradiance spectra obtained from ground-based HR-2000 spectrometer concurrently with the acquisition of sub-nanometer imagery for (a) Experiment-1 and (b) Experiment-2.

4.2.3 Methodology for estimating leaf nitrogen concentration

The irradiance spectra obtained from the HR-2000 spectrometer were convolved to the spectral characteristics of the sub-nanometer imager using Gaussian convolution (Fig. 4-4). Using this convolved irradiance and the mean radiance derived from each plot, SIF_{760} and red SIF (SIF_{687})

were quantified using the *in-filling* approach, employing the Fraunhofer Line Depth (FLD) principle with a total of three spectral bands (3FLD) (Maier *et al*., 2003). Furthermore, we identified 17 pure FLs across the 670–780 nm spectral range of the sub-nanometer imager, excluding regions with significant water vapour and oxygen absorption (Albert *et al*., 2023). The FLs identified were divided into two groups according to their positions in the spectral region. Five of these FLs were located in the red region of the spectrum (670–685 nm, named 'red FLs' here), while the remaining twelve were located in the far-red region (740–759 nm and 770–780 nm, named first and second 'far-red FLs' groups, respectively). The exact locations of the band centres corresponding to all FLs, and the O_2-A and O_2-B oxygen absorption bands are illustrated in Fig. 4-5. The positions of band centres corresponding to all FLs, and oxygen absorption features were computed as the mode of band centres corresponding to all the plots used for the analysis.

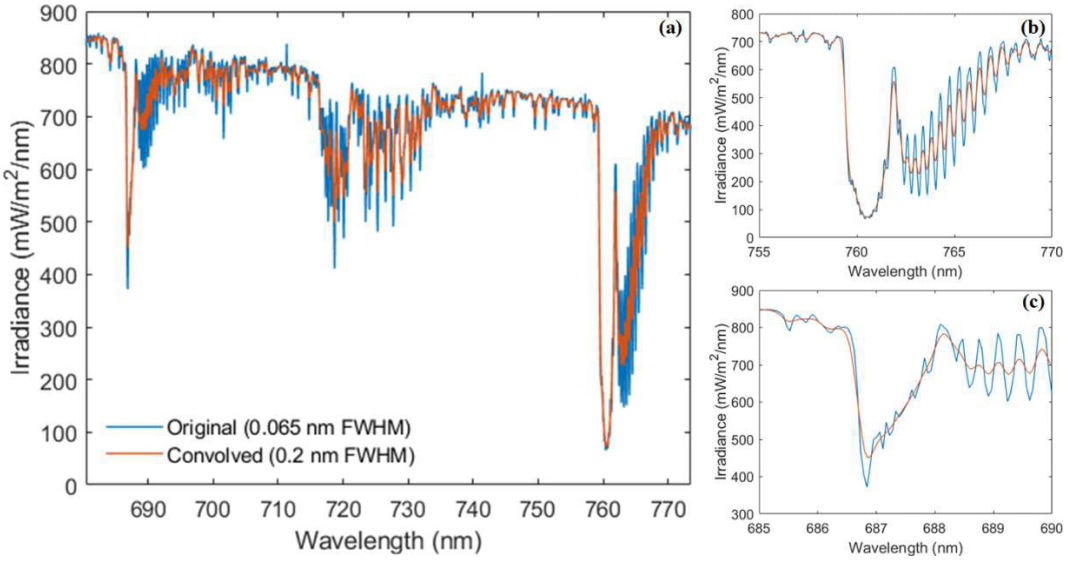

Fig. 4-4. Comparison of original and convolved HR-2000 derived irradiance spectra for Experiment-1: (a) in the entire 680-773 nm spectral region; (b) in the O_2-A absorption region; (c) in the O_2-B absorption region (c).

Unlike the O_2-A absorption feature, the detected FLs are quite narrow, so the assumption of a Gaussian spectral response function for convolving the solar irradiance spectra corresponding to individual FLs is not valid. Hence, instead of SIF, we computed the depth of individual FLs and used FL depth as a proxy for SIF. For each FL, the absolute depth in radiance units was computed as the

difference between the radiance at the left shoulder wavelength and the wavelength at the bottom of the FL. The left shoulder wavelength was selected by searching for the wavelength providing highest radiance within 1 nm of the bottom wavelength (Fig. 4-6).

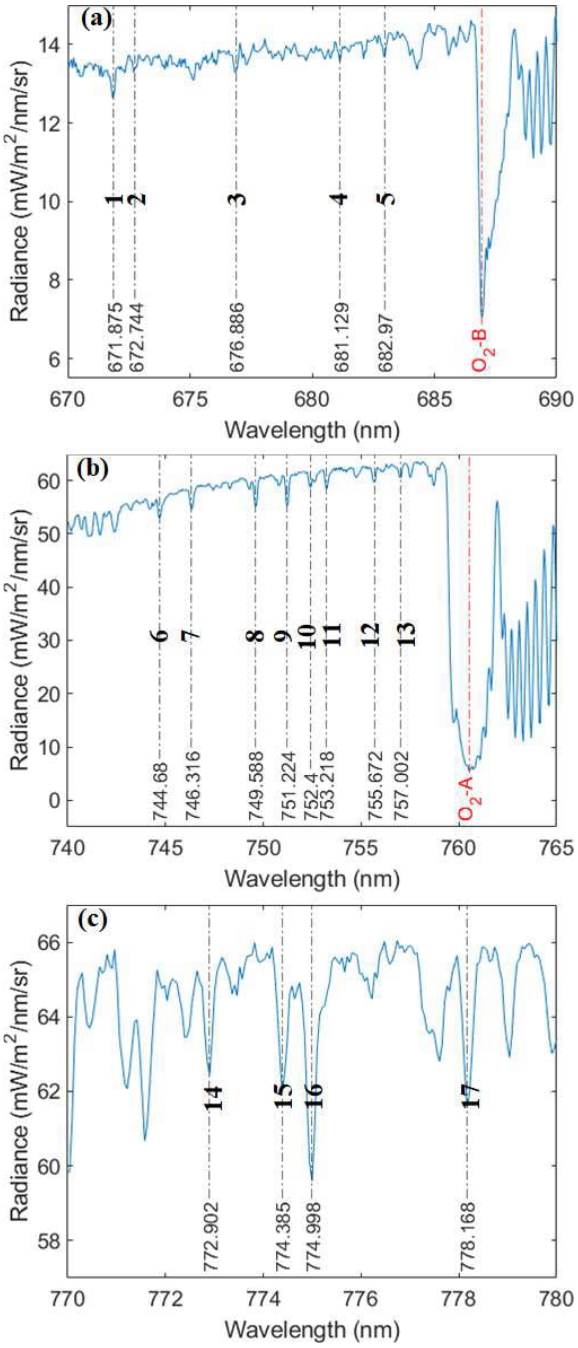

Fig. 4-5. Locations of the band centres corresponding to red FLs (a), group-1 far-red FLs (b), and group-2 far-red FLs (c) shown in dashed black, and oxygen absorption lines (a, b) shown in dashed red identified from the average radiance spectra of one of the plots imaged by the sub-nanometer hyperspectral imager.

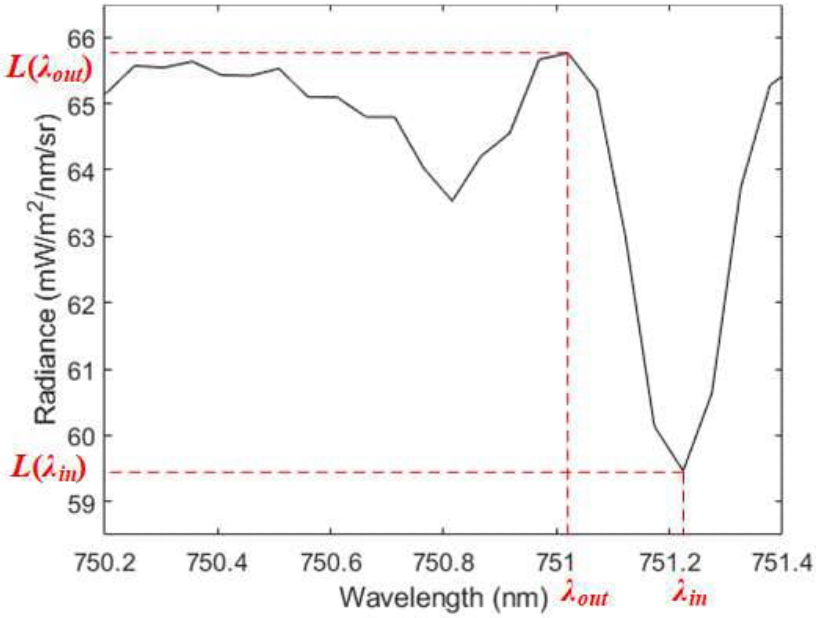

Fig. 4-6. Example of selection of left shoulder wavelength (λ_{out}) and the wavelength at the bottom of the FL (λ_{in}) for calculating absolute FL depth corresponding to $FL_{751.224\ nm}$ using sub-nanometer mean radiance extracted from one of the plots in Experiment-1.

Regression models based on GPR were trained to empirically estimate leaf N concentration using C_{a+b}, SIF_{760}, SIF_{687} and the depth of distinct FLs as a pool of potential predictor variables. C_{a+b}, SIF_{760}, and depth corresponding to a single FL were used to initially train GPR models. Subsequently, GPR models were trained on leaf N estimation using C_{a+b}, and one FL depth each from the red and far-red FL groups to further examine the effect of using FL depths corresponding to both the red and far-red FL groups as predictor variables. The GPR models were trained in parallel (MATLAB parallel computing toolbox) and the hyperparameters were optimised by incorporating Bayesian optimisation into the leave-one-out cross-validation (LOOCV). The performance evaluation of the trained GPR models was carried out using the coefficient of determination (R^2), root-mean-square error (RMSE), and normalised root-mean-square error (nRMSE). To limit random errors, for each possible combination of predictor variables, five GPR models were independently trained, and the average estimate was then used to determine R^2, RMSE, and nRMSE.

Soil-Canopy Observation of Photosynthesis and Energy (SCOPE) (Van der Tol *et al.*, 2009) RTM-based hybrid inversion with random forest regression (Belwalkar *et al.*, 2022b) was used to

estimate C_{a+b} from the mean reflectance spectra obtained from the narrow-band hyperspectral imager in the 400-800 nm spectral region. To determine if the leaf N estimates could be further improved by including SIF emission regions other than the O_2-A absorption band, we used the GPR model developed with C_{a+b} and SIF_{760} as a benchmark. Then we compared against this benchmark by adding the depth of distinct solar FLs into the models. Since PSII largely influences the red spectral region, the contributions of SIF_{687} and red FLs are attributed only to PSII. In contrast, the contributions of SIF_{760} and far-red FLs are attributed to both photosystems.

4.2.4 Methodology for assessing the sensitivity of distinct FLs for biotic stress detection

Similarly to the identification of distinct FLs in Experiment-1, 16 FLs (5 in the red region and 11 in the far-red region) were identified across the 670–776 nm spectral range in Experiment-2. Due to recalibration of the sub-nanometer hyperspectral imager in 2020, the band centres for experiment-2's 16 FLs and Experiment-1's 17 FLs were not identical. The absolute depths for all red and far-red FLs were computed using the methodology described in section 4.2.3. In addition, absolute depths corresponding to both O_2-A and O_2-B absorption features were computed, and the wavelengths with the maximum radiance in the ranges of 755–759 nm for O_2-A and 685–686 nm for O_2-B were chosen as the left shoulder wavelengths. The absorption depths were further normalised using a proxy for photosynthetically absorbed radiation (PAR), which was calculated by spectrally integrating the HR-2000 derived irradiance spectra within the 680–700 nm spectral region corresponding to the acquisition time of each radiance image. This normalisation was required to account for the effect of incoming solar radiation on the absolute depth of the absorption features derived from the four sub-nanometer resolution radiance images at varying acquisition times.

The sensitivity of different absorption features (16 FLs and 2 oxygen features) for detecting *Vd*-induced symptoms was investigated for three different stages of disease progression – early, intermediate, and all. The trees were categorised as either asymptomatic (SEV = 0) or symptomatic (SEV $\geq$ 1) if they exhibited one of three rising disease progression levels. Trees with early-stage

disease were those rated as symptomatic with a SEV of 1; trees in the intermediate stage were those rated as symptomatic with a SEV of 1-2; and trees in all stages were those rated as symptomatic with a SEV of 1-3. To determine if disease symptoms affect absorption features differently over the course of disease, the depths of absorption features of asymptomatic trees were compared to those of symptomatic trees with three levels of severity – SEV = 0 vs. SEV = 1; SEV = 0 vs. SEV ≤2; and SEV = 0 vs. SEV ≥1 – using an Analysis of Variance (ANOVA) statistical test. This analysis of absorption feature depths enabled the assessment of the capability of different absorption features to detect disease progression in relation to the intensity of pathogen-induced stress. Additionally, using the narrow-band radiance imagery, absolute depths corresponding to the O_2-A absorption features were computed to examine the sensitivity of narrow-band derived O_2-A depth for detecting different stages of disease progression and to compare its performance against sub-nanometer derived O_2-A band depth.

4.3 Results and discussion

4.3.1 Leaf N estimation using depths of distinct FLs

GPR models trained with a single FL as one of the three predictor variables produced a total of 17 distinct GPR models (5 models for the red FL group and 12 models for the far-red FL group). Among the red FL group, the performance of the GPR model with FL1 depth was comparable with the benchmark (R^2 = 0.56; RMSE = 0.229%; nRMSE = 5.89%; Fig. 4-7a and 4-7b), whereas the performance of the other four red FL depths did not improve prediction. Among the far-red FLs, the model that included FL_{13} depth showed the highest performance, outperforming the benchmark (R^2 = 0.63; RMSE = 0.21%; nRMSE = 5.41%; Fig. 4-7c).

Since FL_{13} performed the best among all red and far-red FLs, for the next set of GPR models with two FLs and C_{a+b} as predictors, we selected FL_{13} among the far-red FLs and independently

evaluated all five red FLs as potential GPR model predictors. When compared to the benchmark model, the GPR model trained with FL_5 (682.97 nm) and FL_{13} (757.002 nm) had substantially improved leaf N estimation (R^2 = 0.71; RMSE = 0.188%; nRMSE = 4.84%; Fig. 4-7d), with more data points closer to the 1:1 line. The model's performance did not improve further after including more FLs from either of the two FL groups.

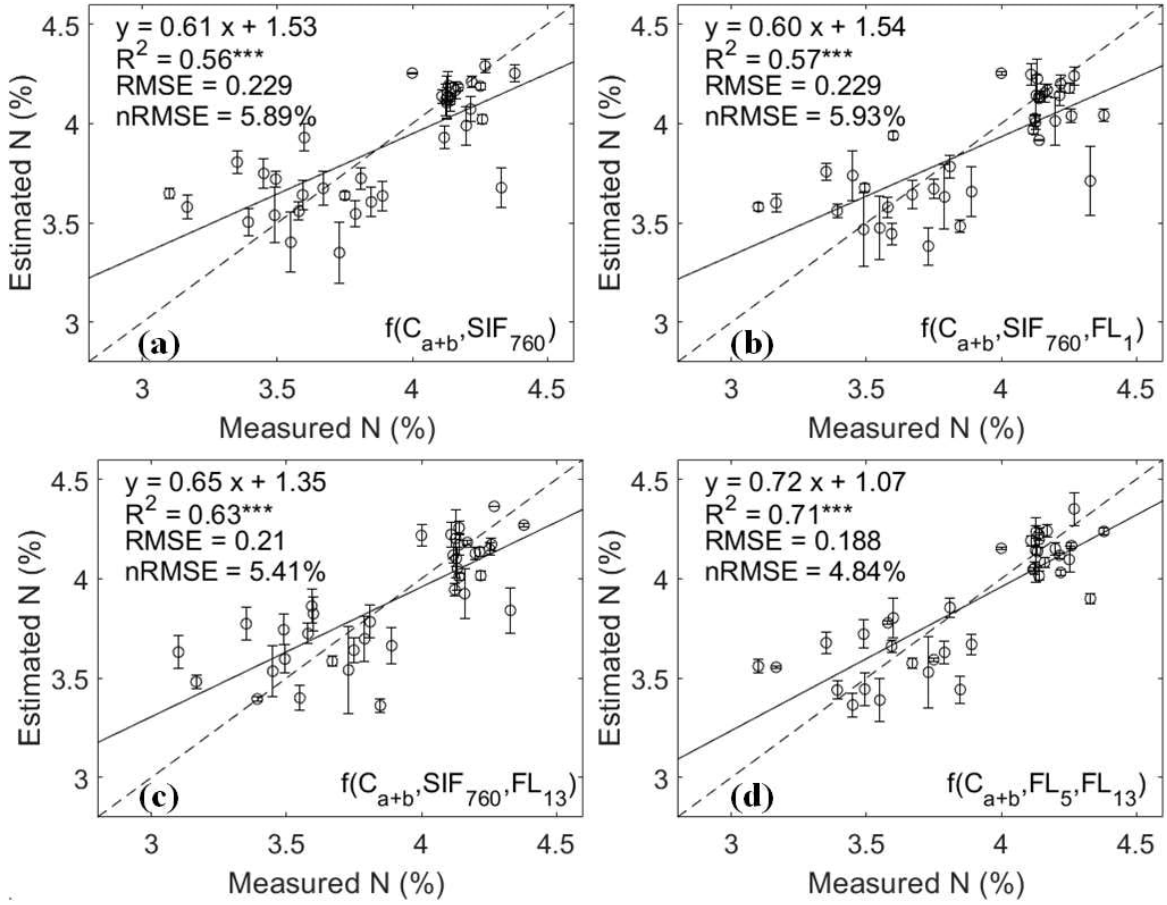

Fig. 4-7. Measured vs estimated mean leaf N concentration using the best GPR models as a function of: (a) C_{a+b} and SIF_{760}; (b) C_{a+b}, SIF_{760}, and best-performing red FL; (c) C_{a+b}, SIF_{760}, and best-performing far-red FL; (d) C_{a+b} and best-performing combination of one red and one far-red FL. The dashed line indicates the 1:1 line. The error bars indicate the standard deviation based on five runs of the GPR model. The GPR model as a function of C_{a+b} and SIF_{760} was used as a benchmark. ****p*-value <0.05.

Furthermore, we found that the model's performance decreased when it included SIF_{687} with any combination of predictor variables. This result could possibly be attributed to the high collinearity observed between C_{a+b} and SIF_{687}. Our results suggest that FL depths corresponding to 757.002 nm

(FL_{13}) and 682.97 nm (FL_5), in conjunction with C_{a+b} estimated by RTM simulations, provided improved estimation of leaf N concentration. These findings of the current exploratory study for the investigation of individual FLs provide a foundation for future research into the use of FLs identified in sub-nanometer imagery for plant phenotyping and precision agriculture applications.

4.3.2 Sensitivity of distinct FLs for biotic stress detection

Firstly, the evaluation of the distribution of relative absorption feature depths corresponding to red FLs, the two far-red FLs groups, and the two oxygen absorption features was carried out using Dunnett's test, comparing them with the asymptomatic trees for early, intermediate, and all stages of disease progression (Figs. C1-C4, Appendix C). The sensitivity of different absorption features identified from sub-nanometer hyperspectral imagery to detect different stages of disease progression caused by *Vd* infection is shown in Fig. 4-8. Only $FL_{671.73\ nm}$, $FL_{756.90\ nm}$, and the O_2-B (686.86 nm) absorption feature were found to be sensitive for detecting the early stage of disease progression. The same three absorption features, along with one additional FL in the red spectral region ($FL_{676.74\ nm}$), were found to be sensitive for both the intermediate and all stages of disease progression. With increasing stress severity levels, the O_2-A (760.48 nm) feature, an additional red FL ($FL_{680.95\ nm}$) and three additional far-red FLs ($FL_{746.22\ nm}$, $FL_{751.12\ nm}$, $FL_{774.28\ nm}$) could detect all stages of disease progression. Among the 16 FLs investigated, nine FLs including two red FLs ($FL_{672.65\ nm}$, $FL_{682.87\ nm}$) and seven far-red FLs ($FL_{744.58\ nm}$, $FL_{749.54\ nm}$, $FL_{752.30\ nm}$, $FL_{753.12\ nm}$, $FL_{755.52\ nm}$, $FL_{772.80\ nm}$, $FL_{774.90\ nm}$) were found to be incapable of distinguishing asymptomatic trees from symptomatic trees at any level of infection (Fig. 4-8). The O_2-A band depth quantified from the narrow-band imagery could only detect all stages of disease progression showing agreement with the trend observed for the O_2-A band depth quantified from the sub-nanometer imagery.

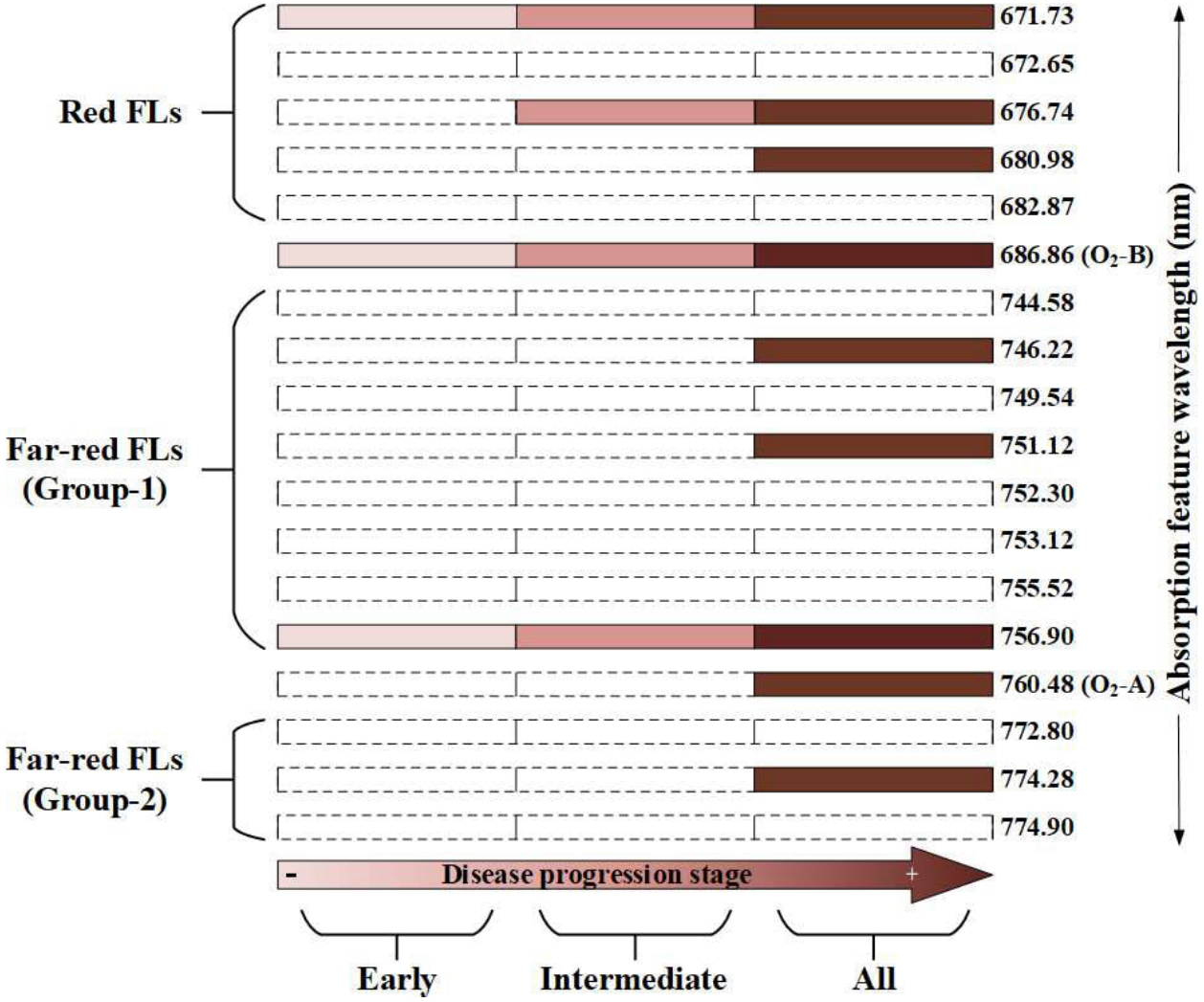

Fig. 4-8. Sensitivity of different absorption features (FLs, O_2-A and O_2-B band depths) identified from sub-nanometer hyperspectral imagery to distinguish asymptomatic trees from symptomatic trees with varying stages of disease progression caused by *Vd* infection. The comparison between symptomatic and asymptomatic trees was conducted using a one-way ANOVA test with a significance level of 0.05.

Some individual FLs detected from sub-nanometer imagery were found to be sensitive to *Vd*-induced symptoms at varying stages of disease progression, suggesting that further research into their potential is needed. Specifically, $FL_{671.73\ nm}$ and $FL_{756.90\ nm}$ were able to distinguish asymptomatic trees from those in the early stage of disease progression, which is crucial to allow producers to make decisions for successful containment of disease. Although it would be most beneficial to quantify SIF levels corresponding to these distinct FLs to better understand biotic stress-induced dynamics, our

exploratory analysis using FL depth is the first step towards realising the potential of these narrow Fraunhofer lines for biotic and abiotic stress detection.

4.4 Conclusions

1. The quantification of the depth of narrow Fraunhofer lines in the SIF emission region improves leaf N estimations and the detection of biotic stress in vegetation.
2. With RMSEs of less than 0.19%, the best results for leaf N estimation were achieved by the regression model constructed using C_{a+b}, red FL closest to O_2-B band (682.97 nm), and far-red FL closest to O_2-A band (757.002 nm).
3. It was found that the red FL furthest from the O_2-B band (671.73 nm) and one far-red FL closest to the O_2-A band (756.90 nm), along with the O_2-B absorption feature, could detect the three stages of disease progression (early, intermediate, and all). As expected, more FLs were found to be sensitive as levels of disease progression increased.
4. The results of this exploratory investigation of FL's potential provides a foundation for future research on the use of FLs identified from sub-nanometer imagery in the context of precision agriculture, plant physiology monitoring, and for the detection of biotic and abiotic vegetation stress.

References

Albert, L.P., Cushman, K.C., Zong, Y., Allen, D.W., Alonso, L., Kellner, J.R., 2023. Sensitivity of solar-induced fluorescence to spectral stray light in high resolution imaging spectroscopy. Remote Sens. Environ. 285, 113313.

Atzberger, C., 2013. Advances in remote sensing of agriculture: context description, existing operational monitoring systems and major information needs. Remote Sens. 5, 949–981.

Belwalkar, A., Poblete, T., Longmire, A., Hornero, A., Hernandez-Clemente, R., Zarco-Tejada, P.J., 2022a. Evaluation of SIF retrievals from narrow-band and sub-nanometer airborne hyperspectral imagers flown in tandem: modelling and validation in the context of plant phenotyping. Remote Sens. Environ. 273, 112986.

Belwalkar, A., Poblete, T., Hornero, A., Zarco-Tejada, P.J., 2022b. Accounting for the spectral resolution on SIF retrieval from a narrow-band airborne imager using SCOPE. In: Proc. IEEE International Geoscience and Remote Sensing Symposium (IGARSS), 17–22 July, Kuala Lumpur, Malaysia, pp. 5440-5443.

Berger, K., Machwitz, M., Kycko, M., Kefauver, S. C., Van Wittenberghe, S., Gerhards, M., Verrelst, J., Atzberger, C., van der Tol, C., Damm, A., Rascher, U., Herrmann, I., Paz, V. S., Fahrner, S., Pieruschka, R., Prikaziuk, E., Buchaillot, Ma. L., Halabuk, A., Celesti, M., … Schlerf, M. (2022). Multi-sensor spectral synergies for crop stress detection and monitoring in the optical domain: A review. Remote Sens. Environ. 280, 113198.

Berger, K., Verrelst, J., Féret, J.B., Wang, Z., Wocher, M., Strathmann, M., Danner, M., Mauser, W., Hank, T., 2020. Crop nitrogen monitoring: Recent progress and principal developments in the context of imaging spectroscopy missions. Remote Sens. Environ. 242, 111758.

Calderón, R., Navas-Cortés, J.A., Lucena, C., Zarco-Tejada, P.J., 2013. High-resolution airborne hyperspectral and thermal imagery for early detection of Verticillium wilt of olive using fluorescence, temperature and narrow-band spectral indices. Remote Sens. Environ. 139, 231–245.

Calderón, R., Navas-Cortés, J.A., Zarco-Tejada, P.J., 2015. Early detection and quantification of Verticillium wilt in olive using hyperspectral and thermal imagery over large areas. Remote Sens. 7, 5584–5610.

Camino, C., Calderón, R., Parnell, S., Dierkes, H., Chemin, Y., Román-Écija, M., Montes-Borrego, M., Landa, B.B., Navas-Cortes, J.A., Zarco-Tejada, P.J., Beck, P.S.A., 2021. Detection of Xylella fastidiosa in almond orchards by synergic use of an epidemic spread model and remotely sensed plant traits. Remote Sens. Environ. 260, 112420.

Camino, C., González-Dugo, V., Hernández, P., Sillero, J.C., Zarco-Tejada, P.J., 2018. Improved nitrogen retrievals with airborne-derived fluorescence and plant traits quantified from VNIR-SWIR hyperspectral imagery in the context of precision agriculture. Int. J. Appl. Earth Obs. Geoinf. 70, 105-117.

Cogato, A., Meggio, F., De Antoni Migliorati, M., Marinello, F., 2019. Extreme weather events in agriculture: a systematic review. Sustain. 11, 2547.

Evans, J.R., 1989. Photosynthesis and nitrogen relationships in leaves of C3 plants. Oecologia, 78, 9-19.

Fernández-Escobar, R., De la Rosa, R., Leon, L., Gomez, J.A., Testi, L., Orgaz, F., GilRibes, J.A., Quesada-Moraga, E., Trapero, A., Msallem, M., 2013. Evolution and sustainability of the olive production systems. Opt. Mediterraneennes 106, 11–42.

Frankenberg, C., Butz, A., Toon, G.C., 2011. Disentangling chlorophyll fluorescence from atmospheric scattering effects in O_2 A-band spectra of reflected sun-light. Geophys. Res. Lett. 38, L03801.

Frankenberg, C., Köhler, P., Magney, T.S., Geier, S., Lawson, P., Schwochert, M., McDuffie, J., Drewry, D.T., Pavlick, R., Kuhnert, A., 2018. The chlorophyll fluorescence imaging spectrometer (CFIS), mapping far red fluorescence from aircraft. Remote Sens. Environ. 217, 523–536.

Gramaje, D., Pérez-Serrano, V., Montes-Borrego, M., Navas-Cortés, J.A., Jiménez-Díaz, R.M., Landa, B.B., 2013. A comparison of real-time PCR protocols for the quantitative monitoring of asymptomatic olive infections by Verticillium dahliae pathotypes. Phytopathology, 103, 1058-1068.

Guanter, L., Frankenberg, C., Dudhia, A., Lewis, P.E., Gómez-Dans, J., Kuze, A., Suto, H., Grainger, R.G., 2012. Retrieval and global assessment of terrestrial chlorophyll fluorescence from GOSAT space measurements. Remote Sens. Environ. 121, 236–251.

Guanter, L., Rossini, M., Colombo, R., Meroni, M., Frankenberg, C., Lee, J.-E., Joiner, J., 2013. Using field spectroscopy to assess the potential of statistical approaches for the retrieval of sun-induced chlorophyll fluorescence from ground and space. Remote Sens. Environ. 133, 52–61.

Jimenez-Diaz, R.M., Cirulli, M., Bubici, G., del Mar Jimenez-Gasco, M., Antoniou, P.P., Tjamos, E.C., 2012. Verticillium wilt, a major threat to olive production: current status and future prospects for its management. Plant disease, 96, 304-329.

Lemaire, G., Jeuffroy, M.H., Gastal, F., 2008. Diagnosis tool for plant and crop N status in vegetative stage: Theory and practices for crop N management. Eur. J. Agron. 28, 614-624.

Maier, S.W., Günther, K.P., Stellmes, M., 2003. Sun-induced fluorescence: a new tool for precision farming. In: Schepers, J., VanToai, T. (Eds.), Digital Imaging and Spectral Techniques: Applications to Precision Agriculture and Crop Physiology. ASA Spec. Publ. 66. ASA, CSSA, and SSSA, Madison (Wisconsin), USA, pp. 209–222.

Plascyk, J.A., Gabriel, F.C., 1975. The Fraunhofer Line Discriminator MKII – an airborne instrument for precise and standardized ecological luminescence measurement. IEEE Trans. Instrum. Meas. 24, 306–313.

Pegg, G.F., Brady, B.L., 2002. Verticillium wilts. CABI, Wallingford, UK.

Poblete, T., Navas-Cortes, J.A., Camino, C., Calderon, R., Hornero, A., Gonzalez-Dugo, V., Landa, B.B., Zarco-Tejada, P.J., 2021. Discriminating Xylella fastidiosa from Verticillium dahliae infections in olive trees using thermal- and hyperspectral-based plant traits. ISPRS J. Photogramm. Remote Sens. 179, 133–144.

Poblete, T., Navas-Cortes, J.A., Hornero, A., Camino, C., Calderon, R., Hernandez-Clemente, R., Landa, B.B., Zarco-Tejada, P.J., 2023. Detection of symptoms induced by vascular plant pathogens in tree crops using high-resolution satellite data: Modelling and assessment with airborne hyperspectral imagery. Remote Sens. Environ. 295, 113698.

Schmidhuber, J., Tubiello, F. N., 2007. Global food security under climate change. Proc. Natl. Acad. Sci. U.S.A. 104, 19703-19708.

Stokstad, E., 2015. Italy's olives under siege. Science 348, 620-620.

Sun, Y., Frankenberg, C., Jung, M., Joiner, J., Guanter, L., Köhler, P., Magney, T.S., 2018. Overview of solar-induced chlorophyll fluorescence (SIF) from the orbiting carbon observatory-2: retrieval, cross-mission comparison, and global monitoring for GPP. Remote Sens. Environ. 209, 808–823.

Van der Tol, C., Verhoef, W., Timmermans, J., Verhoef, A., Su, Z., 2009. An integrated model of soil-canopy spectral radiances, photosynthesis, fluorescence, temperature and energy balance. Biogeosci. 6, 3109-3129.

Wang, R., Gamon, J.A., Hmimina, G., Cogliati, S., Zygielbaum, A.I., Arkebauer, T.J., Suyker, A., 2022. Harmonizing solar induced fluorescence across spatial scales, instruments, and extraction methods using proximal and airborne remote sensing: A multi-scale study in a soybean field. Remote Sens. Environ. 281, 113268.

Wang, Y., Suarez, L., Gonzalez-Dugo, V., Ryu, D., Moar, P., Zarco-Tejada, P.J., 2022b. Leaf nitrogen assessment with ISS DESIS imaging spectrometer as compared to high-resolution airborne hyperspectral imagery. In: Proc. IEEE International Geoscience and Remote Sensing Symposium (IGARSS), 17–22 July, Kuala Lumpur, Malaysia, pp. 5444-5447.

Wang, Y., Suarez, L., Poblete, T., Gonzalez-Dugo, V., Ryu, D., Zarco-Tejada, P.J., 2022a. Evaluating the role of solar-induced fluorescence (SIF) and plant physiological traits for leaf nitrogen assessment in almond using airborne hyperspectral imagery. Remote Sens. Environ. 279, 113141.

Zampieri, M., Ceglar, A., Dentener, F., Toreti, A., 2017. Wheat yield loss attributable to heat waves, drought and water excess at the global, national and subnational scales. Environ. Res. Lett. 12, 064008.

Zarco-Tejada, P.J., Camino, C., Beck, P.S.A., Calderon, R., Hornero, A., Hernández-Clemente, R., Kattenborn, T., Montes-Borrego, M., Susca, L., Morelli, M., Gonzalez-Dugo, V., North, P.R.J., Landa, B.B., Boscia, D., Saponari, M., Navas-Cortes, J.A., 2018. Previsual symptoms of Xylella fastidiosa infection revealed in spectral plant-trait alterations. Nat. Plants 4, 432–439.

Zarco-Tejada, P.J., Poblete, T., Camino, C., Gonzalez-Dugo, V., Calderon, R., Hornero, A., Hernandez-Clemente, R., Román-Écija, M., Velasco-Amo, MP., Landa, BB., Beck, PSA., Saponari, M., Boscia, D., Navas-Cortes, JA., 2021. Divergent abiotic spectral pathways unravel pathogen stress signals across species. Nat. Commun. 12, 6088.

Chapter 5

Conclusions

The results of each study have been thoroughly and specifically discussed in the preceding chapters. This chapter's objective is to provide a concise overview of the research, contextualise the findings, emphasise their applications and limitations, and suggest future research directions.

5.1 Salient features and research outcomes

The research undertaken for this thesis establishes the utility of SIF_{760} quantified by airborne narrow-band imaging sensors for plant physiology monitoring, plant phenotyping, and precision agriculture applications. It also outlines the potential for these purposes of using narrow solar Fraunhofer lines detected from sub-nanometer resolution imaging sensors. Some of the salient features of this research are:

- Airborne SIF_{760} derived from a narrow-band imaging sensor (5.8-nm FWHM) exhibited strong correlations with both ground-based and airborne sub-nanometer resolution SIF_{760} estimates, demonstrating its utility for stress-detection applications requiring the quantification of relative SIF_{760} differences.
- A modelling framework integrating SCOPE RTM and machine learning methods was proposed to scale the overestimated narrow-band SIF_{760} levels to appropriate absolute levels, which allow the use of narrow-band quantified SIF_{760} for applications that require SIF_{760} estimates in absolute physical units.
- The inclusion of the depth quantity calculated at the Fraunhofer lines derived from sub-nanometer imagery (≤0.2 nm FWHM) around the two oxygen absorption bands improved the

estimates of leaf nitrogen concentration as compared to standard methods based on SIF_{760} and chlorophyll content.

- The depth of individual Fraunhofer lines derived from sub-nanometer imagery demonstrated sensitivity to the different stages of disease progression caused by *Verticillium dahlia* infections. This finding lays the framework for further investigation into the utility of FLs for plant physiology monitoring applications.

5.2 General conclusions

Hyperspectral imaging of SIF can be used as a proxy for vegetation stress and an indicator of crop photosynthetic activity for large-scale plant phenotyping and stress detection applications. The extremely low strength of the SIF signal (1-2% of the total incoming solar radiation) necessitates the use of sub-nanometer resolution sensors for its accurate estimation. Improving the spectral resolution of imaging sensors onboard airborne platforms has been a focus of technological development over the past decade, leading to the development of sub-nanometer resolution imaging sensors for accurate SIF quantification. However, their high cost and operational complexity prevent their widespread use in the context of precision agriculture, plant physiology monitoring and stress detection applications.

Although a few theoretical studies have evaluated the impact of the spectral configuration of sensors on SIF accuracy, the literature lacks studies focusing on such assessments in practical applications with airborne hyperspectral imaging sensors. This thesis examined the applicability of cost-effective narrow-band imaging sensors as an alternative to sub-nanometer imaging sensors for the precise estimation of SIF_{760} in physical units and absolute levels. In particular, the application of a modelling methodology integrating RTM and machine learning algorithms resulted in improved SIF_{760} estimates derived from a narrow-band imaging sensor in absolute physical units. Improved leaf nitrogen estimates and the ability to differentiate between disease stages when detecting biotic-

induced stress in infected vegetation were additional outcomes of an exploratory study designed to evaluate the prospects of using individual FL depths derived from the sub-nanometer imaging sensor.

First, a dataset from three plant phenotyping experiments integrating narrow-band hyperspectral imagery, sub-nanometer imagery, field observations, and radiative transfer modelling demonstrated the reliability of narrow-band imagery for detecting relative SIF_{760} variability induced by variable nitrogen fertiliser application across a field. Strong significant correlations were found between SIF_{760} quantified by both narrow-band and sub-nanometer imaging sensors flown in tandem, demonstrating consistency across experimental wheat and maize phenotyping sites and airborne campaigns conducted at different times and flight altitudes, and in different years. Although strongly correlated with both ground-based and sub-nanometer resolution SIF_{760} estimates, the narrow-band imaging sensor yielded larger SIF_{760} estimates than the typical range of 0–3 $mW/m^2/nm/sr$ expected from healthy vegetation. The effect of spectral configuration on SIF accuracy was observed in the elevated SIF_{760} values obtained from the narrow-band imagery. This limits the applicability of narrow-band SIF_{760} levels to only those investigations that require relative assessment of SIF variability in the field. However, if the overestimated narrow-band SIF_{760} estimates are readjusted to appropriate absolute physical levels via modelling, narrow-band imaging sensor's low cost and light weight could enable the operational collection of high-spatial resolution fluorescence data for diverse applications. The next part of this thesis was therefore focused on improving the absolute SIF_{760} levels derived from narrow-band imaging sensors using modelling methods based on the integration of machine learning and radiative transfer models.

Since plant pigments and canopy structure greatly affect TOC SIF, there was a need for research into the role that leaf-biochemical and structural traits might play in improving narrow-band SIF_{760} estimations. Of the seven-leaf biochemical and structural traits evaluated using simulated data corresponding to resolutions ranging from 2–6 nm FWHM, C_{a+b}, LAI, and $LIDF_a$ showed the highest sensitivity for estimating SIF_{760} at 1-nm FWHM. Incorporating leaf biochemical and structural traits

could be a useful strategy for enhancing the interpretation of relative SIF_{760} levels derived from narrow-band imaging sensors, as evidenced by validations performed for the two airborne datasets with simultaneously acquired sub-nanometer resolution airborne data with a RMSE of 4.5–16%. Extensive validations conducted for SCOPE-simulated datasets corresponding to other resolutions ranging from 2–6 nm demonstrated consistency with the results obtained from the narrow-band imaging sensor, illustrating the robustness of the modelling approach.

The concluding work for this thesis focused on an exploratory analysis of the prospects of individual Fraunhofer lines derived from sub-nanometer imagery, which had not been explored to date and could potentially yield important insights into the physiological status of vegetation. It was demonstrated that incorporating the depths of two distinct FLs proximal to oxygen absorption features improved leaf nitrogen estimations, as compared to recently proposed approaches involving RTM-derived leaf-biochemical constituents and SIF_{760}. Furthermore, the activation of separate FLs in the red and far-red spectral range was found to be correlated with three stages of disease progression due to *Verticilium dahliae* infections. The O_2-B feature, one red FL, and one far-red FL were all found to be sensitive for the early, intermediate, and all stages. As the level of disease stress increased from early to intermediate and from intermediate to all, more FLs became sensitive for differentiating symptomatic from asymptomatic trees.

The first results from this exploratory research suggest that it would be worthwhile to dive deeper into the potential benefits of these narrow FLs, in particular by quantifying the SIF associated with specific FLs, in order to better understand and manage the factors that influence plant health. This is particularly important in the context of stress detection and plant physiology monitoring applications using airborne imaging sensors. In such studies, SIF_{760} has typically been used as a proxy for stress. However, the need for accurate characterisation of atmospheric effects in the O_2-A absorption region introduces uncertainties into the retrieval of SIF_{760}. Since pure FLs are insensitive to atmospheric effects, quantifying SIF at individual FLs provides an appealing alternative to the use

of SIF_{760}. However, it remains challenging to achieve the high SNR needed for accurate SIF estimation with FLD-based approaches at such narrow absorption features.

5.3 Limitations

This research has the following limitations:

- Narrow-band SIF_{760} estimates were compared to ground-based and airborne sub-nanometer SIF_{760} estimates at plant phenotyping experimental sites growing wheat and maize under nutritional variability. Further research is needed to evaluate the robustness of narrow-band SIF_{760} quantification in complex heterogenous canopies due to the potentially increased effects of shadows and within-crown multiple scattering processes.
- Due to the use of SCOPE RTM, which is a one-dimensional model, the narrow-band SIF_{760} scaling methodology cannot be readily applied to complex heterogeneous canopies. Further validation is required for complex canopies using 3-D modelling approaches.
- Narrow-band SIF_{760} estimates were scaled using a modelling strategy that involved creating RTM-based simulated training datasets that reflected the actual field conditions observed at a given study site. As a result, the trained model is not transferable to new environments due to a lack of generalisation capabilities.
- The need for accurate characterisation of the shape of distinct narrow Fraunhofer line absorption features in the solar irradiance spectrum prevents the quantification of SIF corresponding to distinct narrow Fraunhofer lines, so this research used the depth of the Fraunhofer lines as proxy for SIF.

5.4 Future directions

The following are some possible avenues for additional research:

- To better understand how canopy structure, plant physiological status, and meteorological factors influence narrow-band SIF_{760} levels and its relationship with sub-nanometer SIF_{760} estimates, large-scale airborne campaigns could be conducted over a variety of canopies under varying physiological and environmental conditions. Such assessment is particularly important for canopies impacted by biotic- and abiotic-induced stress.
- More research is needed to identify a methodology based on three-dimensional RTMs to properly characterise heterogenous canopies that will enable understanding of the impact of the clumping effect in the context of scaling narrow-band SIF_{760} estimates.
- Developing a novel retrieval method targeting SIF estimation at distinct Fraunhofer lines found to be sensitive for biotic and abiotic stress detection.
- Evaluating the capability of SIF derived from distinct Fraunhofer lines detected from sub-nanometer resolution airborne imagery to distinguish between pre-visual biotic- and abiotic-induced stress.

Appendices

Appendix A: Supplementary Material for Chapter-2

Table A-1. Definitions and the assigned variation ranges of all input parameters of the Soil Canopy Observation, Photochemistry and Energy fluxes (SCOPE) model.

Parameter	Definition	Range/Value	Unit
FLUSPECT			
C_{ab}	Leaf chlorophyll concentration	10–50	$\mu g \cdot cm^{-2}$
C_{ca}	Leaf carotenoid concentration	2.5–12.5 ($C_{ab}/4$)	$\mu g \cdot cm^{-2}$
C_{dm}	Leaf dry matter content	0.001–0.05	$g \cdot cm^{-2}$
C_w	Equivalent water thickness in leaves	0.001–0.05	cm
C_s	Leaf senescence parameters	0	-
C_{ant}	Anthocyanin content	1	$\mu g \cdot cm^{-2}$
N	Leaf structure parameter	1.2–1.8	-
ρ(thermal)	Broadband leaf thermal reflectance	0.01	-
τ(thermal)	Broadband leaf thermal transmittance	0.01	-
Leaf biochemical			
Vcmo	Maximum carboxylation capacity	20–120	$\mu mol \cdot m^{-2} s^{-1}$
m	Ball-Berry stomatal parameter (slope)	8	-
B_0	Ball-Berry stomatal parameter (intercept)	0.01	-
Type	Photochemical pathway	0 (C3)	-
K_v	Extinction coefficient for vertical Vcmax profile	0.64	-
Rdparam	Parameter for dark respiration	0.015	-
Tyear	Mean annual temperature	15	ºC
β	Fraction of photons partitioned to PSII	0.51	-
kNPQs	Rate constant of sustained thermal dissipation	0	s^{-1}
qLs	Fraction of functional reaction centers	1	-
stress factor	Stress factor to reduce Vcmax	1	-
Fluorescence			
fqe	Fluorescence quantum yield efficiency at photosystem level	0.001–0.015	-
Soil			
spectrum	Type of soil reflectance spectrum	1 (type 1)	-
rss	Soil resistance for evaporation from the pore space	500	$s \cdot m^{-1}$
rs_t	Broadband soil thermal reflectance	0.06	-
cs	Specific heat capacity of the soil	1180	$J \cdot kg^{-1} \cdot K^{-1}$
ρ_s	Specific mass of the soil	1800	$kg \cdot m^{-3}$
λ_s	Heat conductivity of the soil	1.55	$J \cdot m^{-1} \cdot K^{-1}$

SMC	Volumetric soil moisture content in the root zone	25	-
BSMBrightness	BSM model parameter for soil brightness	0.5	-
BSMlat	BSM model parameter 'lat'	25	-
BSMlon	BSM model parameter 'long'	45	-
Canopy			
LAI	Leaf area index	2–6	$m^2 \cdot m^{-2}$
hc	Vegetation height	2	m
$LIDF_a$	Leaf inclination parameter for the mean leaf zenith angle	-1–0	-
$LIDF_b$	Bimodality of the leaf angle distribution	0	-
leafwidth	Leaf width	0.1	m
Meteorological			
z	Measurement height of meteorological data	5	m
Rin	Broadband incoming shortwave radiation (0.4–2.5 um)	600–1000	$W \cdot m^{-2}$
Ta	Air temperature	19.2*	°C
Rli	Broadband incoming longwave radiation	300	$W \cdot m^{-2}$
p	Air pressure	1002.8*	hPa
ea	Atmospheric vapor pressure	15	hPa
u	Wind speed at height z	2	$m \cdot s^{-1}$
C_a	Atmospheric CO_2 concentration	410	ppm
O_a	Atmospheric O_2 concentration	209	per mile
Angles			
tts	Solar zenith angle	35.42	deg.
tto	Observation zenith angle	0	deg.
ψ	Azimuthal difference between solar and observation angle	0	deg.

*Meteorological variables retrieved from portable weather station during the airborne campaign

Appendix B: Supplementary Material for Chapter-3

We assessed the feasibility of using narrow-band derived FCVIP and NIRvP as predictor variables for estimating SIF_{760} at 1-nm FWHM using SCOPE-simulated datasets. The method consisted of building two linear models with NIRvP and FCVIP as the predictor variables to estimate SIF_{760} at 1-nm FWHM from 5.8-nm FWHM data (denoted Simulated Dataset-$3_{site\ 1}$ and Simulated Dataset-$3_{site\ 2}$ in this study). The performance of these linear models was then validated using another independent dataset (Simulated Dataset-4) for both sites and then compared with that of the linear models built using $SIF_{760\text{-}3FLD}$ at 5.8-nm FWHM as the predictor variable. PAR was estimated by spectrally integrating irradiance spectra at 1-nm FWHM from 400–700 nm to replicate field conditions. In this assessment, the linear model built using $SIF_{760\text{-}3FLD}$ at 5.8-nm FWHM outperformed the two linear models based on NIRvP and FCVIP (Fig. B-1). The differences in model performance may be attributed to the stronger correlation between 1-nm FWHM $SIF_{760\text{-}3FLD}$ and 5.8-nm FWHM $SIF_{760\text{-}3FLD}$ than NIRvP and FCVIP calculated at 5.8-nm FWHM (Fig. B-2).

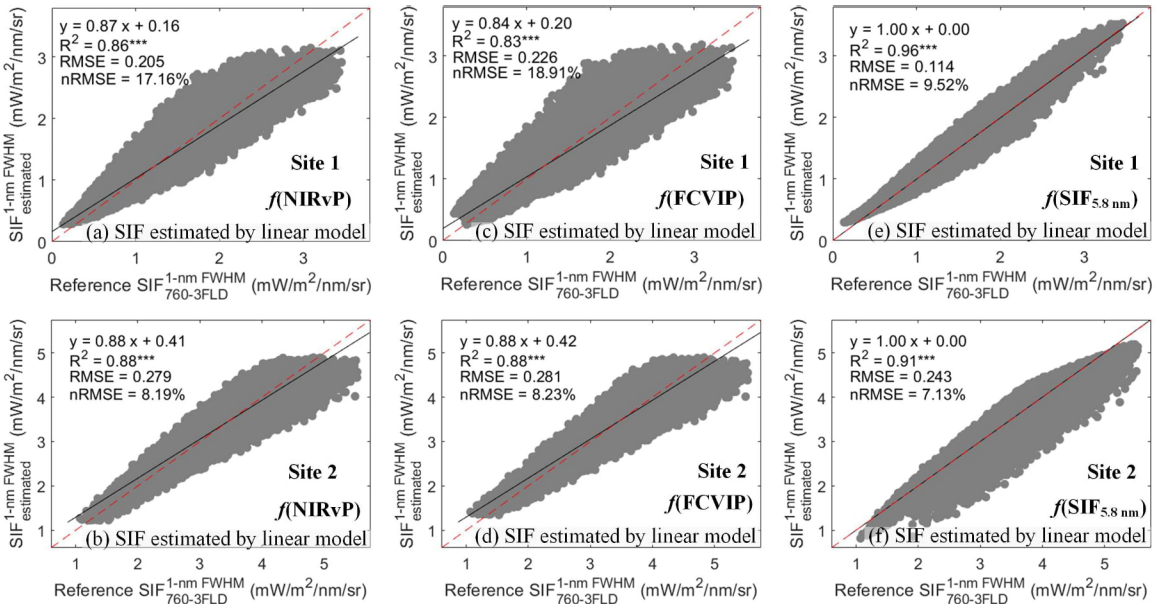

Fig. B-1. Relationships between the $SIF_{760\text{-}3FLD}$ at the default 1-nm FWHM simulated by SCOPE (used here as the reference SIF) and the SIF_{760} estimated at 1-nm FWHM by the linear model using NIRvP (a, b), FCVIP (c, d) and $SIF_{760\text{-}3FLD}$ at 5.8-nm FWHM (e, f) as the predictor for SCOPE-simulated test datasets corresponding to Site 1 and Site 2. The red dashed and black solid lines depict the 1:1 line and regression line, respectively. ***p-value < 0.001.

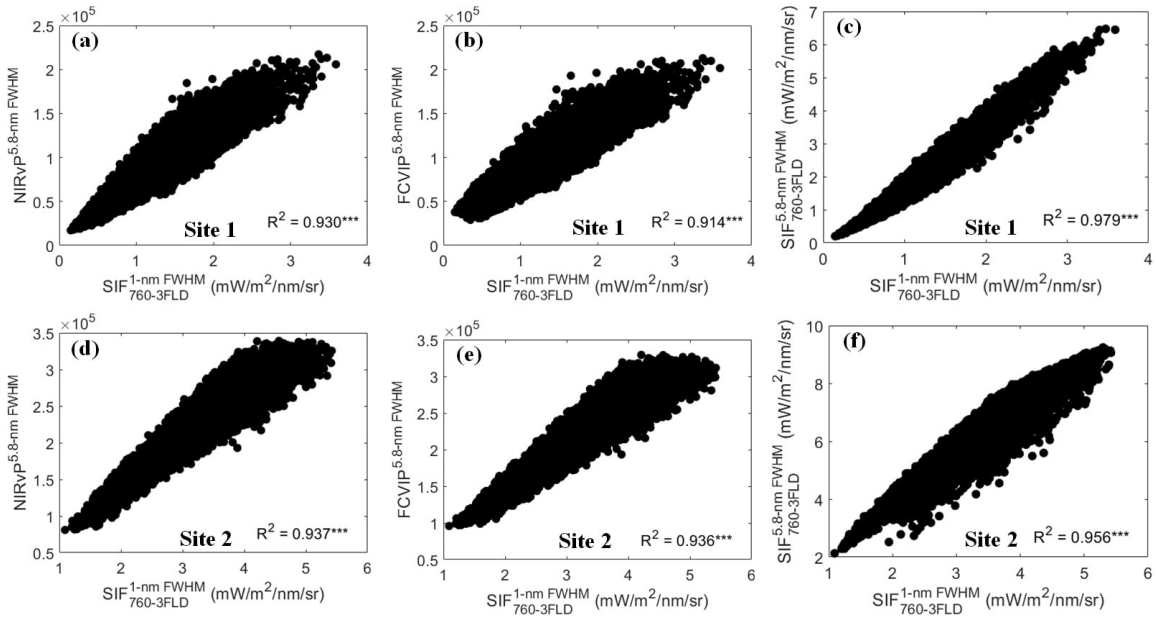

4268 **Fig. B-2.** Relationships between SCOPE-derived $SIF_{760\text{-}3FLD}$ at 1-nm and NIRvP (a, d), FCVIP (b, e)
4269 and SCOPE-derived $SIF_{760\text{-}3FLD}$ (c, f) at 5.8-nm for simulated training datasets corresponding to Site
4270 1 and Site 2.

4271

Table B-1. Definitions and the assigned variation ranges of all input parameters of the Soil Canopy Observation, Photochemistry and Energy fluxes (SCOPE) model.

Parameter	Definition	Range/Value		Unit
		Site 1	Site 2	
FLUSPECT				
C_{a+b}	Leaf chlorophyll concentration	10–70	40–80	$\mu g \cdot cm^{-2}$
C_{ca}	Leaf carotenoid concentration	1–20	1–20	$\mu g \cdot cm^{-2}$
C_{dm}	Leaf dry matter content	0.001–0.05	0–0.001	$g \cdot cm^{-2}$
C_w	Equivalent water thickness in leaves	0.001–0.05	0.001–0.05	cm
C_s	Leaf senescence parameters	0	0	-
C_{ant}	Anthocyanin content	0–8	0–8	$\mu g \cdot cm^{-2}$
N	Leaf structure parameter	1–1.5	1–2.5	-
ρ(thermal)	Broadband leaf thermal reflectance	0.01	0.01	-
τ(thermal)	Broadband leaf thermal transmittance	0.01	0.01	-
Leaf biochemical				
Vcmax	Maximum carboxylation capacity	30–110	40–250	$\mu mol \cdot m^{-2} s^{-1}$
m	Ball-Berry stomatal parameter (slope)	8	8	-
B_0	Ball-Berry stomatal parameter (intercept)	0.01	0.01	-

Type	Photochemical pathway	0	0	-
K_v	Extinction coefficient for vertical Vcmax profile	0.64	0.64	-
Rdparam	Parameter for dark respiration	0.015	0.015	-
Tyear	Mean annual temperature	15	15	ºC
β	Fraction of photons partitioned to PSII	0.51	0.51	-
kNPQs	Rate constant of sustained thermal dissipation	0	0	s^{-1}
qLs	Fraction of functional reaction centers	1	1	-
stress factor	Stress factor to reduce Vcmax	1	1	-
Fluorescence				
fqe	Fluorescence quantum yield efficiency at photosystem level	0.01	0.01	-
Soil				
spectrum	Type of soil reflectance spectrum	1	1	-
rss	Soil resistance for evaporation from the pore space	500	500	$s \cdot m^{-1}$
rs_t	Broadband soil thermal reflectance	0.06	0.06	-
cs	Specific heat capacity of the soil	1180	1180	$J \cdot kg^{-1} \cdot K^{-1}$
ρ_s	Specific mass of the soil	1800	1800	$kg \cdot m^{-3}$
λ_s	Heat conductivity of the soil	1.55	1.55	$J \cdot m^{-1} \cdot K^{-1}$
SMC	Volumetric soil moisture content in the root zone	25	25	-
BSMBrightness	BSM model parameter for soil brightness	0.5	0.5	-
BSMlat	BSM model parameter 'lat'	25	25	-
BSMlon	BSM model parameter 'long'	45	45	-
Canopy				
LAI	Leaf area index	0.5–5	2–6	$m^2 \cdot m^{-2}$
hc	Vegetation height	1.2	1.2	m
$LIDF_a$	Leaf inclination parameter for the mean leaf zenith angle	−1–1	−1–1	-
$LIDF_b$	Bimodality of the leaf angle distribution	0	0	-
leafwidth	Leaf width	0.07	0.07	m
Meteorological				
z	Measurement height of meteorological data	5	5	m
Rin	Broadband incoming shortwave radiation (0.4–2.5 μm)	700	900	$W \cdot m^{-2}$

Ta	Air temperature	19.2*	25.3*	°C
Rli	Broadband incoming longwave radiation	300	300	$W \cdot m^{-2}$
p	Air pressure	1002.8*	1003.6*	hPa
ea	Atmospheric vapor pressure	15	15	hPa
u	Wind speed at height z	2	2	$m \cdot s^{-1}$
C_a	Atmospheric CO_2 concentration	380	380	ppm
O_a	Atmospheric O_2 concentration	209	209	per mile
Angles				
tts	Solar zenith angle	35.42	34.93	deg.
tto	Observation zenith angle	0	0	deg.
ψ	Azimuthal difference between solar and observation angle	0	0	deg.

*Meteorological variables retrieved from portable weather station during the airborne campaign

Appendix C: Supplementary Material for Chapter-4

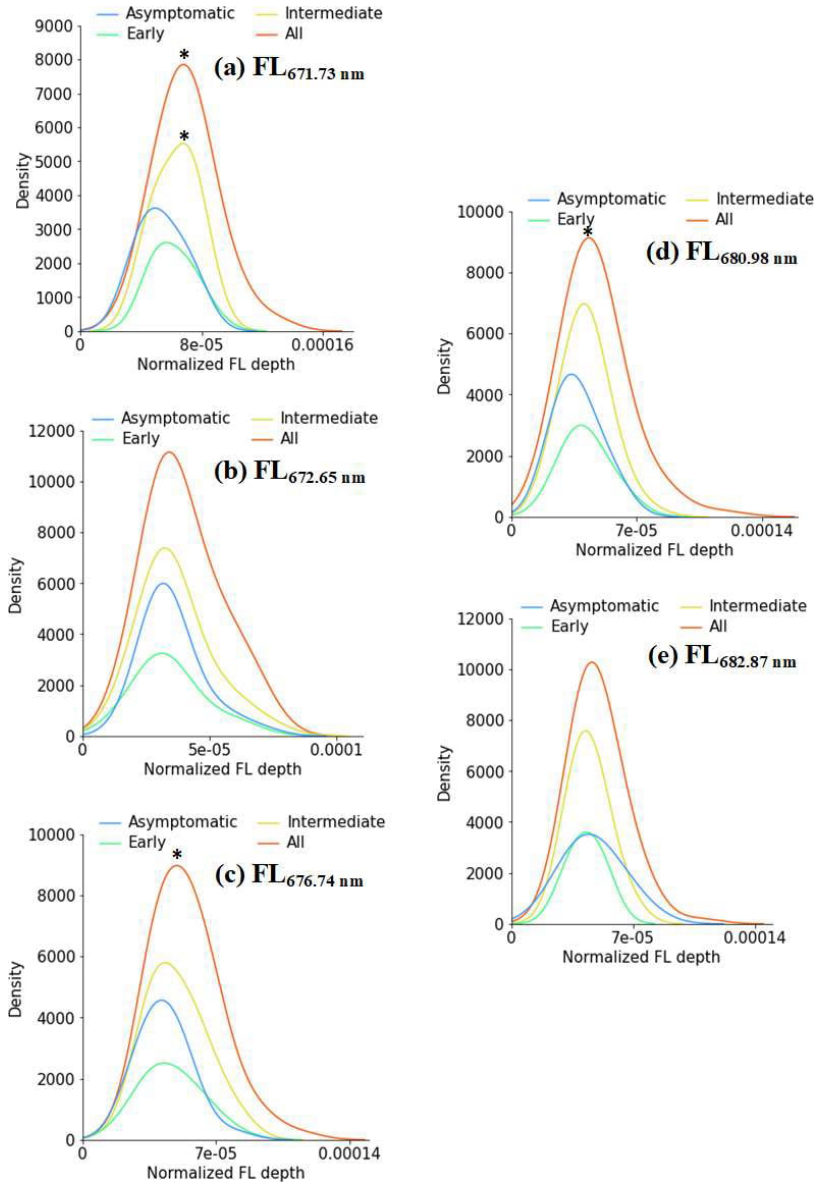

Fig. C-1. Histograms for the assessment of the relationship between asymptomatic trees and those in the three stages of disease progression for the absorption feature depths corresponding to red FLs. Asterisks indicate significant differences from the asymptomatic trees according to Dunnett's test at $\alpha < 0.05$.

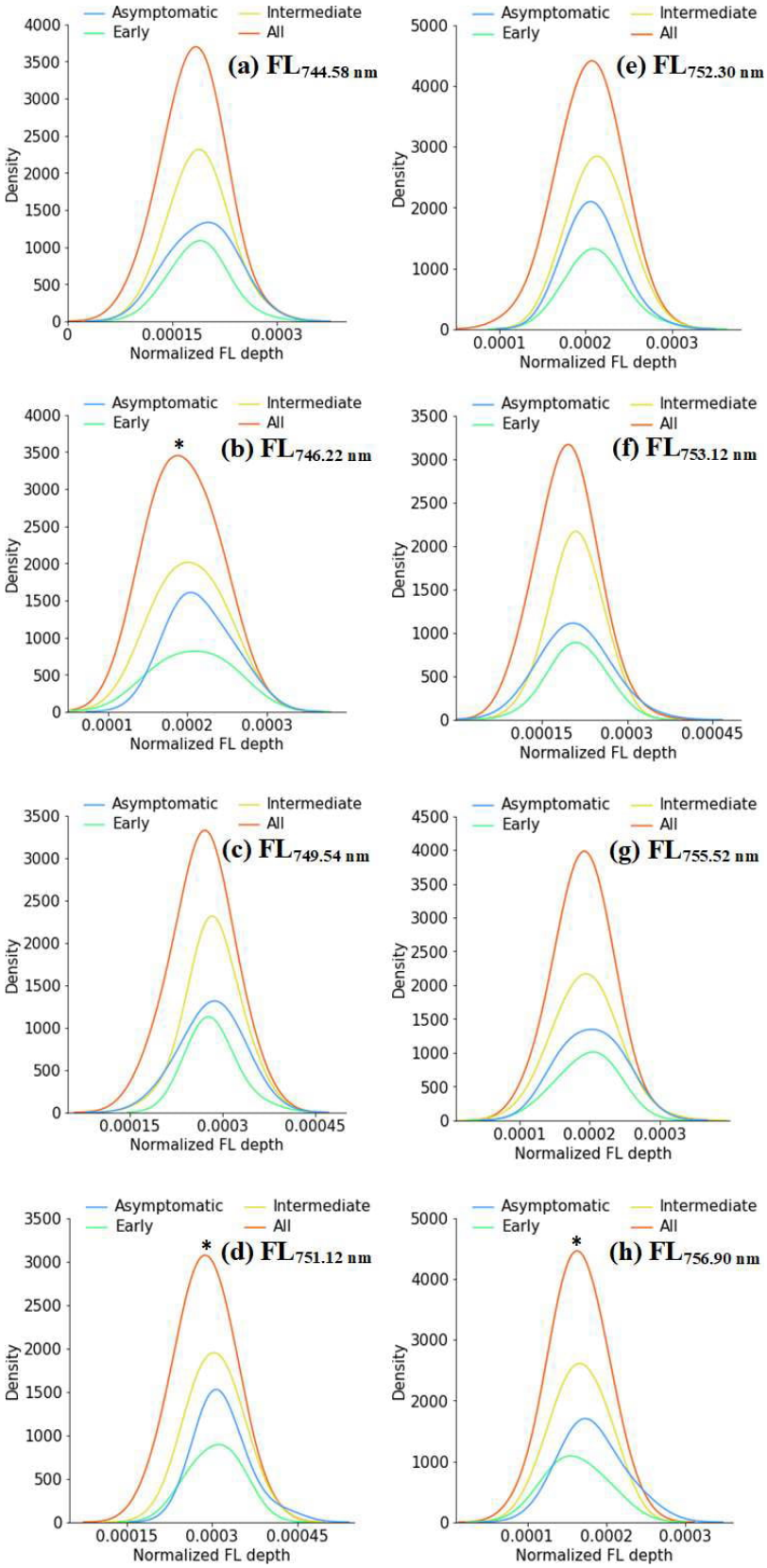

Fig. C-2. Histograms for the assessment of the relationship between asymptomatic trees and those in the three stages of disease progression for the absorption feature depths corresponding to first far-red FLs group. Asterisks indicate significant differences from the asymptomatic trees according to Dunnett's test at $\alpha < 0.05$.

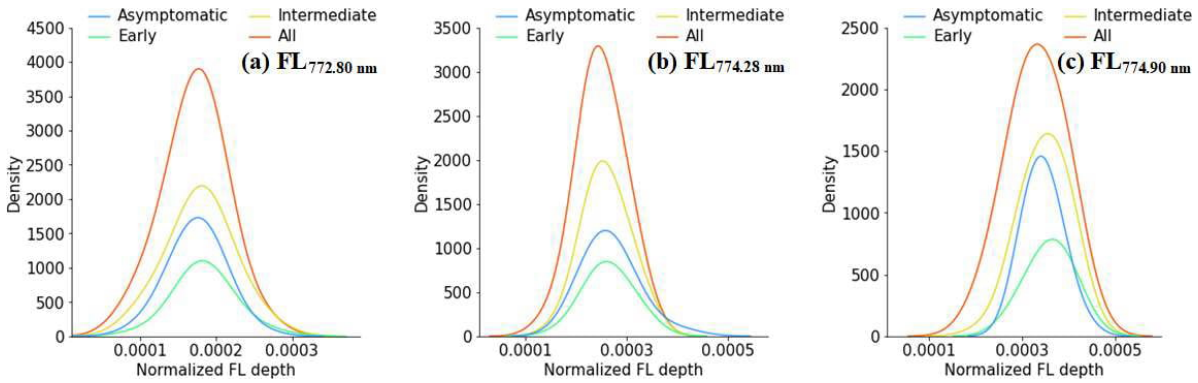

Fig. C-3. Histograms for the assessment of the relationship between asymptomatic trees and those in the three stages of disease progression for the absorption feature depths corresponding to second far-red FLs group.

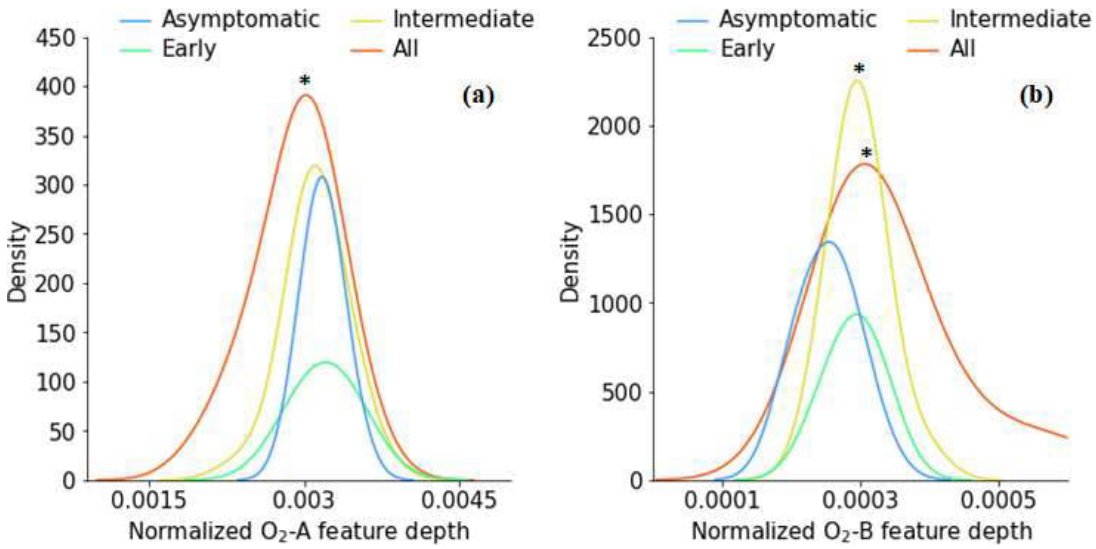

Fig. C-4. Histograms for the assessment of the relationship between asymptomatic trees and those in the three stages of disease progression for the absorption feature depths corresponding to the two oxygen absorption features. Asterisks indicate significant differences from the asymptomatic trees according to Dunnett's test at $\alpha < 0.05$.

Appendix D: Journal paper for Chapter-2

This appendix contains the author-accepted manuscript of the Remote Sensing of Environment paper used for Chapter 2. Below is the bibliographic detail.

Belwalkar, A., Poblete, T., Longmire, A., Hornero, A., Hernandez-Clemente, R., Zarco-Tejada, P.J., 2022. **Evaluation of SIF retrievals from narrow-band and sub-nanometer airborne hyperspectral imagers flown in tandem: modelling and validation in the context of plant phenotyping**. Remote Sens. Environ. 273, 112986. https://doi.org/10.1016/j.rse.2022.112986.

Remote Sensing of Environment 273 (2022) 112986

Contents lists available at ScienceDirect

Remote Sensing of Environment

journal homepage: www.elsevier.com/locate/rse

Evaluation of SIF retrievals from narrow-band and sub-nanometer airborne hyperspectral imagers flown in tandem: Modelling and validation in the context of plant phenotyping

A. Belwalkar [a], T. Poblete [a], A. Longmire [b], A. Hornero [c,d], R. Hernandez-Clemente [d], P. J. Zarco-Tejada [a,b,c,*]

[a] Department of Infrastructure Engineering, Faculty of Engineering and Information Technology (FEIT), University of Melbourne, Melbourne, Victoria, Australia
[b] School of Agriculture and Food, Faculty of Veterinary and Agricultural Sciences (FVAS), University of Melbourne, Melbourne, Victoria, Australia
[c] Instituto de Agricultura Sostenible (IAS), Consejo Superior de Investigaciones Científicas (CSIC), Avenida Menéndez Pidal s/n, 14004 Córdoba, Spain
[d] Department of Geography, Swansea University, SA2 8PP Swansea, United Kingdom

ARTICLE INFO

Editor: Jing M. Chen

Keywords:
Solar-induced chlorophyll fluorescence
SIF
Plant phenotyping
Stress detection
Airborne
Hyperspectral
Hyperspectral imager

ABSTRACT

Solar-induced chlorophyll fluorescence (SIF) can be used as an indicator of crop photosynthetic activity and a proxy for vegetation stress in plant phenotyping and precision agriculture applications. SIF quantification is sensitive to the spectral resolution (SR), and its accurate retrieval requires sensors with sub-nanometer resolutions. However, for accurate SIF quantification from imaging sensors onboard airborne platforms, sub-nanometer imagers are costly and more difficult to operate than the commonly available narrow-band imagers (i.e., 4- to 6-nm bandwidths), which can also be installed on drones and lightweight aircraft. Although a few theoretical and experimental studies have evaluated narrow-band spectra for SIF quantification, there is a lack of research focused on comparing the effects of the SR on SIF from airborne hyperspectral imagers in practical applications. This study investigates the effects of SR and sensor altitude on SIF accuracy, comparing SIF quantified at the 760-nm O_2-A band (SIF_{760}) from two hyperspectral imagers with different spectral configurations (full width at half-maximum resolutions of 0.1–0.2 nm and 5.8 nm) flown in tandem on board an aircraft. SIF_{760} retrievals were compared from two different wheat and maize phenotyping trials grown under different nitrogen fertilizer application rates over the 2019–2021 growing seasons. SIF_{760} from the two sensors were correlated (R^2 = 0.77–0.9, $p < 0.01$), with the narrow-band imager producing larger SIF_{760} estimates than the sub-nanometer imager (root mean square error (RMSE) 3.28–4.69 mW/m^2/nm/sr). Ground-level SIF_{760} showed strong relationships with both sub-nanometer ($R^2 = 0.90$, $p < 0.001$, RMSE = 0.07 mW/m^2/nm/sr) and narrow-band ($R^2 = 0.88$, $p < 0.001$, RMSE = 3.26 mW/m^2/nm/sr) airborne retrievals. Simulation-based assessments of SIF_{760} for SRs ranging from 1 to 5.8 nm using the SCOPE model were consistent with experimental results showing significant relationships among SIF_{760} quantified at different SRs. Predictive algorithms of leaf nitrogen concentration using SIF_{760} from either the narrow-band or sub-nanometer sensor yielded similar performance, supporting the use of narrow-band resolution imagery for assessing the spatial variability of SIF in plant phenotyping, vegetation stress detection and precision agriculture contexts.

1. Introduction

Solar radiation reaching a plant canopy cannot be fully utilized for photosynthesis, and the resulting excess radiation is partly re-emitted as a weak electromagnetic signal termed solar-induced chlorophyll fluorescence (SIF) (see a full review on SIF in Mohammed et al., 2019). SIF flux originates from photosystem II (PSII) and has a spectral range of 650–800 nm with one peak at 685 nm (SIF_{685}) and a second peak at 740 nm (SIF_{740}). The SIF energy dissipation pathway directly competes with the PSII photochemistry and heat dissipation (Krause and Weis, 1984; Lichtenthaler and Rinderle, 1988). Thus, SIF is a proxy for plant photosynthetic rate, which may be related to plant stress levels (Genty

* Corresponding author at: Department of Infrastructure Engineering, Faculty of Engineering and Information Technology (FEIT), University of Melbourne, Melbourne, Victoria, Australia.
E-mail address: pablo.zarco@unimelb.edu.au (P.J. Zarco-Tejada).

https://doi.org/10.1016/j.rse.2022.112986
Received 20 August 2021; Received in revised form 28 February 2022; Accepted 2 March 2022

et al., 1989; Weis and Berry, 1987; Zarco-Tejada et al., 2016). However, SIF emitted from the canopy constitutes a small fraction (1–5%) of the total reflected solar radiation, making it difficult to quantify (Meroni et al., 2009).

Specialized algorithms are necessary for decoupling SIF from total reflected solar radiation. These algorithms are classified based on whether SIF is retrieved within specific absorption bands or over the whole SIF emission region (Mohammed et al., 2019). Most methods utilize discrete solar or telluric absorption lines of the solar spectrum, where the contribution of SIF to the total radiance signal is relatively higher. The terrestrial oxygen absorption bands (O_2-A and O_2-B) centred around 760 nm and 687 nm, respectively, are broader and deeper than the other absorption features and, therefore, commonly used for quantifying SIF (Meroni et al., 2009). The fluorescence *in-filling* method, based on the Fraunhofer Line Depth (FLD) principle (Plascyk, 1975), depends on a few discrete spectral bands inside and outside the oxygen absorption features and is the most widely used method for SIF retrieval due to its ease of implementation. By contrast, spectral fitting methods (SFMs) model the fluorescence and reflectance spectrum by spectral curve fitting, utilizing all the contiguous wavelengths within a fixed spectral window mostly centred around oxygen absorption bands (Meroni et al., 2010; Meroni and Colombo, 2006).

The earliest attempt to incorporate leaf fluorescence into a radiative transfer model (RTM) was the Fluorescence–Reflectance–Transmittance (FRT) model (Zarco-Tejada et al., 2000a, 2000b). This attempt led to the development of the leaf model FluorMODleaf (Pedrós et al., 2008) and a canopy-level RTM named FluorSAIL (Verhoef, 2004). These models prompted the development of an integrated, vertical, one-dimensional, leaf-canopy fluorescence–temperature–photosynthesis model named Soil-Canopy-Observation of Photosynthesis and Energy fluxes (SCOPE) (Van der Tol et al., 2009), which is widely used to assess the linkage between fluorescence–reflectance and photosynthesis (Camino et al., 2019; Celesti et al., 2018; Verhoef et al., 2018). SCOPE simulates top-of-canopy radiance, chlorophyll fluorescence and reflectance for homogenous canopies. It has been used to quantify the effects of the leaf biochemistry, maximum carboxylation rate (Vcmax), and canopy structure on apparent reflectance, including fluorescence effects. Recently, three-dimensional canopy RTMs integrating fluorescence have been developed, such as FluorFLIGHT (Hernández-Clemente et al., 2017), the Fluorescence model with Weight Photon Spread (FluorWPS) (Zhao et al., 2016), and the Discrete Anisotropic Radiative Transfer (DART) model (Gastellu-Etchegorry et al., 2017). These models simulate scattering within the canopy components and thus account for canopy structural heterogeneity.

The earliest experiments involving ground-based sub-nanometer-resolution spectrometers quantified SIF at both leaf (Meroni and Colombo, 2006) and canopy levels (Pérez-Priego et al., 2005), detecting herbicide- and water-induced stress, respectively. The development of sub-nanometer-resolution hyperspectral sensors in the past decade has enabled SIF retrievals from airborne platforms. Sensors include the Chlorophyll Fluorescence Imaging Spectrometer (CFIS) (Frankenberg et al., 2018), the high-resolution airborne imaging spectrometer HyPlant (Rascher et al., 2015), and the Hyperspec High-Resolution Chlorophyll Fluorescence Sensor (Headwall Photonics, Fitchburg, MA, USA) (Belwalkar et al., 2021) with spectral resolutions (SRs) of 0.1, 0.28 and 0.1–0.2 nm, respectively. Sub-nanometer-resolution SIF observations at the global scale are available from satellite sensors such as OCO-2 (Orbiting Carbon Observatory-2) (Frankenberg et al., 2014), GOSAT (Greenhouse gases Observing SATellite) (Guanter et al., 2012), and TROPOMI (TROPOspheric Monitoring Instrument) (Guanter et al., 2015) with spatial resolutions of 1.29 km × 2.25 km, 50 km × 50 km and 5.5 km × 3.5 km, respectively. The European Space Agency is also set to launch the FLuorescence EXplorer (FLEX) (Drusch et al., 2017) in 2024, a mission solely dedicated to measuring SIF at a high SR of 0.3 nm across the globe at 300-m spatial resolution.

As a result of these technical and methodological advances, SIF is frequently used for monitoring crop photosynthesis. SIF is measured from a variety of platforms, including ground-based spectrometers (Cogliati et al., 2015; Daumard et al., 2012; Grossmann et al., 2018; Kim et al., 2021; Li et al., 2020; Pérez-Priego et al., 2005; Rossini et al., 2016), drones and manned aircraft (Bandopadhyay et al., 2019; Damm et al., 2014, 2015; Siegmann et al., 2019; Tagliabue et al., 2020; Zarco-Tejada et al., 2012, 2013a) and satellite platforms (Frankenberg et al., 2014; Guanter et al., 2012, 2015). SIF observations at intermediate scales obtained from airborne platforms are important for i) improving the interpretation of SIF at coarser spatial resolutions and thus bridging the gap between field and global scales, ii) disentangling the contribution of different scene components in aggregated pixels (Hornero et al., 2021a; Zarco-Tejada et al., 2013b), and iii) evaluating the sensitivity of SIF for describing plant physiological processes at high spatial resolutions (e.g., as an early indicator of biotic and abiotic stress in precision agriculture and forestry).

Modelling studies (Damm et al., 2011; Liu et al., 2015) of FLD-based SIF retrieval have shown that sensor SR and the signal-to-noise ratio (SNR) (collectively accounting for more than 80% of the retrieval error) strongly affect SIF measurement accuracy. Several studies have demonstrated the potential of sub-nanometer airborne hyperspectral imagers for precise SIF quantification in a variety of contexts, including estimating gross primary productivity (GPP) (Wieneke et al., 2016), validating satellite-based SIF retrievals (Sun et al., 2017), assessing the physiological effects of age on loblolly pine forest (Colombo et al., 2018) and quantifying functional diversity of terrestrial ecosystems (Tagliabue et al., 2020). Although sub-nanometer-resolution imaging sensors are recommended for obtaining absolute measurements of SIF, relative SIF measurements from narrow-band sensors are useful in a variety of settings, including water stress detection (Camino et al., 2018a; Panigada et al., 2014; Zarco-Tejada et al., 2012), plant phenotyping (Camino et al., 2019, 2018b; Gonzalez-Dugo et al., 2015), biotic-induced stress detection (Calderón et al., 2015, 2013; Hernández-Clemente et al., 2017; Hornero et al., 2021b; Poblete et al., 2020, 2021; Zarco-Tejada et al., 2018) and linking canopy-level SIF_{760} and GPP using sensors such as the Airborne Prism Experiment (APEX) with a full width at half-maximum resolution (FWHM) of 5.7 nm over perennial grassland, cropland and mixed temperate forest (Damm et al., 2015). In these studies, the reported higher levels of the quantified SIF_{760} were consistent with other modelling and experimental studies (Julitta et al., 2016; Nakashima et al., 2021; Nichol et al., 2019; Süß et al., 2016).

The impacts of SR on FLD-based SIF retrievals have been previously assessed with models (Damm et al., 2011; Dechant et al., 2017; Hernández-Clemente et al., 2017; Liu et al., 2015) and experiments (Julitta et al., 2016). Julitta et al. (2016) compared SIF retrievals at both the O_2-A and O_2-B bands using four portable field spectrometers with different spectral sampling intervals (SSIs), SRs, and SNRs simultaneously measuring the same vegetation target. SIF estimates at the O_2-A band from three of the four spectrometers with sub-nanometer resolution (FWHM $\leq$1 nm) were consistent with the expected ranges from ground-based SIF observations over lawn grassland reported by Rossini et al. (2016). In contrast, the average SIF from the coarsest-resolution spectrometer (FWHM = 5.5 nm) was six times higher than the values obtained from the other three spectrometers, reaching values above 4 $mW/m^2/nm/sr$. Our study expands on this previous work by assessing the effects of SR and flight altitude on airborne-based SIF retrievals, which are commonly used in precision agriculture applications. This is, to the best of our knowledge, the first study to do so. Aspects regarding the effects of the atmosphere, flight altitude, and performance of imaging sensors on SIF retrievals need to be studied in addition to the theoretical work and the assessments carried out using close-range spectrometer data.

The need for sub-nanometer imagers for the accurate quantification of SIF brings important challenges in precision agriculture, plant phenotyping and biosecurity applications due to their complexity, higher cost and increased operational difficulties. Standard narrow-band

hyperspectral imagers (i.e., with SR in the range of 4–6 nm FWHM) are an appealing alternative that are increasingly being used with drones and lightweight aircraft to collect high-spatial-resolution imagery (Aasen et al., 2018). However, it is unclear how useful SIF_{760} estimates from these imagers are for plant physiological assessments when compared to ground-based or sub-nanometer airborne SIF_{760} estimates. Such assessment is critical, particularly when the relative quantification of fluorescence across the landscape could be readily used to detect biotic- and abiotic-induced vegetation stress. Empirical work is needed to evaluate whether SIF_{760} retrievals from these narrow-band hyperspectral imagers are sufficient for detecting physiological stress in crops, relative to measurements from sub-nanometer instruments.

Monitoring crop nutrient status is one potentially important application of airborne SIF_{760} quantification (Camino et al., 2018b; Wang et al., 2021). Accurate assessments of plant nutrition across a field can help to ensure crop yields by allowing for more efficient use of N-fertilizers. Excessive N fertilizer application can result in the loss of reactive forms of N (ammonia, nitrate, and nitrogen oxides) to the environment, causing water pollution, climate forcing, and biodiversity loss. As a result, assessing crop response to N-fertilizers is critical for ensuring resource efficiency while optimizing yields.

In this study, we compared SIF_{760} measured from a 5.8-nm FWHM narrow-band hyperspectral imager to a sub-nanometer hyperspectral imager of 0.1- to 0.2-nm FWHM flown in tandem at multiple sensor altitudes and across two wheat and maize trials grown under different nitrogen application rates and for three growing seasons. We validated airborne measures with sub-nanometer ground retrievals and evaluated results against SCOPE simulations. We then assessed the performance of sub-nanometer and narrow-band SIF_{760} estimates for predicting nitrogen concentration using machine learning models. Our findings provide important insights that support the operational use of standard, commercially available narrow-band hyperspectral imagers for

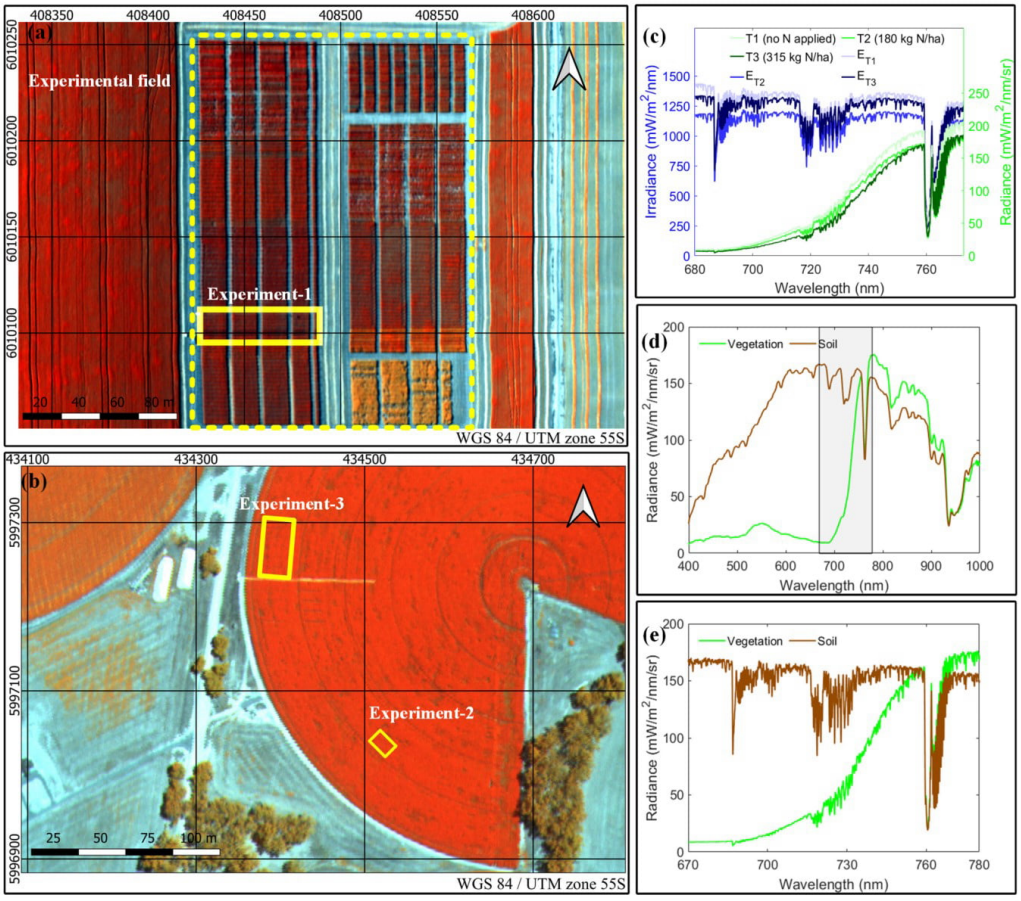

Fig. 1. Overview of experiments at field trial sites 1 (a) and 2 (b). Sample average radiance and the corresponding irradiance (E) spectra for experimental plots subjected to different nitrogen treatments at experiment 3 obtained from HR-2000 (c). Sample radiance spectra acquired from the narrow-band hyperspectral imager (d) and sub-nanometer hyperspectral imager (e) corresponding to the same vegetation and soil targets. (a) was acquired with the narrow-band hyperspectral imager (composite: 760 (R), 710 (G) and 680 (B) nm). (b) was obtained with the sub-nanometer hyperspectral imager (composite: 760 (R), 710 (G) and 680 (B) nm). The solid yellow boxes in (a) and (b) show the location of the plots across the three experiments and the dashed yellow box in (a) shows the location of plots across the entire field. The transparent grey box in (d) shows the spectral region covered by the sub-nanometer hyperspectral imager. (For interpretation of the references to colour in this figure legend, the reader is referred to the web version of this article.)

quantifying relative SIF levels. This is especially important for precision agriculture and plant physiology monitoring purposes that require accurate assessment of the SIF variability within and across experimental fields.

2. Materials and methods

2.1. Study sites and field data collection

Experiments took place at two field trial sites in Victoria, Australia, in 2019, 2020 and 2021 (Fig. 1a and b). Experiment 1 was conducted over 15 plots of dryland wheat (cv. Scepter) (Yang et al., 2018) located at site 1 in Yarrawonga (36°02′55″S, 145°59′02″E). Plots were 26 m^2 (2 m × 13 m) and planted in May 2019. Plots were grown with five different rates of nitrogen fertilizer in the form of urea (46% N) (T1: 0 kg N/ha, T2: 46 kg N/ha, T3: 92 kg N/ha, T4: 138 kg N/ha, T5: 184 kg N/ha). The surrounding areas were planted with several varieties of wheat grown under various physiological conditions and nitrogen fertilizer application rates (Fig. 1a).

Experiments 2 and 3 were conducted in 2020 and 2021 at site 2 in Peechelba East (36°10′04″S, 146°16′23″E) over irrigated maize plots. Experiment 2 consisted of 8 plots and experiment 3 consisted of 20 plots. Plots were sown in October 2019 and October 2020 with two urea application rates for experiment 2 (T1: 207 kg N/ha, T2: 387 kg N/ha) and three for experiment 3 (T1: 0 kg N/ha, T2: 180 kg N/ha, T3: 315 kg N/ha). The plot sizes were 15 m^2 (3 m × 5 m) for experiment 2 and 36 m^2 (3 m × 12 m) for experiment 3. The climate at both field trial sites is humid subtropical (Cfa) according to the Köppen classification. At site 1, the mean annual temperature is 16.3 °C and average rainfall is 559 mm. At site 2, the mean annual temperature is 15.2 °C and average rainfall is 642 mm.

For experiment-3, field measurements of top-of-canopy (TOC) spectral radiances for the computation of ground-based SIF_{760} were collected from all 20 plots on 20 January 2021 at midday from 11:45 to 16:30 solar time under clear sky conditions. TOC spectral radiance was measured using a 0.065-nm FWHM HR-2000 spectrometer (Ocean Insight, Dunedin, FL, USA). The total incoming irradiance was calculated using the radiance reflected from a white reference panel (Labsphere Inc., North Sutton, NH, USA) measured by the spectrometer. The spectral measurements were acquired from the nadir using bare optical fiber, with an angular field of view of 25°, mounted on a tripod of 2.5 m height. The vegetation targets were measured at a distance of 1 m above the canopy. Radiance measurements were recorded at five different locations within each plot and then averaged to reduce noise. Incident solar radiation was measured prior to radiance measurements, and radiance/irradiance measurements were completed within 3 min for each plot. Examples of radiance and irradiance measurements are shown in Fig. 1c, with visible differences in spectra associated with applied nitrogen rate.

A summary of the physiological measurements performed at each experiment is shown in Table 1. The growth stages during the airborne campaigns corresponded to i) grain filling (milking stage) for wheat in 2019, ii) dough stage for maize in 2020, and iii) silking stage for maize in 2021. A portable weather station (model WXT510, Vaisala, Helsinki, Finland) was installed in the field for concurrent readings of meteorological conditions at the time of hyperspectral image acquisitions. For experiments 1 and 3, leaf measurements were carried out under field conditions, coincident with the airborne campaigns. For experiment 2, leaf measurements were performed 4 days prior to the airborne campaign under similar meteorological conditions (Table 1). Measurements were made on 10–15 leaves per plot for experiment 1 and 5–10 leaves per plot for experiments 2 and 3. Measurements were made on leaves at the top of the canopy at noon, under clear skies. Chlorophyll content, nitrogen balance index (NBI), flavonols and anthocyanin content were measured using a handheld Dualex leaf-clip sensor (FORCE-A, Orsay, France). Steady-state leaf fluorescence yield (Ft) was measured using the FluorPen FP110-LM (Photon Systems Instruments, Drásov, Czech Republic) handheld fluorometer. Random samples of 10–15 leaves per plot for experiment 1 and 4–5 leaves per plot for experiments 2 and 3 from the top of the canopy were selected for determining the total N concentration (%) destructively in the laboratory, following the Kjeldahl method (Kjeldahl, 1883). To verify the impacts of fertilization rate on leaf physiological traits, measurements were evaluated using analysis of variance (ANOVA) followed by a Dunnett's test at $\alpha < 0.05$. In addition to the 15 plots at site 1, leaf-level measurements from more than 100 adjacent plots within the entire experimental field (dashed yellow box in Fig. 1a) were also conducted to investigate the intra-field variability.

2.2. Airborne hyperspectral campaigns

Airborne campaigns were conducted in 2019, 2020 and 2021 (Table 2), flying with the aircraft's heading on the solar plane. Two hyperspectral imagers were installed in tandem on a Cessna-172 aircraft operated by the HyperSens Laboratory, University of Melbourne's Airborne Remote Sensing Facility. The first hyperspectral imager was a Hyperspec VNIR *E*-Series model (Headwall Photonics, Fitchburg, MA, USA) and the second hyperspectral imager was a high-resolution Hyperspec Fluorescence sensor (Headwall Photonics, Fitchburg, MA, USA). The spectral characteristics of both hyperspectral imagers are shown in Table 3. Both hyperspectral imagers were radiometrically calibrated in the laboratory using an integrating sphere (Labsphere XTH2000C, Labsphere Inc., North Sutton, NH, USA); as a result, coefficients derived from the constant light source at four different illumination levels were calculated for the flight configuration of each imager. The atmospheric correction for the VNIR imager was performed using the SMARTS model (Gueymard, 2001), with the aerosol optical depth measured at 550 nm with a Microtops II sunphotometer (Solar LIGHT Co., Philadelphia, PA, USA), allowing the conversion of the radiance values to reflectance. Image orthorectification was conducted with PARGE (ReSe Applications Schläpfer, Wil, Switzerland) using inputs from the solidly installed and synchronized inertial measurement units (VN-300-VectorNav Technologies LLC, Dallas, TX, USA for VNIR imager and Trimble APX-15 UAV, Applanix Corporation, Ontario, Canada for Fluorescence imager); more information on data preprocessing and image correction can be found in Zarco-Tejada et al. (2016).

Differences in radiance spectra corresponding to vegetation and soil targets acquired from the two hyperspectral imagers were visually identified as a function of spectral configurations (Fig. 1d and e). Above-ground-level (AGL) altitudes and spatial resolutions of the imagery are detailed in Table 2. The spatial resolution of imagery from both airborne hyperspectral imagers was sufficient for identification of individual plots over the experimental sites (Fig. 2). Differences in fertilization rate could be visually discriminated based on radiance spectra acquired from both the hyperspectral imagers over the entire spectral range (Fig. 3a and c) and in the O_2-A absorption feature (Fig. 3b and d) for experiment 1.

To investigate the impact of sensor altitude on the inter-comparison of airborne-quantified SIF_{760} from both hyperspectral imagers and with ground-based SIF_{760}, images from both hyperspectral imagers were acquired at three different altitudes (900 m, 1200 m and 2200 m) for experiment 3 (Table 2). All images were acquired within a 20-min time interval to minimize the impact of sun-sensor geometry and changes in atmospheric conditions on the SIF_{760} retrievals. The effect of sensor height on O_2-A absorption feature depth and SIF_{760} quantifications was assessed using ANOVA followed by Tukey's honest significant difference (HSD) post-hoc test at $\alpha < 0.05$. Fig. 4 shows the impact of the sensor altitude on the radiance spectra for the sub-nanometer imager. The radiance imagery acquired from the sub-nanometer imager at three different altitudes over the entire field (Fig. 4a, b and c) and over the experimental plots (Fig. 4d, e and f) differed in the 670- to 780-nm

Table 1
Field measurements and meteorological conditions coincident with flights.

Field trial site	Experiment #	Treatment (kg N/ha)	Growth stage	Field measurements	Meteorological conditions		
					T_a	RH	P_a
Yarrawonga (Site 1)	1	T1:0, T2:46, T3:92, T4:138, T5:184	Grain filling	Ft, Chl, NBI, Flav, Anth, TN	19.2	30.1	1002.8
Peechelba (Site 2)	2	T1:207, T2:387	Dough	Ft, Chl, NBI, Flav, Anth, TN	23.3	36.2	1008.5
	3	T1:0, T2:180, T3:315	Silking	Ft, Chl, NBI, Flav, Anth, TN, TOC L	25.3	33.5	1003.6

Ft = Steady-state chlorophyll fluorescence, Chl = Chlorophyll content (μg/cm^2),
NBI = Nitrogen balanced index (Dualex unit (d.u)), Flav = Flavonols (Dualex unit),
Anth = Anthocyanins (Dualex unit), TN = Total Nitrogen concentration (%),
TOC L = Top-of-canopy radiance (mW/m^2/nm/sr) from HR-2000, T_a = Average air temperature (°C),
RH = Relative humidity (%) and P_a = Average air pressure (mBar).

Table 2
Flight dates, flight altitudes and spatial resolution of the acquired hyperspectral images during the three airborne campaigns.

Flight date	Flight time (local)	Experiment	AGL (m)		Spatial resolution (m)	
			NB	SN	NB	SN
09/10/19	15:40–16:30	1	400	900	0.25	0.20
16/03/20	12:50–13:50	2	700	850	0.50	0.20
20/01/21	11:40–12:20	3	900	900	0.65	0.20
			1200	1200	0.9	0.30
			2200	2200	1.7	0.55

NB = Narrow-band hyperspectral imager.
SN = Sub-nanometer hyperspectral imager.
AGL = above ground level.

Table 3
Spectral characteristics of the airborne hyperspectral imagers.

Configuration	Fluorescence sensor (Sub-nanometer imager)	VNIR *E*-Series sensor (Narrow-band imager)
Spectral range	670–780 nm	400–1000 nm
Number of spectral bands	2160	371
Spectral sampling interval	0.051 nm	1.626 nm
FWHM	0.1–0.2 nm	5.8 nm
Number of un-binned spatial pixels	1600	1600
SNR	>300:1*	>300:1*
Field of view	23.5°	66°
Aperture	f/2.5	f/2.5
Bit depth	16	16

* With spatial binning.

spectral region (Fig. 4g) and in the oxygen absorption features (Fig. 4h and i).

2.3. SIF quantification from field data and airborne hyperspectral imagery

A thresholding approach based on the normalized difference vegetation index (NDVI) was used to select the pixels corresponding to vegetation in each individual plot. To ensure that only pure vegetation pixels were considered for the analysis, all pixels with an NDVI greater than 0.6 were selected. For each plot, mean radiance spectra were calculated by averaging spectra from all pure vegetation pixels within the plot, excluding boundary pixels, from hyperspectral images acquired from both imagers. This object-based analysis strategy was used to reduce the uncertainty when using pixel-based SIF retrievals due to the SNR of the instrument. For experiment 1, the total incoming irradiance at the flight time was measured using the HR-2000 spectrometer with a CC-3 VIS-NIR cosine corrector diffuser. Due to the unavailability of cosine corrector diffuser for experiments 2 and 3, the total incoming irradiance at the flight time was calculated by measuring the radiance reflected from the white reference panel by the spectrometer. Ground-based SIF_{760} from eight plots measured concurrently with airborne image acquisition were used to validate the airborne SIF_{760} calculated from both imagers. The relative root mean square error (rRMSE) was calculated between the airborne and ground-based SIF_{760} following Eq. (1):

$$rRMSE = \sqrt{\frac{\sum_{i=1}^{n}\left(\frac{F_{airborne,i}-F_{ground,i}}{F_{ground,i}}\right)^2}{n}} \times 100\% \quad (1)$$

where $F_{airborne,\ i}$ and $F_{ground,\ i}$ are the SIF_{760} values retrieved from airborne and ground-based spectrometers, respectively, for plot *i*, with *n* representing the number of plots.

Field spectrometer radiances/irradiances were calibrated using coefficients derived from a uniform calibrated light source and an integrating sphere (Labsphere XTH2000C). To match the SR of the radiance images acquired from both sensors, the high-resolution irradiance spectra acquired with the HR-2000 spectrometer was resampled through Gaussian convolution (Hornero et al., 2021b; Suarez et al., 2021) corresponding to the SR of the airborne hyperspectral imagers. As the spectral characteristics of the narrow-band hyperspectral imager do not meet the requirements (Drusch et al., 2017; ESA, 2015) for quantifying SIF at the O_2-B (SIF_{687}) absorption feature, SIF_{687} values were not compared. This limitation also affects the applicability of SFMs with the narrow-band hyperspectral imager, as it requires sub-nanometer resolution for accurate SIF quantification. Thus, the retrieval of SIF_{760} using irradiance derived from HR-2000 measurements and average radiance derived from airborne hyperspectral images and ground-based HR-2000 measurements was performed using the O_2-A-band *in-filling* method through the FLD principle, based on a total of three spectral bands (3FLD) (Maier et al., 2003). The spectral window for '*in*' and '*out*' irradiance (E) and radiance (L) used in 3FLD computation was selected based on the spectral characteristics of the measuring instruments. For the narrow-band imager, E_{in}/L_{in} corresponds to the E/L minima in the 755–765 nm region. The minima for both E and L was observed at 762 nm, and this was consistent for all datasets. E_{out}/L_{out} corresponds to the weighted mean of E/L maxima in the spectral regions of 750–755 nm and 771–776 nm, respectively following the methodology proposed in Damm et al. (2011). The spectral window for both ground-based and airborne sub-nanometer sensors was selected using the methodology proposed in Julitta et al. (2017),[1] which considers the FWHM of the sub-nanometer resolution instrument and uses the mean of E/L in the left and right shoulder regions to reduce noise. An additional data quality check was performed for the matching of the '*in*' band for E/L, and in the event of a mismatch, E_{in}/L_{in} was defined as the mean of E_{in}/L_{in} of adjacent wavelengths. The absolute depth (in radiance units) and

[1] R code available on GitHub platform at https://github.com/tommasojulitta

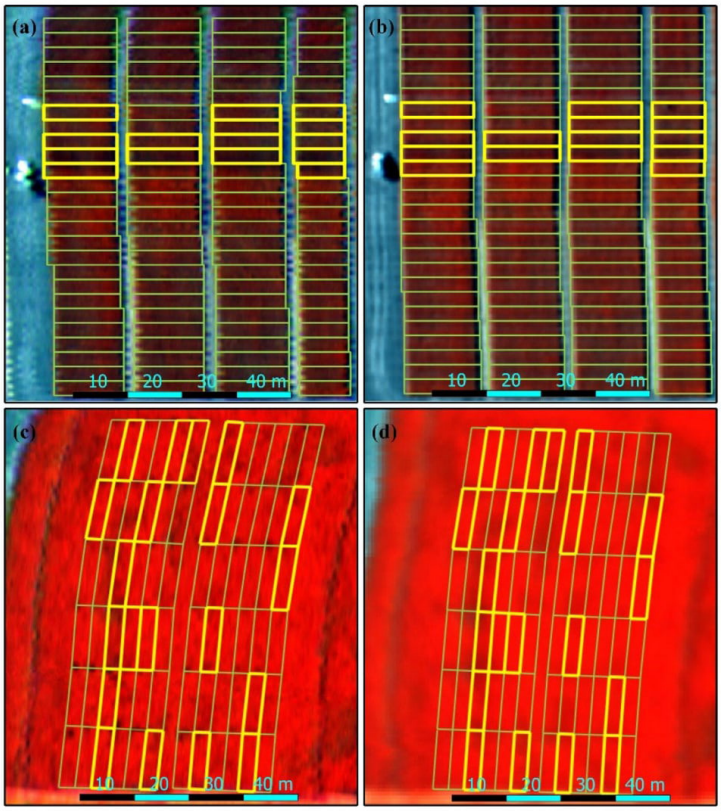

Fig. 2. Hyperspectral imagery showing zoomed-in plots from identical locations in experiments 1 (a, b) and 3 (c, d). Images (a) and (c) were acquired with the sub-nanometer hyperspectral imager (composite: 760 (R), 710 (G) and 680 (B) nm). Images (b) and (d) were acquired with the narrow-band hyperspectral imager (composite: 760 (R), 710 (G) and 680 (B) nm). Green polygons indicate plots under different nitrogen treatments, and yellow polygons indicate the selected plots corresponding to five and three nitrogen treatments, respectively, for experiments 1 and 3. (For interpretation of the references to colour in this figure legend, the reader is referred to the web version of this article.)

relative depth (in percent) of the O_2-A band feature were calculated in addition to the airborne SIF_{760} quantification. The absolute depth was calculated as the difference between the solar radiance at the left shoulder wavelength and the wavelength at the bottom of the O_2-A absorption feature, and the relative depth was calculated as the ratio of absolute depth and the solar radiance at the left shoulder wavelength. The wavelength providing the highest radiance in the 750–759 nm range was selected as the left shoulder wavelength.

In the absence of atmospheric correction, SIF_{760} values could be negative even for fluorescent targets (see Fig. 6 in Marrs et al., 2021). The atmospheric correction process involves estimating several atmospheric parameters such as upwelling transmittance, path scattered radiance, and spherical albedo using atmospheric RTMs. Additionally, to account for uncertainties in the estimation of atmospheric parameters, the transmittance correction technique (Damm et al., 2014; Guanter et al., 2010; Siegmann et al., 2019) is a commonly used approach that forces the non-fluorescent targets to give zero SIF_{760}. Due to the complexities involved in accurately estimating the atmospheric parameters, RTM-based atmospheric correction was not performed in the current study. Instead, on account of the successful implementation of a rescaling scheme to correct negative airborne SIF_{760} and SIF_{687} values in Bandopadhyay et al. (2019), we used a simplified correction technique based on the same principle of using non-fluorescent targets (i.e., bare soil) as in the widely used transmittance correction technique, to compensate for negative SIF_{760} values related to calibration and atmospheric factors such as aerosol scattering and surface pressure. Any deviation from the non-fluorescent behaviour of bare soil targets identified in each image was attributed to spectral miscalibration or atmospheric effects. The method relies on forcing the non-fluorescent target to give zero SIF_{760}, and the non-zero SIF_{760} served as an offset to correct the SIF_{760} from vegetation targets following Eq. (2):

$$SIF_{corrected} = SIF_{vegetation\ target} - SIF_{non-fluorescent\ target} \quad (2)$$

To minimize the directional effects on the airborne-quantified SIF_{760}, the corrected SIF_{760} was normalized to a reference-viewing angle using a reflectance-based angular correction approach (Hao et al., 2021). The normalization method employs a reference SIF_{760} corresponding to a reference viewing angle, as well as near-infrared reflectance of vegetation (NIRv) (Badgley et al., 2017), to normalize SIF_{760} quantified at any viewing direction to a reference viewing angle. Two different approaches were used to compute the reference SIF_{760} for normalization. In the first approach, a single plot located at the centre of each hyperspectral image was selected as the reference SIF_{760} on account of being a nadir-view. In the second approach, locations of the ground-based spectral measurements were identified in the hyperspectral images and used for calculating the reference SIF_{760}. Since the ground-based spectral measurements were primarily conducted along the plot's centre, only pure vegetation pixels located along the plot's centre were used to compute mean radiance for the reference SIF_{760} calculation. This differs from the airborne SIF_{760} corresponding to individual plots, which was calculated using mean radiance from all pure vegetation pixels excluding the boundaries. The second approach was only applied for

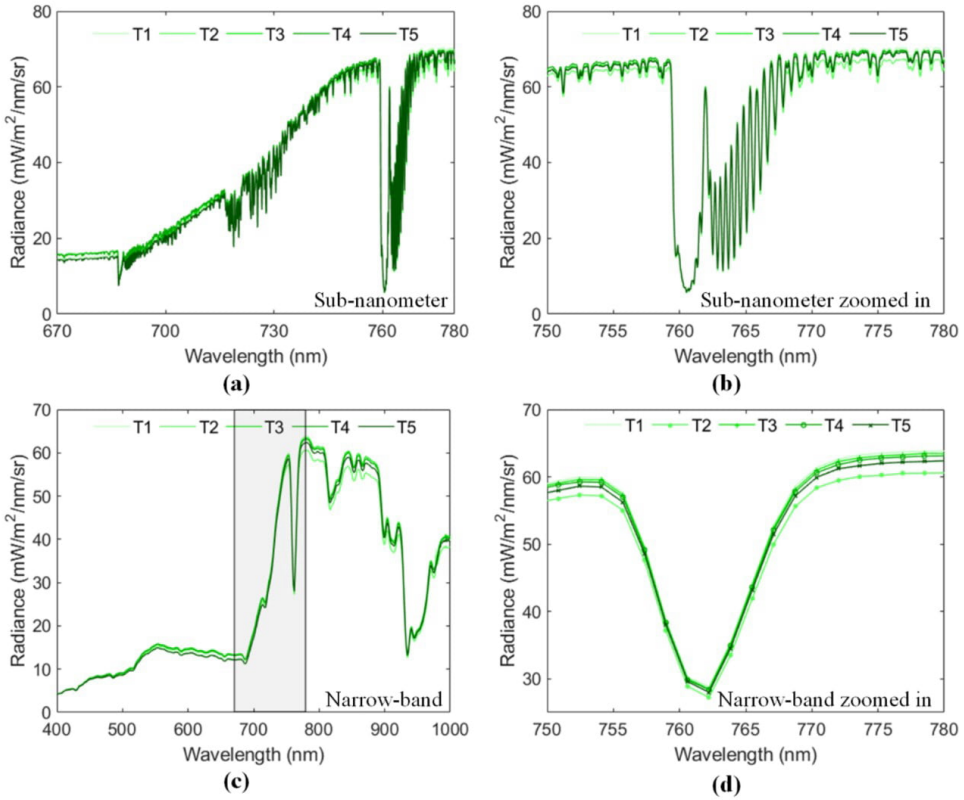

Fig. 3. Average radiance spectra for treated plots in experiment 1. Spectra obtained from (a) the sub-nanometer imager in the 670- to 780-nm region, (b) the sub-nanometer imager in the O_2-A absorption region, (c) the narrow-band imager in the 400- to 1000-nm region and (d) the narrow-band imager in the O_2-A absorption region. The transparent grey box in (c) shows the spectral region covered by the sub-nanometer hyperspectral imager. Codes T1-T5 correspond to the applied nitrogen fertilization rates shown in Table-1.

experiment 3 to validate the airborne-quantified SIF_{760} with the ground-based HR-2000 SIF_{760} measurements so that the reference viewing direction remained identical for ground-based and airborne SIF_{760}. Normalization was conducted according to the nadir-viewing angle for all inter-comparisons of airborne SIF_{760} from both imagers.

The study focused on assessing the spectral configuration of the two instruments, with attempts made to reduce distortions caused by other factors. We used pixels close to the nadir-viewing angle and avoided evaluating areas close to the image borders to reduce the potential effects of instrument 'smile' on assessment of the two instruments. Moreover, the angular correction used to normalize SIF_{760} minimizes the potential instrument smile effects (detailed above). Further work and a corresponding paper will evaluate sensor smile effects and corrections needed when using narrow-band instruments for SIF_{760} retrievals. This additional work is important because entire images, rather than just nadir pixels, are needed for practical applications in precision agriculture.

2.4. Modelling the spectral resolution effects on SIF quantification using SCOPE simulations

The SCOPE model integrates three radiative transfer modules and an energy balance module to estimate outgoing radiation spectra, turbulent heat fluxes, photosynthesis rates and chlorophyll fluorescence (Van der Tol et al., 2009). Surface reflectance and fluorescence spectra are simulated by linking several energy balance, photosynthesis and canopy biophysical parameters with TOC radiance, with SSI and SR of 1.0 nm each. The model assumes a homogenous canopy structure, and the canopy radiative transfer equations are based on the widely used SAIL model (Verhoef, 1984). Net radiation over the canopy is calculated by integrating the contribution from the individual layers with shaded and sunlit leaves at different leaf angles over the canopy depth. The canopy reflectance modelling is conducted based on four different Bidirectional Reflectance Distribution Function (BRDF) terms representing direct and diffused hemispherical contribution from the surrounding and the direct and diffused reflectance in the viewing direction. The leaf-level fluorescence spectra are modelled within the 640- to 850-nm spectral region based on the FLUSPECT model (Vilfan et al., 2016) by utilizing the leaf reflectance and fluorescence outputs derived from the PROSPECT model (Jacquemoud and Baret, 1990).

A simulated dataset using the SCOPE model (version 2.0) was generated to evaluate the influence of the SR of the airborne hyperspectral sensors on the 3FLD-based SIF_{760} quantification. The dataset consisted of 400,000 simulations generated by randomly varying specific input parameters, drawing from a uniform distribution within ranges shown in Table 4. All other SCOPE input parameters were kept at their default values. The air temperature and air pressure inputs for the SCOPE model were measured with a portable weather station during the

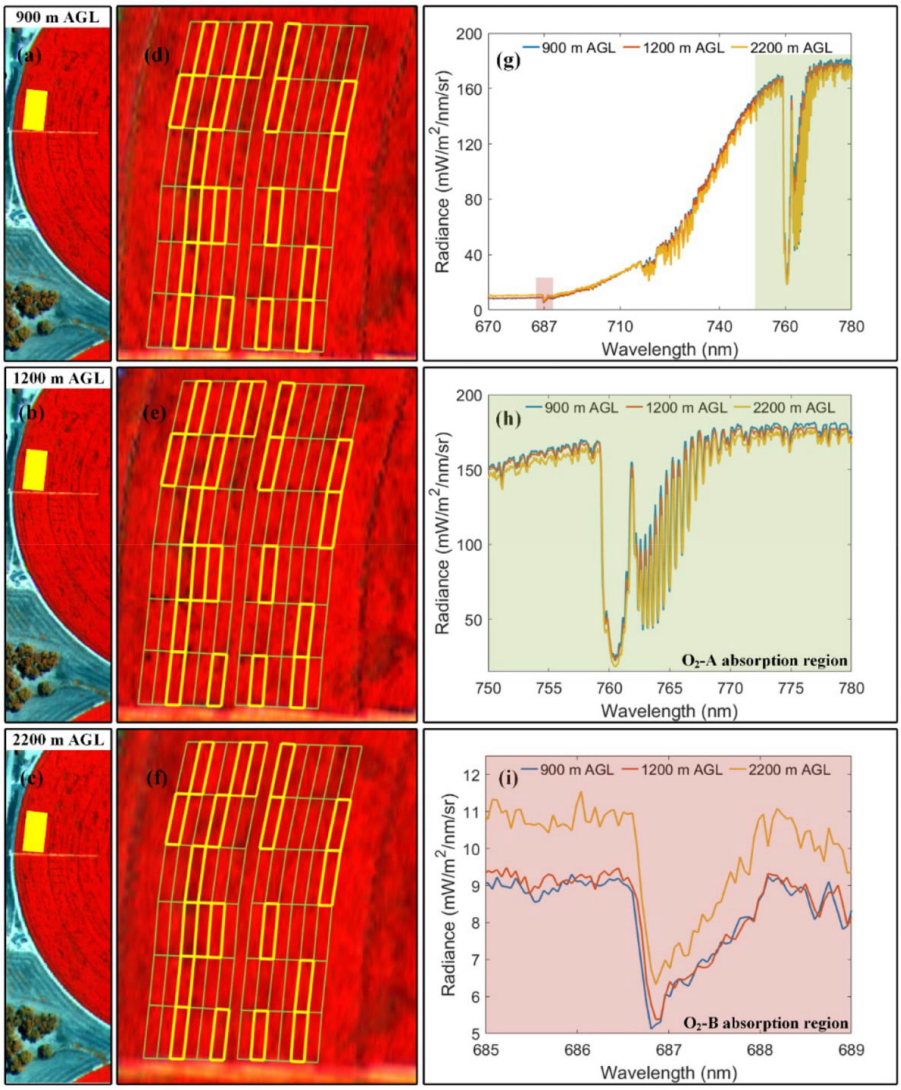

Fig. 4. Hyperspectral imagery from experiment 3. (a–f) Sub-nanometer composite imagery (760 (R), 710 (G) and 680 (B) nm) at various altitudes. (g–i) Average radiance spectra acquired for one of the experimental plots in the 670- to 780-nm region (g), O_2-A absorption region (h) and O_2-B absorption region (i). Area of yellow filled polygons (a, b, c) shown in detail in (d), (e) and (f), respectively. Green polygons indicate plots under different nitrogen treatments, and yellow polygons indicate the selected plots corresponding to three nitrogen treatments. (For interpretation of the references to colour in this figure legend, the reader is referred to the web version of this article.)

airborne campaign at field trial site 1. Details regarding the definition and ranges of all input parameters can be found in Supplementary Data S1. For each case, the TOC spectra of total upwelling radiance, SIF radiance and the corresponding irradiance were simulated using the default 1.0-nm SR and 1.0-nm SSI obtained from SCOPE. To compare the SIF_{760} retrieval performance for SR corresponding to the narrow-band hyperspectral imager, SCOPE-simulated spectra were resampled to 5.8-nm FWHM through Gaussian convolution matching the SSI with the narrow-band imager. The resampled radiance spectra in the 400- to 1000-nm spectral region were compared with the average radiance spectra obtained from the narrow-band imager at experimental field trial site 1 using RMSE as the cost function. For each narrow-band airborne radiance spectrum, we selected the 10 closest resampled radiance spectra from the 400,000 simulations along with their corresponding resampled-irradiance for the analysis. Fig. 5a shows the measured radiance spectra from the narrow-band imager. Fig. 5b and c show the SCOPE-simulated SIF and radiance spectra at 1-nm FWHM corresponding to the selected simulations. A comparison of the simulated SCOPE radiance spectra against the narrow-band imager is shown in Fig. 5d. Additionally, radiance and irradiance spectra corresponding

Table 4
Range of the SCOPE input parameters used in this study.

Parameter	Range/ Value	Unit	Description
C_{ab}	10–50	$\mu g \cdot cm^{-2}$	Chlorophyll $a + b$ content
C_{dm}	0.001–0.05	$g \cdot m^{-2}$	Dry matter content
C_w	0.001–0.05	cm	Leaf water equivalent layer
N	1.2–1.8	–	Leaf thickness parameters
Vcmax	20–120	$\mu mol \cdot m^{-1} \cdot s^{-1}$	Maximum carboxylation capacity at 25 °C
fqe	0.001–0.015	–	Fluorescence quantum yield efficiency at photosystem level
LAI	2–6	$m^2 \cdot m^{-2}$	Leaf area index
$LIDF_a$	−1–0	–	Leaf inclination
$LIDF_b$	0	–	Variation in leaf inclination
R_{in}	600–1000	$W \cdot m^{-2}$	Broadband incoming shortwave radiation
Ta	19.2	°C	Air temperature
p	1002.8	hPa	Air pressure
tts	35.42	deg.	Solar zenith angle

to SRs of 2.0 nm, 3.0 nm, 4.0 nm and 5.0 nm were generated by resampling SCOPE-simulated 1.0-nm SR spectra with Gaussian convolution but keeping the SSI at 1.0-nm. Fig. 5e and f show the comparison between the radiance spectra simulated by SCOPE at different SRs in the O_2-B and O_2-A absorption regions, respectively. The O_2-B absorption feature could only be identified at the default 1.0-nm SR. The decrease of SR from the default 1 nm to 5.8 nm resulted in O_2-A-band depth reduction and an increment in the radiance signal corresponding to the absorption minima.

2.5. Nitrogen assessments using narrow-band and sub-nanometer SIF retrievals

The effects of sensor SR on nitrogen estimation was assessed using models with chlorophyll content and SIF traits as inputs (Camino et al., 2018b). Nitrogen content was predicted using Random Forest (RF) (Breiman, 2001) models fit to data from field trial site 1, using i) C_{ab} derived from the narrow-band hyperspectral imagery through the inversion of PRO4SAIL RTM and ii) SIF_{760} quantified from each of the hyperspectral imagers as inputs. The PRO4SAIL model used coupled PROSPECT-D (Féret et al., 2021) and 4SAIL (Verhoef et al., 2007) to retrieve the biochemical constituents and canopy structural parameters, respectively. A look-up table with 200,000 simulations was built by randomly varying the biochemical and biophysical parameters with a uniform distribution within the ranges shown in Table 5.

Support vector machines (SVMs) were trained using simulated reflectance as inputs. Reflectance spectra were matched with the spectral resolution of the narrow-band hyperspectral imager (5.8-nm FWHM). SVMs were first trained in parallel (MATLAB parallel computing toolbox) using a radial basis function and optimizing the hyperparameters during training to predict C_{ab}. Then, using the average reflectance spectra extracted from pure-vegetation pixels, C_{ab} was estimated for each experimental plot. Subsequently, RF regression models were fit for each hyperspectral sensor, using crop N concentration as a response variable and the estimated C_{ab} from the narrow-band VNIR reflectance spectra ($C_{ab\text{-}narrow}$) and SIF_{760} derived from each hyperspectral imager (i.e., $C_{ab\text{-}narrow} + SIF_{760\text{-}narrow}$ vs. $C_{ab\text{-}narrow} + SIF_{760\text{-}sub\text{-}nanometer}$) as predictors.

3. Results

In experiment 1, leaf physiological traits were significantly different in plots fertilized at different rates ($p < 0.05$; Fig. 6). For experiments 2 and 3, differences were non-significant, but there was visible variation in leaf physiological variables among plots receiving different nitrogen treatments (Fig. 6). Differences in leaf total N concentration measured by destructive sampling were generally consistent with the trends observed in leaf steady-state fluorescence (Ft) with minor exceptions (e.g., values observed for T3 in experiment 1). Ft was lower in plots with the least N applied compared to other plots in all the experiments (Fig. 6, Ft and Total N panels). Fertilization rate was positively associated with chlorophyll a+b content and the leaf nitrogen balance index (NBI), while leaf flavonols and anthocyanins were inversely associated with fertilization rate. Leaf physiological values were more variable in experiment 1 (T1–T5: 0–184 kg N/ha) than in experiments 2 (T1–T2: 207–387 kg N/ha) or 3 (T1–T3: 0–315 kg N/ha).

The absorption features at O_2-A and O_2-B absorption regions were evident in the radiance spectra from both airborne hyperspectral imagers (Fig. 7). However, their shape and depth were strongly influenced by the SR. As a result of the coarser SR of the narrow-band imager, the absorption feature at the O_2-B band in the 685- to 690-nm spectral region could not be identified in the narrow-band radiance spectra (Fig. 7, inset). This result restricts the comparison between the narrow-band and sub-nanometer hyperspectral imagers for the calculation of SIF at the O_2-B band. Moreover, a reduction in the depth of the O_2-A absorption feature in the 750- to 780-nm spectral region and the corresponding increment in the radiance signal at the absorption minima were observed for the narrow-band radiance spectra, as expected (Fig. 7, inset). The wavelength corresponding to the radiance minimum was shifted towards higher wavelengths when compared to sub-nanometer radiance spectra, as shown in several studies (Cendrero-Mateo et al., 2019; Damm et al., 2011; Julitta et al., 2016; Liu et al., 2015).

At site 1, the depths of the O_2-A absorption feature from each of the two imagers were strongly correlated ($R^2 = 0.90$, $p < 0.001$; Fig. 8a), when using data from the full set of >100 plots. Nevertheless, the range of SIF_{760} values quantified with the 3FLD method ($SIF_{760\text{-}3FLD}$) differed between sub-nanometer imager (0.05–1.95 $mW/m^2/nm/sr$) and the narrow-band imager (0.37–8.12 $mW/m^2/nm/sr$; Fig. 8b). Although there was some lack of correspondence in $SIF_{760\text{-}3FLD}$ between the two imagers (RMSE = 3.86 $mW/m^2/nm/sr$), the two were significantly correlated ($R^2 = 0.85$, $p < 0.001$; Fig. 8b).

Airborne $SIF_{760\text{-}3FLD}$ estimates from both hyperspectral imagers are compared in Fig. 9. The best agreement between measures was observed in experiment 3 ($R^2 = 0.9$, RMSE = 3.28 $mW/m^2/nm/sr$, $p < 0.001$). Measures from each sensor were also well correlated in experiments 1 ($R^2 = 0.87$, RMSE = 4.69 $mW/m^2/nm/sr$, $p < 0.001$; Fig. 9a) and 2 ($R^2 = 0.77$, RMSE = 3.95 $mW/m^2/nm/sr$, $p < 0.01$; Fig. 9b). The error between estimates was consistent across experiments, yielding RMSEs within 3.28–4.69 $mW/m^2/nm/sr$.

Low-resolution SCOPE-simulated $SIF_{760\text{-}3FLD}$ values (2- to 5.8-nm FWHM) were significantly correlated with $SIF_{760\text{-}3FLD}$ simulated at 1-nm FWHM ($p < 0.001$, R^2 0.70–0.99; Fig. 10). RMSE values tended to increase with decreasing SR (Fig. 10). The pattern of differing absolute $SIF_{760\text{-}3FLD}$ values but stable relative differences across SRs observed with the SCOPE-simulated data was consistent with the experimental results from the airborne hyperspectral imagers.

A comparison of airborne $SIF_{760\text{-}3FLD}$ retrievals to ground-based $SIF_{760\text{-}3FLD}$ retrievals in experiment 3 is shown in Fig. 11. Ground-based measures were significantly correlated with both the sub-nanometer ($R^2 = 0.90$, $p < 0.001$; Fig. 11a) and the narrow-band ($R^2 = 0.88$, $p < 0.001$) hyperspectral imagers (Fig. 11b). $SIF_{760\text{-}3FLD}$ from the sub-nanometer imager showed strong agreement with the ground-based $SIF_{760\text{-}3FLD}$ values (RMSE = 0.07 $mW/m^2/nm/sr$, rRMSE = 3.7%), whereas the narrow-band imager exhibited greater overall differences from ground-based measures (RMSE = 3.26 $mW/m^2/nm/sr$, rRMSE = 170.5%). SIF-yield, which was estimated by normalizing the corrected $SIF_{760\text{-}3FLD}$ by the average NIR radiance in the 776–780-nm spectral region, was also significantly correlated with the leaf-level steady-state chlorophyll fluorescence in experiment 1 ($R^2 = 0.53$, $p < 0.01$ for sub-nanometer imager; $R^2 = 0.34$, $p < 0.05$ for narrow-band imager).

Measures of O_2-A band depth and airborne $SIF_{760\text{-}3FLD}$ at different altitudes are presented in Fig. 12. $SIF_{760\text{-}3FLD}$ measures with the narrow-

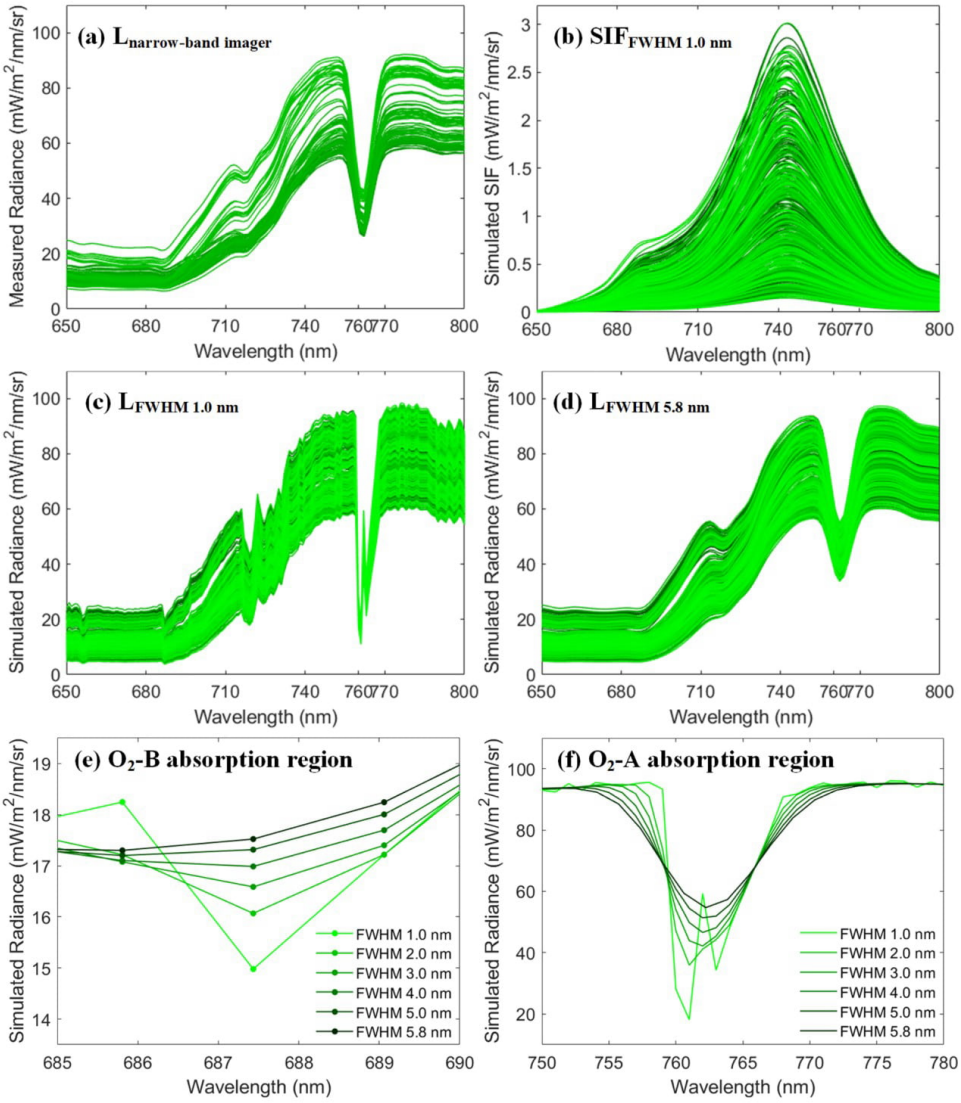

Fig. 5. (a) Measured radiance from the narrow-band imager. (b) SCOPE-simulated SIF at 1.0-nm FWHM. (c) SCOPE-simulated radiance at 1.0-nm FWHM. (d) SCOPE-simulated radiance corresponding to the narrow-band imager's spectral characteristics (FWHM = 5.8 nm, SSI = 1.626 nm). SCOPE-simulated radiance at different SRs in the O_2-B (e) and O_2-A absorption regions (f).

band imager at 2200 m AGL were excluded because pixels were too coarse (1.7 m) relative to plot size (3 m × 12 m). O_2-A absorption feature depth and $SIF_{760\text{-}3FLD}$ differed significantly with altitude (Fig. 12). The depth of the O_2-A absorption feature increased with sensor altitude, and $SIF_{760\text{-}3FLD}$ decreased with sensor altitude for both airborne imagers (Fig. 12).

Sub-nanometer $SIF_{760\text{-}3FLD}$ retrievals were significantly correlated with narrow-band imager retrievals in experiment 3 at both 900 m AGL ($R^2 = 0.85$, $p < 0.001$; Fig. 13a) and 1200 AGL ($R^2 = 0.9$, $p < 0.001$; Fig. 13a). The slope of the relationship between sub-nanometer and narrow-band retrievals was steeper for 900 m AGL than for 1200 m AGL. RMSE at 900 m AGL (4.29 mW/m^2/nm/sr) was higher than that of 1200 m AGL (3.28 mW/m^2/nm/sr), possibly explained by larger $SIF_{760\text{-}3FLD}$ values at lower altitudes. $SIF_{760\text{-}3FLD}$ at 900 m AGL was significantly correlated with $SIF_{760\text{-}3FLD}$ at 1200 m AGL ($R^2 = 0.92$, $p < 0.001$; Fig. 13b) and 2200 m AGL ($R^2 = 0.8$, $p < 0.001$; Fig. 13b) using the sub-nanometer imager. $SIF_{760\text{-}3FLD}$ values decreased with imager altitude, and the relationship between low-altitude and high-altitude measurements also changed, with shallower slopes at higher altitudes (Fig. 13b). RMSE was higher at 2200 m AGL than at 1200 m AGL altitude, when compared to 900 m AGL. A similar pattern was observed for narrow-band $SIF_{760\text{-}3FLD}$ retrievals, with an overall significant correlation (R^2

Table 5
Parameters and ranges used for the look-up table generation for the PRO4SAIL RTM.

Parameter	Abbreviation	Value/range
Chlorophyll $a + b$ content [µg/cm^2]	C_{ab}	4–70
Carotenoid content [µg/cm^2]	C_{x+c}	1–20
Anthocyanin content [µg/cm^2]	Anth	0–15
Dry matter content [g/cm^2]	C_m	0.007
Water content [g/cm^2]	C_w	0.001
Mesophyll structure Coeff.	N	0.5–3
Leaf area index [m^2/m^2]	LAI	0.3–5
Average leaf angle [deg.]	$LIDF_a$	0–90
Hot spot parameter	h	0.01
Soil reflectance	R_{soil}	PRO4SAIL dry soil spectra
Observer angle [deg.]	tt_o	0
Sun zenith angle [deg.]	tt_s	35.42
Relative azimuth angle [deg.]	Ψ	0

= 0.82, RMSE = 1.36 mW/m^2/nm/sr, $p < 0.001$; Fig. 13c) and lower $SIF_{760\text{-}3FLD}$ values at higher altitudes.

Sub-nanometer $SIF_{760\text{-}3FLD}$ was significantly correlated with ground-based $SIF_{760\text{-}3FLD}$ at all sensor altitudes ($p < 0.001$, all $R^2 > 0.9$; Fig. 14a). RMSEs between airborne and ground-based SIF retrievals at 900 and 1200 m AGL were lower than 0.1 mW/m^2/nm/sr and rRMSEs were lower than 4%. $SIF_{760\text{-}3FLD}$ at 2200 m AGL consistently underestimated ground-based SIF (RMSE = 0.5 mW/m^2/nm/sr and rRMSE = 28.2%; Fig. 14a). Ground-based $SIF_{760\text{-}3FLD}$ was also significantly correlated with airborne $SIF_{760\text{-}3FLD}$ from the narrow-band imager ($p < 0.001$, $R^2 > 0.85$) at both altitudes (Fig. 14b). Narrow-band imager $SIF_{760\text{-}3FLD}$ estimates at 1200 m AGL tended to be smaller than ground-based measures (Fig. 14b), and error was high for both 900 m AGL (RMSE = 3.77 mW/m^2/nm/sr, rRMSE = 200.8%) and 1200 m AGL (RMSE = 3.26 mW/m^2/nm/sr, rRMSE = 170.5%).

Nitrogen predictions from both RF models were significantly correlated ($p < 0.01$) with the field-level nitrogen content measurements obtained by destructive sampling (Fig. 15). $SIF_{760\text{-}FLD}$ from the sub-nanometer hyperspectral imager by itself was significantly correlated with field-level nitrogen content ($R^2 = 0.71$, $p < 0.001$; Fig. 15a), as was SIF_{760} quantified from the narrow-band imager ($R^2 = 0.67$, $p < 0.001$; Fig. 15b). The RF algorithm using $SIF_{760\text{-sub-nanometer}}$ performed slightly better ($R^2 = 0.93$, RMSE = 0.09%; Fig. 15c) than the RF using $SIF_{760\text{-narrow-band}}$ ($R^2 = 0.87$, RMSE = 0.12%; Fig. 15d).

4. Discussion

In this study we examined the relationship between airborne $SIF_{760\text{-}3FLD}$ quantified using sub-nanometer resolution (i.e., 0.1- to 0.2-nm FWHM) and narrow-band resolution (i.e., 5.8-nm FWHM) hyperspectral imagers in the context of plant phenotyping for homogenous crop canopies. Our results support the assertion that airborne SIF retrievals from narrow-band hyperspectral imagers can successfully track small physiological changes induced by plant pathogens and environmental stresses, as reported elsewhere (Calderón et al., 2015, 2013; Camino et al., 2021, 2018a; Hernández-Clemente et al., 2017; Panigada et al., 2014; Poblete et al., 2021, 2020; Zarco-Tejada et al., 2018, 2012). Precise SIF_{760} quantification at absolute scales was not essential for detecting plant stress in these studies. In our study, narrow-band airborne $SIF_{760\text{-}3FLD}$ was significantly associated with both sub-nanometer airborne and ground-based SIF observations. Our results particularly illustrate the capability of these narrow-band hyperspectral imagers for characterizing the intra-field SIF_{760} variability induced by different nitrogen fertilization rates.

Previous studies have highlighted the importance of sensor configuration for detecting spectral absorption features occurring over very narrow spectral ranges, particularly the need for high SR and SNR when quantifying SIF (Mohammed et al., 2019). The literature has emphasized the need for instruments with sub-nanometer resolutions to accurately characterize narrow absorption features for reliable SIF estimates in physical units (Cogliati et al., 2015; Julitta et al., 2016; Meroni and

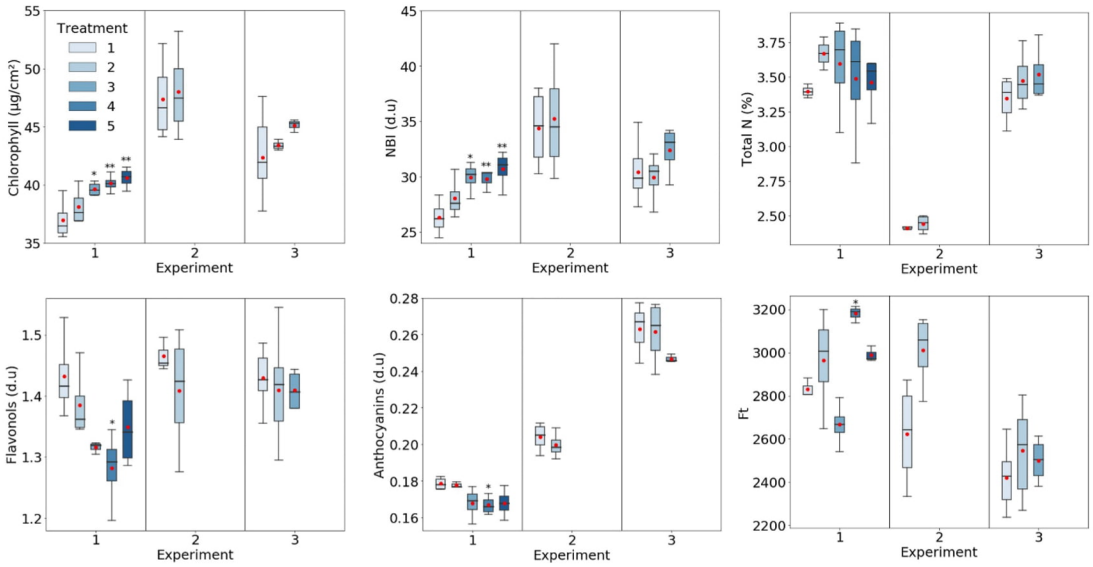

Fig. 6. Leaf physiological traits by fertilization rate across experiments. Average values indicated by red points. The black lines within boxes represent medians, and the top and bottom of each box represent the 75th and 25th quartile, respectively. Whiskers represent ±1.5 × Inter Quartile Range. Asterisks indicate significant differences from the treatment 1 plots according to Dunnett's test at $\alpha < 0.05$. *$p \leq 0.05$; **$p \leq 0.01$. (For interpretation of the references to colour in this figure legend, the reader is referred to the web version of this article.)

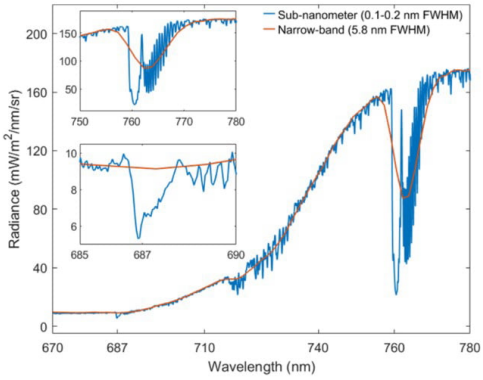

Fig. 7. Comparison of average radiance spectra from one of the plots within experiment-3 in the 670- to 780-nm region obtained from both hyperspectral imagers. The insets show the comparison within O_2-A and O_2-B absorption features in the 750- to 780-nm region and 685- to 690-nm region, respectively.

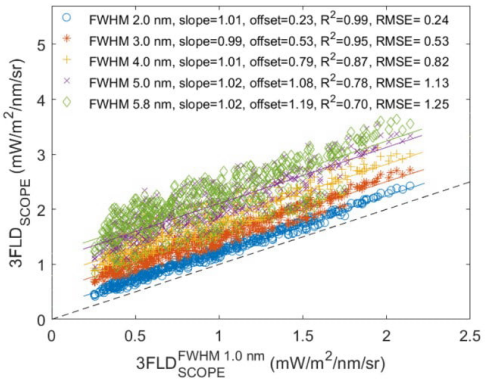

Fig. 10. Relationships between $SIF_{760\text{-}3FLD}$ for SCOPE simulations with different SRs against $SIF_{760\text{-}3FLD}$ quantified at 1.0-nm FWHM. The dotted line represents the 1:1 line.

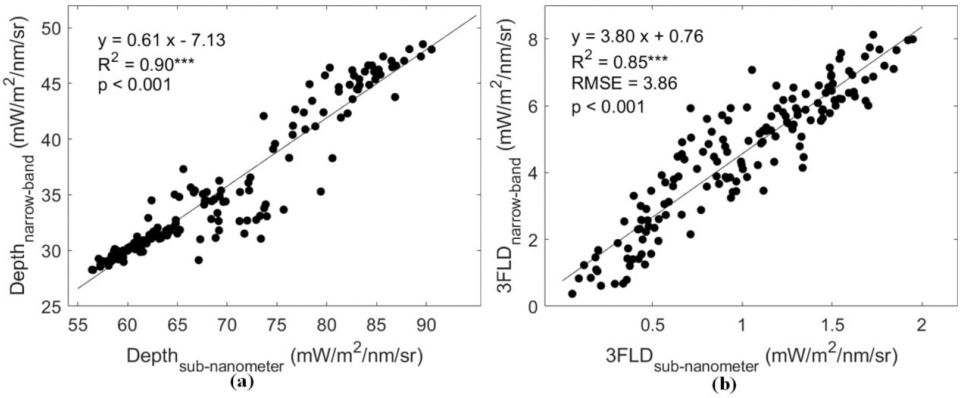

Fig. 8. Relationship between depth at the O_2-A absorption feature (a) and $SIF_{760\text{-}3FLD}$ (b) over the experimental field at site 1 from both hyperspectral imagers. The range of absolute $SIF_{760\text{-}3FLD}$ levels derived from the narrow-band imager was higher than the typical range of 0–3 mW/m^2/nm/sr quantified from healthy vegetation due to the impact of the spectral resolution of the instrument.

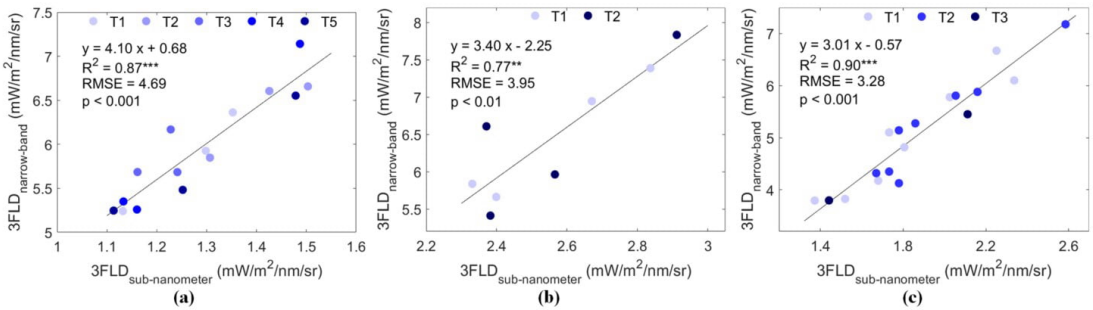

Fig. 9. Relationship between airborne $SIF_{760\text{-}3FLD}$ measures from different hyperspectral imagers across experiments 1 (a), 2 (b) and 3 (c). The range of absolute $SIF_{760\text{-}3FLD}$ levels derived from the narrow-band imager was higher than the typical range of 0–3 mW/m^2/nm/sr quantified from healthy vegetation due to the impact of the spectral resolution of the instrument.

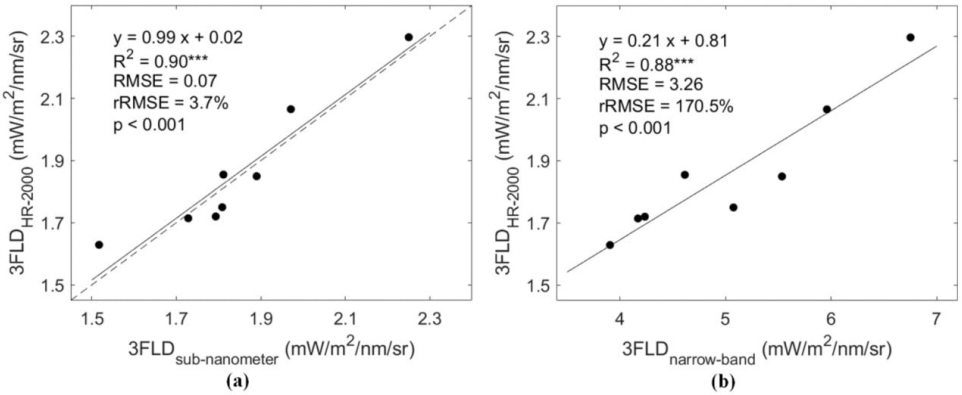

Fig. 11. Relationship between ground-based $SIF_{760\text{-}3FLD}$ quantified from the HR-2000 field spectrometer and airborne $SIF_{760\text{-}3FLD}$ quantified from the sub-nanometer (a) and the narrow-band (b) hyperspectral imagers for experiment 3. The dotted line represents the 1:1 line. The range of absolute $SIF_{760\text{-}3FLD}$ levels derived from the narrow-band imager was higher than the typical range of 0–3 mW/m^2/nm/sr quantified from healthy vegetation due to the impact of the spectral resolution of the instrument.

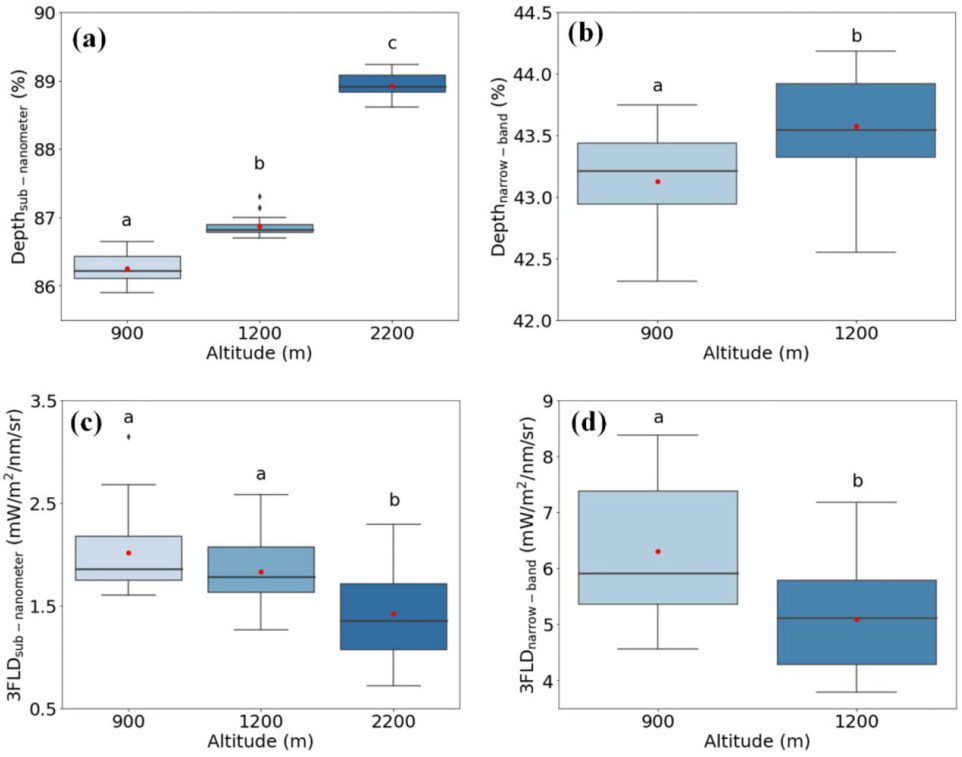

Fig. 12. Effect of sensor altitude on O_2-A band depth and $SIF_{760\text{-}3FLD}$ in experiment 3. Letters (a, b and c) within each plot represent the results of Tukey's honest significant difference (HSD) post-hoc comparisons of group means with $\alpha < 0.05$. Groups sharing the same letter are not significantly different. In the boxplots, the average values are shown with a red circle. The black line within the box is the median, and the top and bottom of the box is the 75th and 25th quartile, respectively. The whiskers represent $\pm 1.5 \times$ Interquartile range. The outliers are represented as diamonds. The range of absolute $SIF_{760\text{-}3FLD}$ levels derived from the narrow-band imager was higher than the typical range of 0–3 mW/m^2/nm/sr quantified from healthy vegetation due to the impact of the spectral resolution of the instrument. $SIF_{760\text{-}3FLD}$ measures with the narrow-band imager at 2200 m AGL were excluded because pixels were too coarse (1.7 m) relative to plot size (3 m $\times$ 12 m). (For interpretation of the references to colour in this figure legend, the reader is referred to the web version of this article.)

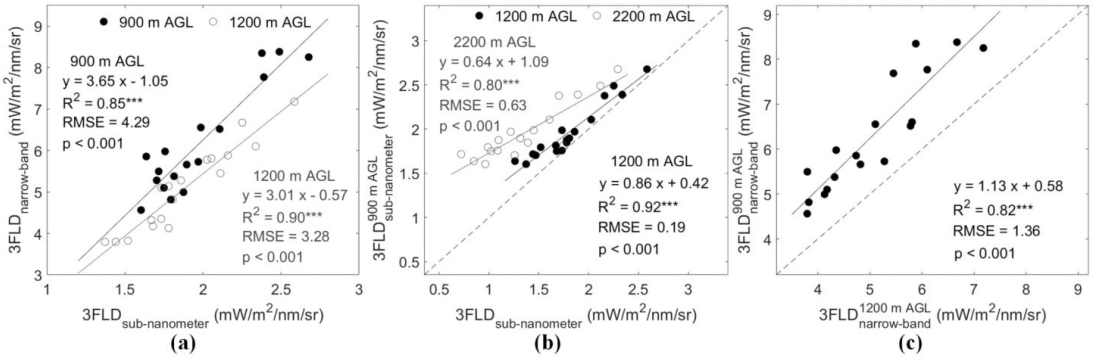

Fig. 13. (a) Relationships between $SIF_{760\text{-}3FLD}$ estimates from narrow-band and sub-nanometer hyperspectral imagers by sensor altitude. (b) Relationships between airborne $SIF_{760\text{-}3FLD}$ from sub-nanometer imager at 1200 and 2200 m AGL compared to the $SIF_{760\text{-}3FLD}$ quantified at 900 m AGL. (c) Relationship between airborne $SIF_{760\text{-}3FLD}$ from the narrow-band hyperspectral imager at 900 and 1200 m AGL. The range of absolute $SIF_{760\text{-}3FLD}$ levels derived from the narrow-band imager was higher than the typical range of 0–3 mW/m^2/nm/sr quantified from healthy vegetation due to the impact of the spectral resolution of the instrument. $SIF_{760\text{-}3FLD}$ measures with the narrow-band imager at 2200 m AGL were excluded because pixels were too coarse (1.7 m) relative to plot size (3 m × 12 m).

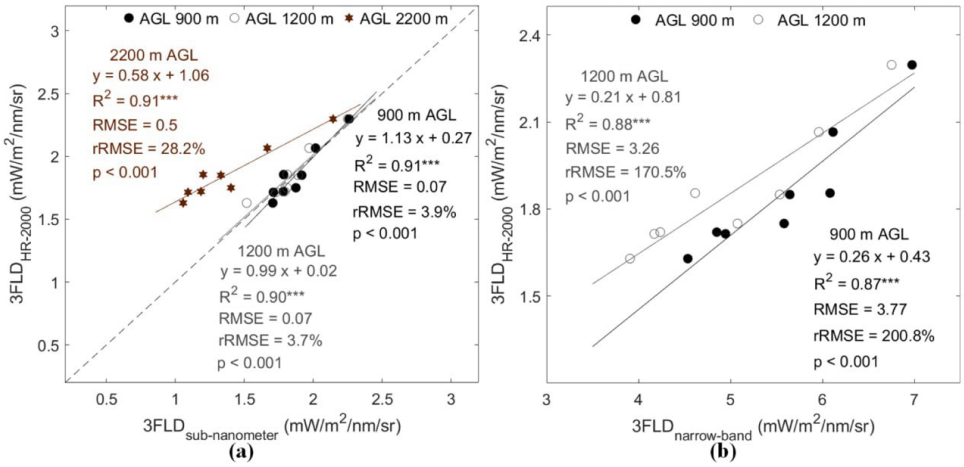

Fig. 14. Relationship between ground-based $SIF_{760\text{-}3FLD}$ quantified with a HR-2000 field spectrometer and airborne $SIF_{760\text{-}3FLD}$ at 900 m, 1200 m and 2200 m AGL retrieved from the sub-nanometer imager (a) and the narrow-band imager (b). The range of absolute $SIF_{760\text{-}3FLD}$ levels derived from the narrow-band imager was higher than the typical range of 0–3 mW/m^2/nm/sr quantified from healthy vegetation due to the impact of the spectral resolution of the instrument. $SIF_{760\text{-}3FLD}$ measures with the narrow-band imager at 2200 m AGL were excluded because pixels were too coarse (1.7 m) relative to plot size (3 m × 12 m).

Colombo, 2006; Meroni et al., 2011; Rossini et al., 2010). The experimental results from these studies are consistent with modelling studies based on FluorSAIL3 (Damm et al., 2011; Cendrero-Mateo et al., 2019) and SCOPE (Liu et al., 2015), which showed an increase in the SIF_{760} retrieval accuracy with increasing sensor SR. These modelling studies also found strong correlations between modelled and estimated SIF_{760} for low SR (5 nm) instruments using 3FLD ($r = 0.78$, RMSE = 0.31 mW/m^2/nm/sr) and iFLD ($r = 0.81$, RMSE = 0.081 mW/m^2/nm/sr) (Damm et al., 2011). The SCOPE modelling results presented in this study support the findings of previous modelling efforts, illustrating statistically significant relationships ($p < 0.001$, $R^2 = 0.70$–0.99, RMSE = 0.24–1.25 mW/m^2/nm/sr; Fig. 10) between $SIF_{760\text{-}3FLD}$ at 1 nm and $SIF_{760\text{-}3FLD}$ at coarser SRs ranging from 2-nm to 5.8-nm FWHM. The offset of the linear relationship with $SIF_{760\text{-}3FLD}$ at 1 nm increased steadily as the SR decreased from 2 to 5.8 nm, while the slope remained close to 1. This offset increase can be attributed to differences in radiance corresponding to the O_2-A band minima, which showed a 200% increase (Fig. 5f) when resampling radiance spectra from 1 to 5.8 nm SR. Our modelling results and those of previous studies suggest that narrow-band resolution sensors (4- to 6-nm FWHM) with sufficient SNR can sufficiently characterize relative SIF_{760} levels despite their inability to provide reliable absolute SIF_{760} estimates.

Differential nitrogen application rates in the three experiments were associated with variability of leaf physiological measurements (Fig. 6) and airborne $SIF_{760\text{-}3FLD}$. Narrow-band and sub-nanometer $SIF_{760\text{-}3FLD}$ estimates were strongly correlated across experiments, and both differed by nitrogen fertilization level. The best correlation, observed in experiment 3, may be attributed to the identical flight altitude at which the narrow-band and the sub-nanometer hyperspectral images were collected for this experiment (site 2; Table 2) in addition to the higher

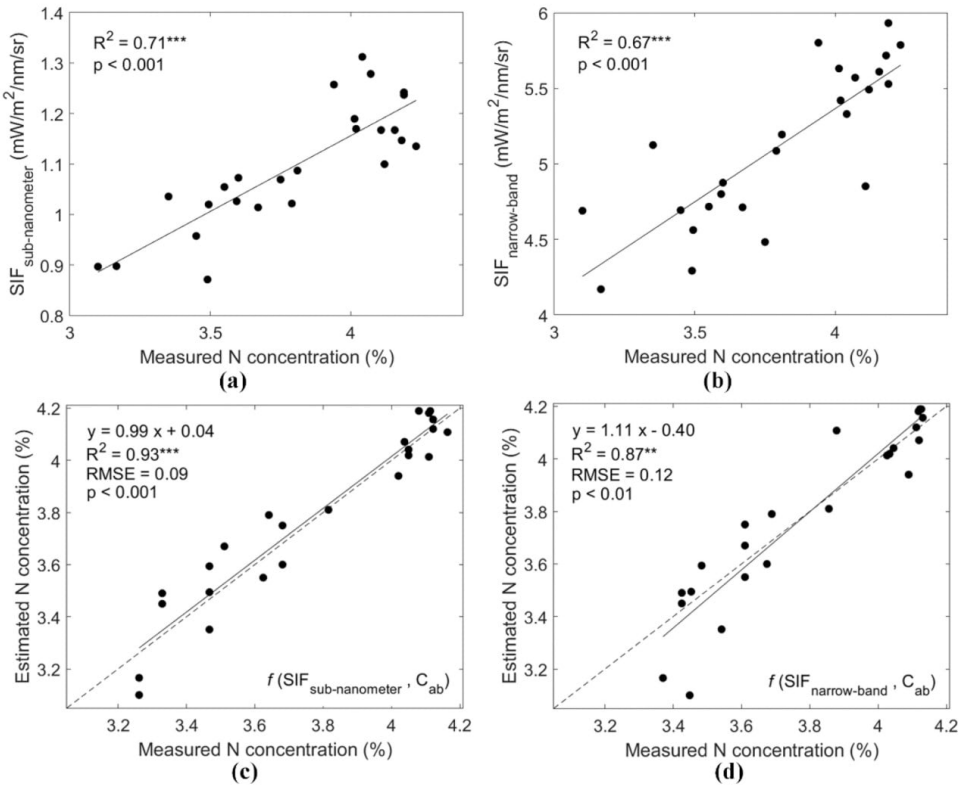

Fig. 15. Relationships between N concentration and airborne $SIF_{760\text{-}3FLD}$ quantified from a sub-nanometer (a) and narrow-band imager (b). Measured vs. estimated N concentration using Random Forest regression models, which included RTM-based C_{ab} and $SIF_{760\text{-}3FLD}$ generated from either a sub-nanometer (c) or narrow-band imager (d). The dotted line represents the 1:1 line. The range of absolute $SIF_{760\text{-}3FLD}$ levels derived from the narrow-band imager was higher than the typical range of 0–3 $mW/m^2/nm/sr$ quantified from healthy vegetation due to the impact of the spectral resolution of the instrument.

relative $SIF_{760\text{-}3FLD}$ variability observed within the experimental plots compared to experiments 1 and 2 (Fig. 9). The results demonstrated consistency across experimental sites and airborne campaigns carried out at different times, flight altitudes and years, showing robust relationships in terms of the relative $SIF_{760\text{-}3FLD}$ variability quantified by the two hyperspectral imagers. The differences obtained in absolute levels of $SIF_{760\text{-}3FLD}$ quantified in the three experiments can be associated with the differences in crop varieties, crop growth stages and the slightly different acquisition times of the airborne hyperspectral images. These results are consistent with previous studies showing differences in both ground-based and airborne SIF_{760} measurements according to nitrogen treatment (Cendrero-Mateo et al., 2016; Jia et al., 2018, 2021; Quemada et al., 2014; Watt et al., 2020a, 2020b).

Sensor altitude was identified as a critical factor in determining SIF accuracy (Daumard et al., 2015; Ni et al., 2016). MODTRAN (Berk et al., 2014) was used in these studies to show that the depth of the O_2-A absorption feature increases with sensor altitude. This is consistent with our findings, which show that the O_2-A band depth increased with altitude for both airborne hyperspectral imagers (Fig. 12) due to an increase in the radiance of the O_2-A band minima (Fig. 4h). Despite correcting for the atmospheric effects, $SIF_{760\text{-}3FLD}$ decreased with altitude for both airborne hyperspectral imagers. Such a decrease is linked to the correction method used, which relies on non-fluorescent targets. The relative increase in O_2-A band depth with increasing altitude is greater for vegetation targets than for bare soil targets (Daumard et al., 2015). This difference results in a bias in the corrected $SIF_{760\text{-}3FLD}$. Although $SIF_{760\text{-}3FLD}$ was overestimated at higher altitudes with both hyperspectral imagers, airborne estimates remained well correlated with ground-based measurements across altitudes (Figs. 12 and 14). This result has important implications for drone and airborne-based SIF quantifications in plant phenotyping studies and precision agriculture applications, in which sensor altitude is generally adapted depending on the flight efficiency and areal coverage. Although the relative variability needs to be assessed for detecting physiological changes induced by biotic or abiotic factors, understanding the effects of sensor altitude on SIF retrievals is critical for accurately interpreting SIF when used as input in stress-detection models.

Few studies have validated airborne-quantified SIF_{760} from narrow-band hyperspectral imagers against ground-based observations from high-resolution field spectrometers, due to the challenges associated with complex and heterogenous canopies including forest areas and cash crops such as vineyards and tree orchards. Damm et al. (2015) demonstrated the relationship between the medium-resolution Airborne Prism Experiment (APEX) sensor and a ground-based ASD (PANalytical, Boulder, US) field spectrometer for three different types of ecosystems. Measures were correlated ($R^2 = 0.71$), but airborne SIF_{760} systematically overestimated ground-based SIF_{760} by a proportionality factor (slope of airborne vs. ground SIF_{760} relationship) of 1.93 and an rRMSE

of 28.9%. Guanter et al. (2007) found good agreement ($R^2 = 0.85$) between airborne SIF_{760} derived from the Compact Airborne Spectrographic Imager (CASI, Itres Research Ltd., Canada) and ground-based SIF_{760} derived from the ASD FieldSpec FR spectroradiometer. The airborne vs. ground-based relationship found in the current study ($R^2 = 0.88$, proportionality factor = 4.76) is consistent with the results from both studies above. Due to the impact of SR on the absolute $SIF_{760\text{-}3FLD}$ quantification, larger deviations in terms of rRMSE and proportionality factor were observed compared with the results from Damm et al. (2015), which can be attributed to the sub-nanometer resolution (0.065-nm FWHM) of the reference ground-based HR-2000 spectrometer used in our study as compared to the moderate spectral resolution of ASD spectrometers (>1.0-nm FWHM) used elsewhere.

The potential effects of the canopy structure are important to consider when comparing the narrow-band vs. sub-nanometer SIF retrievals. The TOC SIF observations from ground-based, airborne and spaceborne platforms are strongly affected by plant canopy structure due to the re-absorption and scattering of light within the canopy (Fournier et al., 2012; Porcar-Castell et al., 2014; Dechant et al., 2020; Yang and Van der Tol, 2018; Zeng et al., 2019). This structure is usually characterized by parameters such as leaf area index and the leaf inclination distribution function and may be approximated with vegetation indices such as Modified Triangular Vegetation Index (MTVI2) (Haboudane et al., 2004) and Enhanced Vegetation Index (EVI) (Huete et al., 2002) when assessing the effects of structure on SIF. In our study, the structural differences across experimental plots were generally small as structural changes were generally not associated with experimental treatments. Nevertheless, we tested whether treatment-associated variability in canopy structure could be related to $SIF_{760\text{-}3FLD}$ from the narrow-band hyperspectral imager. We found that the relationships of both MTVI2 and EVI with narrow-band airborne $SIF_{760\text{-}3FLD}$ were weak and non-significantly correlated at both field trial sites ($p > 0.1$, R^2 = 0–0.11; Fig. 16). These results suggest that the $SIF_{760\text{-}3FLD}$ variability captured by the narrow-band imager in the experiments was not driven by changes arising from structural effects. Moreover, it shows that the fluorescence *in-filling* at the O_2-A band was unaffected by structure, with the variability across experimental plots due to subtle physiological differences.

Predictive models of leaf N concentration improved only slightly when using SIF_{760} from the sub-nanometer imager compared to the narrow-band imager, with a marginal increase in the model performance ($R^2 = 0.87$ vs. 0.93) and a decrease in the error (RMSE = 0.12% vs. 0.09%). The direction of this improvement is consistent with the greater accuracy of the sub-nanometer SR imager. Nevertheless, these results suggest that data from the narrow-band hyperspectral imager may be sufficient for predicting N concentration in plant phenotyping and precision agriculture applications. Narrow-band imagery may be particularly suitable since relative changes in SIF linked to physiological conditions, nutritional deficiencies and stress levels are often the focus of such studies.

For assessing crop physiological status, standard commercially available hyperspectral imagers with 4- to 6-nm FWHM and SNRs greater than 300:1 can provide reliable relative SIF_{760} estimates (Zarco-Tejada et al., 2012, 2013a). These sensors are lightweight and can be carried on drone platforms that provide very high spatial resolution images due to low flying altitude. This capacity to generate very high spatial resolution imagery with narrow spectral bands is particularly important for plant phenotyping and precision agriculture applications for mapping physiological condition (Mohammed et al., 2019). Additional work using RTMs such as SCOPE and others is needed for improving the interpretation of SIF quantified using broader resolutions in precision agriculture.

5. Conclusions

We assessed the relationships between airborne $SIF_{760\text{-}3FLD}$ quantified from narrow-band (5.8-nm FWHM) and sub-nanometer (0.1- to 0.2-nm FWHM) hyperspectral imagers flown in tandem over three experimental fields with varying nitrogen application rates across 3 years. $SIF_{760\text{-}3FLD}$ estimates derived from each imager were significantly correlated with each other for all the three experiments ($p < 0.01$, R^2 = 0.77–0.90). Ground-level HR-2000 $SIF_{760\text{-}3FLD}$ was significantly correlated with that of the sub-nanometer ($p < 0.001$, $R^2 = 0.9$) and the narrow-band hyperspectral imager ($p < 0.001$, $R^2 = 0.88$). These strong correlations among the narrow-band, sub-nanometer and ground-based $SIF_{760\text{-}3FLD}$ retrievals support the use of narrow-band hyperspectral sensors for detecting relative SIF differences in the context of plant phenotyping, vegetation stress detection and plant physiological condition. Although sub-nanometer SR is required for the accurate retrieval of SIF in absolute units, broader-band hyperspectral imaging technology of 4- to 6-nm bandwidth used in this study provides reliable assessment of relative SIF_{760} variability. The broader-band hyperspectral technology is also cost-effective, compact and facilitates the collection of high-spatial resolution fluorescence data required in precision agriculture.

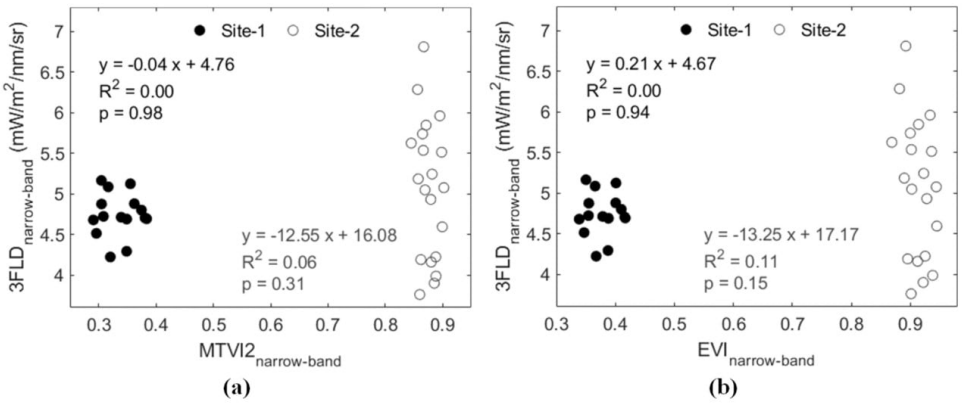

Fig. 16. Relationships between airborne $SIF_{760\text{-}3FLD}$ from the narrow-band hyperspectral imager and MTVI2 (a) and EVI (b). The range of absolute $SIF_{760\text{-}3FLD}$ levels derived from the narrow-band imager was higher than the typical range of 0–3 $mW/m^2/nm/sr$ quantified from healthy vegetation due to the impact of the spectral resolution of the instrument.

Credit author statement

A.B., T.P. and P.J.Z.-T. designed the objectives of this study and designed research; A.B., T.P. and A.L. carried out field work and airborne data collections; A.B. analysed data and performed research; A. L. provided field support and access to experimental sites; A.B. wrote the paper, and T.P., A.H., R.H-C. and P.J.Z.-T. contributed and provided comments. All authors read and approved the final submission.

Declaration of Competing Interest

The authors declare that they have no known competing financial interests or personal relationships that could have appeared to influence the work reported in this paper.

Acknowledgements

The authors gratefully acknowledge the Foundation for Arable Research Australia, in particular Michael Straight and Ben Morris; the Grains Research and Development Corporation Australia; and Riverine Plains Incorporated for their provision and management of the field trials. A. Gracia-Romero and Y. Wang are acknowledged for their technical support during the field and airborne campaigns.

Appendix A. Supplementary data

Supplementary data to this article can be found online at https://doi.org/10.1016/j.rse.2022.112986.

References

Aasen, H., Honkavaara, E., Lucieer, A., Zarco-Tejada, P.J., 2018. Quantitative remote sensing at ultra-high resolution with UAV spectroscopy: a review of sensor technology, measurement procedures, and data correction workflows. Remote Sens. 10, 1091.

Badgley, G., Field, C.B., Berry, J.A., 2017. Canopy near-infrared reflectance and terrestrial photosynthesis. Sci. Adv. 3, e1602244.

Bandopadhyay, S., Rastogi, A., Rascher, U., Rademske, P., Schickling, A., Cogliati, S., Julitta, T., Arthur, A. Mac, Hueni, A., Tomelleri, E., Celesti, M., Burkart, A., Strózecki, M., Sakowska, K., Gabka, M., Rosadziński, S., Sojka, M., Iordache, M.D., Reusen, I., Van der Tol, C., Damm, A., Schuettemeyer, D., Juszczak, R., 2019. HyPlant-derived sun-induced fluorescence - a new opportunity to disentangle complex vegetation signals from diverse vegetation types. Remote Sens. 11, 1691.

Belwalkar, A., Poblete, T., Longmire, A., Hornero, A., Zarco-Tejada, P.J., 2021. Comparing the retrieval of chlorophyll fluorescence from two airborne hyperspectral imagers with different spectral resolutions for plant phenotyping studies. In: Proc. IEEE International Geoscience and Remote Sensing Symposium (IGARSS), 12–16 July 2021, Brussels, Belgium, pp. 5845–5848.

Berk, A., Conforti, P., Kennett, R., Perkins, T., Hawes, F., Van den Bosch, J., 2014. MODTRAN6: A major upgrade of the MODTRAN radiative transfer code. In: Proc. SPIE 9088, Algorithms and Technologies for Multispectral, Hyperspectral, and Ultraspectral Imagery XX, 90880H, 13 June 2014.

Breiman, L., 2001. Random Forests. Mach. Learn. 45, 5–32.

Calderón, R., Navas-Cortés, J.A., Lucena, C., Zarco-Tejada, P.J., 2013. High-resolution airborne hyperspectral and thermal imagery for early detection of Verticillium wilt of olive using fluorescence, temperature and narrow-band spectral indices. Remote Sens. Environ. 139, 231–245.

Calderón, R., Navas-Cortés, J.A., Zarco-Tejada, P.J., 2015. Early detection and quantification of Verticillium wilt in olive using hyperspectral and thermal imagery over large areas. Remote Sens. 7, 5584–5610.

Camino, C., Zarco-Tejada, P.J., Gonzalez-Dugo, V., 2018a. Effects of heterogeneity within tree crowns on airborne-quantified SIF and the CWSI as indicators of water stress in the context of precision agriculture. Remote Sens. 10, 604.

Camino, C., González-Dugo, V., Hernandez, P., Sillero, J.C., Zarco-Tejada, P.J., 2018b. Improved nitrogen retrievals with airborne-derived fluorescence and plant traits quantified from VNIR-SWIR hyperspectral imagery in the context of precision agriculture. Int. J. Appl. Earth Obs. Geoinf. 70, 105–117.

Camino, C., Gonzalez-Dugo, V., Hernandez, P., Zarco-Tejada, P.J., 2019. Radiative transfer Vcmax estimation from hyperspectral imagery and SIF retrievals to assess photosynthetic performance in rainfed and irrigated plant phenotyping trials. Remote Sens. Environ. 231, 111186.

Camino, C., Calderón, R., Parnell, S., Dierkes, H., Chemin, Y., Román-Écija, M., Montes-Borrego, M., Landa, B.B., Navas-Cortes, J.A., Zarco-Tejada, P.J., Beck, P.S.A., 2021. Detection of Xylella fastidiosa in almond orchards by synergic use of an epidemic spread model and remotely sensed plant traits. Remote Sens. Environ. 260, 112420.

Celesti, M., Van der Tol, C., Cogliati, S., Panigada, C., Yang, P., Pinto, F., Rascher, U., Miglietta, F., Colombo, R., Rossini, M., 2018. Exploring the physiological information of Sun-induced chlorophyll fluorescence through radiative transfer model inversion. Remote Sens. Environ. 215, 97–108.

Cendrero-Mateo, M.P., Moran, M.S., Papuga, S.A., Thorp, K.R., Alonso, L., Moreno, J., Ponce-Campos, G., Rascher, U., Wang, G., 2016. Plant chlorophyll fluorescence: active and passive measurements at canopy and leaf scales with different nitrogen treatments. J. Exp. Bot. 67, 275–286.

Cendrero-Mateo, M.P., Wieneke, S., Damm, A., Alonso, L., Pinto, F., Moreno, J., Guanter, L., Celesti, M., Rossini, M., Sabater, N., Cogliati, S., Julitta, T., Rascher, U., Goulas, Y., Aasen, H., Pacheco-Labrador, J., Mac Arthur, A., 2019. Sun-induced chlorophyll fluorescence III: benchmarking retrieval methods and sensor characteristics for proximal sensing. Remote Sens. 11, 962.

Cogliati, S., Rossini, M., Julitta, T., Meroni, M., Schickling, A., Burkart, A., Pinto, F., Rascher, U., Colombo, R., 2015. Continuous and long-term measurements of reflectance and sun-induced chlorophyll fluorescence by using novel automated field spectroscopy systems. Remote Sens. Environ. 164, 270–281.

Colombo, R., Celesti, M., Bianchi, R., Campbell, P.K.E., Cogliati, S., Cook, B.D., Corp, L. A., Damm, A., Domec, J.C., Guanter, L., Julitta, T., Middleton, E.M., Noormets, A., Panigada, C., Pinto, F., Rascher, U., Rossini, M., Schickling, A., 2018. Variability of sun-induced chlorophyll fluorescence according to stand age-related processes in a managed loblolly pine forest. Glob. Chang. Biol. 24, 2980–2996.

Damm, A., Erler, A., Hillen, W., Meroni, M., Schaepman, M.E., Verhoef, W., Rascher, U., 2011. Modeling the impact of spectral sensor configurations on the FLD retrieval accuracy of sun-induced chlorophyll fluorescence. Remote Sens. Environ. 115, 1882–1892.

Damm, A., Guanter, L., Laurent, V.C.E., Schaepman, M.E., Schickling, A., Rascher, U., 2014. FLD-based retrieval of sun-induced chlorophyll fluorescence from medium spectral resolution airborne spectroscopy data. Remote Sens. Environ. 147, 256–266.

Damm, A., Guanter, L., Paul-Limoges, E., Van der Tol, C., Hueni, A., Buchmann, N., Eugster, W., Ammann, C., Schaepman, M.E., 2015. Far-red sun-induced chlorophyll fluorescence shows ecosystem-specific relationships to gross primary production: an assessment based on observational and modeling approaches. Remote Sens. Environ. 166, 91–105.

Daumard, F., Goulas, Y., Champagne, S., Fournier, A., Ounis, A., Olioso, A., Moya, I., 2012. Continuous monitoring of canopy level sun-induced chlorophyll fluorescence during the growth of a sorghum field. IEEE Trans. Geosci. Remote Sens. 50, 4292–4300.

Daumard, F., Goulas, Y., Ounis, A., Pedrós, R., Moya, I., 2015. Measurement and correction of atmospheric effects at different altitudes for remote sensing of sun-induced fluorescence in oxygen absorption bands. IEEE Trans. Geosci. Remote Sens. 53, 5180–5196.

Dechant, B., Ryu, Y., Yang, K., Kim, J., 2017. A comprehensive analysis of spectral resolution effects on SIF retrieval and potential correction methods. In: Proc. American Geophysical Union, Fall Meeting, 11–15 December 2017, New Orleans, USA.

Dechant, B., Ryu, Y., Badgley, G., Zeng, Y., Berry, J.A., Zhang, Y., Goulas, Y., Li, Z., Zhang, Q., Kang, M., Li, J., Moya, I., 2020. Canopy structure explains the relationship between photosynthesis and sun-induced chlorophyll fluorescence in crops. Remote Sens. Environ. 241, 111733.

Drusch, M., Moreno, J., Del Bello, U., Franco, R., Goulas, Y., Huth, A., Kraft, S., Middleton, E.M., Miglietta, F., Mohammed, G., Nedbal, L., Rascher, U., Schüttemeyer, D., Verhoef, W., 2017. The FLuorescence EXplorer mission concept - ESA's Earth Explorer 8. IEEE Trans. Geosci. Remote Sens. 55, 1273–1284.

ESA (European Space Agency), 2015. Report for Mission Selection: FLEX. ESA SP-1330/2 (2 Volume Series). 197 pp., Noordwijk (The Netherlands). https://esamultimedia.esa.int/docs/EarthObservation/SP1330-2_FLEX.pdf.

Féret, J.B., Berger, K., de Boissieu, F., Malenovský, Z., 2021. PROSPECT-PRO for estimating content of nitrogen-containing leaf proteins and other carbon-based constituents. Remote Sens. Environ. 252, 112173.

Fournier, A., Daumard, F., Champagne, S., Ounis, A., Goulas, Y., Moya, I., 2012. Effect of canopy structure on sun-induced chlorophyll fluorescence. ISPRS J. Photogramm. Remote Sens. 68, 112–120.

Frankenberg, C., O'Dell, C., Berry, J., Guanter, L., Joiner, J., Köhler, P., Pollack, R., Taylor, T.E., 2014. Prospects for chlorophyll fluorescence remote sensing from the orbiting carbon observatory-2. Remote Sens. Environ. 147, 1–12.

Frankenberg, C., Köhler, P., Magney, T.S., Geier, S., Lawson, P., Schwochert, M., McDuffie, J., Drewry, D.T., Pavlick, R., Kuhnert, A., 2018. The chlorophyll fluorescence imaging spectrometer (CFIS), mapping far red fluorescence from aircraft. Remote Sens. Environ. 217, 523–536.

Gastellu-Etchegorry, J.-P., Lauret, N., Yin, T., Landier, L., Kallel, A., Malenovský, Z., Al Bitar, A., Aval, J., Benhmida, S., Qi, J., Medjdoub, G., Guilleux, J., Chavanon, E., Cook, B., Morton, D., Chrysoulakis, N., Mitraka, Z., 2017. DART: recent advances in remote sensing data modeling with atmosphere, polarization, and chlorophyll fluorescence. IEEE J. Sel. Top. Appl. Earth Obs. Remote Sens. 10, 2640–2649.

Genty, B., Briantais, J.M., Baker, N.R., 1989. The relationship between the quantum yield of photosynthetic electron transport and quenching of chlorophyll fluorescence. Biochim. Biophys. Acta 990, 87–92.

Gonzalez-Dugo, V., Hernandez, P., Solis, I., Zarco-Tejada, P.J., 2015. Using high-resolution hyperspectral and thermal airborne imagery to assess physiological condition in the context of wheat phenotyping. Remote Sens. 7, 13586–13605.

Grossmann, K., Frankenberg, C., Magney, T.S., Hurlock, S.C., Seibt, U., Stutz, J., 2018. PhotoSpec: a new instrument to measure spatially distributed red and far-red solar-induced chlorophyll fluorescence. Remote Sens. Environ. 216, 311–327.

Guanter, L., Alonso, L., Gómez-Chova, L., Amorós-López, J., Vila, J., Moreno, J., 2007. Estimation of solar-induced vegetation fluorescence from space measurements. Geophys. Res. Lett. 34, L08401.

Guanter, L., Alonso, L., Gómez-Chova, L., Meroni, M., Preusker, R., Fischer, J., Moreno, J., 2010. Developments for vegetation fluorescence retrieval from spaceborne high-resolution spectrometry in the O_2-A and O_2-B absorption bands. J. Geophys. Res. 115, 19303.
Guanter, L., Frankenberg, C., Dudhia, A., Lewis, P.E., Gómez-Dans, J., Kuze, A., Suto, H., Grainger, R.G., 2012. Retrieval and global assessment of terrestrial chlorophyll fluorescence from GOSAT space measurements. Remote Sens. Environ. 121, 236–251.
Guanter, L., Aben, I., Tol, P., Krijger, J.M., Hollstein, A., Köhler, P., Damm, A., Joiner, J., Frankenberg, C., Landgraf, J., 2015. Potential of the TROPOspheric Monitoring Instrument (TROPOMI) onboard the Sentinel-5 precursor for the monitoring of terrestrial chlorophyll fluorescence. Atmos. Meas. Tech. 8, 1337–1352.
Gueymard, C.A., 2001. Parameterized transmittance model for direct beam and circumsolar spectral irradiance. Sol. Energy 71, 325–346.
Haboudane, D., Miller, J.R., Pattey, E., Zarco-Tejada, P.J., Strachan, I.B., 2004. Hyperspectral vegetation indices and novel algorithms for predicting green LAI of crop canopies: modeling and validation in the context of precision agriculture. Remote Sens. Environ. 90, 337–352.
Hao, D., Zeng, Y., Qiu, H., Biriukova, K., Celesti, M., Migliavacca, M., Rossini, M., Asrar, G.R., Chen, M., 2021. Practical approaches for normalizing directional solar-induced fluorescence to a standard viewing geometry. Remote Sens. Environ. 255, 112171.
Hernández-Clemente, R., North, P.R.J., Hornero, A., Zarco-Tejada, P.J., 2017. Assessing the effects of forest health on sun-induced chlorophyll fluorescence using the FluorFLIGHT 3-D radiative transfer model to account for forest structure. Remote Sens. Environ. 193, 165–179.
Hornero, A., North, P.R.J., Zarco-Tejada, P.J., Rascher, U., Martín, M.P., Migliavacca, M., Hernández-Clemente, R., 2021a. Assessing the contribution of understory sun-induced chlorophyll fluorescence through 3-D radiative transfer modelling and field data. Remote Sens. Environ. 253, 112195.
Hornero, A., Zarco-Tejada, P.J., Quero, J.L., North, P.R.J., Ruiz-Gómez, F.J., Sánchez-Cuesta, R., Hernández-Clemente, R., 2021b. Modelling hyperspectral- and thermal-based plant traits for the early detection of Phytophthora-induced symptoms in oak decline. Remote Sens. Environ. 263, 112570.
Huete, A., Didan, K., Miura, T., Rodriguez, E.P., Gao, X., Ferreira, L.G., 2002. Overview of the radiometric and biophysical performance of the MODIS vegetation indices. Remote Sens. Environ 83, 195–213.
Jacquemoud, S., Baret, F., 1990. PROSPECT: a model of leaf optical properties spectra. Remote Sens. Environ. 34, 75–91.
Jia, M., Zhu, J., Ma, C., Alonso, L., Li, D., Cheng, T., Tian, Y., Zhu, Y., Yao, X., Cao, W., 2018. Difference and potential of the upward and downward sun-induced chlorophyll fluorescence on detecting leaf nitrogen concentration in wheat. Remote Sens. 10, 1315.
Jia, M., Colombo, R., Rossini, M., Celesti, M., Zhu, J., Cogliati, S., Cheng, T., Tian, Y., Zhu, Y., Cao, W., Yao, X., 2021. Estimation of leaf nitrogen content and photosynthetic nitrogen use efficiency in wheat using sun-induced chlorophyll fluorescence at the leaf and canopy scales. Eur. J. Agron. 122, 126192.
Julitta, T., Corp, L.A., Rossini, M., Burkart, A., Cogliati, S., Davies, N., Hom, M., Arthur, A. Mac, Middleton, E.M., Rascher, U., Schickling, A., Colombo, R., 2016. Comparison of sun-induced chlorophyll fluorescence estimates obtained from four portable field spectroradiometers. Remote Sens. 8, 122.
Julitta, T., Wutzler, T., Rossini, M., Colombo, R., Cogliati, S., Meroni, M., Burkart, A., Migliavacca, M., 2017. An R package for field spectroscopy: From system characterization to sun-induced chlorophyll fluorescence retrieval. In: Proc. 6th International Workshop on Remote Sensing of Vegetation Fluorescence, 17–19 January 2017, Frascatti, Italy.
Kim, J., Ryu, Y., Dechant, B., Lee, H., Kim, H.S., Kornfeld, A., Berry, J.A., 2021. Solar-induced chlorophyll fluorescence is non-linearly related to canopy photosynthesis in a temperate evergreen needleleaf forest during the fall transition. Remote Sens. Environ. 258, 112362.
Kjeldahl, J., 1883. Neue Methode zur Bestimmung des Stickstoffs in organischen. J. Anal. Chem. 22, 366–382.
Krause, G.H., Weis, E., 1984. Chlorophyll fluorescence as a tool in plant physiology. II. Interpretation of fluorescence signals. Photosynth. Res. 5, 139–157.
Li, Z., Zhang, Q., Li, J., Yang, X., Wu, Y., Zhang, Z., Wang, S., Wang, H., Zhang, Y., 2020. Solar-induced chlorophyll fluorescence and its link to canopy photosynthesis in maize from continuous ground measurements. Remote Sens. Environ. 236, 111420.
Lichtenthaler, H.K., Rinderle, U., 1988. The role of chlorophyll fluorescence in the detection of stress conditions in plants. Crit. Rev. Anal. Chem. 19 (Suppl. 1), S29–S85.
Liu, L., Liu, X., Hu, J., 2015. Effects of spectral resolution and SNR on the vegetation solar-induced fluorescence retrieval using FLD-based methods at canopy level. Eur. J. Remote Sens. 48, 743–762.
Maier, S.W., Günther, K.P., Stellmes, M., 2003. Sun-induced fluorescence: a new tool for precision farming. In: Schepers, J., VanToai, T. (Eds.), Digital Imaging and Spectral Techniques: Applications to Precision Agriculture and Crop Physiology. ASA Spec. Publ. 66. ASA, CSSA, and SSSA, Madison (Wisconsin), USA, pp. 209–222.
Marrs, J.K., Jones, T.S., Allen, D.W., Hutyra, L.R., 2021. Instrumentation sensitivities for tower-based solar-induced fluorescence measurements. Remote Sens. Environ. 259, 112413.
Meroni, M., Colombo, R., 2006. Leaf level detection of solar induced chlorophyll fluorescence by means of a subnanometer resolution spectroradiometer. Remote Sens. Environ. 103, 438–448.
Meroni, M., Rossini, M., Guanter, L., Alonso, L., Rascher, U., Colombo, R., Moreno, J., 2009. Remote sensing of solar-induced chlorophyll fluorescence: review of methods and applications. Remote Sens. Environ. 113, 2037–2051.
Meroni, M., Busetto, L., Colombo, R., Guanter, L., Moreno, J., Verhoef, W., 2010. Performance of spectral fitting methods for vegetation fluorescence quantification. Remote Sens. Environ. 114, 363–374.
Meroni, M., Barducci, A., Cogliati, S., Castagnoli, F., Rossini, M., Busetto, L., Di Cella, U. M., 2011. The hyperspectral irradiometer, a new instrument for long-term and unattended field spectroscopy measurements. Rev. Sci. Instrum. 82, 043106.
Mohammed, G.H., Colombo, R., Middleton, E.M., Rascher, U., Van der Tol, C., Nedbal, L., Goulas, Y., Pérez-Priego, O., Damm, A., Meroni, M., Joiner, J., Cogliati, S., Verhoef, W., Malenovský, Z., Gastellu-Etchegorry, J.P., Miller, J.R., Guanter, L., Moreno, J., Moya, I., Berry, J.A., Frankenberg, C., Zarco-Tejada, P.J., 2019. Remote sensing of solar-induced chlorophyll fluorescence (SIF) in vegetation: 50 years of progress. Remote Sens. Environ. 231, 111177.
Nakashima, N., Kato, T., Morozumi, T., Tsujimoto, K., Akitsu, T.K., Nasahara, K.N., Murayama, S., Muraoka, H., Noda, H.M., 2021. Area-ratio Fraunhofer line depth (aFLD) method approach to estimate solar-induced chlorophyll fluorescence in low spectral resolution spectra in a cool-temperate deciduous broadleaf forest. J. Plant Res. 134, 713–728.
Ni, Z., Liu, Z., Li, Z.L., Nerry, F., Huo, H., Sun, R., Yang, P., Zhang, W., 2016. Investigation of atmospheric effects on retrieval of sun-induced fluorescence using hyperspectral imagery. Sensors 16, 480.
Nichol, C.J., Drolet, G., Porcar-Castell, A., Wade, T., Sabater, N., Middleton, E.M., Maclellan, C., Levula, J., Mammarella, I., Vesala, T., Atherton, J., 2019. Diurnal and seasonal solar induced chlorophyll fluorescence and photosynthesis in a boreal scots pine canopy. Remote Sens. 11, 273.
Panigada, C., Rossini, M., Meroni, M., Cilia, C., Busetto, L., Amaducci, S., Boschetti, M., Cogliati, S., Picchi, V., Pinto, F., Marchesi, A., Colombo, R., 2014. Fluorescence, PRI and canopy temperature for water stress detection in cereal crops. Int. J. Appl. Earth Obs. Geoinf. 30, 167–178.
Pedrós, R., Moya, I., Goulas, Y., Jacquemoud, S., 2008. Chlorophyll fluorescence emission spectrum inside a leaf. Photochem. Photobiol. Sci. 7, 498–502.
Pérez-Priego, O., Zarco-Tejada, P.J., Miller, J.R., Sepulcre-Cantó, G., Fereres, E., 2005. Detection of water stress in orchard trees with a high-resolution spectrometer through chlorophyll fluorescence *in-filling* of the O_2-A band. IEEE Trans. Geosci. Remote Sens. 43, 2860–2869.
Plascyk, J.A., 1975. The MK II Fraunhofer line discriminator (FLD-II) for airborne and orbital remote sensing of solar-stimulated luminescence. Opt. Eng. 14, 144339.
Poblete, T., Camino, C., Beck, P.S.A., Hornero, A., Kattenborn, T., Saponari, M., Boscia, D., Navas-Cortes, J.A., Zarco-Tejada, P.J., 2020. Detection of Xylella fastidiosa infection symptoms with airborne multispectral and thermal imagery: assessing bandset reduction performance from hyperspectral analysis. ISPRS J. Photogramm. Remote Sens. 162, 27–40.
Poblete, T., Navas-Cortes, J.A., Camino, C., Calderon, R., Hornero, A., Gonzalez-Dugo, V., Landa, B.B., Zarco-Tejada, P.J., 2021. Discriminating *Xylella fastidiosa* from *Verticillium dahliae* infections in olive trees using thermal- and hyperspectral-based plant traits. ISPRS J. Photogramm. Remote Sens. 179, 133–144.
Porcar-Castell, A., Tyystjärvi, E., Atherton, J., Van der Tol, C., Flexas, J., Pfündel, E.E., Moreno, J., Frankenberg, C., Berry, J.A., 2014. Linking chlorophyll a fluorescence to photosynthesis for remote sensing applications: mechanisms and challenges. J. Exp. Bot 65, 4065–4095.
Quemada, M., Gabriel, J.L., Zarco-Tejada, P., 2014. Airborne hyperspectral images and ground-level optical sensors as assessment tools for maize nitrogen fertilization. Remote Sens. 6, 2940–2962.
Rascher, U., Alonso, L., Burkart, A., Cilia, C., Cogliati, S., Colombo, R., Damm, A., Drusch, M., Guanter, L., Hanus, J., Hyvärinen, T., Julitta, T., Jussila, J., Kataja, K., Kokkalis, P., Kraft, S., Kraska, T., Matveeva, M., Moreno, J., Muller, O., Panigada, C., Pikl, M., Pinto, F., Prey, L., Pude, R., Rossini, M., Schickling, A., Schurr, U., Schüttemeyer, D., Verrelst, J., Zemek, F., 2015. Sun-induced fluorescence - a new probe of photosynthesis: first maps from the imaging spectrometer HyPlant. Glob. Chang. Biol. 21, 4673–4684.
Rossini, M., Meroni, M., Migliavacca, M., Manca, G., Cogliati, S., Busetto, L., Picchi, V., Cescatti, A., Seufert, G., Colombo, R., 2010. High resolution field spectroscopy measurements for estimating gross ecosystem production in a rice field. Agric. For. Meteorol. 150, 1283–1296.
Rossini, M., Meroni, M., Celesti, M., Cogliati, S., Julitta, T., Panigada, C., Rascher, U., Van der Tol, C., Colombo, R., 2016. Analysis of red and far-red sun-induced chlorophyll fluorescence and their ratio in different canopies based on observed and modeled data. Remote Sens. 8, 412.
Siegmann, B., Alonso, L., Celesti, M., Cogliati, S., Colombo, R., Damm, A., Douglas, S., Guanter, L., Hanuš, J., Kataja, K., Kraska, T., Matveeva, M., Moreno, J., Muller, O., Pikl, M., Pinto, F., Vargas, J.Q., Rademske, P., Rodriguez-Morene, F., Sabater, N., Schickling, A., Schüttemeyer, D., Zemek, F., Rascher, U., 2019. The high-performance airborne imaging spectrometer HyPlant-from raw images to top-of-canopy reflectance and fluorescence products: introduction of an automatized processing chain. Remote Sens. 11, 2760.
Suarez, L., Gonzalez-Dugo, V., Camino, C., Hornero, A., Zarco-Tejada, P.J., 2021. Physical model inversion of the green spectral region to track assimilation rate in almond trees with an airborne nano-hyperspectral imager. Remote Sens. Environ. 252, 112147.
Sun, Y., Frankenberg, C., Wood, J.D., Schimel, D.S., Jung, M., Guanter, L., Drewry, D.T., Verma, M., Porcar-Castell, A., Griffis, T.J., Gu, L., Magney, T.S., Köhler, P., Evans, B., Yuen, K., 2017. OCO-2 advances photosynthesis observation from space via solar induced chlorophyll fluorescence. Science 358 eaam5747.
Süß, A., Hank, T., Mauser, W., 2016. Deriving diurnal variations in sun-induced chlorophyll-a fluorescence in winter wheat canopies and maize leaves from ground-based hyperspectral measurements. Int. J. Remote Sens. 37, 60–77.

Tagliabue, G., Panigada, C., Celesti, M., Cogliati, S., Colombo, R., Migliavacca, M., Rascher, U., Rocchini, D., Schüttemeyer, D., Rossini, M., 2020. Sun–induced fluorescence heterogeneity as a measure of functional diversity. Remote Sens. Environ. 247, 111934.
Van der Tol, C., Verhoef, W., Timmermans, J., Verhoef, A., Su, Z., 2009. An integrated model of soil-canopy spectral radiances, photosynthesis, fluorescence, temperature and energy balance. Biogeosci 6, 3109–3129.
Verhoef, W., 1984. Light scattering by leaf layers with application to canopy reflectance modeling: the SAIL model. Remote Sens. Environ. 16, 125–141.
Verhoef, W., 2004. Extension of SAIL to model solar - induced canopy fluorescence spectra. In: Proc. 2nd International Workshop on Remote Sensing of Vegetation Fluorescence, 17–19 November 2004, Montreal, Canada.
Verhoef, W., Jia, L., Xiao, Q., Su, Z., 2007. Unified optical-thermal four-stream radiative transfer theory for homogeneous vegetation canopies. IEEE Trans. Geosci. Remote Sens. 45, 1808–1822.
Verhoef, W., Van der Tol, C., Middleton, E.M., 2018. Hyperspectral radiative transfer modeling to explore the combined retrieval of biophysical parameters and canopy fluorescence from FLEX – Sentinel-3 tandem mission multi-sensor data. Remote Sens. Environ. 204, 942–963.
Vilfan, N., Van der Tol, C., Muller, O., Rascher, U., Verhoef, W., 2016. Fluspect-B: a model for leaf fluorescence, reflectance and transmittance spectra. Remote Sens. Environ. 186, 596–615.
Wang, Y., Suarez, L., Qian, X., Poblete, T., Gonzalez-Dugo, V., Ryu, D., Zarco-Tejada, P. J., 2021. Assessing the contribution of airborne-retrieved chlorophyll fluorescence for nitrogen assessment in almond orchards. In: Proc. IEEE International Geoscience and Remote Sensing Symposium (IGARSS), 12–16 July 2021, Brussels, Belgium, pp. 5853–5856.
Watt, M.S., Buddenbaum, H., Leonardo, E.M.C., Estarija, H.J., Bown, H.E., Gomez-Gallego, M., Hartley, R.J.L., Pearse, G.D., Massam, P., Wright, L., Zarco-Tejada, P.J., 2020a. Monitoring biochemical limitations to photosynthesis in N and P-limited radiata pine using plant functional traits quantified from hyperspectral imagery. Remote Sens. Environ. 248, 112003.
Watt, M.S., Buddenbaum, H., Leonardo, E.M.C., Estarija, H.J.C., Bown, H.E., Gomez-Gallego, M., Hartley, R., Massam, P., Wright, L., Zarco-Tejada, P.J., 2020b. Using hyperspectral plant traits linked to photosynthetic efficiency to assess N and P partition. ISPRS J. Photogramm. Remote Sens. 169, 406–420.
Weis, E., Berry, J.A., 1987. Quantum efficiency of photosystem II in relation to 'energy'-dependent quenching of chlorophyll fluorescence. Biochim. Biophys. Acta 894, 198–208.
Wieneke, S., Ahrends, H., Damm, A., Pinto, F., Stadler, A., Rossini, M., Rascher, U., 2016. Airborne based spectroscopy of red and far-red sun-induced chlorophyll fluorescence: implications for improved estimates of gross primary productivity. Remote Sens. Environ. 184, 654–667.
Yang, P., Van der Tol, C., 2018. Linking canopy scattering of far-red sun-induced chlorophyll fluorescence with reflectance. Remote Sens. Environ. 209, 456–467.
Yang, R., Juhasz, A., Zhang, Yujuan, Chen, X., Zhang, Yinjun, She, M., Zhang, J., Maddern, R., Edwards, I., Diepeveen, D., Islam, S., Ma, W., 2018. Molecular characterisation of the NAM-1 genes in bread wheat in Australia. Crop Pastur. Sci. 69, 1173–1181.
Zarco-Tejada, P.J., Miller, J.R., Mohammed, G.H., Noland, T.L., 2000a. Chlorophyll fluorescence effects on vegetation apparent reflectance: I. Leaf-level measurements and model simulation. Remote Sens. Environ. 74, 582–595.
Zarco-Tejada, P.J., Miller, J.R., Mohammed, G.H., Noland, T.L., Sampson, P.H., 2000b. Chlorophyll fluorescence effects on vegetation apparent reflectance: II. Laboratory and airborne canopy-level measurements with hyperspectral data. Remote Sens. Environ. 74, 596–608.
Zarco-Tejada, P.J., González-Dugo, V., Berni, J.A.J., 2012. Fluorescence, temperature and narrow-band indices acquired from a UAV platform for water stress detection using a micro-hyperspectral imager and a thermal camera. Remote Sens. Environ. 117, 322–337.
Zarco-Tejada, P.J., Catalina, A., González, M.R., Martín, P., 2013a. Relationships between net photosynthesis and steady-state chlorophyll fluorescence retrieved from airborne hyperspectral imagery. Remote Sens. Environ. 136, 247–258.
Zarco-Tejada, P.J., Suarez, L., Gonzalez-Dugo, V., 2013b. Spatial resolution effects on chlorophyll fluorescence retrieval in a heterogeneous canopy using hyperspectral imagery and radiative transfer simulation. IEEE Geosci. Remote Sens. Lett. 10, 937–941.
Zarco-Tejada, P.J., González-Dugo, M.V., Fereres, E., 2016. Seasonal stability of chlorophyll fluorescence quantified from airborne hyperspectral imagery as an indicator of net photosynthesis in the context of precision agriculture. Remote Sens. Environ. 179, 89–103.
Zarco-Tejada, P.J., Camino, C., Beck, P.S.A., Calderon, R., Hornero, A., Hernández-Clemente, R., Kattenborn, T., Montes-Borrego, M., Susca, L., Morelli, M., Gonzalez-Dugo, V., North, P.R.J., Landa, B.B., Boscia, D., Saponari, M., Navas-Cortes, J.A., 2018. Previsual symptoms of Xylella fastidiosa infection revealed in spectral plant-trait alterations. Nat. Plant 4, 432–439.
Zeng, Y., Badgley, G., Dechant, B., Ryu, Y., Chen, M., Berry, J.A., 2019. A practical approach for estimating the escape ratio of solar-induced chlorophyll fluorescence. Remote Sens. Environ. 232, 111209.
Zhao, F., Dai, X., Verhoef, W., Guo, Y., Van der Tol, C., Li, Y., Huang, Y., 2016. FluorWPS: a Monte Carlo ray-tracing model to compute sun-induced chlorophyll fluorescence of three-dimensional canopy. Remote Sens. Environ. 187, 385–399.

Appendix E: Conference paper 1

This appendix contains the author-accepted manuscript of the IGARSS Conference paper 1. Below is the bibliographic detail.

Belwalkar, A., Poblete, T., Longmire, A., Hornero, A., Zarco-Tejada, P.J., 2021. **Comparing the retrieval of chlorophyll fluorescence from two airborne hyperspectral imagers with different spectral resolutions for plant phenotyping studies**. In: Proc. IEEE International Geoscience and Remote Sensing Symposium (IGARSS), 12–16 July 2021, Brussels, Belgium, pp. 5845–5848. https://doi.org/10.1109/IGARSS47720.2021.9553265.

COMPARING THE RETRIEVAL OF CHLOROPHYLL FLUORESCENCE FROM TWO AIRBORNE HYPERSPECTRAL IMAGERS WITH DIFFERENT SPECTRAL RESOLUTIONS FOR PLANT PHENOTYPING STUDIES

A. Belwalkar[1], T. Poblete[2], A. Longmire[2], A. Hornero[3,4], P.J. Zarco-Tejada[1,2,3]

[1]Department of Infrastructure Engineering, Faculty of Engineering and Information Technology (FEIT), The University of Melbourne, Melbourne, Victoria, Australia
[2]School of Agriculture and Food, Faculty of Veterinary and Agricultural Sciences (FVAS), The University of Melbourne, Melbourne, Victoria, Australia
[3]Instituto de Agricultura Sostenible (IAS), Consejo Superior de Investigaciones Científicas (CSIC), Alameda del Obispo s/n, 14004 Córdoba, Spain
[4]Department of Geography, Swansea University, SA2 8PP Swansea, United Kingdom

ABSTRACT

Several studies have demonstrated the influence of the spectral resolution (SR) on the retrieval of solar-induced chlorophyll fluorescence (SIF) from ground-based sensors with different spectral configurations. However, research studying the implications of the SR of airborne hyperspectral imagers on the retrieved SIF is lacking, and its interpretation is critical for precision agriculture, plant stress detection and phenotyping studies. This work investigates the effects of SR on SIF performance through the Fraunhofer Line Depth (FLD) principle at the O_2-A absorption feature (760.4 nm) using two airborne hyperspectral imagers with different spectral characteristics. A sub-nanometer hyperspectral imager with 0.1-0.2 nm full-width at half-maximum (FWHM) resolution and a broader-band hyperspectral imager of 5.8 nm FWHM were flown in tandem. The campaigns were conducted over a winter wheat field with randomized experimental design, with plots receiving different nitrogen rates to ensure SIF variability. Results showed a bias on the SIF levels quantified by both airborne imagers (RMSE=3.7 mW/m^2/nm/sr), but a strong relationship between both sensors at the O_2-A absorption feature (R^2=0.84, $p<0.001$). Results confirm the utility of hyperspectral imagers ca. 5 nm FWHM resolution for stress detection and plant phenotyping where assessing the relative variability of SIF across experimental plots is sought.

Index Terms— Airborne, hyperspectral, SIF, FLD, chlorophyll fluorescence, plant phenotyping

1. INTRODUCTION

The energy dissipation pathway by the photosynthetic apparatus in the form of SIF serves as a direct indicator of the physiological state of plants and can assist understanding of plant functioning, crop performance and the early symptoms of biotic and abiotic stress. Over the last two decades, top-of-canopy (TOC) SIF has been retrieved at various scales and spatial resolutions using ground-based, airborne and satellite platforms [1]-[3]. SIF has largely been retrieved using leaf and ground-based canopy-level sensors, gradually scaling up to satellite platforms for global vegetation monitoring purposes. However, the intermediate scales provided by airborne platforms are critical to bridge the gap between field and satellite-based SIF observations and to disentangle the contribution by the different scene components in aggregated pixels [4], [5]. In this context, assessing the spectral configurations and spatial requirements for the operational use of SIF in precision agriculture and plant phenotyping trials is crucial.

The SR of the sensor is a critical factor that influences the accuracy of the quantified SIF. Modelling based studies [6], [7] have demonstrated that the use of broader-band sensors leads to a higher SIF retrieval bias from FLD-based approaches. As a result, very high-resolution imaging sensors are needed to quantify SIF in absolute terms accurately. Although broader-band sensors (e.g. in the range of 5-6 nm FWHM SR) are sub-optimal for the absolute quantification of SIF at the O_2-A feature, several studies have demonstrated that the relative SIF variability captured by such sensors is a valuable plant trait in the context of plant physiology, gross primary productivity monitoring and for the early detection of biotic and abiotic stress [2], [8]-[10]. Studies comparing SIF retrievals from narrow-band (i.e. below 1 nm FWHM) vs. broader-band hyperspectral imagers (ca. 5-6 nm FWHM) flown in tandem over experimental fields displaying a range of physiological condition are therefore needed. This study aims to evaluate the SIF quantification from broader-band vs. sub-nanometer airborne imagers for stress detection and assessment of crop physiological conditions.

978-1-6654-0369-6/21/$31.00 ©2021 IEEE

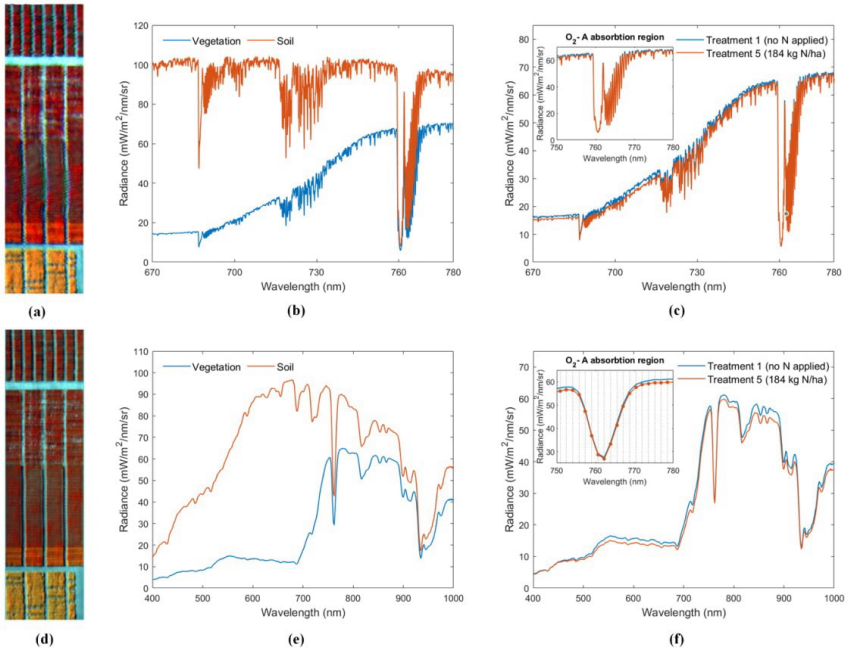

Fig. 1: Subset of the imagery acquired from the aircraft yielding 20 cm pixel resolution and the corresponding sample radiance spectra from the narrow-band hyperspectral imager (a; b) and from the broader-band hyperspectral imager (d; e). Comparison of the radiance spectra for treatment 1 plot with no N applied vs. treatment 5 with the highest levels of N applied (184 kg N/ha) extracted from the narrow-band (c) and broader-band imagers (f). The vertical lines in (f) indicate the location of the 18 spectral bands within the O_2-A absorption region for SIF quantification with the broader-band hyperspectral imager.

2. MATERIALS AND METHODS

2.1. Study sites, field experiment and airborne campaign

The experiment was conducted over fifteen dryland wheat (cv. Scepter) [11] plots located at Yarrawonga, Victoria, Australia. The 2 m × 13 m plots were planted in May 2019 and treated with five different nitrogen (N) application rates in the form of Urea (46% N) fertilizer (T1: 0 kg N/ha, T2: 46 kg N/ha, T3: 92 kg N/ha, T4: 138 kg N/ha, T5: 184 kg N/ha). Leaf-level measurements of steady-state chlorophyll fluorescence (F_t) were performed in the field on ten leaves per plot using the FluorPen device (PSI, Czech Republic) at the time of the airborne campaign.

The airborne campaign to collect TOC spectral radiances was carried out under clear sky conditions on 9 October 2019 from 15:40 to 16:30 local time flying with the heading of the aircraft on the solar plane. The payload consisted of two hyperspectral imagers installed in tandem on a Cessna aircraft operated by the HyperSens Laboratory, University of Melbourne's Airborne Remote Sensing Facility. The first linear-array hyperspectral camera used in this study was the Micro-Hyperspec VNIR E-Series model (Headwall Photonics, Fitchburg, MA, USA) operated with a configuration of 371 spectral bands acquired at 1.626 nm/pixel in the 400–1000 nm region, yielding 5.8 nm FWHM. The second hyperspectral camera was the high-resolution chlorophyll fluorescence imager (Headwall Photonics, Fitchburg, MA, USA) operated with a configuration of 2160 spectral bands acquired at 0.051 nm/pixel in the 670–780 nm region, yielding 0.1-0.2 nm FWHM. Fig. 1 shows a portion of the imagery along with sample radiance spectra acquired from both imagers. Differences in the radiance spectra and the O_2-A feature were visually detected as a function of the nitrogen rates applied over the experimental fields (Fig. 1c and Fig. 1f).

2.2. SIF quantification from field data and airborne hyperspectral imagery

The mean radiance spectra from each plot were calculated by computing the average of all pixels within each region of interest, excluding the boundaries and non-vegetation pixels. The total incoming irradiance at the time of the flight was measured using a 0.065 nm FWHM Ocean Optics HR2000 fiber-optics spectrometer (Ocean Optics, Dunedin, FL,

USA) with a CC-3 VIS-NIR cosine corrector diffuser (Ocean Optics, Dunedin, FL, USA).

The radiometric calibration of the spectrometer was carried out using the coefficients derived from a uniform calibrated light source and an integrating sphere (model XTH2000C, Labsphere Inc., North Sutton, NH, USA) using six different levels of illumination. To match the spectral resolution of the radiance images acquired from both imagers, the high-resolution irradiance spectra collected with the HR2000 spectrometer was resampled through Gaussian convolution corresponding to the spectral resolution of the airborne imagers. The SIF quantification from both instruments was conducted using the O_2-A band *in-filling* method through the FLD principle [12], using a total of three spectral bands (3FLD) [13]. SIF was scaled based on an offset derived from non-fluorescence targets extracted from the imagery to account for the effects of negative values due to atmospheric and calibration factors. In addition to the SIF quantification through the 3FLD method, the depth at the O_2-A absorption feature captured by the two imagers was also quantified.

3. RESULTS

The different spectral characteristics of the two hyperspectral imagers caused significant effects in the measured radiances (Fig. 2). As expected, the depth and shape of the absorption features at the O_2-A (760.4 nm) and O_2-B (687.0 nm) were strongly influenced by the SR. The O_2-B absorption feature could not be identified in the broader-band radiance spectra. A reduction in the O_2-A band depth and an increase in the radiance signal of the absorption minimum were also observed. As reported in other studies, the wavelength corresponding to the radiance minimum was shifted towards higher wavelengths when compared to the narrow-band imager.

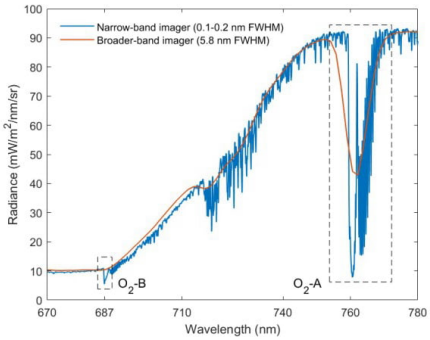

Fig. 2: Comparison of radiance spectra acquired from the narrow-band and broader-band airborne hyperspectral imagers for the same experimental plot.

The O_2-A absorption band depth calculated from the two hyperspectral imagers from radiance spectra extracted from the experimental plots with nitrogen variability exhibited a strong relationship (R^2=0.84, p<0.001; Fig. 3a). Results obtained when comparing SIF quantified through 3FLD from the two airborne hyperspectral imagers is illustrated in Fig 3b. As the retrieval of SIF at O_2-A band using the FLD principle is primarily affected by the depth of the measured O_2-A absorption feature (shown in Fig. 2 & 3a), large differences in the range of SIF levels from both imagers as a function of the spectral resolution were observed. Although in absolute terms the SIF levels were affected by the spectral resolution of both imagers (RMSE=3.7 mW/m²/nm/sr), a significant relationship was obtained (R^2=0.71, p<0.001) which demonstrates the agreement in the relative variability of SIF quantified by the two imagers at the O_2-A feature.

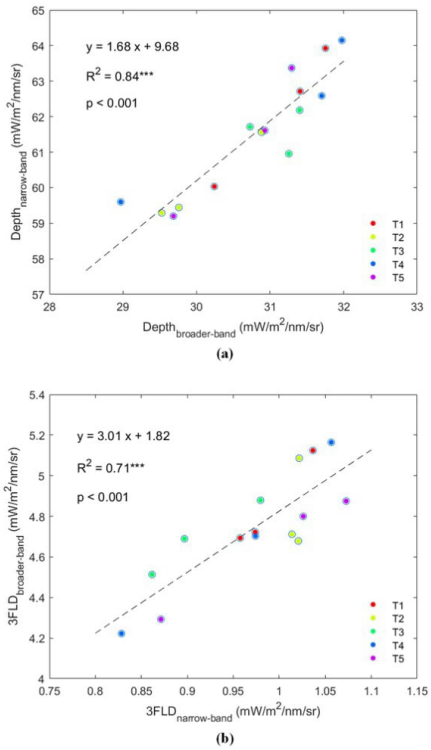

Fig. 3: Relationship between O_2-A band depth captured by the two imagers (a). Relationship between the airborne SIF quantified using the 3FLD method from the two imagers (b).

The assessment of the TOC airborne SIF quantified by both imagers was conducted by comparing against fluorescence measurements carried out at the leaf-level

across the experimental field. The relationships obtained between leaf-level fluorescence and airborne SIF yielded significant results (R^2=0.65, p<0.001 for the narrow-band imager, and R^2=0.42, p<0.01 for broader-band imager).

Our results demonstrate the link between the airborne-retrieved SIF from two hyperspectral imagers with different spectral resolutions. These results obtained by sensors flying in tandem support the findings of past studies [2], [9], [10] that showed the capability of broader-band hyperspectral imagers for SIF quantification in the context of early detection of vegetation stress symptoms and plant physiological assessment.

4. CONCLUSIONS

This study assessed the effects of varying spectral resolution from two airborne hyperspectral imagers on the quantification of SIF at the O_2-A absorption feature for vegetation stress detection and plant phenotyping purposes when flown over experimental wheat plots with variable nitrogen rates. The airborne hyperspectral images acquired at 20 cm spatial resolution from a sub-nanometer (0.1-0.2 nm FWHM) and a broader-band imager (5.8 nm FWHM) flown in tandem yielded a bias (RMSE=3.7 mW/m^2/nm/sr) in the absolute SIF levels quantified by both imagers, but a good agreement when comparing the O_2-A feature depth (R^2=0.84) and the 3FLD quantification (R^2=0.71). These results demonstrate the potentials of using broader-band hyperspectral imagers for operational retrievals of SIF in the context of plant phenotyping and precision agriculture, where quantification of relative stress levels is required. This study also makes progress toward future work to model the effect of sensor spectral resolution on the retrieved SIF from piloted and drone-based airborne hyperspectral imagers for vegetation stress detection.

5. ACKNOWLEDGEMENTS

The authors gratefully acknowledge the Foundation for Arable Research Australia and Riverine Plains Incorporated for their provision and management of the plot trials. A. Gracia-Romero is acknowledged for his technical support during the field and airborne campaigns.

6. REFERENCES

[1] O. Pérez-Priego, P.J. Zarco-Tejada, J.R. Miller, G. Sepulcre-Cantó, and E. Fereres, "Detection of water stress in orchard trees with a high-resolution spectrometer through chlorophyll fluorescence *in-filling* of the O_2-A band," *IEEE Trans. Geosci. Remote Sens.*, vol. 43, no. 12, pp. 2860–2868, Dec. 2005.

[2] P.J. Zarco-Tejada, M.V. González-Dugo, and E. Fereres, "Seasonal stability of chlorophyll fluorescence quantified from airborne hyperspectral imagery as an indicator of net photosynthesis in the context of precision agriculture," *Remote Sens. Environ.*, vol. 179, pp. 89–103, Jun. 2016.

[3] J. Joiner, Y. Yoshida, A. P. Vasilkov, Y. Yoshida, L. A. Corp, and E. M. Middleton, "First observations of global and seasonal terrestrial chlorophyll fluorescence from space," *Biogeosciences*, vol. 8, no. 3, pp. 637–651, 2011.

[4] P. J. Zarco-Tejada, L. Suarez, and V. Gonzalez-Dugo, "Spatial resolution effects on chlorophyll fluorescence retrieval in a heterogeneous canopy using hyperspectral imagery and radiative transfer simulation," *IEEE Geosci. Remote Sens. Lett.*, vol. 10, no. 4, pp. 937–941, Jul. 2013.

[5] A. Hornero et al., "Assessing the contribution of understory sun-induced chlorophyll fluorescence through 3-D radiative transfer modelling and field data," *Remote Sens. Environ*., vol. 253, Feb. 2021

[6] A. Damm et al., "Modeling the impact of spectral sensor configurations on the FLD retrieval accuracy of sun-induced chlorophyll fluorescence," *Remote Sens. Environ.*, vol. 115, no. 8, pp. 1882–1892, Aug. 2011.

[7] L. Liu, X. Liu, and J. Hu, "Effects of spectral resolution and SNR on the vegetation solar-induced fluorescence retrieval using FLD-based methods at canopy level," *Eur. J. Remote. Sens.*, vol. 48, pp. 743–762, 2015.

[8] A. Damm, L. Guanter, V. C. E. Laurent, M. E. Schaepman, A. Schickling, and U. Rascher, "FLD-based retrieval of sun-induced chlorophyll fluorescence from medium spectral resolution airborne spectroscopy data," *Remote Sens. Environ.*, vol. 147, pp. 256–266, May 2014.

[9] A. Damm et al., "Far-red sun-induced chlorophyll fluorescence shows ecosystem-specific relationships to gross primary production: An assessment based on observational and modeling approaches," *Remote Sens. Environ.*, vol. 166, pp. 91–105, Sep. 2015.

[10] P. J. Zarco-Tejada et al., "Previsual symptoms of *Xylella fastidiosa* infection revealed in spectral plant-trait alterations," *Nat. Plants*, vol. 4, no. 7, pp. 432–439, Jul. 2018.

[11] R. Yang et al., "Molecular characterisation of the NAM-1 genes in bread wheat in Australia," *Crop and Pasture Science*, vol. 69, no. 12, pp. 1173–1181, 2018.

[12] J. A. Plascyk and F. C. Gabriel, "The Fraunhofer Line Discriminator MKII-An Airborne Instrument for Precise and Standardized Ecological Luminescence Measurement," *IEEE Trans. Instrum. Meas.*, vol. 24, no. 4, pp. 306–313, Dec. 1975.

[13] S. W. Maier, K. P. Gunther, and M. Stellmes, "Sun-Induced Fluorescence: A New Tool for Precision Farming," In: *Digital Imaging and Spectral Techniques: Applications to Precision Agriculture and Crop Physiology*, Vol. 66 (eds M McDonald, J Schepers, L Tartly, T Van Toai, D Major), ASA Spec. Publ., Madison, WI, USA, pp. 209– 222, 2003.

Appendix F: Conference paper 2

This appendix contains the author-accepted manuscript of the IGARSS Conference paper 2. Below is the bibliographic detail.

Belwalkar, A., Poblete, T., Hornero, A., Zarco-Tejada, P.J., 2022. **Accounting for the spectral resolution on SIF retrieval from a narrow-band airborne imager using SCOPE**. In: Proc. IEEE International Geoscience and Remote Sensing Symposium (IGARSS), 17–22 July 2022, Kuala Lumpur, Malaysia, pp. 5440–5443. https://doi.org/10.1109/IGARSS46834.2022.9884564.

ACCOUNTING FOR THE SPECTRAL RESOLUTION ON SIF RETRIEVAL FROM A NARROW-BAND AIRBORNE IMAGER USING SCOPE

A. Belwalkar[1], T. Poblete[1], A. Hornero[1,3,4], P.J. Zarco-Tejada[1,2,3]

[1]Department of Infrastructure Engineering, Faculty of Engineering and Information Technology (FEIT), The University of Melbourne, Melbourne, Victoria, Australia
[2]School of Agriculture and Food, Faculty of Veterinary and Agricultural Sciences (FVAS), The University of Melbourne, Melbourne, Victoria, Australia
[3]Instituto de Agricultura Sostenible (IAS), Consejo Superior de Investigaciones Científicas (CSIC), Alameda del Obispo s/n, 14004 Córdoba, Spain
[4]Department of Geography, Swansea University, SA2 8PP Swansea, United Kingdom

ABSTRACT

Sub-nanometer hyperspectral imagers are increasingly being used to quantify solar-induced chlorophyll fluorescence (SIF) due to their ability to characterize narrow absorption features accurately. However, some limitations prevent their wide use in the operational context due to their high cost, weight, and complexity. On the other hand, more widely-used narrow-band hyperspectral imagers with 4–6 nm full width at half-maximum (FWHM) resolution could be a cost-effective alternative for acquiring high-spatial-resolution hyperspectral imagery to derive SIF. Due to the large effects of the spectral resolution (SR) on the quantified fluorescence, the SIF levels derived from such airborne imagers with 4–6 nm FWHM are overestimated, requiring careful interpretation. In this study, we flew in tandem two airborne hyperspectral imagers with different spectral characteristics. These sensors' imagery was used to model the impact of SR on the SIF quantification using the Soil-Canopy Observation of Photosynthesis and Energy (SCOPE) model. A Support Vector Machine regression (SVR) model trained via SCOPE simulations was employed to quantify SIF at 1 nm SR from the original 5.8 nm FWHM resolution. The performance of the SIF quantification was evaluated theoretically with SCOPE and tested against airborne hyperspectral radiance and the derived SIF. Results showed that the estimated SIF at 1 nm SR agreed well with the reference SCOPE simulations (RMSE=0.097 mW/m^2/nm/sr) and with airborne-quantified SIF (RMSE=0.094 mW/m^2/nm/sr).

Index Terms— Airborne, hyperspectral, SIF, 3FLD, solar-induced fluorescence, SCOPE, radiative transfer.

1. INTRODUCTION

The quantification of SIF using imaging sensors onboard airborne platforms has made significant progress in the last decade. SR has improved from narrow-band hyperspectral imagers (i.e., 4–6 nm FWHM) to sub-nanometer sensors specifically designed for accurate SIF retrievals [1]. These airborne imaging spectroscopy sensors provide spatial patterns of fluorescence across the landscape, enabling the development of indicators of photosynthetic functioning used for pre-visual vegetation stress [2], [3]. Although SIF quantification in absolute physical units requires sub-nanometer resolutions [1], the availability of airborne imaging sensors with such capabilities is limited due to their high cost and operational complexity. On the other hand, narrow-band imaging sensors characterized by spectral resolutions ranging from 4–6 nm FWHM are widely available. They can be installed onboard lightweight platforms for operational SIF retrievals needed in precision agriculture applications. Previous studies [4]-[6] have demonstrated the relevance of retrieving SIF from narrow-band sensors in the context of plant physiology, and particularly for the pre-visual detection of biotic and abiotic stress. Recent research [7] found that SIF estimates derived from a narrow-band hyperspectral imager with a 5.8 nm FWHM correlated strongly with ground-based and sub-nanometer airborne SIF estimates acquired simultaneously. However, such narrow-band SIF estimates are overestimated, and their correct interpretation is critical, particularly in applications of plant phenotyping and precision agriculture. Therefore, work is needed to develop methods based on radiative transfer models (RTMs) to accurately quantify SIF from narrow-band hyperspectral imagers.

Light re-absorption and scattering within the canopy, which is driven by vegetation structure and plant pigments, have a

strong influence on the top of canopy (TOC) SIF [8], [9]. Global sensitivity analyses using SCOPE [10] identified leaf chlorophyll content (C_{a+b}), leaf area index (LAI), and the leaf inclination distribution parameter ($LIDF_a$) as key variables driving the majority of SIF variability [11]. The current study makes progress on the development of modelling methods that account for the spectral resolution when estimating SIF at 1 nm resolution from narrow-band hyperspectral imagery. Leaf biochemistry and structural traits derived from SCOPE model inversions were used as inputs in a modelling approach to assess their impact on the SIF estimates obtained from a narrow-band imager. Sub-nanometer imagery collected concurrently was used for validation purposes to assess the model performance.

2. MATERIALS AND METHODS

2.1. Experimental and simulated datasets

2.1.1. Airborne hyperspectral imagery

On 9 October 2019 an airborne campaign was conducted over a field trial site in Yarrawonga (36°02′55"S, 145°59′02"E), Australia, under clear sky conditions. Several varieties of dryland wheat were grown under varying physiological conditions induced by a range of nitrogen fertilizer application rates. A narrow-band hyperspectral imager (Hyperspec VNIR E-Series model, Headwall Photonics, Fitchburg, MA, USA) in the 400–1000 nm spectral region with 5.8 nm FWHM resolution and a sub-nanometer hyperspectral imager (Hyperspec Fluorescence sensor, Headwall Photonics, Fitchburg, MA, USA) in the 670–780 nm spectral region with 0.1–0.2 nm FWHM were installed in tandem on a Cessna 172R aircraft operated by the HyperSens Laboratory, University of Melbourne's Airborne Remote Sensing Facility. The total incoming irradiance was measured with a 0.065-nm FWHM HR-2000 spectrometer (Ocean Insight, Dunedin, FL, USA) equipped with a CC-3 VIS-NIR cosine corrector diffuser. Mean radiance spectra corresponding to both hyperspectral imagers and reflectance spectra from the narrow-band hyperspectral imager were extracted from pure vegetation pixels identified within individual plots. Radiance and reflectance spectra were used to quantify SIF and estimate plant traits by radiative transfer, respectively (Fig. 1). A full description of the airborne campaign, data preprocessing and image correction can be found in Belwalkar *et al.* [7].

2.1.2. SCOPE model simulations

Simulations were carried out using the SCOPE model (version 2.0), which integrates three radiative transfer modules and an energy balance module to estimate outgoing radiation spectra, reflectance and chlorophyll fluorescence [10]. A training dataset of 10,000 simulations and a test dataset of 1,000 simulations were generated independently by randomly varying specific input parameters drawn from a uniform distribution. The following ranges were set based on field measurements and from the existing literature: C_{a+b} [10–70] µg/cm^2, LAI [0.5–5] m^2/m^2, $LIDF_a$ [-1 to 1], leaf carotenoid content (C_{x+c}) [1–20] µg/cm^2, leaf anthocyanins content (Anth.) [0–8] µg/cm^2, leaf dry matter content (C_{dm}) [0.001–0.05] g/cm^2, leaf water content (C_w) [0.001–0.05] cm, leaf structure parameter (N) [1–1.5], maximum carboxylation capacity (V_{cmo}) [30–110], and the bimodality of the leaf angle distribution ($LIDF_b$) as 0. All other SCOPE input parameters were left at their default settings. The air temperature and air pressure inputs were obtained from a portable weather station during the airborne campaign at the field trial site. The TOC spectra of total upwelling radiance, reflectance, SIF radiance, and corresponding irradiance were simulated for each case using SCOPE at the default 1.0-nm SR and 1.0-nm spectral sampling interval (SSI). All simulations were convolved to the narrow-band hyperspectral imager's wavelength range, SSI, and SR assuming a gaussian band spectral response function.

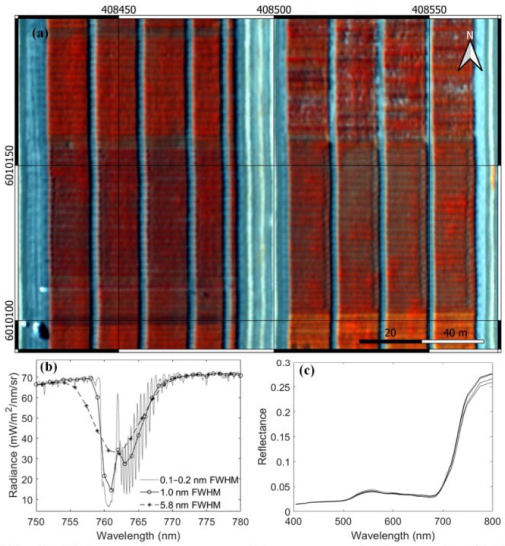

Fig. 1: Airborne hyperspectral image acquired over the field trial site. Airborne radiance (b) and reflectance (c) were used for SIF quantification and plant traits estimation using SCOPE model inversions. The 1.0 nm FWHM radiance shown in (b) were obtained by convolving the original sub-nanometer resolution (0.1–0.2 nm FWHM) spectra.

2.2. SIF quantification and inversion of plant traits

The radiance spectra extracted from the sub-nanometer imager were convolved to the default 1.0-nm SR and 1.0-nm SSI used in SCOPE (Fig. 1b). The resampled sub-nanometer-derived radiance was used to calculate the SIF

used as a reference against the SIF quantified from the narrow-band hyperspectral imager using the modelling approach proposed in this study. The O_2-A band *in-filling* approach was used to quantify SIF from both simulated and airborne datasets, employing the Fraunhofer Line Depth (FLD) principle with a total of three spectral bands (3FLD) [12]. The airborne SIF was further corrected and normalized to account for the atmospheric and directional effects, as described in Belwalkar *et al.* [7]. A look-up table with 100,000 simulations was built by randomly varying the SCOPE input parameters with a uniform distribution within the ranges described in section 2.1.2. Reflectance spectra were matched with the spectral resolution of the narrow-band hyperspectral imager. The reflectance spectra from the SCOPE simulations and the narrow-band hyperspectral imager in the 400–800 nm spectral range (Fig. 1c) were used to estimate C_{a+b}, LAI, and $LIDF_a$ using an RTM-based hybrid inversion with random forest regression [13].

2.3. Estimation of SIF at 1 nm resolution from narrow-band airborne spectra

We evaluated two models for estimating SIF at 1 nm resolution from narrow-band 5.8 nm spectra. The slope and coefficient obtained from the linear relationship between 3FLD retrievals at 1 nm and 5.8 nm from the SCOPE simulated training dataset were used to scale narrow-band SIF retrievals to 1 nm SR in the first model, named here as the linear model. The second model was based on an SVR built using the simulated training dataset, with i) narrow-band SIF quantified using the 3FLD method, and ii) SCOPE-derived C_{a+b}, LAI, and $LIDF_a$ as inputs. The SVR model was first trained in parallel (MATLAB parallel computing toolbox) using a radial basis function and optimizing the hyperparameters during training to predict SIF at 1 nm SR. A 10-fold cross-validation strategy was employed to avoid overfitting on the training samples.

The performance of both models was evaluated using root mean square error (RMSE) and normalized root mean square error (nRMSE) as metrics. The estimated SIF from the simulated test dataset was compared against the reference SCOPE modelled SIF. Additionally, both models were evaluated on the airborne datasets to test the applicability of the models on the experimental data. The SCOPE-based hybrid inversion retrieved the three leaf biochemistry and structural traits. Airborne SIF estimated at 1 nm FWHM from the 5.8 nm spectra was compared against the resampled sub-nanometer SIF, and error metrics were calculated.

3. RESULTS

Fig. 2 shows the range of variation for the leaf traits estimated from the airborne reflectance data using the SCOPE-based hybrid inversion approach. C_{a+b} exhibited the most significant variability across the experimental plots, attributed to the changes in physiological conditions and nitrogen fertilizer application rates.

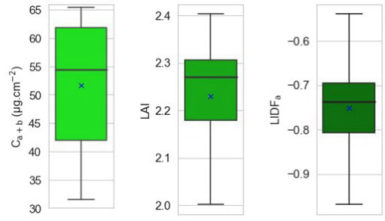

Fig. 2: Range of variation associated with C_{a+b}, LAI and $LIDF_a$ estimated from airborne hyperspectral reflectance. The median and mean values are denoted by a black line within the box, and the marker '×', respectively.

The predicted SIF using both linear and SVR models from SCOPE simulated data showed significant relationships with the reference 1 nm FWHM SIF (R^2>0.9, p<0.001; Fig. 3a and 3b). The SVR model outperformed (nRMSE=8.82%) the linear model (nRMSE=12.16%), but the slope of the linear relationship remained close to 1 for both models.

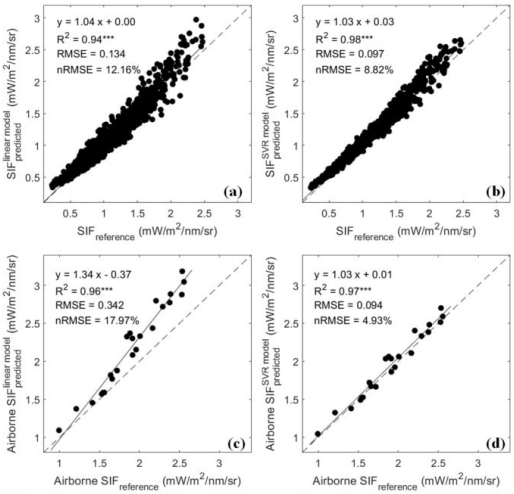

Fig. 3: Relationships between the 1 nm FWHM SIF simulated by SCOPE (used here as the reference SIF) and the SIF estimated by the linear model (a) and by the SVR model (b) from 5.8 nm FWHM spectra. Relationships between the airborne SIF quantified from the sub-nanometer imager and the airborne SIF at 1 nm FWHM estimated by the linear model (c) and SVR model (d) from the 5.8 nm narrow-band airborne spectra. **p-value<0.05; **p-value<0.01; ***p-value<0.001.*

The linear model consistently overestimated the SIF estimated from the narrow-band airborne hyperspectral data, as expected, which was more pronounced for higher SIF values (nRMSE=17.97%, $p<0.001$; Fig. 3c). In contrast, the predicted airborne SIF at 1 nm FWHM from the airborne 5.8 nm FWHM spectra using the SVR model demonstrated strong agreement with the sub-nanometer derived airborne SIF used as reference (nRMSE=4.93%, $p<0.001$; Fig. 3d) and was closer to the 1:1 line.

These results suggest that the 5.8 nm FWHM SIF estimates can be scaled to 1 nm resolution using SCOPE radiative transfer modelling techniques and plant-retrieved parameters. These findings also indicate that machine learning models built with leaf and canopy biochemistry and structural traits in addition to narrow-band SIF quantification can improve the SIF retrieval to match the absolute levels of fluorescence expected at 1-nm resolution.

4. CONCLUSIONS

This study investigated the estimation of SIF at 1 nm FWHM from narrow-band airborne hyperspectral radiance collected at 5.8 nm FWHM using RTM modelling techniques. SIF predictions at 1 nm resolution were carried out with an SVR regression model using SCOPE-simulated narrow-band SIF data and leaf biochemical and canopy structural traits as inputs. The model was validated using simulated and experimental airborne SIF imagery acquired at 0.1–0.2 nm FWHM resolution. Results showed strong agreement with both simulated and experimental airborne datasets, with RMSEs lower than 0.1 $mW/m^2/nm/sr$. These findings suggest that RTM-based modelling methods applied to airborne hyperspectral imagers with >1 nm FWHM resolution, which are commonly used in precision agriculture, enable the retrieval of SIF at appropriate absolute physical levels, avoiding the overestimation typically obtained by lower spectral resolution instruments.

5. ACKNOWLEDGEMENTS

The authors would like to thank the Foundation for Arable Research Australia and Riverine Plains Incorporated for providing and managing the plot trials. A. Gracia-Romero and A. Longmire are acknowledged for their technical assistance during the field and airborne campaign.

6. REFERENCES

[1] G. H. Mohammed et al., "Remote sensing of solar-induced chlorophyll fluorescence (SIF) in vegetation: 50 years of progress," *Remote Sens. Environ.*, vol. 231, Sep. 2019.

[2] P. J. Zarco-Tejada et al., "Previsual symptoms of Xylella fastidiosa infection revealed in spectral plant-trait alterations," *Nat. Plants*, vol. 4, no. 7, pp. 432–439, Jul. 2018.

[3] U. Rascher et al., "Sun-induced fluorescence - a new probe of photosynthesis: First maps from the imaging spectrometer HyPlant," *Glob. Chang. Biol.*, vol. 21, no. 12, pp. 4673–4684, Dec. 2015.

[4] C. Panigada et al., "Fluorescence, PRI and canopy temperature for water stress detection in cereal crops," *Int. J. Appl. Earth Obs. Geoinf.*, vol. 30, no. 1, pp. 167–178, 2014.

[5] P. J. Zarco-Tejada et al., "Divergent abiotic spectral pathways unravel pathogen stress signals across species," *Nat. Comm.*, vol. 12, no. 1, Dec. 2021.

[6] A. Damm et al., "Far-red sun-induced chlorophyll fluorescence shows ecosystem-specific relationships to gross primary production: An assessment based on observational and modeling approaches," *Remote Sens. Environ.*, vol. 166, pp. 91–105, Sep. 2015.

[7] A. Belwalkar, T. Poblete, A. Longmire, A. Hornero, R. Hernandez-Clemente and P. J. Zarco-Tejada, "Evaluation of SIF retrievals from narrow-band and sub-nanometer airborne hyperspectral imagers flown in tandem: Modelling and validation in the context of plant phenotyping," *Remote Sens. Environ*., vol. 273, May 2022.

[8] B. Dechant et al., "Canopy structure explains the relationship between photosynthesis and sun-induced chlorophyll fluorescence in crops," *Remote Sens. Environ.*, vol. 241, May 2020.

[9] Y. Zeng, G. Badgley, B. Dechant, Y. Ryu, M. Chen, and J. A. Berry, "A practical approach for estimating the escape ratio of near-infrared solar-induced chlorophyll fluorescence," *Remote Sens. Environ.*, vol. 232, Oct. 2019.

[10] C. van der Tol, W. Verhoef, J. Timmermans, A. Verhoef, and Z. Su, "An integrated model of soil-canopy spectral radiances, photosynthesis, fluorescence, temperature and energy balance," *Biogeosciences*, vol. 6, pp. 3109–3129, 2009.

[11] J. Verrelst, J. P. Rivera, C. van der Tol, F. Magnani, G. Mohammed, and J. Moreno, "Global sensitivity analysis of the SCOPE model: What drives simulated canopy-leaving sun-induced fluorescence?," *Remote Sens. Environ.*, vol. 166, pp. 8–21, Sep. 2015.

[12] J. A. Plascyk and F. C. Gabriel, "The Fraunhofer Line Discriminator MKII-An Airborne Instrument for Precise and Standardized Ecological Luminescence Measurement," *IEEE Trans. Instrum. Meas.*, vol. 24, no. 4, pp. 306–313, Dec. 1975.

[13] C. Camino et al., "Detection of Xylella fastidiosa in almond orchards by synergic use of an epidemic spread model and remotely sensed plant traits," *Remote Sens. Environ.*, vol. 260, Jul. 2021.

Appendix G: Conference paper 3

This appendix contains the author-accepted manuscript of the IGARSS Conference paper 3. Below is the bibliographic detail.

Belwalkar, A., Poblete, T., Hornero, A., Zarco-Tejada, P.J., 2023. **Evaluating the relative contribution of Photosystems I and II for leaf nitrogen estimation using fractional depth of Fraunhofer lines and SIF derived from sub-nanometer airborne hyperspectral imagery**. In: Proc. IEEE International Geoscience and Remote Sensing Symposium (IGARSS), 16–21 July 2023, Pasadena, CA, USA, pp. 2819–2822.

EVALUATING THE RELATIVE CONTRIBUTION OF PHOTOSYSTEMS I AND II FOR LEAF NITROGEN ESTIMATION USING FRACTIONAL DEPTH OF FRAUNHOFER LINES AND SIF DERIVED FROM SUB-NANOMETER AIRBORNE HYPERSPECTRAL IMAGERY

A. Belwalkar[1], T. Poblete[1,2], A. Hornero[1,3], P.J. Zarco-Tejada[1,2,3]

[1]Department of Infrastructure Engineering, Faculty of Engineering and Information Technology (FEIT), The University of Melbourne, Melbourne, Victoria, Australia
[2]School of Agriculture, Food and Ecosystem Sciences (SAFES), Faculty of Science (FoS), The University of Melbourne, Melbourne, Victoria, Australia
[3]Instituto de Agricultura Sostenible (IAS), Consejo Superior de Investigaciones Científicas (CSIC), Alameda del Obispo s/n, 14004 Córdoba, Spain

ABSTRACT

Integrating far-red solar-induced chlorophyll fluorescence (SIF_{760}) and leaf biochemical constituents (primarily leaf chlorophyll content (C_{a+b})) has recently been demonstrated to improve the estimation of leaf nitrogen (N) concentration from airborne and spaceborne hyperspectral imagery in homogenous and heterogeneous crop canopies. The advent of sub-nanometer resolution imagers capable of detecting narrow solar Fraunhofer lines (FLs) has enabled a novel opportunity to investigate the prospect of leaf N estimation using individual FLs in addition to SIF_{760} and C_{a+b} traits. This study seeks to determine whether incorporating distinct FL depth derived from sub-nanometer airborne hyperspectral imagery could improve leaf N estimates. A sub-nanometer hyperspectral imager with ≤0.2 nm full-width at half-maximum (FWHM) resolution was flown in tandem with a narrow-band hyperspectral imager with 5.8 nm FWHM over a winter wheat field. Plots were fertilized with variable concentrations of nitrogen to enable nutrient variability. Regression models utilizing Gaussian process regression (GPR) were built with different permutations of SIF, C_{a+b} and depths of individual FLs for estimating leaf N concentration. Laboratory-determined leaf N estimates were obtained by destructive sampling. Results show that GPR models incorporating the depth of distinct Fraunhofer lines as predictor variables performed better than the benchmark model constructed using C_{a+b} and SIF_{760} alone. The best leaf N-estimation model built with FLs from the red and far-red regions (C_{a+b}, $FL_{682.97\ nm}$, $FL_{757.002\ nm}$) yielded an R^2 of 0.71, outperforming the standard approach used in previous works (C_{a+b}, SIF_{760}) ($R^2 = 0.56$).

Index Terms— Airborne, Hyperspectral, SIF, GPR, leaf Nitrogen, Fraunhofer lines, sub-nanometer

1. INTRODUCTION

Nitrogen is a macronutrient that plays a crucial role in plant development, yield and grain quality, whilst it is often the dominant limiting factor in photosynthesis [1], [2]. Accurate field-wide assessments of leaf N concentration (N%) enable more targeted use of N-fertilizers, thereby mitigating the environmental effects of N-overfertilization while improving crop yields. Standard destructive sampling for leaf N determination relies on the laboratory analysis of leaf tissue using methods such as Kjeldahl digestion and Dumas combustion. Although accurate, these techniques are time-consuming and expensive for monitoring the leaf N status of large areas. In recent decades, the use of remote sensing technologies has increased, particularly through hyperspectral imagery, for mapping the spatial and temporal variations of crop leaf N concentration at the paddock scale [3]. There are three main categories of leaf N estimation approaches: 1) empirical methods, 2) physically-based model inversion methods, and 3) hybrid regression methods. Among these approaches, hybrid regression methods integrate physically-based models with advanced machine learning (ML) algorithms taking advantage of both the physical basis provided by radiative transfer models (RTMs) and the adaptability and efficiency of ML methods [4].

Recent studies utilizing narrow-band airborne and spaceborne hyperspectral imagers have demonstrated that accurate determination of leaf N concentration is feasible by combining the RTM-derived leaf biochemical constituents with SIF_{760} acquired from high-resolution airborne hyperspectral imagery [5]–[7]. Even though these studies have demonstrated improved leaf N retrievals when including SIF_{760}, the potential of other spectral regions within the 650-800 nm SIF emission region to characterize both PSI and PSII photosystems has not yet been explored. Moreover, the potential information extracted from the red spectral region, i.e. SIF quantified at the O_2-B absorption

band centered around 687 nm (SIF_{687}) and the depth of solar FLs, which are absorption lines in the solar spectrum, could provide valuable insights for improved characterization of photosynthesis and leaf N variability. With the recently developed sub-nanometer resolution airborne hyperspectral imagers, it is now possible to investigate the potential of these narrow FLs within the SIF emission region. This study aims to assess the relative contribution of the solar-induced chlorophyll fluorescence emitted by each of the two photosystems (PSI and PSII) in explaining leaf N variability across the field. SIF_{760}, SIF_{687} and the fractional depth of distinct solar FLs inside PSI and PSII emission regions derived from sub-nanometer airborne hyperspectral imagery are evaluated.

2. MATERIALS AND METHODS

2.1. Study site and airborne hyperspectral imagery

An airborne campaign operated by the HyperSens Laboratory at the University of Melbourne's Airborne Remote Sensing Facility was conducted on 9 October 2019 over a phenotyping trial site in Yarrawonga (36°02′55"S, 145°59′02"E), Australia. Several cultivated varieties of rainfed wheat were grown under varying physiological conditions and N fertilization treatments. A sub-nanometer hyperspectral imager (FWHM ≤0.2 nm; 670–780 nm) and a narrow-band hyperspectral imager (FWHM = 5.8 nm; 400–1000 nm) (Headwall Photonics Inc., Fitchburg, MA, USA) were used to collect airborne hyperspectral imagery at 20 cm spatial resolution. Concurrent with the flights, ground measurements were conducted using a CC-3 VIS-NIR cosine corrector diffuser attached to an HR-2000 spectrometer (Ocean Insight, Dunedin, FL, USA) with a 0.065-nm FWHM for continuous measurement of the total incident radiation at the trial site. Pure vegetation pixels were extracted within individual plots, and mean radiance spectra corresponding to the sub-nanometer imager and reflectance spectra from the narrow-band hyperspectral imager were retrieved. Belwalkar *et al.* [8] provide a full description of the airborne campaign, data preprocessing, and image correction. In addition, the total leaf N concentration (%) was destructively determined in the laboratory using the Kjeldahl method, with samples consisting of 10–15 leaves randomly selected per plot.

2.2. SIF quantification and identification of Fraunhofer lines

The irradiance spectra obtained from the HR-2000 spectrometer were convolved to the spectral characteristics of the sub-nanometer imager using Gaussian convolution. Using this convolved irradiance and the mean radiance derived from each plot, SIF_{760} and SIF_{687} were quantified using the *in-filling* approach, employing the Fraunhofer Line Depth (FLD) principle with a total of three spectral bands (3FLD) [9]. Furthermore, we identified 17 FLs across the 670–780 nm spectral range of the sub-nanometer imager, excluding regions of significant water vapour and oxygen absorption [10]. The identified FLs were divided into two groups according to their positions in the spectral region. Five of these FLs were located in the red region of the spectrum (named here as red FLs), while the remaining twelve were located within the far-red region (named here as far-red FLs). The exact location of the band centres corresponding to all FLs, and the O_2-A and O_2-B oxygen absorption bands is illustrated in Fig. 1. For each FL, the absolute depth in radiance units was computed as the difference between the radiance at the left shoulder wavelength and the wavelength at the bottom of the FL. The left shoulder wavelength was selected by searching for the local maxima closest to the bottom FL wavelength within 1 nm.

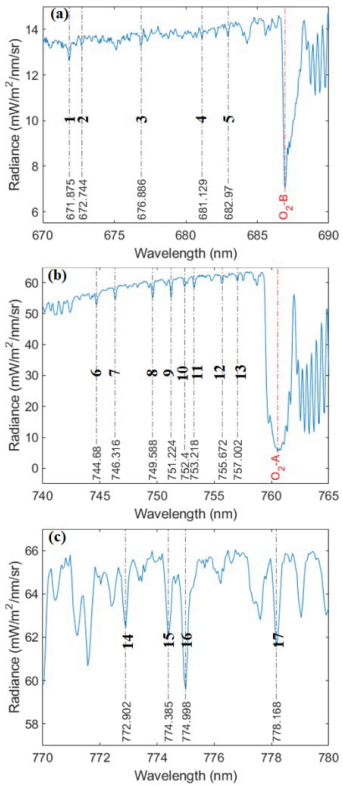

Fig. 1: Locations of the band centres corresponding to red FLs (a) and far-red FLs (b,c) shown in dashed black, and oxygen absorption lines (a,b) shown in dashed red identified from the average radiance spectra of one of the plots imaged by the sub-nanometer hyperspectral imager.

2.3. Regression model for N concentration estimation

We trained regression models based on GPR to empirically estimate leaf N concentration using C_{a+b}, SIF_{760}, SIF_{687} and the depth of distinct FLs as a pool of potential predictor variables. C_{a+b}, SIF_{760}, and depth corresponding to a single FL were used to initially train GPR models. Subsequently, GPR models were trained using C_{a+b}, and one FL depth each from the red and far-red FL groups on leaf N estimation to further examine the effect of using FL depths corresponding to both the red and far-red FL groups as predictor variables. The GPR models were trained in parallel (MATLAB parallel computing toolbox), and the hyperparameters were optimized by incorporating Bayesian optimization into the leave-one-out cross-validation (LOOCV). The performance evaluation of the trained GPR models was carried out using the coefficient of determination (R^2), root-mean-square error (RMSE) and normalized root-mean-square error (nRMSE). To limit random errors, for each possible combination of predictor variables, five GPR models were independently trained, and the average estimate was then used to determine R^2, RMSE and nRMSE.

Soil-Canopy Observation of Photosynthesis and Energy (SCOPE) [11] RTM-based hybrid inversion with random forest regression [12] was used to estimate C_{a+b} from the mean reflectance spectra obtained from the narrow-band hyperspectral imager in the 400-800 nm spectral region. To determine if the leaf N estimates could be further improved by including SIF emission regions other than the O_2-A absorption band, we used the GPR model developed with C_{a+b} and SIF_{760} as a benchmark. Then, we compared this benchmark by adding the depth of distinct solar FLs into the models. Since PSII largely influences the red spectral region, the contributions of SIF_{687} and red FLs would be attributed only to PSII. In contrast, the contributions of SIF_{760} and far-red FLs would be attributed to both photosystems.

3. RESULTS

GPR models trained with a single FL as one of the three predictor variables produced a total of 17 distinct GPR models (5 models for the red FL group and 12 models for the far-red FL group). Among the red FL group, the performance of the GPR model with FL_1 depth was comparable with the benchmark (R^2 = 0.56; RMSE = 0.229%; nRMSE = 5.89%; Fig. 2a and 2b), whereas the performance of the other four red FL depths did not improve the prediction. From the far-red FLs, the model that included FL_{13} depth showed the highest performance, outperforming the benchmark model (R^2 = 0.63; RMSE = 0.21%; nRMSE = 5.41%; Fig. 2c). Since FL_{13} performed the best among all red and far-red FLs, for the next set of GPR models with two FLs and C_{a+b} as predictors, we selected FL_{13} among the far-red FLs and independently evaluated all five red FLs as potential GPR model predictors. When compared to the benchmark model, the GPR model trained with FL_5 (682.97 nm) and FL_{13} (757.002 nm) substantially improved the leaf N estimation (R^2 = 0.71; RMSE = 0.188%; nRMSE = 4.84%; Fig. 2d) with more data points closer to the 1:1 line. The model's performance did not improve further after including more FLs from either of the two FL groups. Furthermore, we found that the model's performance decreased by including SIF_{687} with any combination of predictor variables. This result could be potentially attributed to the high collinearity observed between C_{a+b} and SIF_{687}.

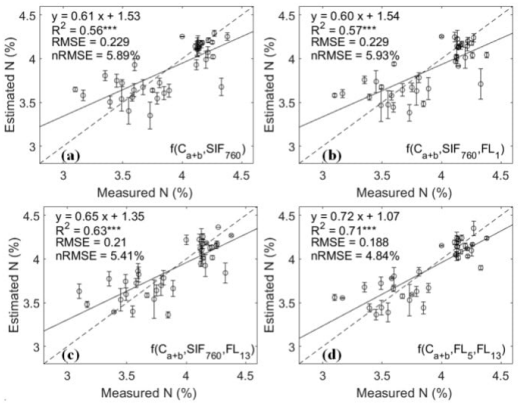

Fig. 2: Measured vs estimated mean leaf N concentration using the best GPR models as a function of C_{a+b} and SIF_{760} (a), C_{a+b}, SIF_{760} and best performing red FL (b), C_{a+b}, SIF_{760} and best performing far-red FL (c), C_{a+b} and best-performing combination of one red and one far-red FL (d). The dashed line indicates the 1:1 line. The error bars indicate the standard deviation based on five runs of the GPR model. The GPR model as a function of C_{a+b} and SIF_{760} was used as a benchmark. ***p-value<0.05.

Our results suggest that FL depths corresponding to 757.002 nm (FL_{13}) and 682.97 nm (FL_5), in conjunction with C_{a+b} estimated by RTM simulations, provided improved estimates of leaf N concentration. These results provide a foundation for future research into the use of FLs identified in sub-nanometer imagery in the context of precision agriculture and plant physiology monitoring. Future work will focus on evaluating their potential for identifying pre-visual signs of vegetation stress.

4. CONCLUSIONS

This study evaluated the capability of 17 narrow solar Fraunhofer lines depth derived from sub-nanometer imagery to estimate leaf N concentration when combined with C_{a+b} and SIF_{760}. With an RMSE of less than 0.19%, the best

results were achieved by the regression model constructed using C_{a+b}, red FL closest to O_2-B band (682.97 nm), and far-red FL closest to O_2-A band (757.002 nm). These results highlight the importance of integrating FLs around the two oxygen absorption bands for more accurate leaf N estimates. Furthermore, the proposed approach based on the depth of distinct FLs demonstrates the importance of sub-nanometer resolution imaging sensors for vegetation trait retrievals, supporting the need for future research focused on the entire SIF emission region for physiological assessment and vegetation stress detection.

5. ACKNOWLEDGEMENTS

The Foundation for Arable Research Australia and Riverine Plains Incorporated provided and managed the plot trials, which the authors gratefully acknowledge. We thank A. Gracia-Romero and A. Longmire for their technical support during the field and airborne campaign.

6. REFERENCES

[1] J. R. Evans, "Photosynthesis and nitrogen relationships in leaves of C3 plants," Oecologia, vol. 78, no. 1, pp. 9–19, 1989.

[2] G. Lemaire, M. H. Jeuffroy, and F. Gastal, "Diagnosis tool for plant and crop N status in vegetative stage: Theory and practices for crop N management," European Journal of Agronomy, vol. 28, no. 4, pp. 614–624, May 2008.

[3] K. Berger et al., "Crop nitrogen monitoring: Recent progress and principal developments in the context of imaging spectroscopy missions," Remote Sensing of Environment, vol. 242, June 2020.

[4] J. Verrelst et al., "Quantifying Vegetation Biophysical Variables from Imaging Spectroscopy Data: A Review on Retrieval Methods," Surveys in Geophysics, vol. 40, no. 3, pp. 589–629, May 2019.

[5] Y. Wang, L. Suarez, T. Poblete, V. Gonzalez-Dugo, D. Ryu, and P. J. Zarco-Tejada, "Evaluating the role of solar-induced fluorescence (SIF) and plant physiological traits for leaf nitrogen assessment in almond using airborne hyperspectral imagery," Remote Sensing of Environment, vol. 279, Sep. 2022.

[6] Y. Wang, L. Suarez, V. Gonzalez-Dugo, D. Ryu, P. Moar and P. J. Zarco-Tejada, "Leaf nitrogen assessment with ISS DESIS Imaging Spectrometer as compared to high-resolution airborne hyperspectral imagery," in IEEE International Geoscience and Remote Sensing Symposium, Kuala Lumpur, Malaysia, pp. 5444–5447, 17–22 July 2022.

[7] C. Camino, V. González-Dugo, P. Hernández, J. C. Sillero, and P. J. Zarco-Tejada, "Improved nitrogen retrievals with airborne-derived fluorescence and plant traits quantified from VNIR-SWIR hyperspectral imagery in the context of precision agriculture," International Journal of Applied Earth Observation and Geoinformation, vol. 70, pp. 105–117, Aug. 2018.

[8] A. Belwalkar, T. Poblete, A. Longmire, A. Hornero, R. Hernandez-Clemente, and P. J. Zarco-Tejada, "Evaluation of SIF retrievals from narrow-band and sub-nanometer airborne hyperspectral imagers flown in tandem: Modelling and validation in the context of plant phenotyping," Remote Sensing of Environment, vol. 273, May 2022.

[9] S. W. Maier, K. P. Gunther, and M. Stellmes, "Sun-Induced Fluorescence: A New Tool for Precision Farming," In: Digital Imaging and Spectral Techniques: Applications to Precision Agriculture and Crop Physiology, Vol. 66 (eds M McDonald, J Schepers, L Tartly, T Van Toai, D Major), ASA Spec. Publ., Madison, WI, USA, pp. 209– 222, 2003.

[10] L. P. Albert, K. C. Cushman, Y. Zong, D. W. Allen, L. Alonso, and J. R. Kellner, "Sensitivity of solar-induced fluorescence to spectral stray light in high resolution imaging spectroscopy," Remote Sensing of Environment, vol. 285, Feb. 2023.

[11] C. van der Tol, W. Verhoef, J. Timmermans, A. Verhoef, and Z. Su, "An integrated model of soil-canopy spectral radiances, photosynthesis, fluorescence, temperature and energy balance," Biogeosciences, vol. 6, pp. 3109–3129, 2009.

[12] A. Belwalkar, T. Poblete, A. Hornero, and P. J. Zarco-Tejada, "Accounting for the spectral resolution on SIF retrieval from a narrow-band airborne imager using SCOPE," in IEEE International Geoscience and Remote Sensing Symposium, Kuala Lumpur, Malaysia, pp. 5440–5443, 17–22 July 2022.